

TRACTION PREDICTION IN ROLLING/SLIDING EHL CONTACTS WITH REFERENCE FLUIDS

Von der Fakultät für Maschinenbau
der Gottfried Wilhelm Leibniz Universität Hannover
zur Erlangung des akademischen Grades

Doktor-Ingenieur

genehmigte Dissertation

von

M. Eng. HAICHAO LIU

geboren am 26.09.1990 in Yantai, China

2020

1. Referent: Prof. Dr. -Ing. Gerhard Poll
2. Referent: Prof. Dr. Ir. Cornelis Henricus Venner
Vorsitzender: Prof. Dr. -Ing. Stephan Kabelac
Tag der Promotion: 15.09.2020

HaiChao LIU: Traction Prediction in Rolling/Sliding EHL Contacts with Reference Fluids, Dissertation, © 2020.

Machine elements such as rolling bearings and gears transmit forces and permit relative motion in concentrated contacts, whereby elastohydrodynamic lubrication (EHL) plays a major role in surface protection. The friction/traction in a rolling/sliding EHL contact is hard to predict due to non-Newtonian rheology and concomitant thermal effects. In the last decade, much effort has been made to study the EHL traction using reference fluids. However, considerable discrepancies still exist between predictions and measurements.

This work continues the effort to predict the EHL traction with model fluids (mainly with squalane) and investigates the influence factors that lead to the differences between simulations and experiments. An EHL model has been developed for traction prediction accounting for non-Newtonian and thermal effects by embedding fluid models of thermo-physical-rheological properties (such as viscosity, thermal conductivity, shear thinning, and limiting shear stress) supported by independent high-pressure measurements. On the experimental aspects, traction curves have been measured on two traction machines with different contact geometries, *i.e.* twin-disc and ball-on-disc.

Three factors have been found to complicate the accuracy of the EHL traction prediction, namely solid body temperature effect, thermal conductivity of solids and lubricants, and scale/geometrical effects. Firstly, the bulk temperature of specimens exceeds the supplied oil temperature during traction measurements. Bulk temperature has been adopted as thermal boundary condition in thermal EHL simulations and it has found that the solid body temperature reduces oil viscosity and then reduces the film thickness and traction. Secondly, solid and lubricant thermal conductivity affects heat conduction and the maximum temperature rise, as well as the traction. For lubricants, thermal conductivity doubles its value at about 1 GPa; for solids, recent measurements have shown that thermal conductivity of through-hardened 52100 bearing steel should be around 21 W/mK rather than the widely cited 46 W/mK in literature. The effects of both solid and liquid thermal conductivity are analyzed. Thirdly, the traction curves measured from the two traction rigs for the same fluid are different at comparable operating conditions, *i.e.* at the same pressure, speed and supplied oil temperature. This phenomenon has been studied through thermal EHL analysis and it shows that the reason lies in the difference in the reduced radius of curvature which affects the film thickness and the heat distribution of the two traction machines. For a thicker EHL film thickness, shear is mainly localized in the middle film due to a temperature-viscosity gradient across the film. The scale effect studied here belongs to thermal effects.

For practical traction predictions, a simplified traction calculation method for highly loaded rolling/sliding EHL contacts has been developed without solving the Reynolds equation and the surface deformation equation. Using a bilinear limiting shear stress model extracted from traction experiments, the discrepancy between measurements and numerical simulations is smaller than 15% over a wide range of operating conditions (*e.g.* velocity, pressure, and slide-to-roll ratio), which is mainly caused by the solid body temperature effect.

Keywords:

Elastohydrodynamic Lubrication; Lubricant Rheology; Traction; Rolling/Sliding Contact; Thermal Effect; Non-Newtonian; Limiting Shear Stress

Zusammenfassung

Maschinenelemente wie Wälzlager und Zahnräder übertragen Kräfte und ermöglichen Relativbewegungen über konzentrierte Kontakte, bei denen die elasto-hydrodynamische Schmierung (EHL) eine wichtige Rolle zum Schutz der Oberflächen spielt. Die EHL-Reibung/Traktion in einem rollenden/gleitenden EHL-Kontakt ist aufgrund der nicht-Newtonschen Rheologie und der thermischen Effekte schwer vorherzusagen. In den letzten zehn Jahren wurden große Anstrengungen unternommen, um die EHL-Traktion mit Modellflüssigkeiten zu untersuchen. Es bestehen jedoch immer noch erhebliche Diskrepanzen zwischen Vorhersagen und Messungen.

Diese Arbeit setzt die Vorhersage der EHL-Traktion mit Referenzflüssigkeiten (hauptsächlich mit Squalan) fort und untersucht die Einflussfaktoren, die zu den Unterschieden zwischen Simulationen und Experimenten führen. Es wurde ein EHL-Modell für die Traktionsvorhersage entwickelt, das nicht-Newtonsche und thermische Effekte berücksichtigt, indem Fluidmodelle für thermophysikalisch-rheologische Eigenschaften genutzt werden. Deren Druckabhängigkeit wurde durch unabhängige Hochdruckmessungen von Viskosität, Wärmeleitfähigkeit, Scherverdünnung und Grenzschubspannung ermittelt. Unter experimentellen Gesichtspunkten wurden Traktionskurven an zwei Traktionsmaschinen mit unterschiedlichen Kontaktgeometrien gemessen, d. h. Zwei-Scheiben und Kugel-Scheibe Geometrie.

Es wurde festgestellt, dass drei Faktoren die Genauigkeit der EHL-Traktionsvorhersage erschweren, nämlich der Festkörpertemperatureffekt, die Wärmeleitfähigkeit von Feststoffen und Schmiermitteln und der Skaleneffekt. Erstens überschreitet die Massentemperatur der Proben während der Traktionsmessungen die zugeführte Öltemperatur. Die Massentemperatur wurde als Randbedingung in thermischen EHL-Simulationen übernommen und somit festgestellt, dass die Festkörpertemperatur die Ölviskosität verringert und damit Schmierfilmdicke und Traktion verringert. Zweitens beeinflusst die Wärmeleitfähigkeit von Feststoffen und Schmierstoffen die Wärmeleitung und den Anstieg der Blitz/Flash-Temperatur und damit die Traktion. Bei Schmierstoffen verdoppelt die Wärmeleitfähigkeit ihren Wert bei etwa 1 GPa. Jüngste Messungen haben gezeigt, dass die Wärmeleitfähigkeit von durchgehärtetem 52100-Lagerstahl (100Cr6) eher bei 21 W/mK als bei den in der Literatur häufig zitierten 46 W/mK liegt. Drittens zeigen die verwendeten zwei Traktionsexperimente unterschiedliche Traktionskurven für dasselbe Fluid bei vergleichbaren Betriebsbedingungen, d. h. bei identischem Druck, Geschwindigkeit und zugeführter Öltemperatur. Durch thermische EHL-Analyse konnte ermittelt werden, dass der Grund im unterschiedlichen reduzierten Krümmungsradius und damit in der Filmdicke und Wärmeverteilung der beiden Traktionsmaschinen liegt. Der hier untersuchte Skaleneffekt gehört zu den thermischen Effekten.

Für praktische Traktionsvorhersagen wurde eine vereinfachte Traktionsberechnungsmethode für hochbelastete Wälzkontakte entwickelt, ohne die Reynolds-Gleichung und die Oberflächenverschiebungsgleichung zu lösen. Der Fehler zwischen Messungen und Vorhersagen ist über einen weiten Bereich von Betriebsbedingungen kleiner als 15%, was hauptsächlich auf den untersuchten Festkörpertemperatureffekt zurückzuführen ist.

Schlagworte:

Elastohydrodynamische Schmierung, Schmiermittelrheologie, Traktion, Wälzkontakt, thermischer Effekt, nicht-Newtonsche, Grenzschubspannung

Publications

This dissertation focuses on the study of friction/traction in rolling/sliding EHL contacts. The main chapters and many figures have been reported in the following publications:

Journal Paper

1. Liu HC, Zhang BB, Bader N, Venner CH, Poll G. (2020): Scale and Contact Geometry Effects on Friction in Thermal EHL: Twin-disc versus Ball-on-disc, *Tribology International*, DOI: 10.1016/j.triboint.2020.106694.
2. Liu HC, Zhang BB, Bader N, Venner CH, Poll G. (2020): Simplified Traction Prediction for Highly Loaded Rolling/Sliding EHL Contacts, *Tribology International*, DOI: 10.1016/j.triboint.2020.106335.
3. Liu HC, Zhang BB, Bader N, Poll G, Venner CH. (2020): Influences of Solid and Lubricant Thermal Conductivity on Traction in an EHL Circular Contact, *Tribology International*, DOI: 10.1016/j.triboint.2019.106059.
4. Liu HC, Zhang BB, Bader N, Guo F, Poll G, Yang PR. (2019): Crucial Role of Solid Body Temperature on Elastohydrodynamic Film Thickness and Traction, *Tribology International*, 131: 386-397. DOI: 10.1016/j.triboint.2018.11.006.

Conference Presentation

5. Liu HC, Zhang BB, Bader N, Li XM, Terwey T, Poll G. (2019): Fast Traction Prediction in Rolling/Sliding EHL Contacts. 46th Leeds-Lyon Symposium on Tribology, September 2nd-4th, 2019, Lyon, France. (oral presentation)
6. Liu HC, Zhang BB, Bader N, Terwey T, Poll G. (2019): Traction in Rolling/Sliding EHL Contacts, 3rd Young Tribological Researcher Symposium, May 9-10th, Vienna, Austria. (Poster)
7. Liu HC, Zhang BB, Bader N, Poll G. (2019): Influences of Thermal Conductivity on EHL Traction, 15. Arnold Tross Kolloquium 25. Mai 2019 Hamburg, Tagungsband, Erik Kuhn (Hrsg.) ISBN: 978-3-8440-7151-1. (oral presentation)
8. Liu HC, Zhang BB, Bader N, Poll G. (2018): On the Crucial Role of Solid Body Temperature in EHL Traction, 14. Arnold Tross Kolloquium 25. Mai 2018 Hamburg, Tagungsband, Erik Kuhn (Hrsg.) ISBN: 978-3-8440-6409-4. (oral presentation)
9. Liu HC, Zhang BB, Bader N, Terwey T, Poll G. (2018): A Quantitative TEHL Analysis of Point Contacts: Using Measured Rheological and Thermo-physical Data for Traction Prediction, 2nd Young Tribological Researcher Symposium, May 8-9th, Berlin. (oral presentation)
10. Bearing World (2018), *International Bearing Conference*, 6-7th March, 2018, Kaiserslautern, Germany. (audience only)

11. Liu HC, Guo F, Wong PL. (2017): Red-Green Laser Interferometry: a Novel Nano to Micro Lubricating Film Thickness Measurement Method, *1st Young Tribological Researcher Symposium, May 16-17th*, Hannover. (oral presentation)

Co-authored Contribution

Not included in this dissertation

12. Zhang BB, Liu HC, Quiñonez AF, Venner CH. (2020): Effects of 3D Anisotropic Heterogeneous Subsurface Topology on Film Thickness, Pressure, and Subsurface Stresses in an Elasto-Hydrodynamically Lubricated Point Contact, *Tribology International*, DOI: 10.1016/j.triboint.2020.106471.
13. Schneider V, Liu HC, Bader N, Furtmann A, Poll G. (2020): Empirical Formulae for the Influence of the Realistic Film Thickness Distribution on the Capacitance of an EHL Point Contact and Applications to Rolling Bearings, *Tribology International*, DOI: 10.1016/j.triboint.2020.106714.
14. Bader N, Liu HC, Zhang BB, Poll G. (2019): Film Thickness Measurements in EHL-Contacts Using Capacitance Measurements. *46th Leeds-Lyon Symposium on Tribology, September 2nd-4th, 2019*, Lyon, France. (Poster)
15. Bader N, Liu HC, Furtmann A, Zhang BB, Poll G (2018): Capacitance Measurement of Film Thickness in EHL contacts, *Proceedings, 21st International Colloquium Tribology, TAE, Esslingen, 9-12. Januar 2018, Germany*, S. 77-78. ISBN: 9783943563337.
16. Terwey JT, Bader N, Liu HC, Poll G. (2018): Efficient Calculation of EHL Traction Using Simplified Approaches and Test Results, *59. Tribologie-Fachtagung 2018, Reibung, Schmierung und Verschleiß, Forschung und praktische Anwendung, Tagungsband 1*, ISBN: 978-3-9817451-3-9.

Acknowledgements

This study was carried out during my time as a research assistant at the Institute of Machine Design and Tribology (IMKT), Gottfried Wilhelm Leibniz Universität Hannover. The project was funded by China Scholarship Council (CSC), AiF- the German Federation of Industrial Research Associations (Arbeitsgemeinschaft industrieller Forschungsvereinigungen “Otto von Guericke” e.V.), and FVV- the Research Association for Combustion Engines e.V. Germany. I would like to thank the following people, without whom I would not have been able to complete this research.

First of all, I would like to express the deepest gratitude to my supervisor Prof. Dr.-Ing. Gerhard Poll (head of IMKT): Thank you very much for your support, encouragement and patience throughout the last four years. Thank you for giving me the freedom to do the project and the opportunities to attend conferences. You are friendly, wise and creative. Each discussion with you is enjoyable.

I would like to thank Dr. Norbert Bader for your valuable discussions on high-pressure rheology, your continued support on twin-disc trouble-shooting, and the experiments and student assignments that we planned and carried out together. I would also like to thank Dr. BinBin Zhang at University of Twente for your continuous help on numerical methods. I want to thank M.Sc. Torben Terwey and M.Sc. Johannes Marx on doing IR temperature experiments together in 2019.

Many thanks to the committee members: Prof. C.H. Venner of EFD (Engineering Fluid Dynamics) of University of Twente, Prof. Stephan Kabelac of IFT (Institute of Thermodynamics) of University of Hannover for spending time and effort for my dissertation. I want to thank Prof. Venner for valuable discussions and for helping to improve the quality of my journal papers and this dissertation.

Many thanks also to the colleagues of IMKT for providing a nice working atmosphere. In particular, thanks Ms. Anna Bock, Ms. Nicole Busch, Dr. Ulrich Wischhöfer, Dr. Roman Böttcher, Dr. Florian Pape, Dr. Bengt Wennehorst, M.Eng. MuYuan Liu, M.Sc. Dilek Bulut, M.Sc. Josephine Kelley, M.Sc. Volker Schneider, M.Sc. Timm Coors, M.Sc. Tim Brieke, Dipl.-Ing. Veith Pelzer, M.Sc. Sebastian Wandel and Dipl.-Ing. Marius Niemeier for their kind help on many aspects.

I would like to thank the project partners in Tribological Fluid Model-II, especially Mr. Klaus Meyer of Bosch as chairman, Prof. Hubert Schwarze of Technical University Clausthal, and Prof. Dirk Bartel of Magdeburg University. I would also like to thank Prof. Philippe Vergne of INSA-Lyon, Dr. Marcus Björling of Luleå University of Technology for providing your traction curves; thank Prof. J.A. Greenwood of University of Cambridge for interesting discussions for developing simplified traction method; thank Dr. Xing Luo of IFT of University of Hannover for proof-reading of the thesis and his advices; thank Dr. Yuanyuan Zhang of Chongqing University for discussions on the influence of roughness to traction; thank Volkswagen, Wolfsburg for allowing us to use the MTM test rig.

I would like to thank the two visiting scholars, Dr. XinMing Li and Dr. QingHua Bai, from Qingdao University of Technology. I am extremely grateful for the interesting discussions with you and for sharing your experience and ideas with me. I also would like to express thanks to Prof. Feng Guo, Prof. PeiRan Yang and Dr. Ping Yang from Qingdao tribology group and Dr. George Wan TY (retired from Fuchs and SKF) for their personal support during my PhD study. I would like to thank Prof. Patrick Wong at City University of Hong Kong, Dr. Xia Li and Dr. JinLei Cui of QUTech for encouraging me to further the study.

Thanks Ms. SiMiao Yang and Mr. XiaoLei Shi, who wrote their bachelor/master thesis with me.

Finally, my deep and sincere gratitude to my girlfriend Ms. Yan Zhao and my family members (my parents, grandfather, sister Haili, brother-in-law Gordy, nephew Jacopo) for your continuous love, care, encouragement and support. Without you, this cannot be achieved.

HaiChao LIU

March 2020, in Hannover

Contents

Abstract	i
Zusammenfassung	iii
Publications	v
Acknowledgements	vii
Contents	ix
List of Figures	xiii
List of Tables	xix
Nomenclature	xxi
1 Introduction	1
1.1 Tribology, friction and sustainability	1
1.1.1 Tribology and the law of friction	1
1.1.2 Friction study and sustainability	2
1.2 Friction in lubricated contacts	2
1.2.1 Reynolds equation and fluid lubrication	2
1.2.2 Stribeck curve for conformal contacts	3
1.2.3 Stribeck curve for non-conformal contacts	3
1.2.4 Typical features of EHL contacts	4
1.3 Subject of this thesis	5
2 Fundamentals of EHL Traction	7
2.1 Quantitative EHL and traction experiments	7
2.1.1 Traction curve and regime	7
2.1.2 EHL philosophy	9
2.1.3 Traction curve measurements	11
2.2 Fluid model	17
2.2.1 Flow curve	17
2.2.2 Shear thinning	18
2.2.3 Limiting shear stress	24
2.2.4 Viscoelastic behavior	28
2.2.5 Density-pressure-temperature relation	30
2.2.6 Viscosity-pressure-temperature relation	32
2.2.7 Lubricant thermal properties	36
2.2.8 Model fluids and properties	37
2.3 Isothermal traction prediction- simplified methods	39
2.3.1 Assumptions	39

2.3.2	Hertzian contact theory	40
2.3.3	EHL film thickness	41
2.3.4	Isothermal traction computation	44
2.4	Thermal EHL Theory for Traction Prediction	44
2.4.1	Theoretical model	45
2.4.2	Governing equations: EHL part	46
2.4.3	Governing equations: thermal part	47
2.4.4	Numerical solutions	49
3	Motivation and Outline	53
4	Thermal Boundary Conditions and Solid Body Temperature Effect	55
4.1	Introduction	55
4.2	Theoretical EHL models	56
4.2.1	Thermal boundary conditions	56
4.2.2	Shear thinning rheological model	57
4.3	Numerical solution	57
4.4	Results and discussion	58
4.4.1	Solid body temperature effect in pure rolling EHL	59
4.4.2	Effect of solid body temperature effect in rolling/sliding	61
4.4.3	Effect of entrainment velocity	63
4.4.4	Film thickness prediction with empirical equations	65
4.5	Conclusions	66
5	Role of Solid and Liquid Thermal Conductivity on EHL Traction	69
5.1	Introduction	69
5.2	Theoretical model and numerical solution	70
5.3	Results and discussion	71
5.3.1	Effect of solid thermal conductivity	72
5.3.2	Effect of lubricant thermal conductivity	74
5.3.3	Traction comparison with experiments	76
5.3.4	Effect of thermal conductivity on film thickness	76
5.4	Outlook and Suggestions	77
5.5	Conclusions	78
6	Fast Traction Prediction Method for Highly Loaded EHL Contacts	79
6.1	Introduction	79
6.2	Simplified EHL traction model	81
6.2.1	Assumptions and governing equations	81
6.2.2	Properties of squalane	83
6.2.3	Maximum shear stress determination at different pressures	84

6.3 Simplified traction calculation method.....	86
6.3.1 Traction and temperature calculation method.....	86
6.3.2 Model validation.....	88
6.4 Results and discussion.....	89
6.4.1 Traction curves at 5 m/s.....	90
6.4.2 Traction curves at higher speeds.....	91
6.5 Possible mechanisms of friction reduction due to solid body temperature effect.....	94
6.6 Limitation of the method and outlook.....	94
6.7 Conclusions.....	95
7 Contact Geometry and Scale Effect on the EHL Traction.....	97
7.1 Introduction.....	97
7.2 Experimental and numerical methods.....	99
7.2.1 Experimental evidence of the scale effect.....	99
7.2.2 Theoretical EHL model.....	101
7.3 Results and discussion.....	102
7.3.1 Isothermal results.....	102
7.3.2 Thermal results.....	104
7.3.3 Comparison between experiments and simulations.....	109
7.4 Outlook.....	110
7.5 Conclusions.....	111
8 Conclusions and Recommendations for Future Work.....	113
8.1 Conclusions.....	113
8.2 Recommendations for future work.....	114
Appendix A Validation of the Non-Newtonian Thermal EHL Model.....	115
Appendix B Mesh Density on the Accuracy of Simulation Results.....	116
Appendix C Computational Zone (Depth) on the Accuracy of Simulation Results.....	117
Appendix D Infrared Temperature Measurements.....	118
Bibliography.....	121
Lebenslauf.....	131

List of Figures

Figure 1-1: Tribological practice in ancient times and in the course of human civilization. (a) drilling wood for fire; (b) evolution of wheels. A modern wheel unit includes axle, bearing, sealing, and lubricant. In ancient times, natural lubricants from vegetable and animal oil were used to reduce friction and noise.	1
Figure 1-2: Schematic of Stribeck curve (coefficient of friction against the Sommerfeld number or the lambda ratio) and the lubrication regimes (boundary lubrication, mixed lubrication, EHL, and HL). The horizontal arrow indicates the boundary between the adjacent regimes may shift in terms of operating conditions, for example speed.	3
Figure 1-3: Schematic of an EHL point contact formed between a ball and the raceway in a rolling element bearing (fully flooded condition is assumed; not to scale $a_{\text{Hertz}} \approx h_{\text{cen}} \times O(10^3)$).....	4
Figure 1-4: Contact pressure in some rolling/sliding EHL lubricated transmission components [the pressure values refer to Zhang, Spikes 2020].....	4
Figure 1-5: Maximum shear stress versus contact pressure for a variety of fluids [Jackson and Webster 2003; Wang and Zhu 2019].....	5
Figure 2-1: Schematic representation of a rolling/sliding EHL contact (xoz view; not to scale; Hertzian pressure distribution is assumed).....	7
Figure 2-2: Typical EHL traction curves measured on a twin-disc machine in a line contact showing different regimes of traction (data reproduced from Johnson and Cameron 1967).....	8
Figure 2-3: Typical traction curves predicted by the rheological model of $\dot{\gamma} = \frac{\dot{\tau}}{G} + \frac{\tau_c}{\mu} \sinh\left(\frac{\tau}{\tau_c}\right)$ together with a limiting shear stress (from Evans and Johnson 1986a; assuming the disc machine as a rheometer), solid line: isothermal; dashed line: with shear heating; (a) linear base; (b) logarithmic base.	9
Figure 2-4: Schematic representation of configurations and contact geometries of the used traction machines (left: twin-disc; right: ball-on-disc)	12
Figure 2-5: Raw traction data from twin-disc machine and the data processing methods to obtain a traction curve. (a) raw data from the four steps; (b) shift curve to coordinate (0, 0) to eliminate influence of supporting bearings; (c) a traction curve comprises the values from the four steps combining both the negative and the positive values. (Squalane, Twin-disc, $T_{\text{oil}} = 40 \text{ }^\circ\text{C}$, $u_e = 5 \text{ m/s}$, $p_H = 2.42 \text{ GPa}$).....	13
Figure 2-6: Typical traction curves at different pressure, speed and temperature conditions measured on a twin-disc machine, (a) pressure effect (5 m/s, 40 °C); (b) speed effect (1.95 GPa, 40 °C); (c) oil temperature effect (1.95 GPa, 5 m/s). (twin-disc, squalane).....	14
Figure 2-7: Representation of variation of friction coefficient with slide-to-roll ratio, <i>i.e.</i> traction curves at different pressure, temperature and speed.	15
Figure 2-8: Evolution of (a) disc body temperature and (b) friction coefficient with slide-to-roll ratio during three continuously repeated running cycles of traction curve measurements (SHC 320 gear oil, supplied oil temperature is 40 °C, 15 m/s, 20 kN, Hertzian pressure of 1.34 GPa, one curve generated during 7 mins, Ring-Roller-Ring configuration)	15
Figure 2-9: Thermal conductivity maps from FDTR method for the specimens of MTM traction rig made of 52100 steel, (a) steel disc; (b) steel ball. (color scale units: W/mK) [Reddyhoff <i>et al</i> 2019].....	16
Figure 2-10: The rheological flow curve (shear stress versus apparent shear rate on a log-log scale) for the naphthenic mineral oil LVI 260 measured with a pressurized Couette rheometer measured by Bair. The curve shows transitions from Newtonian to shear-thinning and then to rate-independent response (LSS). (Data reproduced from Bair 2002b).....	17

Figure 2-11: Flow curve (shear stress versus shear rate): non-linear shear response of a thin compressed liquid based on viscometer measurements at Georgia Tech, (a) linear base; (b) logarithmic base. Solid line: isothermal; dashed line: with shear heating.	18
Figure 2-12: Schematic representation of (a) the constitutive behavior and (b) the effective viscosity of shear thinning fluids. Note that μ is the low-shear (Newtonian) viscosity, while η^* is the high-shear viscosity or called the generalized Newtonian viscosity)	19
Figure 2-13: Influence of the parameter a , n and τ_c on the generalized viscosity versus reduced shear rate for the single Newtonian Carreau-Yasuda shear thinning model. (when $a = 2$, Carreau-Yasuda model becomes Carreau model)	20
Figure 2-14: Generalized viscosity with different shear thinning equations in power-law form: Carreau-Yasuda, Carreau, modified Carreau and Cross, (a) $n = 0.6$; (b) $n = 0.35$	20
Figure 2-15: (A) Flow curves plotted as shear stress versus shear rate for squalane obtained from experiments with a pressurized Couette viscometer (solid points) and from NEMD simulations (open points). (B) The same data replotted as shear stress versus reduced shear rate to obtain a master flow curve, Wi see Eq. (2.9)- Eq. (2.10). From Bair 2019a.	21
Figure 2-16: Influence of the Eyring shear stress on the generalized viscosity for the Eyring rheological model. A Carreau fluid is also plotted for comparison.	23
Figure 2-17: Evidences of limiting shear stress through traction measurements by Ndiaye <i>et al</i> 2017. (Shell T9 turbine mineral oil, performed at $T = 313$ K and $u_e = 1.3$ m/s, for Hertzian contact pressures from 0.75 to 3.0 GPa)	25
Figure 2-18: Pressure and temperature dependences of limiting shear stress measured by Ndiaye <i>et al</i> 2017 through traction measurements. (Shell T9 turbine mineral oil, performed at $T = 293$ -353 K and mean Hertzian contact pressure up to 2.0 GPa).	28
Figure 2-19: Variation of G_∞ with pressure and temperature for di(2-ethylhexyl) phthalate measured by Hutton and Phillips 1972.	29
Figure 2-20: Calculated friction coefficient shows that the elastic property of oil is not important for the EHL traction prediction when independently measured viscoelastic properties are used. Roller elastic creep affects the traction at small SRRs. (DOP, inlet temperature of 50 °C, Hertz pressure of 1.3 GPa, rolling velocity of 3 m/s). From Habchi and Bair 2019.	30
Figure 2-21: Comparison of (a) relative volume and (b) relative density between the Tait EOS and the empirical Dowson-Higginson equation (general parameters for lubricants are used for the two equations). ...	31
Figure 2-22: The temperature and pressure dependence of the relative volume for two model fluids and the EOS, (a) T9 mineral oil; (b) squalane.	32
Figure 2-23: The low-shear viscosity of C12 isomers: 5-propylnonane; 2,4-dimethyldecane; 2-methyl 5-ethylnonane; 2,2,4,6,6-pentamethylheptane, PMH. (From Bair 2019a)	33
Figure 2-24: The temperature and pressure dependence of the low-shear viscosity for two model fluids, (a) T9 mineral oil; (b) squalane. Free-volume models have a good fit to the measured data; The classical Roelands equation fails to show the sigmoidal change of the viscosity.	34
Figure 2-25: The temperature and pressure dependence of the low-shear viscosity scales with $\varphi = \left(\frac{T}{T_R}\right) \left(\frac{V}{V_R}\right)^g$ and $g = 5.0348$ for T9 oil. (From Habchi, Vergne, Bair <i>et al</i> 2010).....	35
Figure 2-26: Pressure (left) and temperature (right) dependence of thermal conductivity of squalane. (The temperature dependence is from Bair-Andersson <i>et al</i> 2018).....	36
Figure 2-27: Geometry and coordinate system of a Hertzian contact problem, Left: contacting elastic solids; Right: the elliptical contact area.	40
Figure 2-28: The reduced model for the Hertzian contact problem in Fig. 2.27: a rigid ellipsoid loaded on an elastic half-space.	41

Figure 2-29: (Left) EHL film shape observed using dichromatic interferometry [Liu, Guo, Wong <i>et al</i> 2015] on a ball-on-disc optical EHL test rig; (right) EHL film thickness and pressure distribution along the central line of the contact.	42
Figure 2-30: Different definitions of Viscosity-pressure coefficient based on a single set of experimental data (reproduced from [Vergne and Bair 2014]).....	43
Figure 2-31: The viscous-plastic fluid model used in EHL traction calculation. The viscous part is non-linear and modelled by non-Newtonian shear thinning rheological fluid models.	44
Figure 2-32: Schematic of a rolling/sliding EHL contact and the essential input parameters for modelling the traction accounting for non-Newtonian and thermal EHL effects with model fluids.	45
Figure 2-33: Schematic of a point contact thermal EHL problem and the temperature boundary conditions (not to scale; because the film thickness is typically thousand times smaller than the contact width)	47
Figure 2-34: Summary of the non-Newtonian thermal EHL model and the numerical methods used in this study. The improvements in this work are marked in bold towards a better traction prediction. For example, 2D non-Newtonian numerical methods, using independently measured viscosity and fluid properties, as well as the change of the temperature boundary condition for solids.	52
Figure 3-1: Frame diagram of the thesis.....	53
Figure 4-1: Schematic of a circular contact thermal EHL problem and the boundary temperatures (not to scale; note that the body/bulk temperature is different from the oil/liquid interface temperature; and the solid body temperature is the boundary conditions in simulations).....	56
Figure 4-2: Film thickness and pressure distribution for three temperature ratios of $\bar{T}_s = T_s/T_0 = 1.00, 1.05, \text{ and } 1.10$, respectively, in a pure rolling circular EHL contact. The temperatures of the supplied oil are the same for all cases. ($U_e = 1.54 \times 10^{-11}$, $u_e = 10$ m/s, $SRR = 0$, $T_0 = 60$ °C). 59	59
Figure 4-3: Variations of (a) film thickness, (b) pressure, and (c) mid-film temperature with three solid body temperatures along the central line of the contact in the x -direction under pure rolling conditions. The operating conditions are the same as that in Fig. 4.2. ($U_e = 1.54 \times 10^{-11}$, $u_e = 10$ m/s, $SRR = 0$, $T_0 = 60$ °C)	60
Figure 4-4: Variations of velocity component U across the film thickness in the plane of $Y=0$ at four X positions under pure rolling conditions. ($U_e = 1.54 \times 10^{-11}$, $u_e = 10$ m/s, $SRR = 0$, $T_0 = 60$ °C, $\bar{T}_s = 1.05$)	61
Figure 4-5: Variations of (a) central film thickness, (b) minimum film thickness, and (c) friction coefficient versus slide-to-roll ratios in an EHL contact with three solid body temperatures. ($U_e = 1.54 \times 10^{-11}$, $u_e = 10$ m/s, $T_0 = 60$ °C)	61
Figure 4-6: Variation of (a) temperature and (b) shear stress in the middle layer of the film along the central line of the contact in x -direction for the slide-to-roll ratio of 20% with three solid body temperatures. ($U_e = 1.54 \times 10^{-11}$, $u_e = 10$ m/s, $SRR = 20\%$, $T_0 = 60$ °C).....	62
Figure 4-7: Distributions of the mid-film temperature at different entrainment velocities with solid body temperature effect for a pure rolling circular EHL contact. Note that the two heat generation terms in oil energy equation are switched off during calculation and only conduction and convection are working. ($U_e = 1.54u_e \times 10^{-12}$, $SRR = 0$, $T_0 = 60$ °C, $\bar{T}_s = 1.05$).....	63
Figure 4-8: Variation of the mid-film temperature at different entrainment velocities with solid body temperature effect for a pure rolling circular EHL contact. Potential full solution, and no term in the energy equation is switched off. ($U_e = 1.54u_e \times 10^{-12}$, $SRR = 0$, $T_0 = 60$ °C, $\bar{T}_s = 1.05$)	63
Figure 4-9: Contributions of inlet shear heating, compressive heating and solid body temperature on the mid-film temperature distribution along the central line of the contact in x -direction at a high speed in pure rolling EHL. ($U_e = 1.54u_e \times 10^{-12}$, $u_e = 40$ m/s, $SRR = 0$, $T_0 = 60$ °C, $\bar{T}_s = 1.05$)	64

Figure 4-10: Predicted central film thickness from numerical simulation and from another two empirical equations for pure rolling EHL with solid body temperature effect. ($U_e = 1.54u_e \times 10^{-12}$, $SRR = 0$, $T_0 = 60$ °C).....	66
Figure 5-1: Traction curves with two solid thermal conductivities of $k_s = 21$ W/mK (solid lines) and 46 W/mK (dash lines), respectively, at four entrainment speeds in a circular EHL contact. (squalane, $T_0 = 40$ °C, $p_H = 1.25$ GPa; 21 W/mK was measured by Reddyhoff <i>et al</i> [2019] for hardened AISI 52100 steel, while 46 W/mK is the common cited but improper value in thermal EHL literature.).....	72
Figure 5-2: Maximum oil temperature rise for two thermal conductivities at a low entrainment speed of 1.03 m/s and a high speed of 9.60 m/s. The running conditions are the same as that in Fig. 5.1. (squalane, $T_0 = 40$ °C, $p_H = 1.25$ GPa)	73
Figure 5-3: Temperature distribution for two thermal conductivities at a low entrainment speed and a high speed. The running conditions are the same as that in Fig. 5.1 with $SRR = 50\%$. Plane $Y = 0$. (squalane, $T_0 = 40$ °C, $p_H = 1.25$ GPa)	74
Figure 5-4: Influence of pressure dependence of lubricant thermal conductivity on traction at three entrainment speeds in a circular EHL contact. (squalane, $T_0 = 40$ °C, $p_H = 1.25$ GPa, $k_s = 21$ W/mK)	74
Figure 5-5: Influence of pressure dependence of lubricant thermal conductivity on maximum oil temperature rise at a low entrainment speed and a high speed. The running conditions are the same as that in Fig. 5.4. (squalane, $T_0 = 40$ °C, $p_H = 1.25$ GPa, $k_s = 21$ W/mK).....	75
Figure 5-6: Temperature distributions of mid-film and two solid interfaces with the influence of lubricant thermal conductivity at a high speed. The running conditions are the same as that in Fig.6 with $SRR = 50\%$. Plane $Y = 0$. (squalane, $T_0 = 40$ °C, $p_H = 1.25$ GPa, $k_s = 21$ W/mK, $u_e = 9.60$ m/s).....	75
Figure 5-7: Quantitative traction curve comparison with squalane at two speeds. The traction curves were measured by two traction machines. ($T_0 = 40$ °C, $p_H = 1.25$ GPa, $k_s = 21$ W/mK, $k_{oil}(p, T)$)	76
Figure 5-8: Non-dimensional central film thickness at different SRRs with different solid thermal conductivities and lubricant thermal conductivities. (squalane, $T_0 = 40$ °C, $p_H = 1.25$ GPa, $u_e = 9.60$ m/s)	77
Figure 6-1: Schematic representation of the EHL film formed in a rolling/sliding elliptical contact at high load conditions (xoz view; not to scale; Hertzian pressure distribution).	81
Figure 6-2: The geometry of the discs of the twin-disc machine (not to scale; $r_{x1} = r_{x2} = 60$ mm, $r_{y2} = 50$ mm, $r_{y1} = \infty$; ellipticity ratio $k_e = 1.43$).....	84
Figure 6-3: Determination of the pressure dependence of the MSS for squalane based on measured traction curves at high contact pressures. (a) the measured traction curves with a twin-disc machine at 5 m/s and 40 °C; (b) the bilinear function of the maximum averaged shear stress versus the mean contact pressure.	85
Figure 6-4: Computational domain and the finite difference meshing for elliptical contacts in non-dimensional coordinates (not to scale) (a) pressure and local shear stress domain on plane XOY ; (b) grids in the temperature computation domain on plane XOZ	87
Figure 6-5: Flow chart of procedures for the simplified calculation of temperature fields and the friction coefficient at one SRR in a rolling/sliding EHL contact.	88
Figure 6-6: Comparison of traction curves between current simulation and the full numerical simulation for squalane fluid ($T_0 = 40$ °C). (a) compared with the full calculation from Habchi <i>et al</i> [Björling, Habchi <i>et al</i> 2013, 2014 and 2019]; (b) compared with the full simulation [Liu, Zhang <i>et al</i> 2019]. ($\tau_{LSS} = 0.075p$ was used here for comparison purposes).....	88
Figure 6-7: Plots of the temperature rise in the solids and in the lubricant from (a) current simplified simulation and (b) the full EHL simulation (Plane XOZ , squalane liquid, $p_H = 1.25$ GPa, $u_e = 1.61$ m/s, $T_0 = 40$ °C, $SRR = 50\%$, $k_s = 21$ W/mK, $\tau_{LSS} = 0.075p$ was assumed).....	89

Figure 6-8: Traction curve comparison of simplified traction calculations (solid lines) and twin-disc measurements (dots) at a low speed of 5 m/s for the seven contact pressures. (Squalane, $T_0 = 40\text{ }^\circ\text{C}$, $k_s = 21\text{ W/mK}$).....	90
Figure 6-9: Traction curve comparison between simplified traction calculation (solid lines) and twin-disc measurements (dots) for higher speeds at (a) 10 m/s and (b) 15 m/s. (Squalane, $T_0 = 40\text{ }^\circ\text{C}$, $k_s = 21\text{ W/mK}$).....	91
Figure 6-10: The four steps for the measurement of one traction curve (a) and the evolution of the solid body temperature of the disc during this process (b). (Squalane, the supplied oil temperature is well-controlled at $T_0 = 40\text{ }^\circ\text{C}$, $u_e = 10\text{ m/s}$, $p_H = 1.95\text{ GPa}$, $t = 7\text{ mins}$).....	92
Figure 6-11: The measured (a) and the simulated (b) maximum friction coefficient at three entrainment velocities of 5, 10 and 15 m/s for highly loaded EHL contacts. (Squalane, $T_0 = 40\text{ }^\circ\text{C}$)	93
Figure 6-12: Comparison of the maximum shear stress at different pressures among simplified traction calculation (open square), twin disc measurements (star), and the corrected simulation results with the mean solid body temperature of the disc (triangle). (Squalane, $T_0 = 40\text{ }^\circ\text{C}$, $u_e = 15\text{ m/s}$).....	94
Figure 7-1 Traction curves measured with two test rigs in different geometrical configurations at constant mean contact pressure, speed and supplied oil temperature, (a) $u_e = 5\text{ m/s}$; (b) $u_e = 10\text{ m/s}$. (open circle: TD twin disc results, $k_e = 1.43$, $R_x = 30\text{ mm}$; solid square: WAM ball-on-disc results, $k_e = 1.0$, $R_x = 10.314\text{ mm}$; with a reference liquid squalane, $p_H = 1.945\text{ GPa}$, $T_0 = 40\text{ }^\circ\text{C}$; at full film lubrication)	100
Figure 7-2: Schematic representation of a rolling/sliding elliptical EHL contact formed by an ellipsoid with reduced radii R_x and R_y and an elastic half-space. ($R_x = R_y$ for circular contacts in this study)	101
Figure 7-3: Isothermal traction curves for three ball radii R_x calculated from Newtonian fluid model with a limiting shear stress at the same speed, mean contact pressure and supplied oil temperature, (a) isothermal traction curves; (b) traction results on a semi-log plot; (c) scaling with film thickness h_{cen} or with $(R_x/R_{ref})^{0.33}$. (circular contact; no thermal effects; squalane; parameters see Table 7.3)	103
Figure 7-4: Isothermal traction curves for three ball radii R_x calculated from non-Newtonian shear thinning model with a limiting shear stress at constant speed, mean contact pressure and supplied oil temperature, (a) isothermal traction curves on a semi-log plot; (b) scaling with film thickness h_{cen} or with $(R_x/R_{ref})^{0.33}$. (circular contact; no thermal effects; Carreau shear thinning model; squalane, parameters see Table 7.3).....	104
Figure 7-5: Comparison of traction curves at three ball radii R_x for a shear thinning fluid with a limiting shear stress and thermal effects at the same speed, mean contact pressure, and supplied oil temperature, (a) traction curves considering thermal effects; (b) the maximum temperature in the EHL film with SRR; (c) scaling with $(R_x/R_{ref})^{0.33}$. (circular contact; squalane, see Table 7.3).....	105
Figure 7-6: Temperature fields in the EHL film and the contacting solids for three ball radii R_x at constant speed, SRR, mean contact pressure and supplied oil temperature. (a) $R_x = 10\text{ mm}$; (b) $R_x = 30\text{ mm}$; (c) $R_x = 100\text{ mm}$ ($\bar{T} = T/T_0$, the operating conditions are the same as that in Fig. 7.3, <i>i.e.</i> squalane, SRR = 10%, $u_e = 1.0\text{ m/s}$, $p_H = 1.25\text{ GPa}$, $T_0 = 40\text{ }^\circ\text{C}$, $k_e = 1$). All figures share the same color scale in Fig. 7.6(c).....	107
Figure 7-7: Friction coefficient, central film thickness and temperature rise as a function of relative radius of curvature R_x for circular contacts at constant speed, mean contact pressure and supplied oil temperature. (squalane, SRR = 10%, $u_e = 1.0\text{ m/s}$, $p_H = 1.25\text{ GPa}$, $T_0 = 40\text{ }^\circ\text{C}$, $k_e = 1$)	108
Figure 7-8: Calculated velocity profile of the EHL film in the z -direction for two radius of curvature R_x of circular contacts at constant speed, mean contact pressure and supplied oil temperature. (squalane, SRR = 10%, $u_e = 1.0\text{ m/s}$, $p_H = 1.25\text{ GPa}$, $T_0 = 40\text{ }^\circ\text{C}$, $k_e = 1$)	108

Figure 7-9: Schematic representation of the film and velocity profile for the studied scale effect of (a) a small R_x and (b) a large R_x . Thermal effects are enhanced and the CoF is reduced for a larger R_x due to thicker film thickness for heat conduction and the localized shear in the middle film.	109
Figure 7-10: Traction curve comparison between experiments and simulations for two different geometrical configurations at constant mean contact pressure, speed, and supplied oil temperature, (a) $u_e = 5$ m/s; (b) $u_e = 10$ m/s. (TD twin disc: $k_e = 1.43, R_x = 30$ mm; WAM ball-on-disc: $k_e = 1.0, R_x = 10.314$ mm; with a reference liquid squalane, $p_H = 1.945$ GPa, $T_0 = 40$ °C).....	110
Figure A-1: Comparison between current simulation and results in literature [Liu, Wang, Bair <i>et al</i> 2007; Bair, Vergne, Querry 2005] (PAO650, $T_0 = 75$ °C, $p_H = 0.528$ GPa, pure rolling).....	115
Figure A-2: Traction curve comparison between current simulation and results in literature [Björling, Habchi, Bair <i>et al</i> 2019] (squalane, $T_0 = 40$ °C, $p_H = 1.07$ GPa, $k_s = 46$ W/mK, $k_{oil}(p, T)$, setting see Sec. 5.2)	115
Figure D-1: Setup of modified twin-disc machine for IR temperature measurements. Left: twin-disc and IR camera; Right: light path and the contact formed between a hollow sapphire shaft and a steel disc [Bader 2018]	118
Figure D-2: Temperature map at different SRRs measured by IR camera for squalane ($T_0 = 20$ °C, $p_H = 1.125$ GPa, $u_e = 5$ m/s).....	119
Figure D-3: Temperature distribution on the centerline for different SRRs (squalane, $T_0 = 20$ °C, $p_H = 1.125$ GPa, $u_e = 5$ m/s)	120

List of Tables

Table 2-1: Controversial points between classical EHL and quantitative EHL	11
Table 2-2: Geometrical configuration and operating range of the three traction machines (p_H for steel/steel contacts)	12
Table 2-3: Properties of AISI 52100 steel (disc/ball material of traction rigs)	12
Table 2-4: Limiting shear stress models.....	27
Table 2-5: Constants in the expression of pressure dependent thermal conductivity for different kinds of lubricants (from Larsson and Andersson 2000).....	37
Table 2-6: Fluid models and rheological parameters for two model fluids, squalane and Shell T9 (from measurements by Bair and co-workers).....	38
Table 4-1: Operating conditions and properties of the lubricant T9 and solids	58
Table 5-1: Material thermo-physical properties and operating conditions	72
Table 6-1: Lubricant properties and operating conditions of the twin-disc machine.....	90
Table 6-2: Solid body temperatures of the disc recorded by a thermal couple for different conditions (the supplied oil is controlled at 40 °C).....	92
Table 7-1: Geometrical configuration and operating conditions of the two traction machines (the contact pressure, supplied oil temperature and speed are kept the same for the two machines; steel/steel contacts; x along the direction of motion and y in the transverse direction; r_{y2} is crown radius).....	99
Table 7-2: Properties of AISI 52100 steel and squalane liquid.....	99
Table 7-3: Operating conditions for the numerical study of scale effects in circular contacts at different R_x ($u_e = 1.0$ m/s, $p_H = 1.25$ GPa, $T_0 = 40$ °C, $k_e = 1.0$; $G = 4153.85$, $W = 3.28 \times 10^{-6}$).....	102
Table B-1: Effect of the mesh densities on the accuracy of a representative case using multigrid method (T9 Oil, $T_o=T_s=60$ °C, SRR=20%, $p_H=0.74$ GPa, 10m/s, $R=12.7$ mm, $U_e = 1.54 \times 10^{-11}$, $W = 6.88 \times 10^{-7}$, $G=4757$, $D_T = 3.15$).....	116
Table C-1: Effect of the computational depth in z -direction of the solids on the accuracy of a representative case using multigrid and line-by-line relaxation method (T9 Oil, $T_o=T_s=60$ °C, SRR=50%, $p_H=0.74$ GPa, 10m/s, $R=12.7$ mm, $U_e = 1.54 \times 10^{-11}$, $W = 6.88 \times 10^{-7}$, $G=4757$, mesh 513×257, in z -direction 12 nodes in the solids and 20 nodes in lubricants).....	117
Table D-1: Material property and geometrical parameters of the two discs used in IR temperature experiments	118

Nomenclature

This nomenclature contains the variables introduced and any corresponding non-dimensionalisation considered in the thesis.

a	m	For elliptical contact, semi-axis of the contact ellipse in the transverse direction, y -direction, $a = \left(\frac{6k_e^2 F_2 R w}{\pi E'}\right)^{1/3}$; or
	m	For circular contact, semi-axis of the Hertzian contact
A	m^2	Contact area
α_V	K^{-1}	Thermal expansion coefficient
b	m	Semi-axis in the direction of motion, x -direction, $b = a/k_e$
B_F	-	Fragility parameter in the thermodynamic scaling viscosity equation
c, c_1, c_2	$J/(kgK)$	Heat capacity of lubricant, solid-1, and solid-2, respectively
D	-	Ratio of reduced radius of curvature, $D = R_y/R_x$
De	-	Deborah number
d_T, D_T	-	Heat penetration depth, m, and dimensionless $D_T = d_T/a$
E'	Pa	Reduced Young's modulus of elasticity, $E' = 2/[(1 - \nu_1^2)/E_1 + (1 - \nu_2^2)/E_2]$
f	-	Friction coefficient
F_f	N	Traction or friction force
f_{max}	-	Maximum friction coefficient in a traction curve
F	-	Dimensionless relative thermal expansivity of the free volume
F_2	-	The elliptic integral of the second kind, $F_2 = [1 + (\pi/2 - 1)D^{-1.0238}][1 + 0.0486D^{-1.3358}(\ln D)^{1.0997}]$ (Markho 1987)
g	-	Thermodynamic interaction parameter
G	-	Dimensionless materials parameter in the HD equation, $G = \alpha E'$; or
	Pa	Elastic shear modulus of the lubricant
G_∞	Pa	Limiting high-frequency shear modulus of the material
G_s	Pa	Shear modulus of the material
h, H	-	Film thickness, m, and dimensionless $H = hR_x/a^2$
h_{00}, H_{00}	m	Rigid central film thickness, and dimensionless $H_{00} = h_{00}R_x/a^2$
h_{cen}	m	Central film thickness
h_{min}	m	Minimum film thickness
k_e	-	Ellipticity ratio, defined as $k_e = a/b$ and $k_e = D^{0.6268}[1 + 0.0632\sin(0.6315\ln D)]$, from Markho 1987
k_0	$W/(mK)$	Thermal conductivity of the lubricant at $p = 0$
$k_{oil}, k_s, k_{s1}, k_{s2}$	$W/(mK)$	Thermal conductivity of the lubricant, solid, solid-1 and solid-2, respectively
K_0	Pa	Isothermal bulk modulus at $p = 0$
K_{00}	Pa	K_0 at zero absolute temperature
K'_0	-	Pressure rate of change of isothermal bulk modulus at $p = 0$
L	-	Brinkman number or thermal loading parameter for inlet thermal reduction to film thickness $L = -\frac{\partial \mu}{\partial T} \frac{u_e^2}{k_{oil}}$ or $\eta_e \beta u_e^2 / k_{oil}$
M	mol	Molecular weight
n	-	Power-law exponent of fluid in shear thinning equations
Na	-	Nahme-Griffith number, $Na = \beta \tau^2 h^2 / (k_{oil} \mu)$
Pe	-	Peclet number, for solids $Pe = 2bu/\chi$
p_H, p_{mean}	Pa	Maximum Hertzian pressure and mean Hertzian pressure
p, P	Pa	Pressure, and dimensionless $P = p/p_H$
q_f	W/m^2	Heat flux

R_q	m	Combined root-mean-square surface roughness, $R_q = (R_{q1}^2 + R_{q2}^2)^{1/2}$
r_{x1}, r_{y1}	m	Radii in x - and y - direction of solid-1, respectively
r_{x2}, r_{y2}	m	Radii in x - and y - direction of solid-2, respectively
R_x, R_y	m	Effective radii in x - and y - direction, respectively, $1/R_x = 1/r_{x1} + 1/r_{x2}$, $1/R_y = 1/r_{y1} + 1/r_{y2}$
R	m	Reduced radius of curvature, $1/R = 1/R_x + 1/R_y$
S	-	Sommerfeld number $S \equiv \eta u_s R_s / w$, where R_s is a length scale characterizing the curvature of the surfaces
t	s	Characteristic time
T_0	K or °C	Temperature of the supplied oil
T_g	K or °C	Glass transition temperature at p
T_{g0}	K or °C	Glass transition temperature at $p = 0$
T_R	K or °C	Reference temperature
T_s, T_{s1}, T_{s2}	K	Bulk temperature, <i>i.e.</i> temperature of the solid body, of solid-1 and solid-2, and dimensionless $\bar{T}_{s1,s2} = T_{s1,s2}/T_0$
\bar{T}_s	-	Ratio between the solid body temperature and the supplied oil temperature, T_s/T_0
T, \bar{T}	K	Absolute temperature, and dimensionless $\bar{T} = T/T_0$
u_1, u_2	m/s	Velocities of surface 1 and 2, and dimensionless $U_{1,2} = u_{1,2}/u_e$
u, v	m/s	Velocities in two directions, and dimensionless $U = u/u_e, V = v/u_e$
u_e	m/s	Entraining velocity, <i>i.e.</i> $u_e = (u_1 + u_2)/2$
u_s	m/s	Sliding velocity or
	m/s	Surface velocity of a solid
U_e	-	Dimensionless speed parameter, $U_e = \eta_0 u_e / (E' R_x)$
Δu	m/s	Velocity difference of the two surfaces, <i>i.e.</i> $\Delta u = u_2 - u_1$
V	m ³	Volume at T and p
	-	Dimensionless velocity in the y - direction
V_0, V_R	m ³	Volume at $p = 0$ or at a reference state of $T_R, p = 0$
w	N	Contact load
W	-	Dimensionless load parameter in the HD equation, $W = w / (E' R_x^2)$
W_i	-	Weissenberg number, $W_i = \lambda_R \dot{\gamma}$
x, y, z	m	Space coordinates
$x_{in}, x_{out}, X_{in}, X_{out}$	m	Domain boundary in x -direction, and dimensionless $X_{in,out} = x_{in,out}/a$
$y_{in}, y_{out}, Y_{in}, Y_{out}$	m	Domain boundary in y -direction, and dimensionless $Y_{in,out} = y_{in,out}/a$
z_1, z_2	m	Coordinates in disc-1 and disc-2, and dimensionless $Z_{1,2} = z_{1,2}/a$ (solids)
X, Y, Z	-	Dimensionless coordinates $X = x/a, Y = y/a, Z = z/h$ (lubricant)
α, α_{film}	m ² /N	Pressure-viscosity coefficient
β, β_K	K ⁻¹	Temperature-viscosity coefficient
ϵ	-	Ellipticity parameter in film thickness equation $\epsilon = 1.03(R_y/R_x)^{0.64}$
λ	-	Lambda ratio characterizing film thickness to roughness
λ_R	s	Characteristic or relaxation time at a reference state
ν	-	Poisson ratio
κ	-	Dimensionless conductivity scaling parameter, $\kappa = (V/V_R)[1 + A(T/T_R)(V/V_R)^q]$
φ	-	Dimensionless viscosity scaling parameter, $\varphi = (T/T_R)(V/V_R)^g$
φ_∞	-	Viscosity scaling parameter for unbounded viscosity
$\rho, \bar{\rho}$	kg/m ³	Density, and dimensionless $\bar{\rho} = \rho/\rho_0$
ρ_0	kg/m ³	Density at T_0 and at ambient pressure
$\mu, \bar{\mu}$	Pas	Low-shear viscosity of the lubricant, and dimensionless $\bar{\mu} = \mu/\eta_0$
μ_2	Pas	Viscosity in the second Newtonian regime
μ_g	Pas	Low-shear viscosity at the glass transition temperature and atmospheric pressure
μ_R	Pas	Low-shear viscosity at a reference state
μ_∞	Pas	Viscosity extrapolated to infinite temperature
η^*	Pas	High-shear viscosity or generalized Newtonian viscosity, and dimensionless $\bar{\eta}^* = \eta^*/\eta_0$

η_0, η_e	Pas	Lubricant viscosity at ambient pressure and at T_0 for η_0 , at T_s for η_e
$\tau, \bar{\tau}$	Pa	Shear stress, and dimensionless $\bar{\tau} = \tau/p_H$
τ_c	Pa	Critical shear stress for onset of shear thinning
τ_E	Pa	Eyring shear stress
τ_{LSS}	Pa	Lubricant limiting shear stress
τ_{Lo}	Pa	Intercept of the shear stress at $p = 0$ for a plot of τ_{MSS} against p_{mean}
τ_{MSS}	Pa	Mean maximum shear stress $\tau_{MSS} = \frac{f_{max}W}{\pi ab}$
τ_x, τ_y, τ_e	s^{-1}	Shear stress in two directions, and composite $\tau_e = \sqrt{\tau_x^2 + \tau_y^2}$
$\dot{\gamma}$	s^{-1}	Shear rate
$\dot{\gamma}_x, \dot{\gamma}_y, \dot{\gamma}_e$	s^{-1}	Shear rate in two directions, and composite, $\dot{\gamma}_e = \sqrt{\dot{\gamma}_x^2 + \dot{\gamma}_y^2}$, and the dimensionless form of $\dot{\gamma}_e$ is $\dot{\Gamma}$
Γ	-	Inlet Weissenberg number, $\Gamma = u_e \eta_0 / (h_{cen,iso} \tau_c)$
χ	m^2/s	Thermal diffusivity, $\chi = k / (\rho c)$
$\varphi_{thermal}$	-	Thermal reduction factor for film thickness
$\varphi_{thinning}$	-	Shear thinning reduction factor for film thickness
Σ	-	Slide-to-roll ratio, SRR, $\Sigma = (u_2 - u_1) / u_e$
Λ, ψ	-	Limiting or maximum stress-pressure coefficient in different LSS equations

Subscript

cen	central
e	effective or elastic
f	friction
iso	isothermal
LSS	limiting shear stress
MSS	maximum shear stress
max	maximum
min	minimum
R, ref	reference

Abbreviation

CoF	Coefficient of friction
EHL	Elastohydrodynamic lubrication
HD	Hamrock-Dowson equation
LSS	Limiting shear stress
MFC	Maximum friction coefficient
MSS	Mean maximum shear stress of an EHL contact
MTM	The MTM mini ball-on-disc traction machine
SRR	Slide-to-roll ratio
TD	Twin-disc machine
TEHL	Thermal elastohydrodynamic lubrication
VisPT	Viscosity-pressure-temperature relation
VPC	Viscosity-pressure coefficient
WAM	The WAM ball-on-disc traction machine

1

Introduction

1.1 Tribology, friction and sustainability

When there is motion there is friction. Friction is immensely useful to our daily life, such as when we speed a bike up through the friction between the tire and the road, or when we apply brakes or let the bike turn corners. Mostly though, friction can be a nuisance, for example, when we drag a heavy box over the ground that it is sliding on. In general, friction is responsible for a great part of our energy consumption and CO₂ emission.

1.1.1 Tribology and the law of friction

Tribology, a study of friction, wear and lubrication, was coined in 1966 as an individual scientific subject and briefly defined as "... the science and technology of interacting surfaces in relative motion and of associated subjects and practices" [Jost 1966 and 1990]. Friction is the resistance to motion, and wear is the loss of material. Lubrication is an effective way to reduce friction and wear.



(a) Drilling wood for fire by Suiren in Chinese mythology

[Source: Stamp issued by Chunghwa Post, Taiwan, China in 1994]



(b) The evolution of wheels

[Source: National Taiwan Science Education Center, China]

Figure 1-1: Tribological practice in ancient times and in the course of human civilization. (a) drilling wood for fire; (b) evolution of wheels. A modern wheel unit includes axle, bearing, sealing, and lubricant. In ancient times, natural lubricants from vegetable and animal oil were used to reduce friction and noise.

Tribological knowledge and technologies existed in ancient times, and many important inventions were related to tribology in the course of human civilization. For example, drilling wood for fire (Fig.

1.1(a)) relies on friction by transforming the mechanical energy into heat. Since then, humans have used fire for cooking, lighting, heating, and smelting. Wheel (Fig. 1.1(b)) is also a great invention that reduces friction using rolling instead of sliding. With the development of wheels, it became possible for humans not only to travel far, but also to transport heavier objects and to build cities.

More than 500 years ago, Leonardo da Vinci (1452-1519) did the first systematic experimental study on dry friction [Dowson 1998]. In his machinery design, friction was important for the analysis of the performance of many components, such as pulleys, screw threads, axles. Over two hundred years later, the classical friction laws for dry sliding contacts were postulated by Amontons (1663-1705) and Coulomb (1736-1806): (1) The friction force F_f is directly proportional to the applied normal load w ; (2) The friction force F_f is independent of the apparent sliding contact area A ; (3) The friction force F_f is independent of the relative sliding velocity u_s . These laws can be described as

$$F_f = fw \text{ (independent of } A \text{ and } u_s) \quad (1.1)$$

where f is the friction coefficient. These laws are macroscopic and, of course, not strictly applicable to all kinds of contact materials with different surface topography at various speed or load conditions [Gao *et al* 2004], but they are practical for engineers dealing with dry sliding contacts.

1.1.2 Friction and sustainability

It has been reported that one fifth of all energy [Holmberg and Erdemir 2015] and 30% of primary energy [WTC 2017] are consumed by friction all over the world. The largest quantities of energy are used by industry (29%) and in transportation (27%). For example, according to the study by Holmberg *et al* [Holmberg and Andersson *et al* 2012]: in passenger cars, one-third of the fuel energy is used to overcome friction in the engine, transmission, tires, and brakes. The direct frictional losses, with braking friction excluded, are 28% of the fuel energy. In total, 21.5% of the fuel energy is used to move the car. Not only for economic reasons but also to reduce CO₂ emissions and for environmental concerns, energy efficient vehicles and machines with minimized friction are being designed and produced. The study of friction and tribology is helping to create a sustainable and green world.

1.2 Friction in lubricated contacts

1.2.1 Reynolds equation and fluid lubrication

Great technological advancements in machine elements, such as gears and journal bearings, have been made during the Industrial Revolution. Meantime, there is the great development in lubrication theory and lubricant technology. Although crude oil based products began to be used as lubricants in steam engines in the 1830s, it was not until 1886 Reynolds published the classic Reynolds equation for thin viscous flow [Reynolds 1886], after the experimental observations on journal bearings by Tower [Tower 1883], that the theory of fluid film lubrication, *i.e.* hydrodynamic lubrication (HL), was established. It proves that the entrained lubricant can prevent contacts between the sliding surfaces (thus eliminating wear), and the load can be borne by the hydrodynamic pressure in the film. The mechanisms of fluid film lubrication and the significant role of lubrication on friction reduction and on wear prevention were revealed. Impressive progress was made in the field of HL based on the Reynolds equation, such as performance improvements for fluid-film bearings and the developments of new types of sliding bearings, *e.g.* thrust bearings.

1.2.2 Stribeck curve for conformal contacts

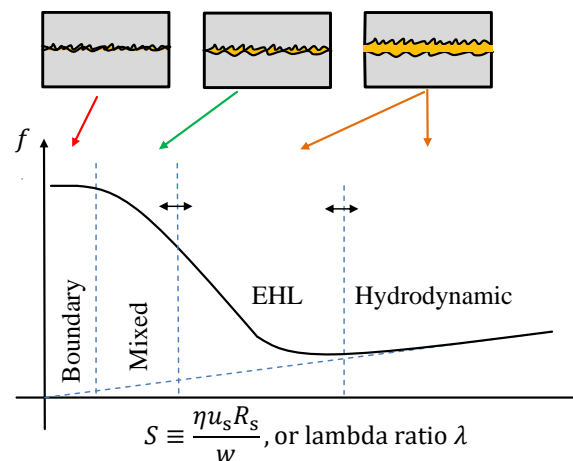


Figure 1-2: Schematic of Stribeck curve (coefficient of friction against the Sommerfeld number or the lambda ratio) and the lubrication regimes (boundary lubrication, mixed lubrication, EHL, and HL). The horizontal arrow indicates the boundary between the adjacent regimes may shift in terms of operating conditions, for example speed.

The hydrodynamic lubrication theory predicts that the friction coefficient f is proportional to the Sommerfeld number $S \equiv \eta u_s R_s / w$ [Stachowiak and Batchelor 1993], where η is the lubricant viscosity, u_s the sliding velocity, R_s a length scale characterizing the curvature of the surfaces, and w is the load. The overall $f(S)$ behavior is often summarized in a semi-empirical Stribeck curve, see Fig. 1.2. Note that the HL scaling of friction coefficient breaks down as $S \rightarrow 0$, and the friction coefficient increases in the mixed and the boundary friction regimes (in boundary lubrication, the load is mainly carried by the asperities in contact rather than by a lubricant film). This is due to the fact that as S decreases the film thickness has to decline to maintain the pressure and thus the load carrying capacity. The reduced film thickness cannot fully separate the sliding surfaces, leading to asperity contact and thus elevated friction and wear. It is not until the middle of the 20th century we knew that boundary friction and hydrodynamic friction are intrinsically different.

1.2.3 Stribeck curve for non-conformal contacts

Unlike the conformal contact in a journal bearings of relatively low contact pressure, there are many machine elements running with highly stressed non-conformal contacts, *i.e.* rolling/sliding line or point contacts. In 1916, Martin derived a minimum film thickness formula for gears base on the classical hydrodynamic-rigid surface theory [Martin 1916]. The calculated film thicknesses were much thinner than the combined surface roughness of general gear teeth, which failed to explain the successful surface protection by the lubricant film. In the subsequent decades, the effects of the lubricant piezo-viscous property and the surface elastic deformation following the pioneering work of Hertz [1881] were independently investigated by researchers; and unfortunately, neither of these two effects on its own could be responsible for the film built up. Until 1949, Ertel/Grubin developed the pioneering inlet solution for film thickness combining these two effects in the analysis of a line contact [Grubin 1949; Mohrenstein-Ertel 1984]. Since then, people believed that a thin film could exist between non-conformal elastic surfaces under high pressures. A specialized lubrication regime - **Elastohydrodynamic Lubrication** (EHL) - has become the most important subject in lubrication science in the late half of the 20th century.

To evaluate the friction regimes in non-conformal contacts, it may be convenient to present the Stribeck curve as a plot of the friction coefficient for a certain slide-to-roll ratio against the film parameter λ , which is often termed the “lambda ratio”. It is the ratio of the predicted oil film thickness with smooth surfaces to the composite surface roughness of the two contacting surfaces. The transition from full film HL friction to mixed friction or the transition from mixed to boundary friction is smooth in a Stribeck curve and there is no exact boundary between the adjacent regimes. In the literatures, *e.g.* [Gohar and Rahnejat 2019], the relation between the “lambda ratio” and the friction/lubrication regimes is usually described as: (1) $\lambda \leq 1$ represents boundary lubrication and wear could occur; (2) $1 < \lambda < 3$ represents mixed lubrication; (3) $\lambda \geq 3$ represents full film lubrication. Noted that a real “lambda ratio” should account for the amplitude reduction of the surface roughness when it enters into a lubricated non-conformal contact [Venner *et al* 1997].

1.2.4 Typical features of EHL contacts

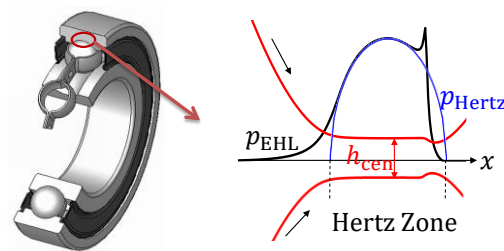


Figure 1-3: Schematic of an EHL point contact formed between a ball and the raceway in a rolling element bearing (fully flooded condition is assumed; not to scale $a_{\text{Hertz}} \approx h_{\text{cen}} \times O(10^3)$)

EHL lubricated machine elements, *e.g.* gears, rolling element bearings, and cam followers, exist widely in modern mechanical devices and operate in a wide range of conditions. In particular, rolling bearings are used in almost every automotive, industrial, and aerospace application. There, EHL contacts mostly work in rolling/sliding (sometimes with spin) conditions with a rather small load-carrying area, as a contrast to the sliding motion in a journal bearing possessing a relatively large conformal contact area. The EHL pressure distribution is very close to the one from the Hertzian dry contact theory (see Fig. 1.3, and Sec. 2.3.2). The maximum or the Hertzian pressure in EHL lubricated machine elements is typically in the order of GPa, say 0.5 ~ 4.0 GPa (Fig. 1.4), which is about hundred times larger than that in HL. Nevertheless, like in HL, a full separation of the rolling/sliding surfaces can still be achieved. The EHL film thickness (typically 30 nm to 2 μm) is usually thinner than that of HL. The contact half-width is typically in the order of $10^3 \mu\text{m}$, which is about thousand times larger than the EHL film thickness. Therefore, for an EHL contact, the film looks like going through a narrow and parallel high-pressure channel.



Figure 1-4: Contact pressure in some rolling/sliding EHL lubricated transmission components [the pressure values refer to Zhang, Spikes 2020]

Two effects contribute to the film build-up at such a high pressure: (1) the elastic deformation of the surfaces; and (2) the dramatic increase of viscosity with pressure in the inlet. The former can be

understood to provide a living space for the EHL film, and the latter may be understood to allow the lubricant to entrain into the contact and to prevent being squeezed out because of its high viscosity when passing through the contact.

It should be noted that the EHL film thickness is determined by the oil amount and the relatively low-pressure properties in the inlet region, and therefore, the ability for EHL film thickness prediction is relatively mature (Sec. 2.3.3). As a contrast, the EHL friction/traction is hard to predict, because it is mainly controlled by the shearing property of the thin compressed film (see Sec. 2.2.1) in the center of the contact. While friction is a general physical term, traction may be defined as [Bayer 1994]: a physical process in which a tangential force is transmitted across an interface between two bodies through dry friction or an intervening fluid film resulting in motion, stoppage or the transmission of power. The two terms are used interchangeably in the EHL study and the term traction is used in this thesis.

1.3 Subject of this thesis

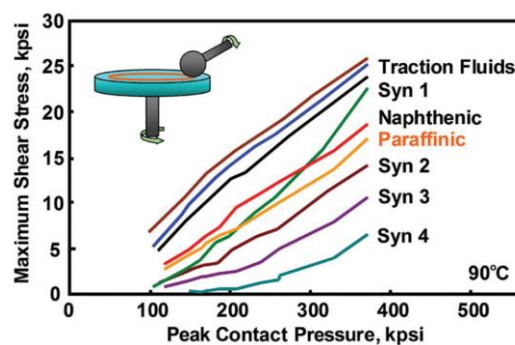


Figure 1-5: Maximum shear stress versus contact pressure for a variety of fluids [Jackson and Webster 2003; Wang and Zhu 2019]

The subject of this study is to predict the traction in rolling/sliding EHL contacts. This is important for the understanding of the performance and the optimizations of rolling/sliding machine elements towards higher reliability, longer life, and smaller size. For most applications, a low traction is desired for energy efficiency and environmental concerns. Synthetic lubricants can reduce friction further than mineral oils (Fig. 1.5) because of better shear properties. With the development of technology, synthetic fluids can be designed to generate both low and high tractions. There are also some applications where an appropriate or even a higher traction is desired. For example, in a rolling element bearing the friction between the roller and raceway can prevent roller slip at high speeds. The Hertzian contact pressure in a CTV transmission can be as high as 4 GPa and the lubricant is traction fluid with special molecular design to achieve the demanded high traction force. Fig. 1.5 shows a traction performance for a variety of lubricants [Jackson and Webster 2003].

Since the 1960s, much effort has been directed towards the prediction of the EHL traction, see for example [Crook 1963; Evans and Johnson 1986b]. With increasing slip in a traction curve, there are several traction regimes (*e.g.* linear, non-linear, thermal regimes), which are governed by different combinations of non-Newtonian effects and thermal effects. However, the best non-Newtonian rheological fluid models for the viscosity at high pressure and high shear rate are still open questions [Bair, Vergne *et al* 2015]. Noticeable progress has been made in quantitative EHL study in the last ten years [Bair 2019b], by predicting traction based on primary measurements of thermo-physical properties of reference fluids, *e.g.* squalane, Shell T9. However, considerable discrepancies still exist between EHL traction simulations and measurements even with these model fluids [Björling, Habchi, Bair *et al* 2013].

This dissertation continues the efforts to understand and to predict the EHL traction with model fluids by carrying out both experimental measurements and numerical simulations. The work aims to show the influence factors that lead to the differences between experiments and simulations for the specific reference fluid, squalane. This is expected to contribute to the quantitative understanding of the EHL traction covering different traction regimes and SRRs.

2

Fundamentals of EHL Traction

This chapter introduces fundamental rheological knowledge of lubricants and methods related to the EHL traction prediction. Sec. 2.1 gives a brief introduction to the experimental techniques in traction curve measurements. Several factors that may affect experimental results are pointed out, such as bulk temperature rise, disc tangential elastic creep, solid thermal conductivity and specimen size/geometry of traction rigs. For full-film EHL lubricated contacts, the traction is dominated by the shear properties of lubricants. The current understanding of the non-Newtonian shear behavior of a thin compressed fluid (flow curve) and fluid models are introduced in Sec. 2.2, *e.g.* shear thinning, limiting shear stress, and viscoelastic behavior. Sec. 2.3 introduces a simplified isothermal traction calculation approach without solving the Reynolds equation. This method works for high pressure and small SRR conditions. Full numerical methods for the EHL traction prediction are described in Sec. 2.4 accounting for non-Newtonian and thermal effects.

2.1 Quantitative EHL and traction experiments

2.1.1 Traction curve and regime

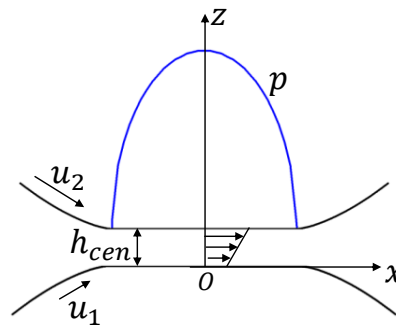


Figure 2-1: Schematic representation of a rolling/sliding EHL contact (xoz view; not to scale; Hertzian pressure distribution is assumed)

Fig. 2.1 shows schematically a rolling/sliding EHL contact. In practice, EHL lubricated contacts rarely work at pure rolling in machine elements and there is sliding/slip superimposed to the rolling motion. A small amount of sliding leads to a sharp rise of traction. The influence of slip on the traction is characterized by a traction curve, which is usually a plot of the friction/traction coefficient f against the slide-to-roll ratio (SRR).

2.1.1.1 SRR and traction

SRR is defined as the ratio of the speed difference Δu to the average entrainment speed u_e of the two surfaces,

$$\text{SRR} = \frac{\Delta u}{u_e} = \frac{(u_2 - u_1)}{(u_1 + u_2)/2} = \frac{2(u_2 - u_1)}{u_1 + u_2} \quad (2.1)$$

Macroscopically, the friction coefficient f is expressed as the ratio of the tangential forces F_f to the normal load w for an EHL contact,

$$f = \frac{F_f}{w} \quad (2.2)$$

Experimentally, F_f can be measured using a traction rig (Sec. 2.1.3), and, theoretically, it is the integral of the shear stress along the entrainment direction τ_x over the entire EHL pressure zone, *i.e.*

$$F_f = \iint \tau_x dx dy = \iint \min[\dot{\gamma}_x \eta^*(p, T, \dot{\gamma}_e), \tau_{LSS}(p, T)] dx dy \quad (2.3)$$

This equation shows that the EHL traction F_f depends on the piezo-viscous behavior $\mu(p, T)$ at low $\dot{\gamma}$, the non-Newtonian behavior $\eta^*(p, T, \dot{\gamma})$ of the fluid at high p and $\dot{\gamma}$ (Sec. 2.2.2), the plastic behavior indicated by a limiting shear stress $\tau_{LSS}(p, T)$ (Sec. 2.2.3), as well as the thermal effects (Sec. 2.4.3), caused by shear heating. It is generally agreed that neither thermal effects nor non-Newtonian effects can be the sole factor for the complete explanation of measured tractions. In other words, to explain the experimental results, both shear thinning and thermal effects are needed to be modeled. Additionally, the LSS seems to be an essential concept for the traction prediction for highly loaded rolling/sliding contacts; see Sec. 2.2.3. The related fluid models and thermo-physical-rheological properties will be described in Sec. 2.2.

2.1.1.2 Traction regimes

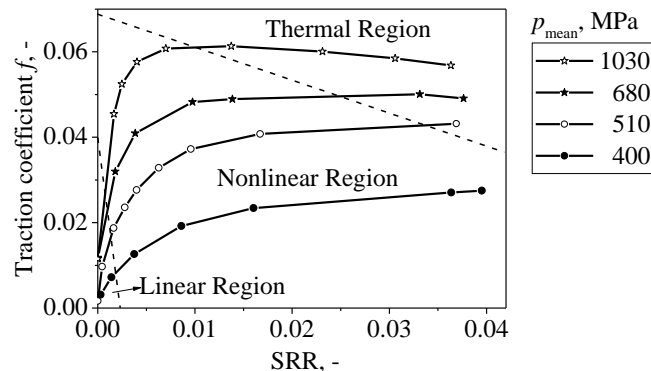


Figure 2-2: Typical EHL traction curves measured on a twin-disc machine in a line contact showing different regimes of traction (data reproduced from Johnson and Cameron 1967)

Typically, an EHL traction curve can be divided into several regimes, which are dominated by different mechanisms [Evans and Johnson 1986b; Habchi, Bair, Vergne 2013]. Fig. 2.2 shows a set of measured traction curves at four mean contact pressures [Johnson and Cameron 1967]. Several regimes may exist in one traction curve with increasing slip/SRR:

(1) Linear Regime: this regime is mainly a result of the isothermal Newtonian viscous shear and the slope of the curve may be influenced by the elastic response of the lubricant and also the contacting solids;

(2) Non-linear Regime: it results from the non-Newtonian response of the fluid at high pressure and high shear rate, *e.g.* shear thinning behavior and possibly the locally reached LSS;

(3) Plateau Regime: if it occurs, it is widely believed to be dominated by the LSS property of the fluid;

(4) Thermo-viscous Regime: it is mainly caused by shear heating and thermal effects, *e.g.* reduced and fewer portion of the contact area can reach the LSS.

Machine elements are running at different SRRs and thus in different traction regimes. Rolling element bearings are typically working at small SRRs, such as for ball bearings mostly $SRR < 1\%$ and for roller bearing SRR can be as high as 7%. The traction between the raceway and the roller/ball affects the dynamic behavior of the rolling elements. Gears and cam-followers, along the contact path, work over a wide range of SRRs and traction regimes. In a CVT transmission, the EHL contacts have to operate at relatively small SRRs for efficiency and safety, for example in the linear (1) and the nonlinear (2) EHL traction regimes. The maximum friction coefficient of a traction oil at different operating conditions is a key parameter for this application.

2.1.2 EHL philosophy

2.1.2.1 Assumptions in classical EHL

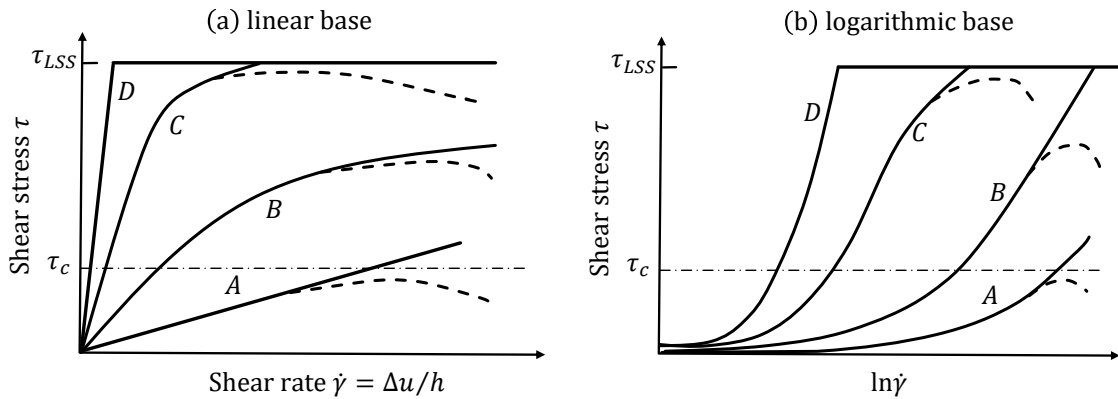


Figure 2-3: Typical traction curves predicted by the rheological model of $\dot{\gamma} = \frac{\tau}{G} + \frac{\tau_c}{\mu} \sinh\left(\frac{\tau}{\tau_c}\right)$ together with a limiting shear stress (from Evans and Johnson 1986a; assuming the disc machine as a rheometer), solid line: isothermal; dashed line: with shear heating; (a) linear base; (b) logarithmic base.

One would fail to predict the EHL traction accurately before knowing the non-Newtonian constitutive behavior and the thermo-physical properties of lubricants at EHL conditions. This was the situation in classical EHL studies, for example lacking of high-pressure viscosity data for a bulk fluid measured in instruments. Disc machines were used as high-pressure rheometers for providing the shear thinning constitutive equation, *i.e.* the relation between the average shear stress and the average shear rate. With mean/average rheological parameters derived from EHL contacts, many important aspects of the EHL traction have been revealed in classical EHL studies. Firstly, it has been known that a traction curve cannot be explained by thermal effects or non-Newtonian effects independently. Secondly, visco-elastic-plastic non-Newtonian fluid models (see Fig. 2.3) have been proposed for the explanation of the above-mentioned traction regimes in experiments. Thirdly, the maximum friction coefficient in highly loaded contacts was shown to be dominated by the limiting shear stress, which is proportional to mean contact pressure. However, there are several strong assumptions in classical traction studies [Bair 2019a and 2019b]:

(1) the pressure and temperature dependence of viscosity was described by an empirical equation for lubricants, *e.g.* the widely used Roelands equation [Roelands 1966],

(2) the relation between the average shear stress and average shear rate obtained from a traction curve was assumed to be the constitutive equation of the fluid (flow curve, the shear stress versus shear rate relation for a homogeneous bulk fluid, Sec. 2.2);

(3) the thermal conductivity of lubricant was used as a constant and it is independent of pressure;

(4) the fluid in the inlet EHL zone is Newtonian.

These assumptions are discussed in the next section and they have been removed gradually with the development of experimental techniques in the field of high-pressure rheology.

2.1.2.2 The idea of quantitative EHL

Since 2007 [Liu, Wang, Bair *et al* 2007; Bair, Fernandez, Khonsari *et al* 2009], much progress has been made in the understanding of the EHL traction by removing the above assumptions with independent measurements of thermo-physical properties of reference fluids using high pressure viscometers and other techniques [Habchi, Vergne, Bair *et al* 2010; Bair 2019a].

The viscosity behavior at high pressures is of great importance for the EHL traction prediction. Through independent measurements, it has been shown the super-Arrhenius (greater-than-exponential) piezoviscosity is universal for glass-forming liquids, and therefore, all typical liquid lubricants [Bair, Martinie, Vergne 2016]. The classical Roelands equation fails to describe this behavior and it predicts smaller viscosity values at high pressures, say $p > 400$ MPa. Indeed, many physically-sound free-volume models are available (Sec. 2.2.5 and 2.2.6) for describing the variations of density and viscosity of fluids as a function of pressure and temperature based on independent high-pressure measurements. On the second assumption, the EHL contact of a traction machine was used as a high-pressure viscometer for extracting the shear stress and shear rate relation for lubricants. However, the shear stress in an EHL film is inhomogeneous as a result of the Hertzian semi-elliptical pressure distribution and the measurements could be influenced by thermal effects, such as flash/maximum temperature in the film and bulk temperature rise in the solids. The measured traction curve is not a flow curve. Bair [Bair 2019b] argued that the shear stress versus shear rate relation of a fluid (in power-law) does not have the same form as the average shear stress versus average shear rate obtained from a traction curve (in sinh-law). Rheological properties, *e.g.* high-pressure viscosity, critical shear stress and shear modulus, cannot be obtained accurately from measured traction curves. Regarding the third assumption, independent measurements [Richmond *et al* 1984; Larsson and Andersson 2000] have shown that the thermal conductivity of lubricants increases significantly at elevated pressures. This helps to conduct more generated heat from the film to solids and hence influences the EHL traction for the thermo-viscous regime. The fourth assumption does not apply to oils with long chains or blended lubricants because of the possible inlet shear thinning. The pressure-viscosity coefficient cannot be derived accurately from measured film thicknesses using empirical central film thickness equations when inlet shear thinning does occur.

In classical EHL studies, some rheological parameters (*e.g.* the Eyring stress and the pressure-viscosity coefficient) in the assumed fluid models need to be determined by fitting the simulation results to the measured traction curves. In this way, good comparisons can always be achieved by adjusting these parameters, whereas it is hard to validate/improve the assumed models, and the obtained fluid parameters may be traction rig or system dependent and may fail to predict other EHL performance other than traction, *e.g.* the film thickness. The ongoing debate on Eyring and Carreau shear thinning models [Spikes and Zhang 2014; Bair, Vergne *et al* 2015] was triggered by such concerns. Table 2.1 compares some controversial points between classical EHL and quantitative EHL.

In this thesis, the quantitative approach is adopted for the EHL traction study with the model fluid, squalane, whose thermo-physical parameters have been reported in literature [Björling *et al* 2013; Bair, Andersson, Qureshi *et al* 2018; Bair 2006; Bair, McCabe and Cummings 2002a and 2002b]. The quantitative comparison of traction would allow us to figure out the reasons for the discrepancies between simulations and measurements based on the current understanding of rheological fluid models.

Table 2-1: Controversial points between classical EHL and quantitative EHL

Item	Quantitative EHL	Classical EHL
(1) Study method	Independent and out-of-EHL high-pressure measurements are essential for EHL studies	Traction machine is used as a viscometer (average properties); rheological parameters derived by fitting simulation results to measurements
(2) Viscosity equation	Measurements to be fitted into free-volume models for each lubricant	An empirical equations for different lubricants, <i>e.g.</i> Roelands equation
(3) Pressure-viscosity coefficient	Independent measurement using viscometers	Can be derived from measured film thickness with Hamrock-Dowson equation
(4) Shear thinning model	Power-law Carreau equation	Sinh-law Eyring equation
(5) Oil viscoelasticity $G_{\infty 0}$	Order of 1 GPa	Order of MPa from traction experiments

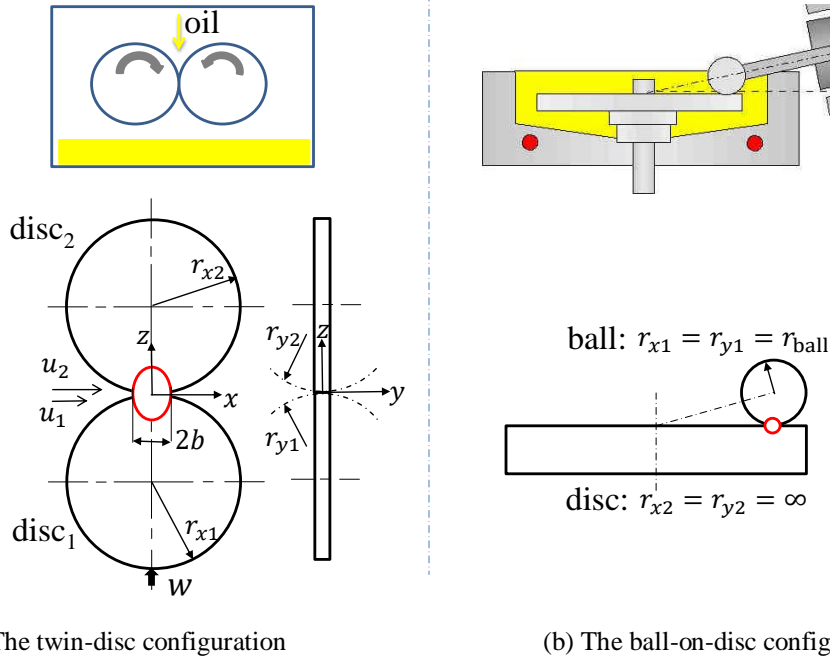
2.1.3 Traction curve measurements

Experimental techniques for traction measurements are introduced in this section. Factors that may have influence on the experimental traction results are pointed out, such as contact size/geometry, disc compliance, bulk temperature rise of the specimens and steel thermal conductivity. These factors are important for understanding the discrepancies between the predicted and measured EHL traction.

2.1.3.1 Traction machine and contact geometry

Traction machines are mostly in twin-disc and ball-on-disc configurations, see Fig. 2.4. The two specimens are loaded together and driven independently with adjustable rotating speeds to shear the fluid at any desired SRR in the presence of temperature-controlled circulating oil. To get a traction curve, the friction coefficient is measured as a function of SRR for a given experimental speed.

In this study, traction rigs in the above-mentioned two types, namely the IMKT twin-disc (TD) machine (University of Hannover, Germany) and the MTM ball-on-disc machine (PCS Instruments, UK), have been used to measure traction curves for the same model fluid, squalane. Traction curves for this fluid have also been measured by Björling at Luleå University of Technology using another commercial ball-on-disc machine, the WAM ball-on-disc machine (Wedeven Associates, US). The contact geometry and the measurement range of the three machines are listed in Table 2.2. All specimens of the traction machines are made of hardened AISI 52100 bearing steel, whose mechanical and thermal properties are listed in Table 2.3.



(a) The twin-disc configuration

(b) The ball-on-disc configuration

Figure 2-4: Schematic representation of configurations and contact geometries of the used traction machines (left: twin-disc; right: ball-on-disc)

Table 2-2: Geometrical configuration and operating range of the three traction machines (p_H for steel/steel contacts)

Item	TD	MTM	WAM
Configuration	Disc-Disc	Ball-Disc	Ball-Disc
Material	52100 steel	52100 steel	52100 steel
Radius r_{x1} , mm	60	9.525	10.314
Radius r_{y1} , mm	∞	9.525	10.314
Radius r_{x2} , mm	60	∞	∞
Radius r_{y2} , mm	50	∞	∞
Reduced radius r_x , mm	30	9.525	10.314
Ellipticity ratio k_e	1.43	1.0	1.0
Combined roughness R_q , nm	224	14	43
Oil temperature T_0 , °C	-20 to 120	-5 to 150	-40 to 140
Max. load w	20 kN	75 N	750 N
Max. Hertz pressure p_H , GPa	3.0	1.25	2.5
Speed u_e , m/s	to 15	to 4	to 10
SRR, Σ	0 – 50%	0 – 100%	0 – 100%

Table 2-3: Properties of AISI 52100 steel (disc/ball material of traction rigs)

Property	Value
Young's modulus E	210 GPa
Poisson ratio ν	0.3 (-)
Heat capacity $c_{1,2}$	470 J/(kgK)
Thermal conductivity, $k_s = k_{s1} = k_{s2}$	21 W/(mK)
Density ρ	7850 kg/m ³

In literature, it is hard to find comparisons of traction curves measured between different traction machines for the same fluid under comparable operating conditions, *i.e.* at the same mean contact

pressure ($p_{\text{mean}} = p_H/1.5$ for point contacts), speed and supplied oil temperature. Influence of contact geometry and scale on the EHL traction is still unknown, even though traction values measured in a specific traction rig have been used to predict the frictional behavior of machine elements of varying sizes and contact geometries, see for examples [Saito *et al* 2018] and [Li *et al* 2019]. Chapter 7 compared traction curves from different traction machines and studied numerically the scale effect on the EHL traction.

2.1.3.2 Measurement procedures

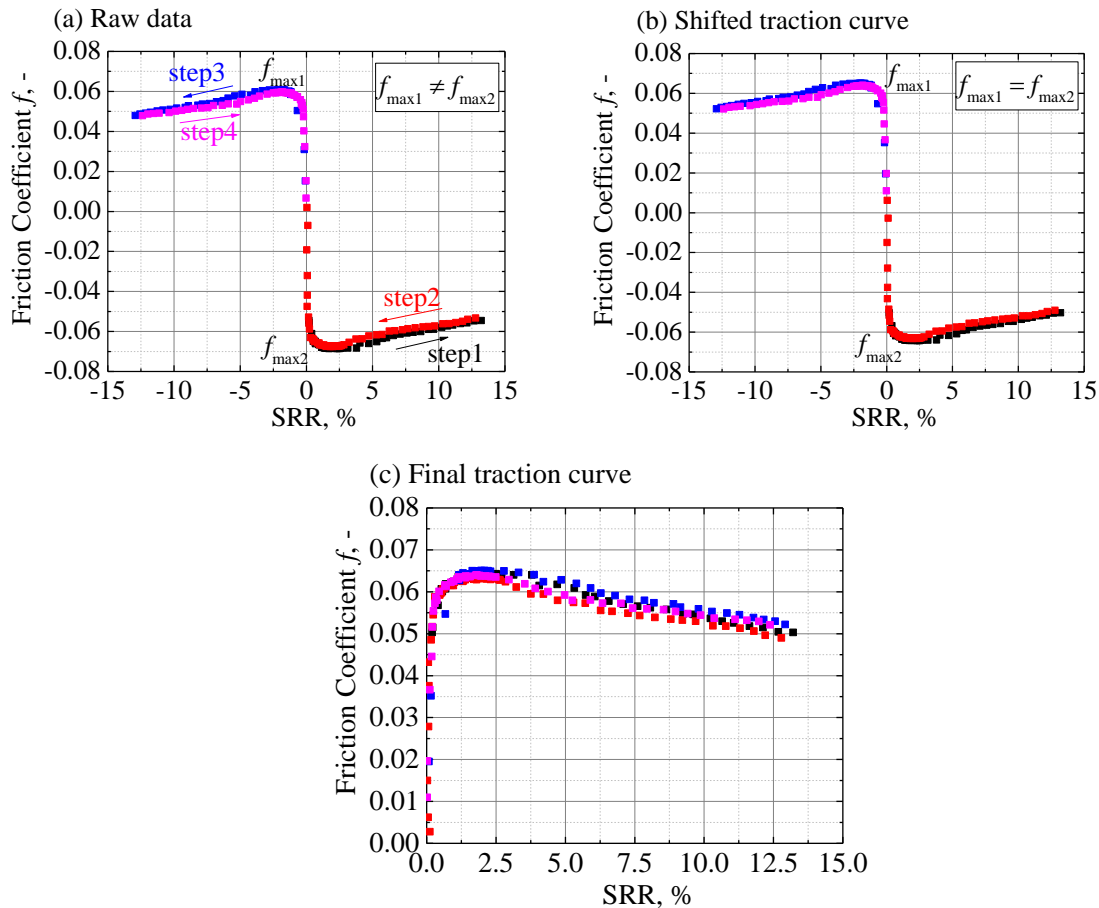


Figure 2-5: Raw traction data from twin-disc machine and the data processing methods to obtain a traction curve. (a) raw data from the four steps; (b) shift curve to coordinate (0, 0) to eliminate influence of supporting bearings; (c) a traction curve comprises the values from the four steps combining both the negative and the positive values. (Squalane, Twin-disc, $T_{\text{oil}} = 40$ °C, $u_e = 5$ m/s, $p_H = 2.42$ GPa)

Taking the TD machine as an example, one traction curve is measured with four steps in 7 minutes: (a) SRR from 0 (pure rolling) to 12.5%, by increasing disc-I velocity and decreasing disc-II velocity to achieve positive growing SRR until a desired SRR (12.5% set here) is reached; (b) SRR from 12.5% back to 0, by increasing disc-II velocity and decreasing disc-I velocity; (c) SRR from 0 to -12.5% , also by increasing disc-II velocity and decreasing disc-I velocity; and (d) SRR from -12.5% to 0 (pure rolling) through increasing disc-I velocity and decreasing disc-II velocity. During a test, the mean entraining surface velocity is a constant. In this way, one measuring cycle is a locked-loop with SRR; see Fig. 2.5(a) for example. After data analysis and re-plotting in Fig. 2.5(b) and (c), one traction curve comprises the absolute values from the four steps. This kind of procedure can eliminate the influence of supporting bearings on measurements and has been widely adopted in traction tests, also for the commercial test rigs, *e.g.* MTM and WAM.

2.1.3.3 Disc creep and SRR correction

It should be noted that disc compliance contributes to the total recorded SRR during traction measurements [Evans and Johnson 1986b; Bair and Kotzalas 2006; Mayer 2010; Poll and Wang 2012]. This influence is significant for highly-loaded contacts at small SRRs, say $SRR < 0.01$. In order to study the traction behavior of the fluid, the true SRR may be calculated by subtracting the portion of roller tangential creep from the total SRR of the rig through the following equation [Bair and Kotzalas 2006],

$$SRR = SRR_{\text{fluid}} = SRR_{\text{total}} - f \frac{p_H}{G_s} \quad (2.4)$$

where f is the friction coefficient, G_s the shear modulus (78 GPa for steel). All measured traction curves are corrected with Eq. (2.4) in this study.

2.1.3.4 Typical traction curves

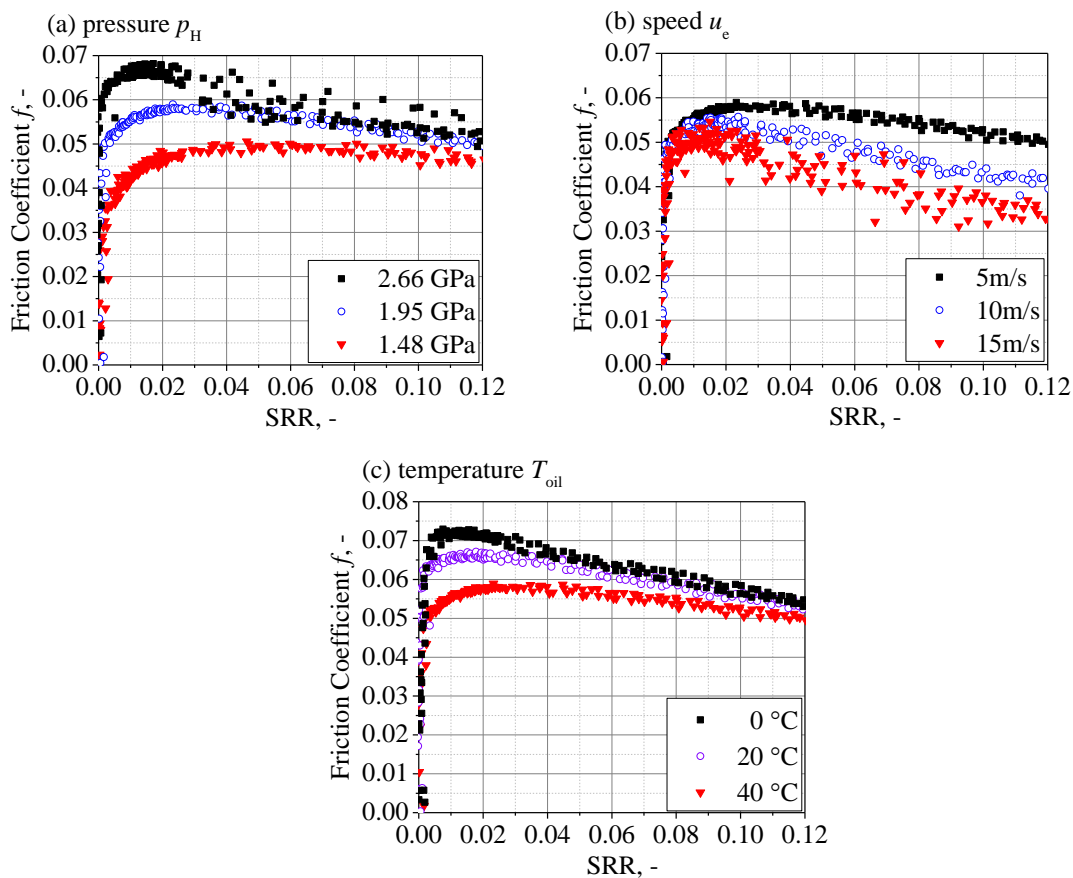


Figure 2-6: Typical traction curves at different pressure, speed and temperature conditions measured on a twin-disc machine, (a) pressure effect (5 m/s, 40 °C); (b) speed effect (1.95 GPa, 40 °C); (c) oil temperature effect (1.95 GPa, 5 m/s). (twin-disc, squalane)

Fig. 2.6 shows measured traction curves on the twin-disc machine (Sec. 2.1.3.1) at different running conditions, namely (a) pressure, (b) speed and (c) supplied oil temperature. The maximum friction coefficient increases under conditions of higher mean contact pressure and lower supplied oil temperature. At a higher speed, the maximum friction coefficient drops gently for a high pressure case in Fig. 2.6(b), while for a low contact pressure, the drop could be significant. Characteristic traction curves are shown in Fig. 2.7 depicting traction machine behavior [Gohar 2001].

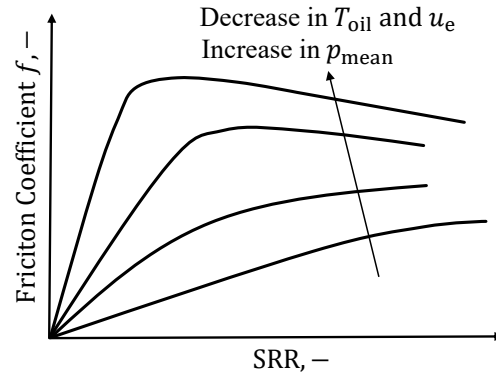


Figure 2-7: Representation of variation of friction coefficient with slide-to-roll ratio, *i.e.* traction curves at different pressure, temperature and speed.

2.1.3.5 Bulk temperature rise

The supplied oil temperature is easy to keep constant during traction measurements, whereas the bulk temperature of the discs/ball is hard to control due to the continuously generated/conducted heat from the film. For the used twin-disc machine, bulk/body temperature is measured by an inserted thermocouple beneath the surface of a disc of about 1.5 mm. Fig. 2.8 gives an example to show the bulk temperature rise and its influence on the traction results during three continuously repeated running cycles of measurements.

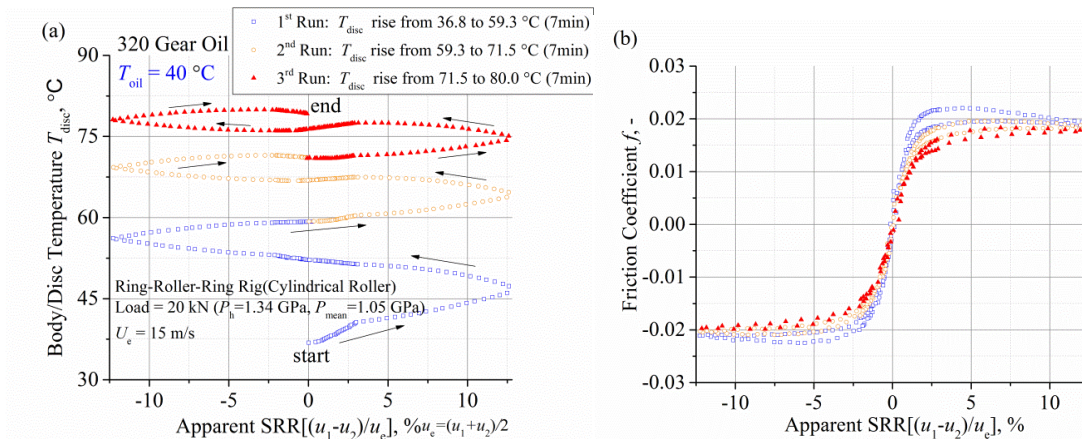


Figure 2-8: Evolution of (a) disc body temperature and (b) friction coefficient with slide-to-roll ratio during three continuously repeated running cycles of traction curve measurements (SHC 320 gear oil, supplied oil temperature is 40 °C, 15 m/s, 20 kN, Hertzian pressure of 1.34 GPa, one curve generated during 7 mins, Ring-Roller-Ring configuration)

With supplied oil temperature at 40 °C, the disc bulk temperature and the corresponding friction coefficient of three consecutive running cycles were measured and plotted in Fig. 2.8. The bulk temperature rose from 36.8 °C to 80 °C, which is twice the supplied oil temperature. It should be noted that the bulk temperature recorded here was a transient value. In practice, however, this is the typical way for traction curve measurements, as has been described in Sec. 2.1.3.2. Because it takes long for the test rig to reach heat equilibrium for each SRR and it is hard to keep the bulk temperature equal to the supplied oil temperature during the whole measurements (SRRs) of a curve.

For the friction coefficient results in Fig. 2.8(b), the three traction curves can be regarded as measurements of traction at three different starting disc body temperatures. The first curve was performed with a starting disc bulk temperature of 36.8 °C. The second one was measured directly after

the first run with a starting body temperature of 59.3 °C and the last traction curve was obtained with a starting disc temperature of 71.5 °C. It can be seen that the maximum friction coefficient and the initial slope of the traction curves are all decreasing with increasing disc mass temperature. Even in one traction curve the friction coefficient of the return stroke (SRR from $\pm 12.5\%$ back to 0) can be smaller than that of the forward stroke (SRR from 0 to $\pm 12.5\%$) as a result of a higher disc bulk temperature.

This kind of solid body temperature effect has also been reported by other researchers during traction measurements [Hirst and Moore 1980; Bader 2018; Castro and Seabra 2018; Isaac *et al* 2018]. However, in thermal EHL simulations, bulk temperature is usually assumed to be the supplied oil temperature, and the solid body temperature effect is seldom considered, except [Clarke *et al* 2006; Yang and Liu 2009]. The higher solid body temperature may reduce the oil viscosity in the inlet region and influence the EHL film thickness. For the EHL traction, the solid body temperature would influence the heat distribution and the viscosity across the film in the zone of high-pressure. In Chapter 4, this effect on the EHL film thickness and the traction is studied numerically by using the body temperature as thermal boundary condition for the solids rather than the widely used supplied oil temperature.

2.1.3.6 Thermal conductivity of 52100 steel

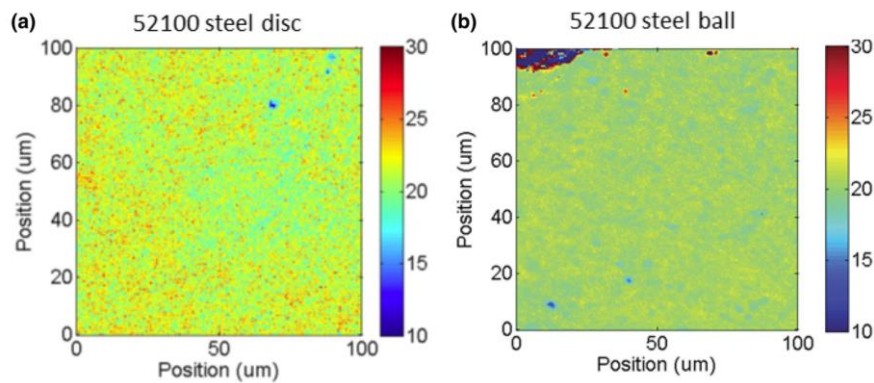


Figure 2-9: Thermal conductivity maps from FDTR method for the specimens of MTM traction rig made of 52100 steel, (a) steel disc; (b) steel ball. (color scale units: W/mK) [Reddyhoff *et al* 2019]

The solid thermal conductivity affects the EHL traction through changing heat removal and temperature rise of a tribological contact. Recently, Reddyhoff *et al* [2019] measured the thermal conductivity of specimens used in the MTM traction machine made of AISI 52100 bearing steel with a frequency domain thermoreflectance (FDTR) method. For both the ball and the disc, the thermal conductivity is around 21 W/mK (Fig. 2.9), which is less than half of the value about 46 W/mK commonly cited in TEHL simulations for a contact made of AISI 52100 steel, *e.g.* in [Habchi *et al* 2010; Björling *et al* 2013; Shirzadegan *et al* 2016]. Reddyhoff *et al* showed that the discrepancy may result from through-hardening of the steel, which supposedly leads to a smaller thermal conductivity. The value of 46 W/mK corresponds to an annealed alloy state. Indeed, out of the Tribology community, this knowledge regarding the relation between hardness and thermal conductivity has been long ago reported, see for examples [Kohlrausch 1888; Wilzer *et al* 2013].

The new measured smaller thermal conductivity would result in a higher maximum temperature in the film and thus lower viscosity and lower friction coefficient for full-film EHL lubricated rolling/sliding contacts. It is important and interesting to know the influence of steel thermal conductivity on the EHL traction and the maximum temperature rise in the film/solids. Chapter 5 did thermal EHL analysis for this effect.

2.2 Fluid model

EHL lubricants work in severe conditions. The maximum pressure can be as high as 4 GPa. The lubricant passes through the EHL contact in milliseconds and experiences high strain rates, typically in the range $10^5 \sim 10^7 \text{ s}^{-1}$. At such high contact pressures and such high shear rates, the shear stress response of the fluid is non-linear (non-Newtonian). With the Newtonian fluid assumption, it has been long noticed that the predicted EHL traction can be orders of magnitude larger than measurements, whereas mostly it works for the prediction of the film thickness. Many low molecular weight liquids (typical of lubricants) exhibit various non-Newtonian effects in rolling/sliding EHL contacts [Crook 1963; Johnson and Tevaarwerk 1977; Hirst and Moore 1979; Johnson 1993; Bair and Winer 1993; Bair 2002a; Bair 2019a], such as shear thinning (see Sec. 2.2.2) and limiting shear stress (LSS, see Sec. 2.2.3). The understanding and accurate modelling of these non-Newtonian behavior of lubricants at high stresses and/or high shear rates is critical for the prediction of both the EHL traction and the film thickness.

2.2.1 Flow curve

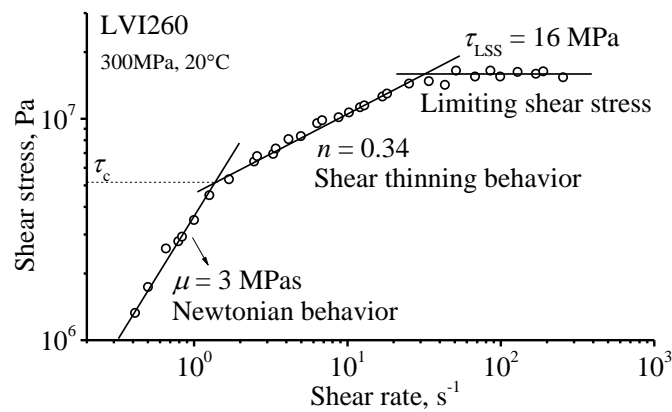


Figure 2-10: The rheological flow curve (shear stress versus apparent shear rate on a log-log scale) for the naphthenic mineral oil LVI 260 measured with a pressurized Couette rheometer measured by Bair. The curve shows transitions from Newtonian to shear-thinning and then to rate-independent response (LSS). (Data reproduced from Bair 2002b)

Before predicting the inhomogeneous shear behavior in an EHL film, it is important to know the shear and the constitutive behavior of a bulk fluid in a rather homogenous state, *e.g.* in a high-pressure viscometer. The constitutive behavior here refers to the variation of shear stress with respect to shear rate for a bulk fluid under pressure. This is also known as a flow curve, *i.e.* shear stress versus shear rate or effective viscosity versus shear rate. Bair and Winer at Georgia Tech measured flow curves for many lubricants at high stress and investigated their non-Newtonian responses [Bair and Winer 1992; Bair 2002a; Bair 2019a]. Note that flow curve is not a traction curve, as explained in Sec. 2.1.2.

Fig. 2.10 shows the measured flow curve for a model fluid by Bair with a pressurized Couette rheometer [Bair 2002b]. With increasing shear rate, the lubricant shows Newtonian, shear thinning, and limiting shear stress behavior. For shear stress less than a critical shear stress τ_c , the viscous shear stress increases linearly with shear rate and the slope of the flow curve on a log-log scale is one, indicating Newtonian behavior:

$$\tau \propto \dot{\gamma} \text{ and } \mu = \tau/\dot{\gamma} \quad (2.5)$$

μ is the low shear viscosity and its relation with pressure and temperature can be found in Sec. 2.2.6 with different models. Eq. (2.5) is known as the Newton's law of viscosity.

For $\tau_c < \tau < \tau_{LSS}$ in Fig. 2.10, the shear stress approximates a straight line with a slope smaller than one, indicating shear-thinning. For $\tau > \tau_{LSS}$, shear stress reaches a limit value (LSS, τ_{LSS}) and becomes rate-independent, indicating plastic behavior of flow (*e.g.* cohesive slip and liquid failure). The transition from Newtonian to plastic flow was also observed with many other fluids at Georgia Tech, such as 5P4E [Bair and Winer 1990; Bair and McCabe 2004] and a branched PFPE (perfluorinated polyalkyl ether) [Bair 2002a]. According to these high-pressure rheological measurements, the shear behavior of a thin compressed fluid may be depicted by Fig. 2.11. The related non-Newtonian models are introduced in the following three sections, Sec. 2.2.2 to 2.2.4.

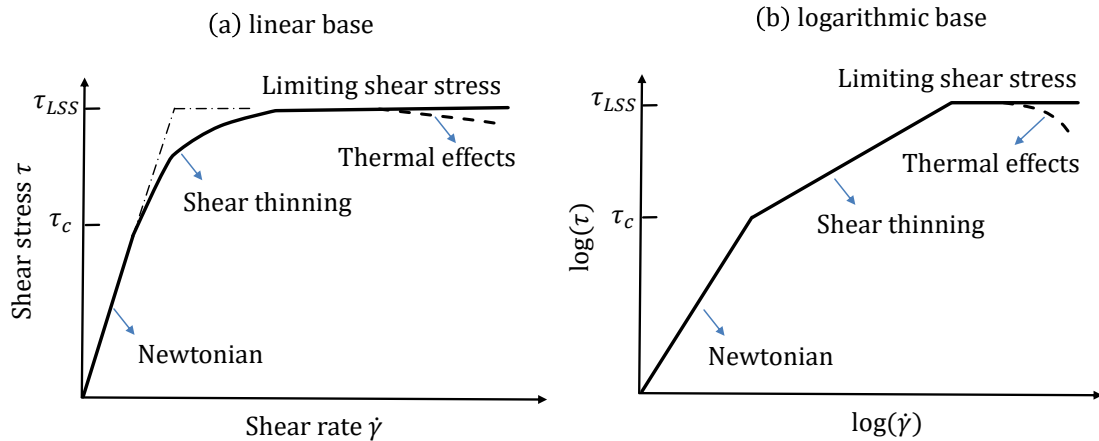


Figure 2-11: Flow curve (shear stress versus shear rate): non-linear shear response of a thin compressed liquid based on viscometer measurements at Georgia Tech, (a) linear base; (b) logarithmic base. Solid line: isothermal; dashed line: with shear heating.

2.2.2 Shear thinning

Generally, glass-forming liquids show shear thinning behavior at high shear stress. This phenomenon is usually believed to be related to the alignment of molecules along the flow direction [Hutton 1972; Davis *et al* 1992; Bair 2019a]. Shear thinning describes the shear dependence of viscosity and it plays an important role on the EHL traction at moderate SRRs for low to moderate pressure conditions (say $p_H < 1$ GPa). For polymer blended oils and large molecular weight liquids, shear thinning could also affect the EHL film thickness by decreasing the effective viscosity in the inlet region [Bair and Winer 1997; Liu and Wang *et al* 2007]. Fig. 2.12 schematically shows the constitutive relation and the effective viscosity of a shear thinning fluid compared with a Newtonian fluid (Eq. (2.5)). Shear thinning may be an indication of time/frequency-dependent or viscoelastic behavior (evidenced by normal stress difference due to elastic effects) [Dyson 1965; Bair 2002a; Bair 2019a]. High pressure viscometers, molecular mechanics and non-equilibrium molecular dynamics simulations (NEMD) are the main methods in the constitutive study of shear thinning for lubricants. In EHL studies, the concept of generalized viscosity $\eta^* = \tau/\dot{\gamma}$ as a function of shear rate is exclusively used. In this way, a non-Newtonian problem could be solved as a generalized Newtonian problem. This may be sufficient for the predictions of EHL behavior at steady shear.

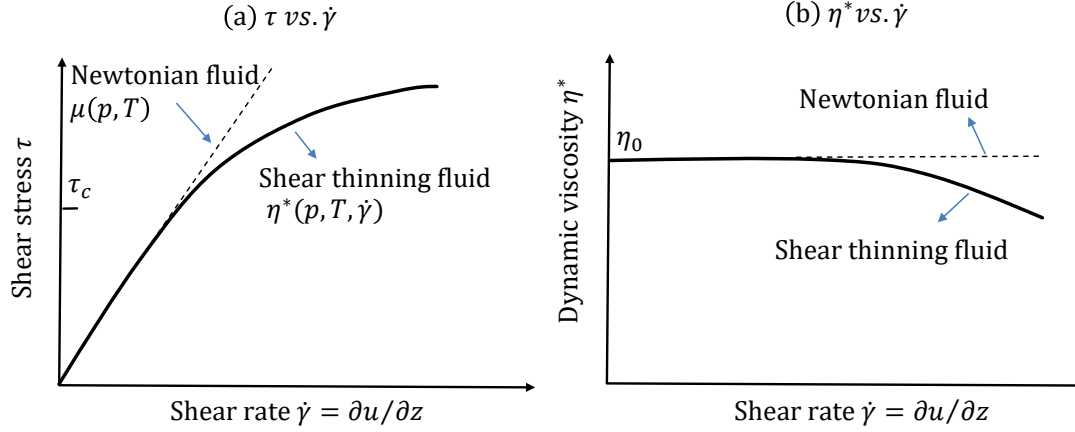


Figure 2-12: Schematic representation of (a) the constitutive behavior and (b) the effective viscosity of shear thinning fluids. Note that μ is the low-shear (Newtonian) viscosity, while η^* is the high-shear viscosity or called the generalized Newtonian viscosity)

It should be noted that there is still an ongoing debate on which is the most suitable model for describing the shear thinning of an EHL film under high shear stresses [Spikes and Zhang 2014; Bair and Vergne *et al* 2015; Jadhao and Robbins 2019]. In this section, two widely used shear thinning models in EHL studies are briefly introduced. One is the power-law Carreau-type model, and the other is the sinh-law Eyring model.

2.2.2.1 Carreau-type shear thinning equations

The flow curve for a lubricant can be measured with specially designed rheometers (*e.g.* in Couette and capillary forms) at elevated pressures. The measured data can be fitted to phenomenological constitutive equations. Results from high-pressurized Couette rheometers at isothermal conditions by Bair and coworkers [Bair 1995; Bair 2002a; Bair and Gordon 2006; Bair 2019a] showed that the generalized viscosity for shear thinning displays a power-law form above the Newtonian limit. Measured shear thinning flow curves can be represented by many power-law functions and one of them is the Carreau-Yasuda empirical equation [Yasuda 1981; Hieber 1992; Bair 2002a]:

$$\eta^* = (\mu - \mu_2) \left[1 + \left(\frac{\mu \dot{\gamma}}{\tau_c} \right)^a \right]^{\frac{n-1}{a}} + \mu_2 \quad (2.6)$$

where τ_c is the critical shear stress or the Newtonian limit stress of a fluid. When the shear stress is larger than τ_c , the high shear viscosity $\eta^* = \tau/\dot{\gamma}$ becomes less than the low shear (Newtonian) viscosity μ . μ_2 is the viscosity in the second Newtonian regime, for example in multicomponent fluids. For a single-component lubricant, $\mu_2 = 0$ and Eq. (2.6) becomes the single Newtonian Carreau-Yasuda equation. Fig. 2.13 shows the influence of parameters, a , n and τ_c , on the generalized viscosity for the Carreau-Yasuda equation. The parameter a represents the length of the transition from Newtonian to power-law response; and the smaller, the broader of the transition. The parameter n represents the slope of the curve, *i.e.* $n - 1$. The parameter τ_c indicates the onset of shear thinning. For $a = 1 - n$, Eq. (2.6) becomes the Cross equation [Hieber 1992]. For $a = 2$, Eq. (2.6) becomes the Carreau model [Carreau 1972; Bair 2019a]:

$$\eta^* = (\mu - \mu_2) \left[1 + \left(\frac{\mu \dot{\gamma}}{\tau_c} \right)^2 \right]^{\frac{n-1}{2}} + \mu_2 \quad (2.7)$$

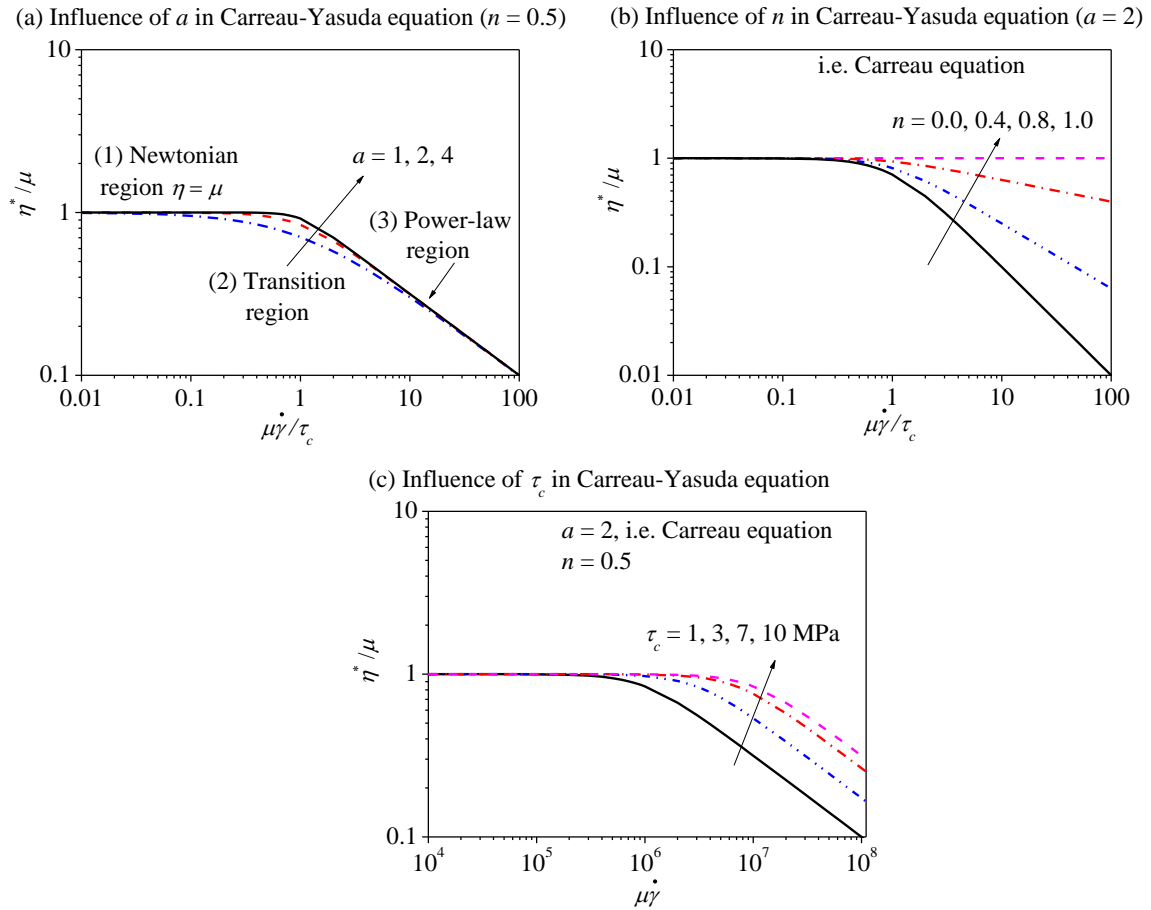


Figure 2-13: Influence of the parameter a , n and τ_c on the generalized viscosity versus reduced shear rate for the single Newtonian Carreau-Yasuda shear thinning model. (when $a = 2$, Carreau-Yasuda model becomes Carreau model)

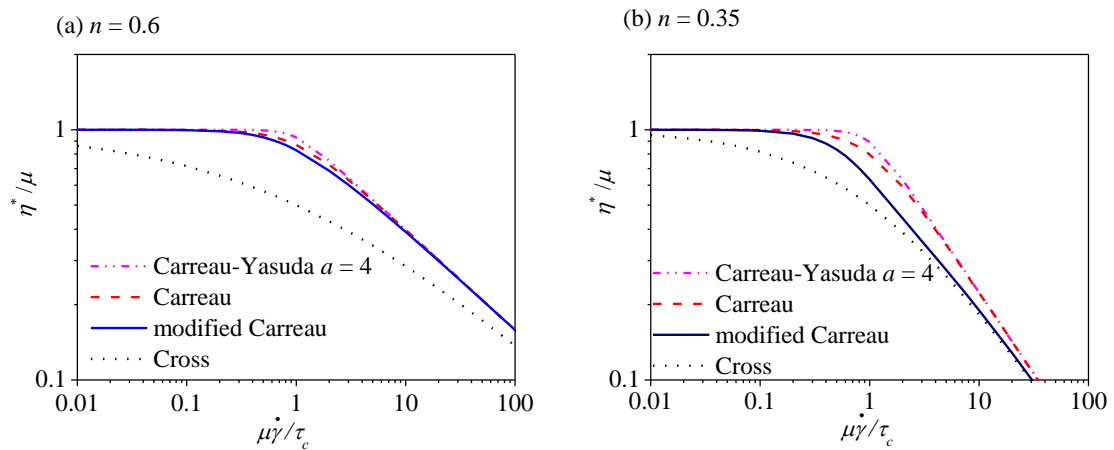


Figure 2-14: Generalized viscosity with different shear thinning equations in power-law form: Carreau-Yasuda, Carreau, modified Carreau and Cross, (a) $n = 0.6$; (b) $n = 0.35$.

In Eqs. (2.6) and (2.7), the generalized viscosity is expressed as a function of shear rate. Bair proposed modified equations using shear stress as the independent variable, and the modified Carreau equation reads [Bair 2019a]

$$\eta^* = (\mu - \mu_2) \left[1 + \left(\frac{\tau}{\tau_c} \right)^2 \right]^{\frac{1-(1/n)}{2}} + \mu_2, \text{ where } \tau = \eta^* \dot{\gamma} \quad (2.8)$$

For $n > 0.5$, Eq. (2.7) and Eq. (2.8) yield similar results. This can be seen in the comparisons of the generalized viscosity for different power-law shear thinning models in Fig. 2.14.

2.2.2.2 NEMD simulation and t - T - p superposition

It is crucial to keep isothermal conditions in the study of the constitutive behavior of fluids for true shear thinning. The measurement range of high-pressure Couette viscometers is limited by thermal softening, for example $\dot{\gamma}$ is usually smaller than 10^4 s^{-1} and shear stress $\tau < 30 \text{ MPa}$ [Bair and Winer 1993; Bair 2019a]. Note that, for an EHL contact, the shear rate $\dot{\gamma}$ is typically in the range of 10^5 s^{-1} to 10^7 s^{-1} and the local shear stress can be as high as 200 MPa.

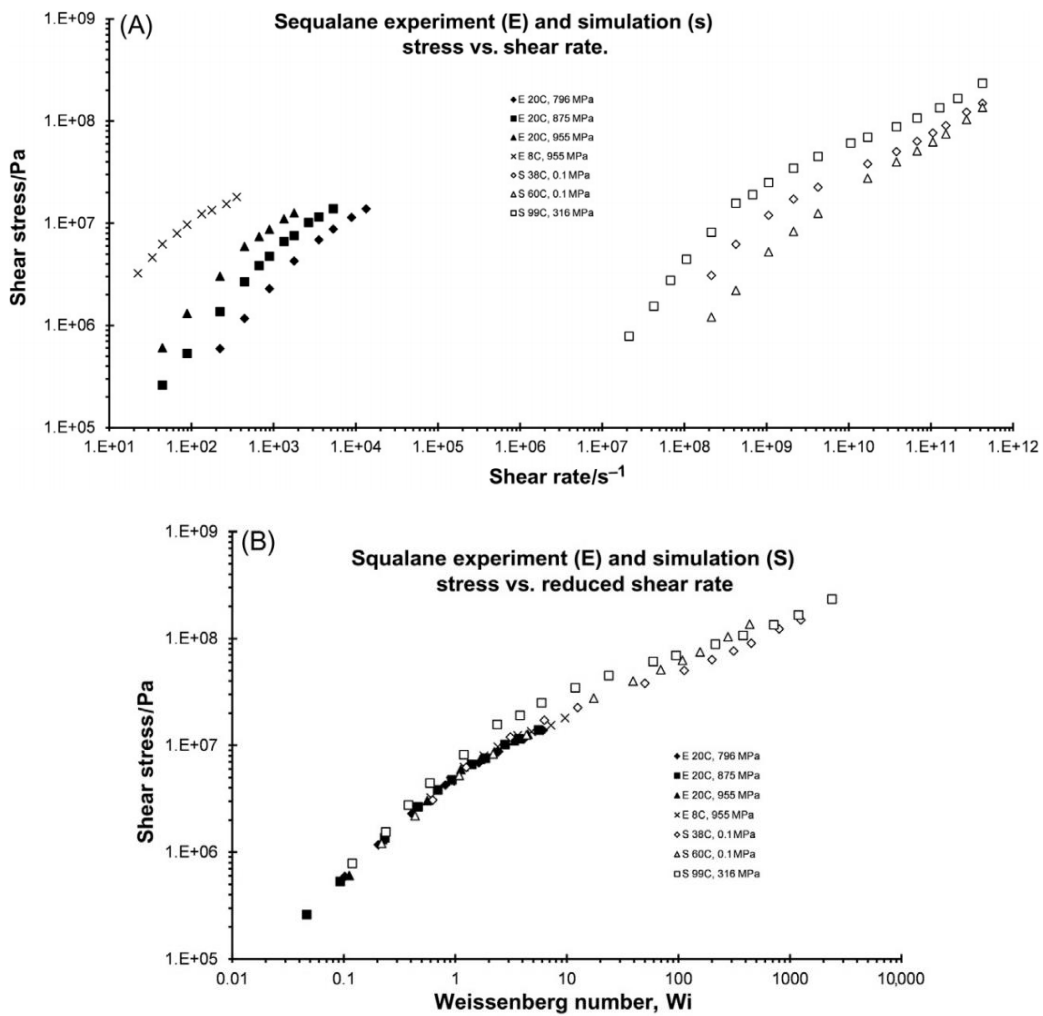


Figure 2-15: (A) Flow curves plotted as shear stress versus shear rate for squalane obtained from experiments with a pressurized Couette viscometer (solid points) and from NEMD simulations (open points). (B) The same data replotted as shear stress versus reduced shear rate to obtain a master flow curve, Wi see Eq. (2.9)- Eq. (2.10). From Bair 2019a.

To overcome the above-mentioned limitations, non-equilibrium molecular dynamics simulations (NEMD) are used to probe the molecular origin of shear thinning, see for examples [Evans and Morriss 1984; Bair, McCabe and Cummings 2002a; Liu *et al* 2017; Jadhao and Robbins 2019]. The molecules are collected in a box under pressure, and a simple and homogeneous planar Couette shear is imposed upon

these molecules. Computation time interval should be small enough (about 10^{-15} s) to simulate the molecular thermal vibration and interaction. A large shear strain should be obtained in order to show macroscopically observable properties using statistical analysis at a high signal-to-noise ratio. This leads to a high shear rate in NEMD. Additionally, with consideration of the computational burden, the number of molecules in the computation box is limited giving a very thin film thickness (typically 10 nm) and a very high shear rate ($\dot{\gamma} \subseteq (10^7 \text{s}^{-1}, 10^{12} \text{s}^{-1})$) when compared with a typical EHL film. One standard rheological analysis principle, the time-temperature-pressure superposition (t - T - p superposition) [Horowitz 1958; Tanner 1985; Bair 2002a and 2019a], may be used to construct a master flow curve to cover the range of the shear rate in EHL based on the range of data available in NEMD. This shifting principle is very important for EHL simulations. For high-pressure measurements with viscometers, this means flow curves obtained at conditions of experimental convenience may be extended to describe the shear dependence of viscosity at severe conditions of EHL. Bair *et al* [2002a; 2019a] provided the verification of the master flow curve constructed from the t - T - p superposition with a model fluid, squalane, combining the relatively low shear measurements from Couette viscometers and the extremely large shear data from NEMD simulations; see Fig. 2.15.

2.2.2.3 Onset of shear thinning

The Newtonian limit or the onset of shear thinning under simple shear may be estimated at a shear rate letting the Weissenberg number be of order one [Tanner 1985], *i.e.*,

$$W_i = \lambda_R \dot{\gamma} \approx 1 \quad (2.9)$$

where the relaxation time λ_R is approximately expressed by the Einstein-Debye rotational relation time λ_{EB} for a molecule based on the kinetic theory of molecules [Tanner 1985]

$$\lambda_R \approx \lambda_{EB} = \frac{\mu V_m}{k_B T} = \frac{\mu M}{\rho R_g T} \quad (2.10)$$

where V_m is a molecular volume $V_m = \frac{M k_B}{\rho R_g}$, k_B is the Boltzmann constant, R_g/k_B is Avogadro's number and M is the molecular weight. The relaxation time can be understood as the time required for Brownian (thermal) oscillations to remove the molecular alignment and to revert to a random distribution after removal of the applied shear stress [Bair 2002a]. Therefore, in terms of shear rate, the Newtonian limit is approximately

$$\dot{\gamma} \approx \frac{1}{\lambda_R} = \frac{\rho R_g T}{\mu M} \quad (2.11)$$

In terms of shear stress, the Newtonian limit is approximately [Bair 2002a]

$$\tau_c = \mu \dot{\gamma} \approx \frac{\mu}{\lambda} = \frac{\rho R_g T}{M} \quad (2.12)$$

The critical shear stress τ_c is usually in the range of 1 kPa to 10 MPa for lubricants. τ_c is around two orders-of-magnitude smaller than the elastic shear modulus G_∞ (order of GPa) measured from a small-strain oscillatory shear experiment at high frequencies, *e.g.* using a high-frequency piezoelectric transducer [Hutton and Phillips 1972].

It is interesting to see that dynamic oscillatory shear measurements at ambient pressure showed the same onset of shear thinning as that through steady shear measurements at elevated pressures for di(2-ethylhexyl) phthalate (DOP) [Bair 2019a], which is representative of synthetic lubricants. However,

when it comes to the whole shear thinning behavior, the relation between frequency-dependent viscosity and steady $\dot{\gamma}$ -dependent viscosity cannot be totally described by the Cox-Merz rule for different liquids [Bair and Yamaguchi *et al* 2014].

2.2.2.4 Eyring model

Eyring [Eyring 1936; Ewell and Eyring 1937] gave a molecular theory to explain the shear dependent viscosity (thought to be thixotropy that time [Hahn, Ree and Eyring 1959]) measured by capillary [Hahn and Eyring *et al* 1958] and Couette [Hahn, Ree and Eyring 1959] viscometers based on the idea that shear flow is a stress-biased thermal activation process [Spikes 2018]. The resulting sinh-law Eyring model was the first molecular model for $\eta^*(\dot{\gamma})$, even though its molecular mechanics were questioned early on [Mooney 1957]. The Eyring model reads

$$\dot{\gamma} = \frac{\tau_E}{\mu} \sinh\left(\frac{\tau}{\tau_E}\right) \quad (2.13)$$

where τ_E is the Eyring shear stress or the Newtonian limit stress, below which the model in Eq. (2.13) goes back to the Newtonian model as described in Eq. (2.5). τ_E is the only parameter in Eyring model and is usually assumed to be a material constant in the range of 1 MPa to 15 MPa depending on lubricants. The generalized viscosity can be expressed using either the shear rate or the shear stress as the independent variable:

when $\dot{\gamma}$ as the independent variable:

$$\eta^* = \frac{\tau_E}{\dot{\gamma}} \sinh^{-1}\left(\frac{\mu\dot{\gamma}}{\tau_E}\right) \text{ or } \eta^* = \frac{\tau_E}{\dot{\gamma}} \ln\left(\frac{\mu\dot{\gamma}}{\tau_E} + \sqrt{\left(\frac{\mu\dot{\gamma}}{\tau_E}\right)^2 + 1}\right) \quad (2.14)$$

when τ as the independent variable:

$$\eta^* = \frac{\mu\tau}{\tau_E \sinh\left(\frac{\tau}{\tau_E}\right)}$$

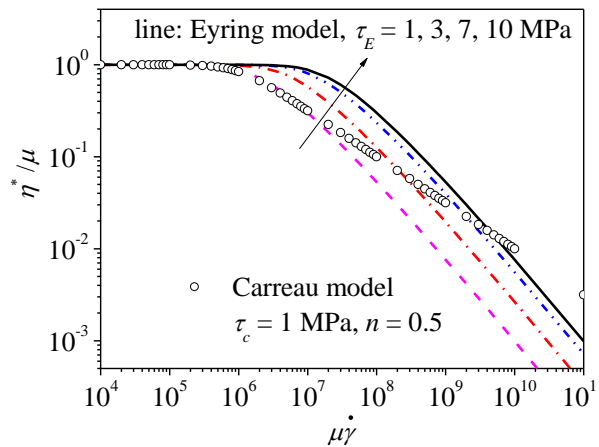


Figure 2-16: Influence of the Eyring shear stress on the generalized viscosity for the Eyring rheological model. A Carreau fluid is also plotted for comparison.

Johnson and Tevaarwerk [1977] carried out a huge number of traction measurements with disc machines and proved that the relation between the average shear stress and the apparent shear rate can be expressed by the Eyring model with a single parameter τ_E . Since the work of Johnson and Tevaarwerk, Eyring model has been widely adopted to describe the shear thinning behavior for an EHL film in

simulations. Bair [Bair 2002b; Bair 2019b] argued that the sinh-law confirmed by the averaged results with the disc machine is not a constitutive equation but rather a system model depending on real rheological models (*e.g.* the piezo-viscous behavior and the limiting shear stress) and contact conditions (*e.g.* contact geometry and pressure distribution), *i.e.* the traction curve is not a flow curve (the second assumption in classical EHL, as discussed in Sec. 2.1.2). Through Couette rheometer measurements and NEMD simulations for the model fluid squalane (see Fig. 2.15), he showed that the shear thinning behavior should be in power-law form [Bair, McCabe, Cummings 2002a and 2002b], rather than in sinh or (equally) in log function in Eq. (2.14). The effect of τ_E on the generalized viscosity for the Eyring model is shown in Fig. 2.16. At high shear rates, the Eyring model also shows similar shear thinning behavior as a power-law model on a log-log scale. However, the slope of the Eyring model is a constant and independent of the single variable τ_E , while the slope for the Carreau-type shear thinning model is adjustable through the parameter n (see Fig. 2.13(b)).

2.2.2.5 Constitutive behavior and thermal feedback

What is the best shear thinning equation for an EHL film still remains an open question. Recently, Jadhao and Robbins [2017, 2019] also did NEMD simulations using the same reference fluid squalane as was simulated by Bair and coworkers [Bair, McCabe, Cummings 2002a and 2002b], in order to know the rheological shear thinning model under conditions of EHL. They showed that the transition from Carreau to Eyring is generic, as soon as the alignment of squalane molecules saturates. However, Bair [2020] reproduced a transition from power-law to sinh-law in Couette viscometers above some viscous power. He thought the transition found by Jadhao and Robbins was caused by viscous heating and thermal softening, which could be exactly the reason why Eyring [1936] used the sinh-law to describe the experimental observations on capillary and circular Couette viscometers. Bair [2020] also argued that the transition from Carreau to Eyring would break the rule of t - T - p superposition (Sec.2.2.2.2).

NEMD simulation results from Jadhao and Robbins [2019] and from Bair-McCabe-Cummings [2002a and 2002b], to some extent, contradict each other for the same reference fluid squalane. The reason for the contradiction is beyond the knowledge of the author; whereas, what is clear is that it is important to keep isothermal conditions and to distinguish constitutive behavior and thermal feedback in both NEMD simulations and rheometer measurements. In order to facilitate the generated heat to be conducted out, Bair and Winer [1993] utilized a thin shearing gap for fluid ($h \approx 1 \mu\text{m}$) in the viscometer. They proposed that thermal feedback for a plane Couette flow of thickness h under steady shear may be characterized by the Nahme-Griffith number, Na ,

$$Na = \frac{\beta \tau^2 h^2}{k\mu} \quad (2.15)$$

where β is the temperature-viscosity coefficient, k the liquid thermal conductivity, μ the zero shear viscosity at a uniform temperature. The viscosity measurements may be considered isothermal for $Na < 0.2$ [Bair 2020].

2.2.3 Limiting shear stress

2.2.3.1 Concept, evidence, and physical nature

The concept of limiting shear stress (LSS) was introduced by Smith in the 1960s [Smith 1960] considering the fact that the measured mean shear stress in a traction rig rarely exceeds one-tenth of the mean contact pressure. He assumed that there is a limit to the shear stress that a fluid can transmit, even when under pressures great enough to prevent tensile failure. When the LSS is reached, a further increase

in shear rate does not produce increase in shear stress anymore, *i.e.* the fluid under pressure behaves like a solid with a plastic yield strength.

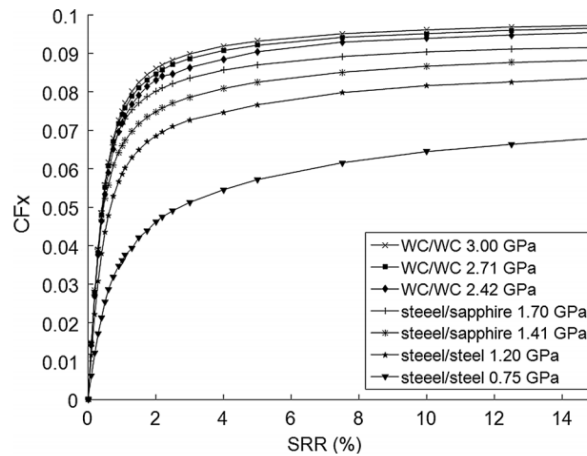


Figure 2-17: Evidences of limiting shear stress through traction measurements by Ndiaye *et al* 2017. (Shell T9 turbine mineral oil, performed at $T = 313$ K and $u_e = 1.3$ m/s, for Hertzian contact pressures from 0.75 to 3.0 GPa)

In literature, there are mainly two kinds of experimental evidence to show the existence of the LSS. One is that a plateau may appear in a traction curve measured from traction machines, indicating rate-independent response of lubricants at high pressure and shear [Plint 1967; Johnson and Tevaarwerk 1977; Evans and Johnson 1986a; Poll and Wang 2012; Ndiaye *et al* 2017, 2020; Bader 2018], see the traction curves from Ndiaye *et al* measured on a ball-on-disc machine in Fig. 2.17. The plateau regime is usually believed to be dominated by the LSS, while it should be noted that there were some doubts that it could also be a manifestation of shear heating during traction measurements [Johnson and Greenwood 1980; Zhang and Spikes 2020]. However, the plateau can extend for more than one order-of-magnitude in shear rate under ‘isothermal’ measurement conditions [Johnson and Tevaarwerk 1977; Evans and Johnson 1986a; Ndiaye *et al* 2017], which is unlike to be caused by thermal effects showing only a local maximum. Additionally, thermal EHL simulations of the EHL traction without the LSS modelling sometimes predict unrealistically large friction coefficient than measurements when using fluid properties based on high pressure measurements, especially for high contact pressure conditions. The second strong experimental evidence came from high-pressure cells. The Couette viscometer measurements by Bair and Winer [1979a, 1982, 1990, and 1993] also showed rate-independent shear behavior of lubricants, for example the flow curve in Fig. 2.10. The experiments were carried out at appropriate shear rates so that shear heating effects could be negligible.

The physical origin of the LSS is unknown. Evans and Johnson [1986a] associated this form of liquid failure with operations of shear bands based on the yield behavior of amorphous solid polymers [Imai and Brown 1976]. When the fluid stress reaches a value of order $G_\infty/30$, the mechanism of flow changes from motion of independent molecular segments to the formation of a shear band through the collaborative motion of adjacent segments. Bair *et al* [Bair, Qureshi and Winer 1993; Bair and McCabe 2004] observed inclined shear bands and intermittent shear localization in liquid through a specially designed high pressure flow visualization cell (280 MPa). The phenomenon of shear bands was also observed by Ohno when shearing a fluid at elevated pressures [Ohno *et al* 1997]. Other possible mechanisms of the LSS, such as glass transition, boundary slip, and plug flow can be found in the review paper by Martinie and Vergne [2016]. They suggested that the physical mechanism initiating the LSS is shear localization.

However, many questions remain on the shear localization initiation itself [Martinie and Vergne 2016]. In this thesis, the author assumes that the LSS exists but does not attempt to probe its molecular basis.

2.2.3.2 Measurement methods

For highly loaded EHL contacts operating at small SRRs, typically in ball/roller bearings and in CVT transmissions, traction is dominated by lubricant pressure fragility and the LSS [Bair 2002b]. The maximum friction coefficient in a traction curve at high pressure is also mainly influenced by the LSS. Considering its importance for the EHL traction prediction, several methods or techniques have been developed to measure the LSS as a function of pressure and temperature. These methods can be classified into two groups according to in- or out of an EHL contact. The first group is based on real EHL contacts, such as using traction rigs [Plint 1967; Johnson and Tevaarwerk 1977; Hirst and Moore 1979; Evans and Johnson 1986a; Bair, McCabe, and Cummings 2002; Poll and Wang 2012; Ndiaye *et al* 2017; Bader 2018], bouncing ball experiments [Jacobson 1985; Wikström and Höglund 1994] and impact ball-on-disc micro-viscometers [Paul and Cameron 1979; Wong *et al* 1995]. These measurements are carried out in a model EHL contact and the measured LSS is a mean value over the non-homogeneous contact zone. The second group of the LSS measurements is independent of EHL-contacts with special devices by shearing a bulk of pressurized homogeneous fluid while maintaining a nearly constant temperature, such as the thin-film high-pressure Couette viscometer [1990] or the axially translating concentric cylinder device [1982] designed by Bair and Winer at a condition either below or above the glass transition, as well as the high pressure chamber designed by Jacobson [Höglund and Jacobson 1986; Jacobson 1991 and 2006]. Among the above-mentioned methods, traction measurements seem to be the easiest one for the mean LSS characterization. Usually, the maximum mean shear stress in a traction curve is chosen to represent the mean LSS for that mean pressure and temperature. The pressure and temperature dependence of LSS can be obtained by measuring a set of traction curves at different pressures and temperatures. In order to reduce thermal influence, the entrainment velocity should be kept small as long as full film lubrication is reached. Suggestions for the mean LSS measurements towards measuring “isothermal” traction curves will be discussed in Chapter 7.

2.2.3.3 Empirical equations for LSS

Many different models for the LSS as functions of pressure and temperature have been proposed, see Table 2.4, based on experimental techniques introduced in the last section. Generally, it is agreed that the LSS is nearly proportional to pressure and may be slightly temperature dependent [Johnson 1993; Bair 2019a].

One of the most widely used LSS model is a linear relation proposed by Johnson and Tevaarwerk [1977] based on the measured mean shear stresses and the mean contact pressures in disc machines:

$$\tau_{LSS} = \tau_{L0} + \psi p \quad (2.16)$$

where ψ is the pressure-LSS coefficient. It appears to vary from 0.03 to 0.12 depending on lubricants, even though Johnson [1997] measured $\psi \approx 0.09$ for a range of fluids. The second parameter τ_{L0} is the y -intercept of the shear stress at $p = 0$, which is generally small compared with ψp at EHL pressures. Letting $\tau_{L0} = 0$, Eq. (2.16) can be simplified to

$$\tau_{LSS} = \Lambda p \quad (2.17)$$

The coefficient Λ could be determined by measuring only one traction curve at a high pressure by assuming the LSS is reached all over the contact area and $\Lambda \approx f_{max}$, because

$$f_{\max} = \frac{\iint \tau_{\text{LSS}} dx dy}{w} = \frac{\iint \Lambda p dx dy}{\iint p dx dy} = \Lambda \quad (2.18)$$

When fitting the measured traction data into Eq. (2.16), τ_{L0} is smaller than 0 for most lubricants. In order to avoid the unphysical negative LSS values at low pressures, the critical shear stress τ_c (see Sec. 2.2.2 shear thinning models) is set as the lower limit for Eq. (2.16) [Poll and Wang 2012]. Therefore, the pressure-LSS relation can be expressed by a bilinear form

$$\tau_{\text{LSS}} = \begin{cases} \psi (p - p_0), & \text{for } p \geq p_0 + \tau_c/\psi \\ \tau_c, & \text{for } p < p_0 + \tau_c/\psi \end{cases} \quad (2.19)$$

ψ and p_0 need to be determined by measuring a set of traction curves at high pressures.

Table 2-4: Limiting shear stress models

Models	Authors and Methods	Oil and Conditions
(1) $\tau_{\text{LSS}} = \tau_{\text{L0}} + \psi p$	Johnson and Tevaarwerk 1977, Evans and Johnson 1986a: Twin disc tests	T33, LVI260, 5P4E, Santotrac 50, HVI 650: $p_{\text{mean}} \in (0.5, 2.4)$ GPa, $T \in (17, 100)^\circ\text{C}$.
(2) $\tau_{\text{LSS}} = \Lambda p$	Bair <i>et al</i> 2002, 2012: Traction tests	T9, Squalane: $p_{\text{mean}} = 1.28$ GPa.
(3) $\tau_{\text{LSS}} = \begin{cases} \psi (p - p_0), & \text{for } p \geq p_0 + \tau_c/\psi \\ \tau_c, & \text{for } p < p_0 + \tau_c/\psi \end{cases}$	Poll and Wang 2012: Twin disc traction tests	A mineral oil and an ester oil: $p_{\text{mean}} \in (0.5, 1.3)$ GPa, $T \in (20, 80)^\circ\text{C}$.
(4) $\tau_{\text{LSS}} = \tau_{\text{L0}} + \psi p - \beta T$	Ndiaye <i>et al</i> 2017: Ball-on-disc traction tests	Benzyl benzoate and Shell T9: $p_{\text{mean}} \in (0.6, 2.0)$ GPa, $T \in (20, 80)^\circ\text{C}$.
(5) $\tau_{\text{LSS}} = (\psi p - a)e^{\beta(\frac{1}{T} - \frac{1}{T_0})}$	Houpert <i>et al</i> 1981: Twin disc traction test	A synthetic diester oil: $p_{\text{mean}} \in (0.38, 0.76)$ GPa, $T \in (25, 95)^\circ\text{C}$.
(6) $\tau_{\text{LSS}} = (\psi - aT)p$	Bair and Winer 1992: Couette viscometer [1990] and the axially translating concentric cylinder device [1982]	5P4E: low $\dot{\gamma}$, $p \in (0, 1)$ GPa, $T \in (20, 80)^\circ\text{C}$.
(7) $\psi = a + bp + cT + dpT$ for $\tau_{\text{LSS}} = \tau_{\text{L0}} + \psi p$; or $\tau_{\text{LSS}} = (\tau_{\text{L0}} + \psi p)[1 - \varepsilon(T - T_R)]$	Wikström and Höglund 1994 $T \in (-20, 110)^\circ\text{C}$, Reshetov and Gryazin 1990 $T \in (27, 150)^\circ\text{C}$: Bouncing ball	PAO and a naphthenic oil: $\dot{\gamma} \sim 10^6 \text{s}^{-1}$, $p \in (5.8, 7)$ GPa, $T \in (-20, 110)^\circ\text{C}$.

Based on traction measurements for a synthetic ester and a turbine mineral oil (Fig. 2.18), Ndiaye *et al* [2017] found that the dependences of LSS on pressure and temperature are both in a simple linear function and the two influence factors can be decoupled. The mean limiting shear stress equation is:

$$\tau_{\text{LSS}} = \tau_{\text{L0}} + \psi p - \beta T \quad (2.20)$$

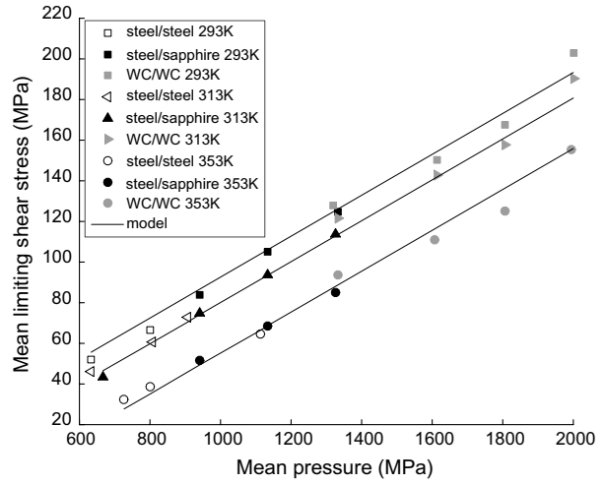


Figure 2-18: Pressure and temperature dependences of limiting shear stress measured by Ndiaye *et al* 2017 through traction measurements. (Shell T9 turbine mineral oil, performed at $T = 293\text{-}353\text{ K}$ and mean Hertzian contact pressure up to 2.0 GPa).

2.2.4 Viscoelastic behavior

2.2.4.1 Shear modulus of fluids

Viscous fluids exhibit viscoelastic behavior when subjected to rapid rates of shear. Barlow *et al* [1967, 1972] demonstrated this effect using high-frequency oscillating shear experiments. The fluid showed a transition from viscous to predominantly elastic response when the oscillation frequency was comparable with or exceeded the relaxation time of the fluid, *i.e.*, when the Deborah number $De > 1$.

$$De = \frac{t_{\text{relaxation}}}{t_{\text{observation}}} = \frac{\lambda_{\infty}}{t_0} = \frac{\mu/G_{\infty}}{t_0} \quad (2.21)$$

where G_{∞} is the limiting high-frequency shear modulus of lubricants (order 10^9 Pa for mineral oils). At room temperature and ambient pressure, oil is hard to show any elastic behavior due to the relative short relaxation time, *i.e.* $De \ll 1$. At a sufficiently high pressure or a low temperature, the viscosity μ is very high and the relaxation time is expected to increase. When μ is in the order of 10^6 Pas, the relaxation time is of order 10^{-3} s, which is also the magnitude of the observation time t_0 in EHL ($t_0 = 2a/u_e$, $2a$ of order 10^{-3} m and u_e of order 1 m/s). This kind of order of viscosity μ can be met in EHL contacts (*e.g.* for squalane $p_H > 1.5$ GPa at 40 °C). Since then $De > 1$ and oil viscoelastic may play a role on the EHL traction. The Maxwell model can be the simplest way to describe the response of viscoelastic fluid to transient simple shear when the strain is infinitesimal [Johnson and Tevaarwerk 1977]

$$\dot{\gamma} = \dot{\gamma}_e + \dot{\gamma}_v = \frac{d}{dt} \left(\frac{\tau}{G_{\infty}} \right) + F(\tau) \quad (2.22)$$

where subscripts e and v indicate the elastic and viscous elements, respectively. $F(\tau)$ represents the viscous function, for example Eq. (2.7) for the Carreau shear thinning fluids. Note that the measured elastic shear modulus G_{∞} is different from (indeed larger than) the critical shear stress τ_c (sometimes being called the effective shear modulus) in shear thinning equations, as a fluid element translates, rotates and deforms in simple shear [Hutton 1972]. G_{∞} is equally important with the viscosity term in Eq. (2.22) and it needs to be measured at high frequency shear (small-strain oscillatory shear) over a wide range of EHL contact pressures and temperatures.

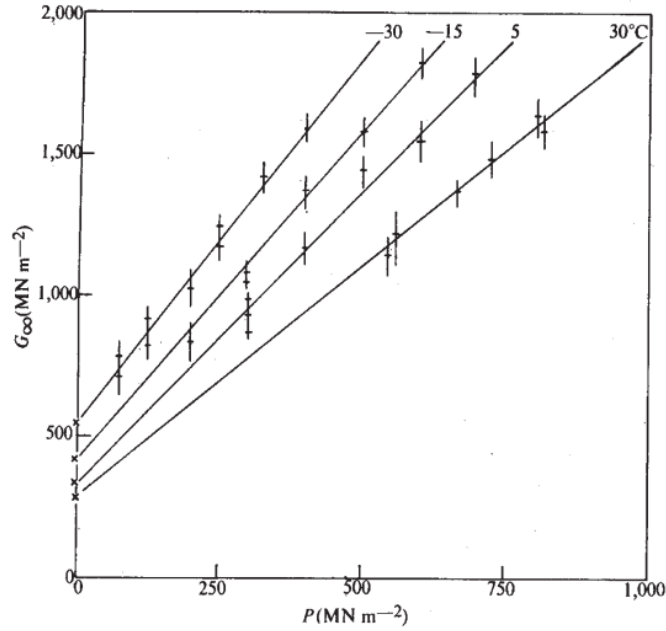


Figure 2-19: Variation of G_{∞} with pressure and temperature for di(2-ethylhexyl) phthalate measured by Hutton and Phillips 1972.

For a certain temperature, G_{∞} is usually assumed to increase linearly with pressure

$$G_{\infty}(p, T) = G_{\infty 0}(T) + G'_{\infty}(T)p \quad (2.23)$$

$G_{\infty 0}(T)$ is of the order of 1 GPa [Bair 2019a]. Some values of G'_{∞} near room temperature are 1.6 for DOP [Hutton and Phillips 1972], 4-5 for 5P4E [Barlow and Lamb 1972; Bezot *et al* 1986]. The temperature dependence of the two coefficients in Eq. (2.23) may be described by a function of $(a + bT)^{-2}$ [Hutton and Phillips 1972].

In a thought-provoking paper, Tabor [1981] discussed the relation between shear modulus and shear strength of materials including lubricants, which may be expressed by a general formula

$$G_{\infty} = 30\tau_{LSS} \quad (2.24)$$

2.2.4.2 Role of viscoelasticity on EHL traction

In literature, lubricant viscoelasticity is usually believed to affect the EHL traction at small SRRs for highly loaded contacts. In classical EHL traction studies, shear modulus has been mainly used as an adjustable parameter to reconcile simulations with measurements. In order to fit experimental traction results, G_{∞} usually needs to be of two orders-of-magnitude smaller than the independently measured value. DOP, a representative of synthetic lubricants, is reported to have the weakest pressure dependence of G_{∞} among widely studied liquids ($G'_{\infty} = 1.6$), making it ideal to manifest the effect of oil viscoelasticity on the traction compared with other fluids. Habchi and Bair [2019] did traction simulations with DOP for a line contact in steady-state using measured viscoelastic properties measured by Hutton and Phillips in 1972. They concluded that shear viscoelasticity is negligible on the EHL friction when measured properties were adopted. They thought the reason for invoking a much smaller G_{∞} to explain the traction is attributed to the wrong rheological assumptions in classical EHL theory [Bair 2019a], for example the viscosity-pressure relation. In this thesis, the viscoelastic response of fluid is simply not considered for the EHL traction prediction.

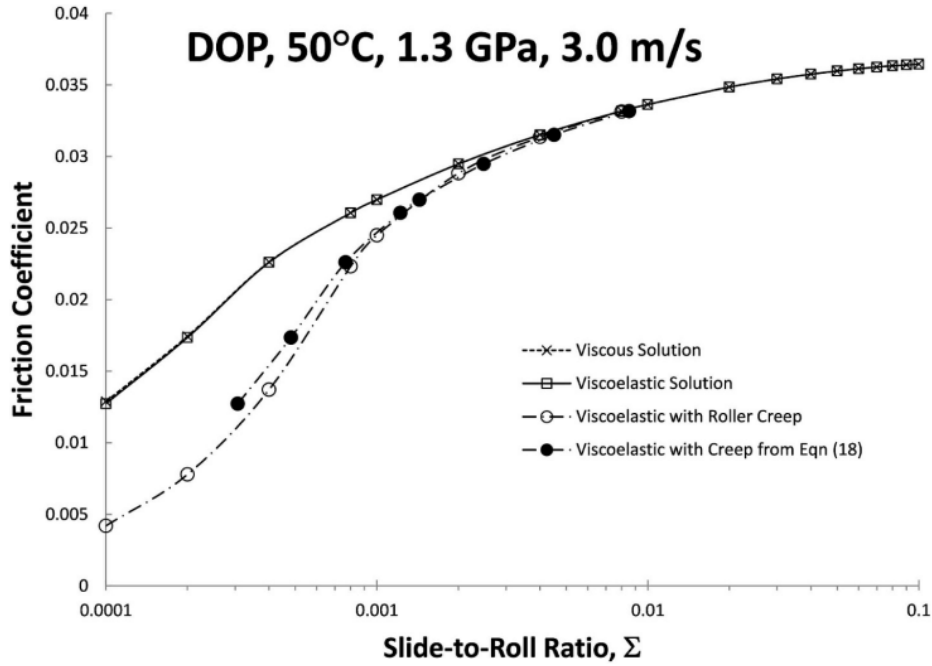


Figure 2-20: Calculated friction coefficient shows that the elastic property of oil is not important for the EHL traction prediction when independently measured viscoelastic properties are used. Roller elastic creep affects the traction at small SRRs. (DOP, inlet temperature of 50 °C, Hertz pressure of 1.3 GPa, rolling velocity of 3 m/s). From Habchi and Bair 2019.

2.2.5 Density-pressure-temperature relation

The density of a lubricant can be influenced by pressure and temperature, even though it is not as large as that for the viscosity. In hydrodynamic lubrication, density variation is quite small because of the relatively low pressures in MPa. At EHL pressures, however, liquid lubricants are compressible. At 1 GPa, the relative compression of a lubricant can be 20% at 0 °C and 30% at 200 °C [Bair 2019a]. The compressibility and the pressure-volume-temperature (PVT) relation of lubricants not only influences the EHL film thickness, but is also useful for the understanding and estimation of the pressure dependence of viscosity (by free-volume or thermodynamic scaling), thermal conductivity, permittivity and refractive index. Two popular equations of state (EOS) [Bair 2019a], Tait EOS [MacDonald 1966] and Murnaghan EOS [Murnaghan 1966], are available and can be utilized to describe the pressure and temperature dependence of volume or density for EHL lubricants.

2.2.5.1 Tait EOS

The volume V at certain temperature and pressure relative to the volume at ambient pressure V_0 can be modelled by the isothermal Tait EOS

$$\frac{V}{V_0} = 1 - \frac{1}{1 + K'_0} \ln \left[1 + \frac{p}{K_0} (1 + K'_0) \right] \quad (2.25)$$

where K_0 is the isothermal bulk modulus at $p = 0$ and K'_0 is the change rate of isothermal bulk modulus regarding pressure at $p = 0$. K'_0 is usually believed to be temperature independent and it varies from 9 to 12 according to the molecular weight of lubricants [Cutler 1958]. A universal value of 10.2 has been assigned by MacDonald [1966]. Eq. (2.25) is an isothermal EOS. A temperature modified version may be obtained as follows. Firstly, the isothermal bulk modulus K_0 is assumed to vary with temperature,

$$K_0 = K_{00} \exp(-\beta_K T) \quad (2.26)$$

where K_{00} is K_0 at zero absolute temperature (approximately 9 GPa) and β_K is the temperature coefficient (approximately 0.0065 K^{-1}) [Bair 2019a]. Secondly, the volume at ambient pressure V_0 relative to the ambient pressure volume V_R at the reference temperature T_R is assumed to vary linearly with temperature as

$$\frac{V_0}{V_R} = 1 + a_V(T - T_R) \quad (2.27)$$

The parameters in the temperature-modified Tait equations (Eq. (2.25) to Eq. (2.27)) can be determined by PVT measurement techniques for a lubricant, such as dilatometers and bellows piezometers. Bair [2019a] offered a set of general parameters of Tait EOS for EHL simulations with $K'_0 = 11$, $a_V = 8 \times 10^{-4} \text{ K}^{-1}$, $K_{00} = 9 \text{ GPa}$, $\beta_K = 0.0065 \text{ K}^{-1}$. These should be accurate for simulations of the EHL film thickness. Fig. 2.21 shows variations of the relative volume and the relative density with pressure at two kinds of temperatures using the set of general parameters from Bair. The results from the classical Dowson-Higginson equation (Sec. 2.2.5.3) are also shown. When $p > 500 \text{ MPa}$, the difference between the two correlations is getting larger.

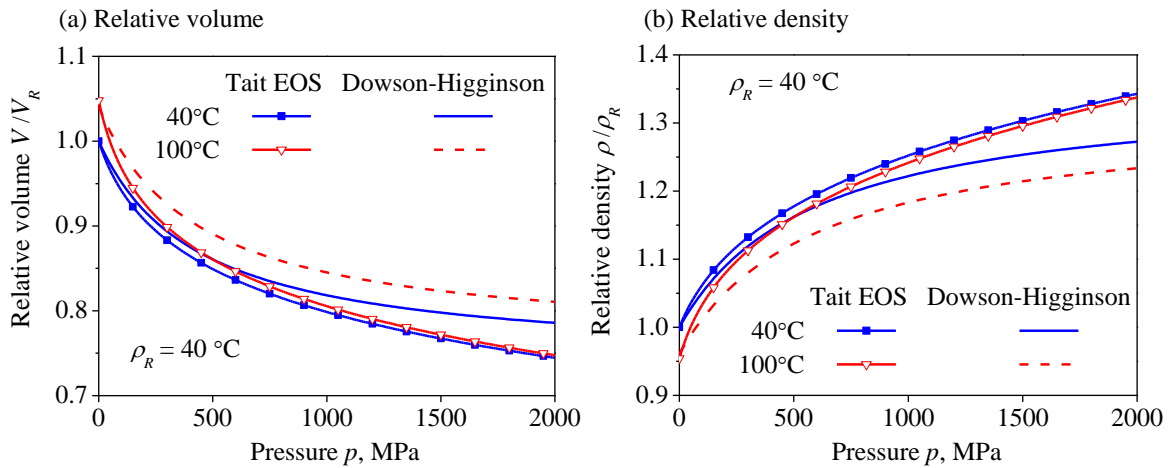


Figure 2-21: Comparison of (a) relative volume and (b) relative density between the Tait EOS and the empirical Dowson-Higginson equation (general parameters for lubricants are used for the two equations).

2.2.5.2 Murnaghan EOS

The isothermal Murnaghan equation was derived from a linear theory of finite strain [Murnaghan 1966] and it reads:

$$\frac{V}{V_0} = \left(1 + \frac{K'_0}{K_0} p\right)^{\left(-\frac{1}{K'_0}\right)} \quad (2.28)$$

Eq. (2.26) and Eq. (2.27) can also be applied to modify K_0 and V_0 , respectively, for this equation to accommodate changes in temperatures.

2.2.5.3 Dowson-Higginson EOS

The Dowson-Higginson isothermal EOS is

$$\frac{V}{V_0} = \frac{1 + \frac{K'_0 - 1}{2K_0} p}{1 + \frac{K'_0 + 1}{2K_0} p} \quad (2.29)$$

In classical EHL simulations, universal values of $K_0 = 1.67$ GPa and $K'_0 = 6.67$ are widely used and Eq. (2.29) becomes

$$\rho = \rho_0 \left[1 + \frac{0.5988 \times 10^{-9} p}{1 + 1.697 \times 10^{-9} p} \right] \quad (2.30)$$

This expression shares a limiting value of $V/V_0 \rightarrow 0.74$ and the corresponding density increment is about 33%. When temperature influence is taken into account, Eq. (2.30) is usually modified to

$$\rho = \rho_0 \left[1 + \frac{0.5988 \times 10^{-9} p}{1 + 1.697 \times 10^{-9} p} - 0.00065(T - T_0) \right] \quad (2.31)$$

Bair pointed out that this EOS is generally only accurate for low pressure conditions, as it was obtained by curve fitting of measurements till a relatively low pressure about 350 MPa at low temperatures [Dowson and Higginson 1966].

Fig. 2.22 shows the changes in volume for variable temperature and pressure measured with a metal bellow piezometer for two reference fluids by Bair [2019a]. The data were fit by two temperature modified equations of state, the Tait EOS and the Murnaghan EOS.

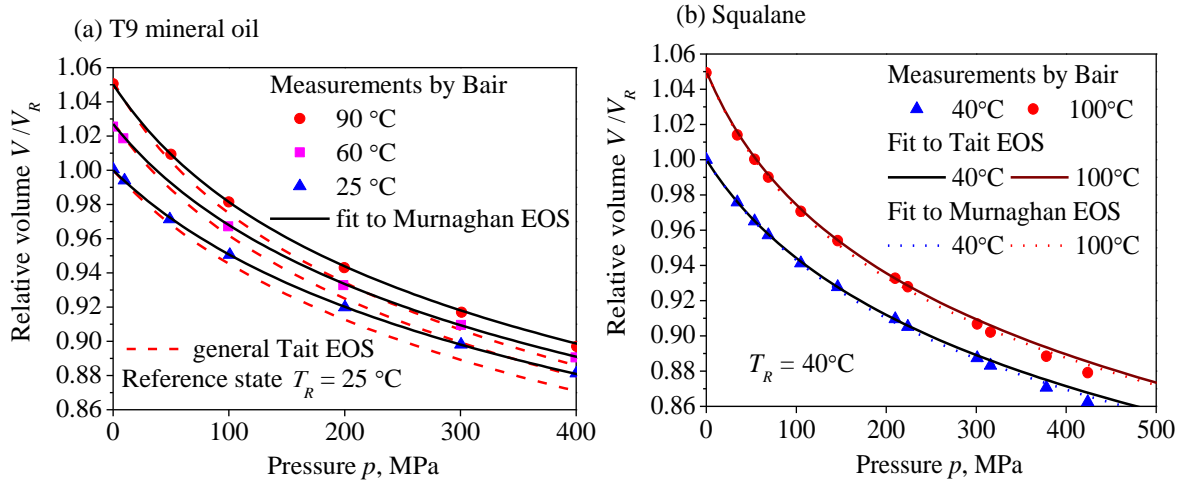


Figure 2-22: The temperature and pressure dependence of the relative volume for two model fluids and the EOS, (a) T9 mineral oil; (b) squalane.

2.2.6 Viscosity-pressure-temperature relation

Viscosity could be the most important property of a lubricant for full film lubrication and is very important for the predictions of film thickness, traction and temperature rise in an EHL. Viscosity can be influenced by pressure, temperature and shear rate. EHL film formation relies on the increase in viscosity under inlet pressure. The effect of shear rate on viscosity (the high-shear viscosity η^*) has been introduced in Sec.2.2.2. This section will focus on the low-shear viscosity μ ($\tau < 100$ Pa in [Bair 2019a]) and the viscosity-pressure-temperature (VisPT) relations for lubricants.

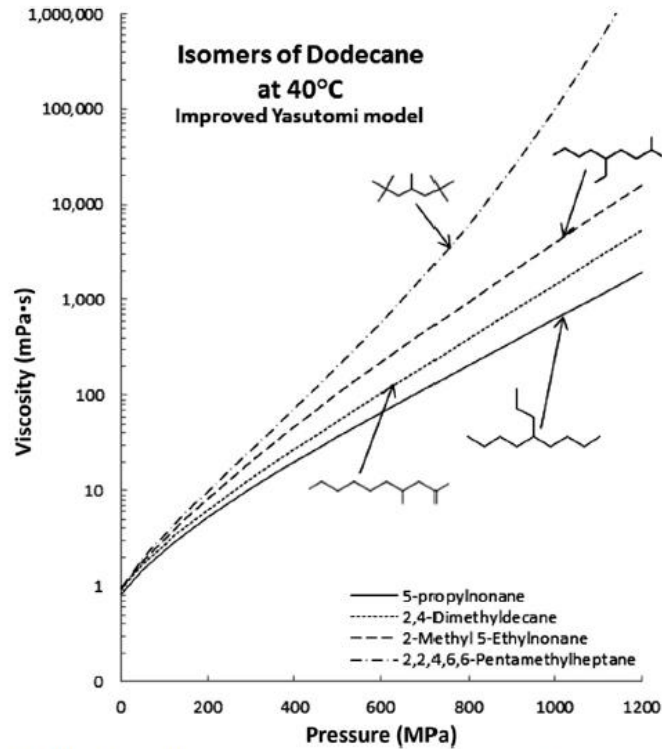


Figure 2-23: The low-shear viscosity of C12 isomers: 5-propylnonane; 2,4-dDimethyldecane; 2-methyl 5-ethylnonane; 2,2,4,6,6-pentamethylheptane, PMH. (From Bair 2019a)

For glass-forming liquids (all typical lubricants), the pressure response of viscosity is greater-than-exponential beyond a critical pressure p_c [Bair, Martinie, Vergne 2016], often following a less-than-exponential regime at low pressures. See Fig. 2.23 for example. This sigmoidal shape on a semi-log scale results from the changes in free volume and compressibility under pressure and this means the viscosity-pressure coefficient (VPC) for fluids increases with pressure when $p > p_c$. The non-linear response from independent measurements cannot be described by a classical VisPT equation (the first assumption in classical EHL as discussed in Sec. 2.1.2), *e.g.* the Roelands equation. The classical empirical equations would limit the accuracy of traction prediction and sometimes oil viscoelasticity had to be invoked with improper shear modulus values to fit the simulation results to the measured traction curves.

For the pressure dependence of viscosity at high pressures, free volume viscosity models have been used almost exclusively in physics [Bair 2006]. At the present of time, it is still hard to obtain the VisPT equation through molecular dynamics simulations for most lubricants, even though viscosity has been shown to be a function of ρ^g/T by NEMD simulations as early as 1975 [Ashurst and Hoover 1975]; see the scaling parameter in Sec. 2.2.6.3. Therefore, empirical free-volume models and equations are widely used for the description of the low shear viscosity μ at different temperatures and pressures. Three popular correlations in quantitative EHL and the classical Roelands equation for VisPT relations are given below. Fig. 2.24 shows the comparison of the low-shear viscosity among these models for two reference fluids, Shell T9 and squalane. Note that the time dependence of volume and viscosity is unlikely to occur for the time scale of EHL, especially for the viscous response of traction [Bair, Jarzynski and Winer 2001].

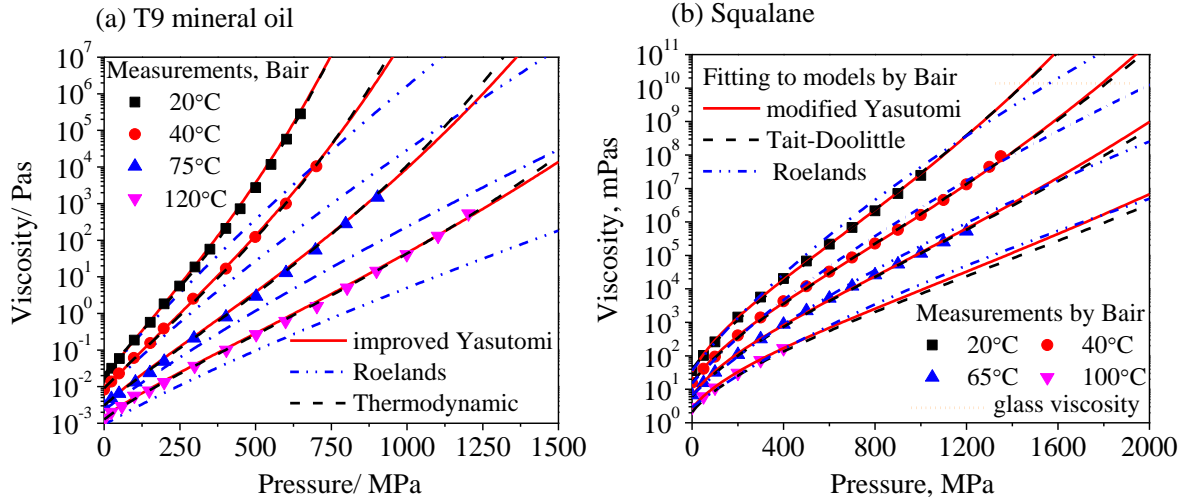


Figure 2-24: The temperature and pressure dependence of the low-shear viscosity for two model fluids, (a) T9 mineral oil; (b) squalane. Free-volume models have a good fit to the measured data; The classical Roelands equation fails to show the sigmoidal change of the viscosity.

2.2.6.1 Doolittle free-volume equation

The Doolittle free-volume equation is

$$\mu = \mu_R \exp \left\{ BR_0 \left[\frac{\frac{V_\infty}{V_\infty R}}{\frac{V}{V_R} - R_0 \frac{V_\infty}{V_\infty R}} - \frac{1}{1 - R_0} \right] \right\} \quad (2.32)$$

where the viscosity at the reference state is $\mu_R = \mu(T_R, p = 0)$ and the occupied volume fraction at the reference state is $R_0 = \frac{V_\infty R}{V_R}$. The relative occupied volume to the reference state is

$$\frac{V_\infty}{V_\infty R} = 1 + \varepsilon(T - T_R) \quad (2.33)$$

and the relative volume V/V_R is given by EOSs, *e.g.* Eq. (2.25) and Eq. (2.28) in the last section.

2.2.6.2 The improved Yasutomi correlation

This correlation was derived from the Doolittle free volume theory by Yasutomi and coworkers [1984]. It is a pressure-modified version of the Williams-Landel-Ferry (WLF) superposition principle and it does not require any EOS [Bair 2006].

$$\mu = \mu_g \exp \left[\frac{-2.303 C_1 (T - T_g) F}{C_2 + (T - T_g) F} \right] \quad (2.34)$$

where C_1 and C_2 are the WLF parameters, $T_g(p)$ is the glass transition temperature which varies with pressure as

$$T_g = T_{g0} + A_1 \ln(1 + A_2 p) \quad (2.35)$$

and the relative free volume expansivity F can be expressed by

$$F = (1 + b_1 p)^{b_2} \quad (2.36)$$

The measurement of T_g as a function of pressure by dilatometry is relatively easy [Weitz and Wunderlich 1974] compared to viscometry at high pressures. The other parameters need to be regressed from independently measured viscosity data for a specific fluid. This function is accurate at elevated pressures [Bair *et al* 2018].

2.2.6.3 Ashurst-Hoover thermodynamic scaling rule

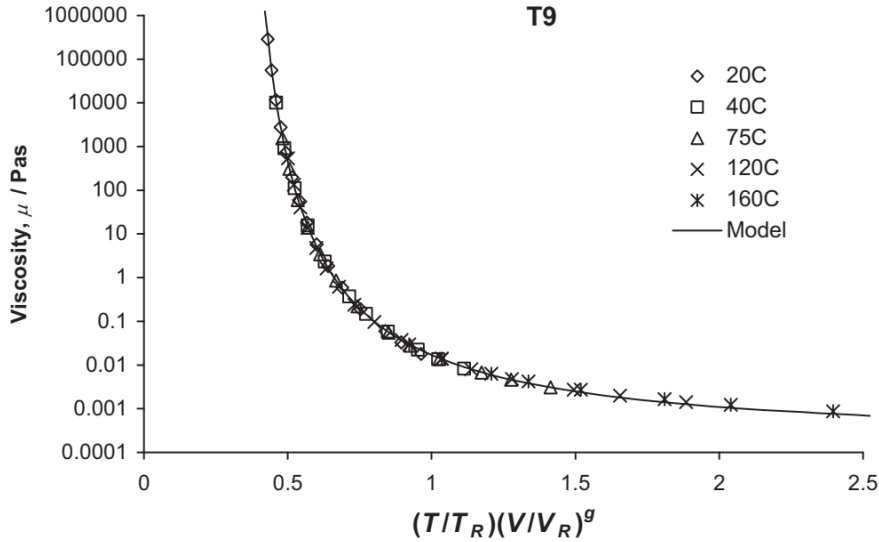


Figure 2-25: The temperature and pressure dependence of the low-shear viscosity scales with $\varphi = \left(\frac{T}{T_R}\right)\left(\frac{V}{V_R}\right)^g$ and $g = 5.0348$ for T9 oil. (From Habchi, Vergne, Bair *et al* 2010)

A thermodynamic scaling rule that has been found to be accurate for many organic liquids is $\mu = f(TV^g)$ [Roland *et al* 2006; Bair 2019a], where $-3g$ is the exponent of the repulsive Lennard-Jones intermolecular potential. A useful scaling parameter from Ashurst-Hoover is

$$\varphi = \left(\frac{T}{T_R}\right)\left(\frac{V}{V_R}\right)^g \quad (2.37)$$

g is in the range of 4 to 8 for hydrocarbons [Roland *et al* 2006]. An accurate scaling function can be obtained from a Vogel-like form:

$$\mu = \mu_\infty \exp\left[\frac{B_F \varphi_\infty}{\varphi - \varphi_\infty}\right] \quad (2.38)$$

2.2.6.4 Roelands equation

In classical EHL simulations, Barus equation and Roelands equation [Roelands 1966] have been widely used because of their simplicity (less parameters) and lack of independently measured data. However, it should be noted that these two equations failed to capture the greater-than-exponential behavior at high pressures. The Roelands equation may be used to describe the viscosity to 0.4 GPa, which is adequate for the film thickness prediction but not for the traction.

The Barus equation in a temperature modified version reads:

$$\mu(p) = \mu_0 \exp(\alpha p) \text{ and } \mu(p, T) = \mu_0 \exp[\alpha p - \beta(T - T_0)] \quad (2.39)$$

where α is the viscosity-pressure coefficient (VPC) and β is the viscosity-temperature coefficient (VTC). The Roelands equation is based on the Barus equation by modifying the VPC from α to α^*

$$\alpha^* = \frac{1}{p} (\ln \mu_0 + 9.67) \left[-1 + (1 + 5.1 \times 10^{-9} p)^z \left(\frac{T - 138}{T_0 - 138} \right)^{-s} \right] \quad (2.40)$$

where the two dimensionless parameters, z and s , may be related to VPC α and VTC β by [Houpert 1985]

$$\begin{aligned} z &= \alpha / [5.1 \times 10^{-9} (\ln \mu_0 + 9.67)] \\ s &= \beta (T_0 - 138) / (\ln \mu_0 + 9.67) \end{aligned} \quad (2.41)$$

2.2.7 Lubricant thermal properties

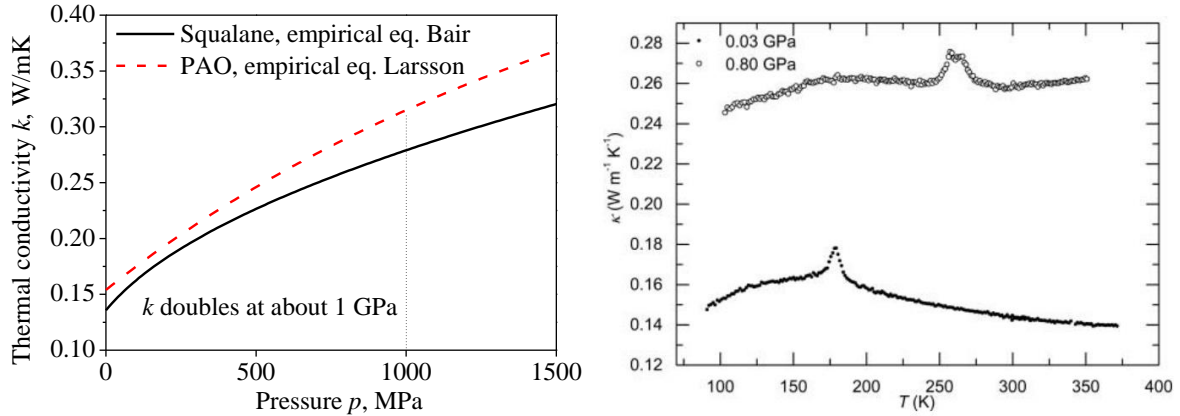


Figure 2-26: Pressure (left) and temperature (right) dependence of thermal conductivity of squalane. (The temperature dependence is from Bair-Andersson *et al* 2018)

Thermal effects are important for predictions of the EHL traction at moderate to high SRRs. The generated heat needs to be transferred by heat conduction across the thin EHL film. The temperature rise in the film may also cause instability and degradation of some oil additives. Lubricant thermal conductivity plays an important role in this process. In classical EHL simulations, oil thermal conductivity was usually assumed to be a constant value (≈ 0.14 W/mK) and independent of pressures (the third assumption in classical EHL, as discussed in Sec. 2.1.2). However, transient hot-wire measurements showed that thermal conductivity doubles its value at approximately 1 GPa [Richmond *et al* 1984; Larsson and Andersson 2000; Nelias *et al* 2002; Bair, Andersson *et al* 2018], see Fig. 2.26. The increase depends on the free volume and the coefficient of isothermal compressibility (*i.e.* bulk modulus) of fluids [Kamal and McLaughlin 1964; Werner *et al* 2008]. The pressure dependence of thermal conductivity of liquids may influence the temperature rise in the film and thus the traction prediction.

Empirical equations for lubricant thermal conductivity and thermal capacity as functions of pressure and temperature are briefly introduced here. The thermal conductivity k depends on temperature and pressure according to a scaling parameter and an empirical equation [Bair 2019a]

$$k_{\text{oil}} = B_k + C_k \kappa^{-s}, \quad \text{with } \kappa = \left(\frac{V}{V_R} \right) \left[1 + A \left(\frac{T}{T_R} \right) \left(\frac{V}{V_R} \right)^q \right] \quad (2.42)$$

where B_k , C_k , s and q are parameters depending on lubricants. These parameters need to be determined through measured thermal conductivity at different temperatures and pressures for a specific lubricant. As for the volumetric heat capacity $c = \rho c_p$ of oil, it depends on temperature and pressure, according to

$$c = C' + m \chi_c, \quad \text{with } \chi_c = \left(\frac{T}{T_R} \right) \left(\frac{V}{V_R} \right)^{-g} \quad (2.43)$$

where C' , m and g are parameters depending on lubricants. The term V/V_R in the above two equations equals ρ_R/ρ , Sec. 2.2.5. The other parameters should be determined from measurements at different pressures and temperatures by a least squares fit. Note that transition from a liquid to an amorphous solid or glassy state could be detected in the measurements of heat capacity.

Larsson and Andersson [2000] measured the thermal conductivity and the volumetric heat capacity for a number of lubricants and empirical equations have been proposed for describing the pressure and temperature dependence of thermodynamic properties. The thermal conductivity may be modelled as temperature independent between 295 and 380 K and the pressure dependence of thermal conductivity may be expressed by:

$$k_{\text{oil}} = k_0 \left(1 + \frac{a_1 p}{1 + a_2 p} \right) \quad (2.44)$$

where p is the pressure in GPa and the constants k_0 , a_1 and a_2 were given in Table 2.5 for different lubricants.

Table 2-5: Constants in the expression of pressure dependent thermal conductivity for different kinds of lubricants (from Larsson and Andersson 2000)

Lubricant type	k_0 , W/(mK)	a_1	a_2
Paraffinic mineral	0.137	1.72	0.54
Naphthenic mineral	0.118	1.54	0.33
PAO	0.154	1.40	0.34
Polyglycol	0.148	1.56	0.61
Santotrac	0.104	1.85	0.50
Ester (TMP oleat)	0.162	1.44	0.56
Rapeseed oil	0.164	1.41	0.58

2.2.8 Model fluids and properties

Model fluids here refer to reference fluids whose physical, rheological and thermal properties have been characterized independently by experimental techniques. Meanwhile, model fluids should be able to represent the viscosity dependence on temperature, pressure and shear that may be observed in EHL lubrication. Doing experiments and simulations with model fluids is important for the understanding of traction, film thickness and temperature rise. FVA (Research Association for Drive Train Technologies, Germany) supplies a number of reference fluids (gear oils) in mineral oil and synthetic types. One of the most widely used one is the mineral oil FVA-3. According to Bair [2019a], established reference liquids for quantitative EHL are di(2-ethylhexyl) sebacate, squalane (2,6,10,15,19,23-hexamethyltetracosane), diisododecyl phthalate, di(2-ethylhexyl) trimelitate, and dipentaerythritol hexaisononanoate or di(pentaerythritol) hexa(7-methyloctanoate).

In this thesis, squalane and a turbine mineral oil Shell T9 have been used. Squalane, a low-molecular-weight branched alkane (422.81 g/mol), can represent the pressure and temperature dependence of viscosity for a low viscosity paraffinic mineral oil or polyalphaolefin (PAO) [Bair 2006]. These two liquids have been well-characterized by Bair and co-workers and have been extensively studied [Habchi, Vergne, Bair *et al* 2010-2013; Björling, Habchi, Bair *et al* 2013-2015; Liu, Zhang, Bader, Poll *et al* 2018- 2020]. Especially, squalane could be one of the best characterized fluids regarding thermo-physical properties and fluid models for EHL studies, and it has also been widely used in molecular dynamics simulations [Bair, McCabe *et al* 2002a; Liu, Lu, Yu *et al* 2017; Jadhao and Robbins 2019]. Fluid models and

parameters for these two liquids are summarized in Table 2.6. Only the shear thinning models are given here because the equations are modified versions of the Carreau-type equation.

Table 2-6: Fluid models and rheological parameters for two model fluids, squalane and Shell T9 (from measurements by Bair and co-workers)

Fluid model	Parameter	Squalane	T9
1 Carreau shear Thinning	T_R	40 °C	25 °C
		Eq. (2.45)	Eq. (2.46)
2 Density free-volume based	a_V	$8.35 \times 10^{-4} \text{ K}^{-1}$	$7.73 \times 10^{-4} \text{ K}^{-1}$
	ρ_R	795.8 kg/m ³	875.0 kg/m ³
	β_K	$6.321 \times 10^{-3} \text{ K}^{-1}$	$6.09 \times 10^{-3} \text{ K}^{-1}$
Tait EOS Eqs. (2.25-2.27)	K'_0	11.74	-
	K_{00}	8.658 GPa	-
Murnaghan EOS Eqs. (2.26-2.28)	K'_0	10.85	10.545
	K_{00}	8.824 GPa	9.234 GPa
3 Low shear viscosity Improved Yasutomi Eqs. (2.34-2.36)	A_1	263.8 °C	188.86 °C
	A_2	0.3527 GPa ⁻¹	0.719 GPa ⁻¹
	B_1	13.73 GPa ⁻¹	8.2 GPa ⁻¹
	B_2	-0.3426	-0.5278
	C_1	11.66	16.09
	C_2	39.17 °C	17.38 °C
	T_{g0}	-88.69 °C	-83.2 °C
	μ_g	$1.23 \times 10^7 \text{ Pas}$	$1.0 \times 10^{12} \text{ Pas}$
Doolittle Eqs. (2.32-2.33)	B	4.256	-
	μ_R	0.0157 Pas	-
	R_0	0.6683	-
	ε	$-7.871 \times 10^{-4} \text{ °C}^{-1}$	-
Thermodynamic scaling Eqs. (2.37-2.38)	B_F	24.5	12.898
	φ_∞	0.1743	0.26844
	μ_∞	$9.506 \times 10^{-3} \text{ Pas}$	$0.1489 \times 10^{-3} \text{ Pas}$
	g	3.921	5.0348
4 Thermal conductivity Eq. (2.42)	B_k	0	0.053 W/mK
	A	-0.115	-0.101
	C_k	0.074 W/mK	0.026 W/mK
	s	4.5	7.6
	q	2	3
5 Thermal capacity Eq. (2.43)	C'	$0.94 \times 10^6 \text{ J/m}^3\text{K}$	$1.17 \times 10^6 \text{ J/m}^3\text{K}$
	m	$0.62 \times 10^6 \text{ J/m}^3\text{K}$	$0.39 \times 10^6 \text{ J/m}^3\text{K}$
	g	3	4
6 Limiting shear stress Eq. (2.17) assumed	Λ	0.075	0.083

For squalane, a Carreau equation is used to describe the shear dependent viscosity from high-pressure measurements and NEMD simulations,

$$\eta^*(\dot{\gamma}) = \mu \left[1 + \left(\dot{\gamma}_e \lambda_R \frac{\mu}{\mu_R} \frac{T_R}{T} \frac{V}{V_R} \right)^2 \right]^{(n-1)/2} \quad (2.45)$$

where $T_R = 40$ °C, $\mu_R = 15.6$ mPas, $\lambda_R = 2.26 \times 10^{-9}$ s and $n = 0.463$ [Björling, Habchi, Bair *et al* 2013].

For T9 oil, a single-Newtonian modified Carreau-Yasuda equation was graphically fitted to the measured shear dependent viscosity in a pressurized Couette viscometer,

$$\eta^*(\dot{\gamma}) = \mu \left[1 + \left(\frac{\tau}{\tau_c} \right)^a \right]^{\frac{1-(1/n)}{a}} \quad (2.46)$$

where $a = 0.5$, $n = 0.35$ and τ_c was used as a constant of 7.0 MPa [Habchi, Vergne, Bair *et al* 2010].

2.3 Isothermal traction prediction- simplified methods

The simplified methods refer to the traction solutions without solving the Reynolds equation and the solid deformation equation when compared with full numerical simulations in Sec. 2.4. The pressure distribution and the mean film thickness are usually calculated with the Hertzian contact theory (Sec. 2.3.2) and empirical central film thickness equations (Sec. 2.3.3), respectively. The simplified method is practical for engineering applications, especially for small SRRs, because it saves computation time and there is no convergence problem for highly loaded conditions. The related knowledge and isothermal traction calculation methods are briefly introduced in this section. In Chapter 6, the isothermal method is extended to thermal solutions by solving simplified energy equations of solid and liquid in order to predict the traction over a wide range of SRRs.

2.3.1 Assumptions

The following assumptions are made for the rolling/sliding elliptical EHL contact of smooth surfaces, which has been schematically shown in Fig. 2.1.

(1) A Hertzian pressure distribution. Except for low pressure conditions, the EHL pressure can be approximated by the Hertzian pressure distribution [Johnson 1987]:

$$p(x, y) = p_H \sqrt{1 - \left(\frac{x}{b} \right)^2 - \left(\frac{y}{a} \right)^2} \quad (2.47)$$

The contact axes, a and b , can be calculated based on the Hertzian contact theory and empirical formulas, for example Markho [1987] given in Sec. 2.3.2.

(2) Couette dominant flow. The shear stress contribution of the Poiseuille or pressure-driven flow may be negligible for traction prediction. It is justified to assume that the shear resistance is dominated by the surface-driven flow. For isothermal EHL at small SRRs, the shear rate in the film can be expressed as,

$$\dot{\gamma}_x = \partial u / \partial z \approx \Delta u / h_{cen} = (u_2 - u_1) / h_{cen} \quad (2.48)$$

(3) Use of empirical equations and correction factors (*e.g.* inlet shear thinning and heating correction factors) for central film thickness, *e.g.* the widely used Hamrock-Dowson (HD) equation. It is assumed that the contact is fully flooded and the film thickness can be represented by central film thickness in the EHL contact zone. See Sec. 2.3.3 for the equations.

2.3.2 Hertzian contact theory

Perhaps the most characteristic feature of EHL lubricated concentrated contacts is the near Hertzian pressure distribution and the importance of Hertzian static contact theory [Hertz 1881] to EHL is obvious. This is due to the fact that the EHL film thickness is smaller than the elastic deformations of the surfaces in the normal direction and it is much smaller than the half-width of the Hertzian contact zone.

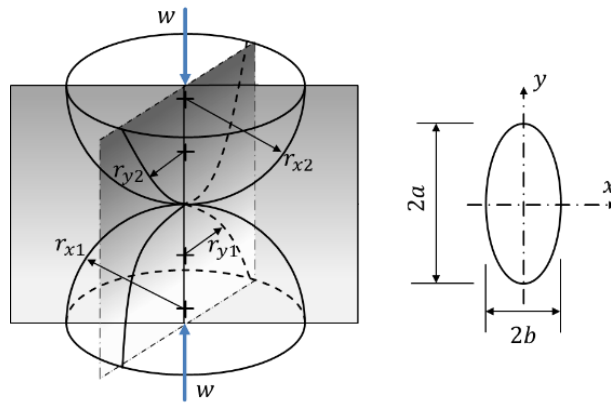


Figure 2-27: Geometry and coordinate system of a Hertzian contact problem, Left: contacting elastic solids; Right: the elliptical contact area.

As has been stated in Sec. 2.1.3, two traction machines in different configurations have been used in this study. One is the twin-disc machine forming an elliptical contact area ($k_e = 1.43$) when the two bodies are normally loaded against each other. The other is a ball-on-disc machine forming a circular contact zone, which can be regarded as a special case of elliptical contact when the ellipticity ratio $k_e = 1$. The ball and discs have low surface roughness and they are typically made of hardened bearing steel. Both of the contacts are in line with the assumptions of Hertzian contact theory, *i.e.* (1) elastic half-space approximation and $a \ll R$; (2) semi-elliptical pressure distribution; (3) small strain and homogeneous material. According to the Hertzian contact theory, the contact geometrical parameters in Fig. 2.27 and the maximum contact pressure for the elliptical contacts are given by [Johnson 1987]

$$\begin{cases} a = \left(\frac{6k_e^2 F_2 R w}{\pi E'} \right)^{1/3}, & b = \frac{a}{k_e} \\ p_H = \frac{3w}{2\pi ab} \end{cases} \quad (2.49)$$

where a and b are the Hertzian half-contact length in the transverse and motion directions, respectively; p_H is the maximum Hertzian pressure, k_e the ellipticity ratio (see Eq. (2.50)), and F_2 the elliptic integral of the second kind. The reduced radius of curvature $r = 1/(1/r_x + 1/r_y)$ and the effective radii in x - and y - direction (by assuming principle planes of solids coincide), $R_x = 1/(1/r_{x1} + 1/r_{x2})$, $R_y = 1/(1/r_{y1} + 1/r_{y2})$, respectively. E' is the reduced Young's modulus of elasticity and $E' = 2/[(1 - \nu_1^2)/E_1 + (1 - \nu_2^2)/E_2]$ (Note that there is the factor of 2 in the EHL literature, whereas in contact mechanics $E^* = 1/[(1 - \nu_1^2)/E_1 + (1 - \nu_2^2)/E_2]$). The contact problem in Fig. 2.27 can be

reduced to a rigid ellipsoid loaded on an elastic half-space, see Fig. 2.28. There are many empirical formulas available for the description of the relations of k_e and F_2 to the effective radius ratio of $D = r_y/r_x$. The equations from Markho [1987] is used here and they are

$$\begin{cases} k_e = D^{0.6268}[1 + 0.0632\sin(0.6315\ln D)] \\ F_2 = [1 + (\pi/2 - 1)D^{-1.0238}][1 + 0.0486D^{-1.3358}(\ln D)^{1.0997}] \end{cases} \quad (2.50)$$

Similar formulas can be found from Hamrock and Brewe [1983], Greenwood [1985], among others. Note that the Hertzian contact parameters, *e.g.* the semi-axis of the Hertzian contact ellipse and the maximum Hertzian pressure, are used as dimensionless references for the Reynolds equation and the film thickness equations in Sec. 2.4.

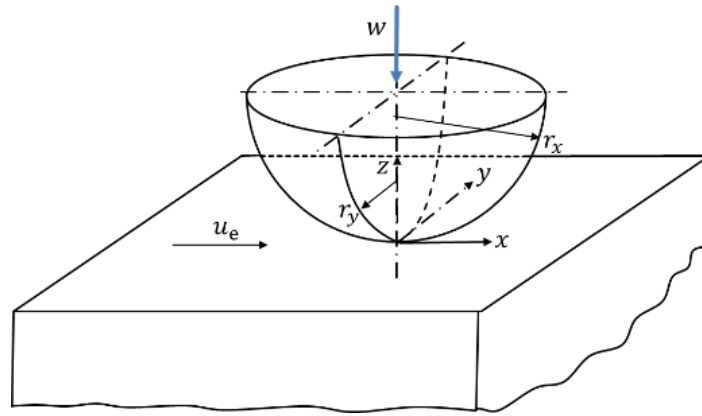


Figure 2-28: The reduced model for the Hertzian contact problem in Fig. 2.27: a rigid ellipsoid loaded on an elastic half-space.

2.3.3 EHL film thickness

For the simplified EHL traction calculation, an appropriate central film thickness is necessary for the evaluation of the shear rate, Eq. (2.48). The lubricating film can be built in a point contact because of surface elastic deformation and the lubricant piezoviscous behavior (Sec. 2.2.6). Depending upon the extents of these two factors, four lubrication regimes have been identified [Hamrock and Dowson 1981], namely piezoviscous-elastic, piezoviscous rigid, isoviscous rigid and isoviscous elastic regimes. This work focuses on the piezoviscous-elastic regime, which is the case of “hard EHL” for highly-stressed rolling/sliding contacts in machine elements.

2.3.3.1 Mechanism

Since the introduction of the inlet solution from Ertel [Mohrenstein-Ertel 1984] published by Grubin [Grubin 1949], the EHL film thickness has been revealed to be inlet dominated. It is mainly related to the ambient viscosity and the pressure-viscosity coefficient at relatively low inlet pressures (typically lower than 0.4 GPa).

Typically, the EHL film shape looks like a horse-shoe (see Fig. 2.29) characterized by a wide central flat zone with a nearly constant film thickness h_{cen} and constrictions near the outlet and two sides of the contact. From the point of view of flow, EHL film thickness results from the competition of Couette flow and Poiseuille flow in the inlet region. Once the fluid enters the Hertzian contact zone, it behaves like a solid to be transported to the outlet. In the contact center, the flow is mainly Couette flow and the film thickness is rather uniform, *i.e.* the so-called central film thickness h_{cen} . When the fluid is going to leave the contact zone, both the Couette and the Poiseuille flow help to push the fluid out. In

order to assure mass conservation, constrictions with a minimum film thickness h_{\min} are formed close to the outlet. The EHL film thickness can be measured by optical interferometry, electrical capacitance method, ultrasonic, fluorescence method, and so on.

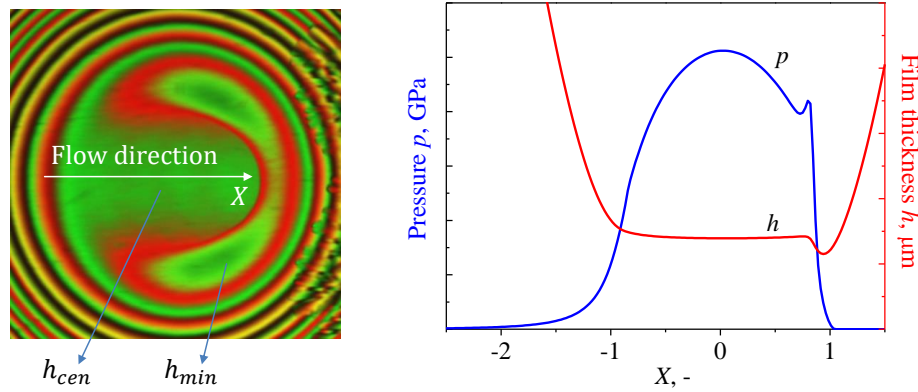


Figure 2-29: (Left) EHL film shape observed using dichromatic interferometry [Liu, Guo, Wong *et al* 2015] on a ball-on-disc optical EHL test rig; (right) EHL film thickness and pressure distribution along the central line of the contact.

2.3.3.2 Empirical equation and correction factors

Through dimensional analysis, EHL film thickness h/R is found to be governed by three independent variables, which are known as the Dowson-Higginson parameters, *i.e.* the material parameter $G = \alpha E'$, the speed parameter $U_e = u_e \eta_0 / (E' R_x)$ and the load parameter $W = w / (E' R_x)$ for line contact ($W = w / (E' R_x^2)$ for point contact). For elliptical contacts, there is another parameter to characterize the ellipticity ϵ . By fitting numerical results with these parameters into a form of $h/R = c U_e^x G^y W^z$, many regression equations have been proposed for the EHL central and minimum film thickness [Dowson and Higginson 1959; Cheng 1972; Hamrock and Dowson 1976, 1977; Chittenden *et al* 1985; Venner and Lubrecht 2000]. Note that the EHL film thickness can also be described by two independent variables M and L , for theoretical but not for experimental purpose, following the optimal similarity analysis by Moes [1992]. The Hamrock-Dowson formula [Hamrock and Dowson 1977] is still one of the most widely used ones. For point contacts lubricated with a Newtonian fluid at pure rolling and isothermal conditions, HD equation reads

$$\begin{aligned} h_{\text{HDcen,iso}} &= 2.69 R_x U_e^{0.67} G^{0.53} W^{-0.067} (1 - 0.61 e^{-0.73 \epsilon}) \\ h_{\text{HDmin,iso}} &= 3.63 R_x U_e^{0.68} G^{0.49} W^{-0.073} (1 - e^{-0.68 \epsilon}) \end{aligned} \quad (2.51)$$

where ϵ is the ellipticity parameter $\epsilon = 1.03 (R_y / R_x)^{0.64}$. From the exponents in the equation, it can be concluded that the EHL film thickness is sensitive to rolling speed u_e , oil viscosity η_0 and pressure-viscosity coefficient α . The viscosity at relatively low inlet pressures is comparatively easy to measure and could be described fairly well by many empirical equations (see Sec. 2.2.6). The definition of α_{film} [Bair *et al* 2006] for the pressure-viscosity coefficient is used in this study, see Sec. 2.3.3.3.

Several effects could reduce the EHL film thickness by influencing the inlet conditions or lubricant rheological properties, such as inlet shear heating, inlet shear thinning, second-Newtonian rheology, oil/grease starvation, surface roughness and solid body temperature effect (Chapter 4). These effects on the EHL central film thickness have been studied experimentally and numerically in the literature and some of them could be accounted for with analytical/empirical correction factors. For a better film thickness prediction, especially for high speed and/or high load conditions, inlet shear heating

and shear thinning may be taken into account with correction factors, among others, from Gupta [1992] and from Bair [2005], respectively, *i.e.*

$$\varphi_{\text{thermal}} = \frac{1 - 13.2(p_H/E')L^{0.42}}{1 + 0.213(1 + 2.23\Sigma^{0.83})L^{0.640}} \quad (2.52)$$

$$\varphi_{\text{thinning}} = 1.0/\{1 + 0.79[(1 + \Sigma)\Gamma]^{1/(1+0.2\Sigma)}\}^{3.6(1-n)^{1.7}}$$

where the thermal loading parameter (Brinkman number) $L = -\frac{\partial\mu}{\partial T} \frac{u_e^2}{k_{oil}}$, the inlet Weissenberg number $\Gamma = \frac{u_e \eta_0}{h_{HDcen,iso} \tau_c}$, the slide-to-roll ratio $\Sigma = SRR = \Delta u/u_e$, and n is the power-law component in the shear thinning equation (Sec. 2.2.2). The central film thickness is then calculated by

$$h_{cen} = h_{HDcen,iso} * \varphi_{\text{thermal}} * \varphi_{\text{thinning}} \quad (2.53)$$

2.3.3.3 Viscosity-pressure coefficient (VPC) for film thickness

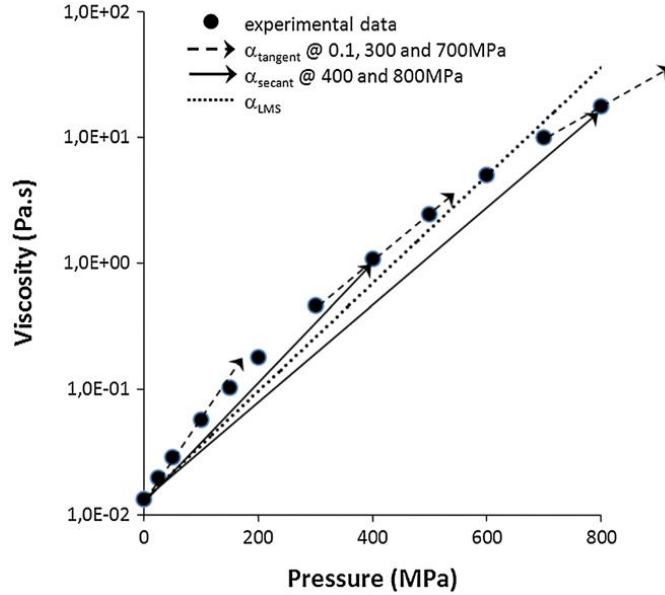


Figure 2-30: Different definitions of Viscosity-pressure coefficient based on a single set of experimental data (reproduced from [Vergne and Bair 2014])

VPC is necessary for film thickness calculation with empirical equations, *e.g.* in Eq. (2.51). The VPC for film thickness needs to represent the low pressure behavior of lubricants (< 400 MPa), and there are several different definitions in the literature, such as α_{tangent} , α_{secant} , $\alpha_{\text{least-mean-square}}$ in Fig. 2.30 [Vergne and Bair 2014]. Bair *et al* [2006] defined a new VPC, namely α_{film} , to satisfy the requirement that a Newtonian fluid with the same ambient viscosity and the same VPC should generate the same central film thickness.

$$\alpha_{\text{film}} = \frac{[1 - \exp(-3)]}{\left[\int_0^{\frac{3}{\alpha^*}} \frac{\mu(0) dp}{\mu(p)} \right]}, \text{ where } 1/\alpha^* = \int_0^{\infty} \mu(0) dp / \mu(p) \quad (2.54)$$

In the case of Barus equation $\mu = \eta_0 \exp(\alpha p)$, $\alpha_{\text{film}} = \alpha$. Interested readers are referred to [Vergne and Bair 2014].

Note that the regression method of deriving VPC from measured film thickness with an optical EHL rig may only work for Newtonian fluids at well-controlled conditions. For polymer blended oils and high viscous fluids, inlet shear thinning may exist and the derived VPC from film thickness measurements would be smaller than the value determined from high-pressure viscometers.

2.3.4 Isothermal traction computation

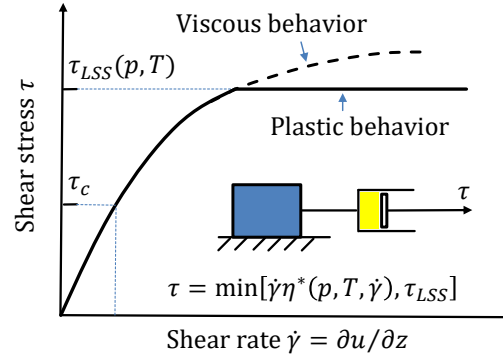


Figure 2-31: The viscous-plastic fluid model used in EHL traction calculation. The viscous part is non-linear and modelled by non-Newtonian shear thinning rheological fluid models.

A viscous-plastic rheological fluid model was used for the EHL traction prediction:

$$\tau_x = \min[\dot{\gamma}_x \eta^*(p, T, \dot{\gamma}_x), \tau_{LSS}] \quad (2.55)$$

Eq. (2.55) can be schematically represented by Fig. 2.31. Shear thinning behavior refers to Sec. 2.2.2 and the limiting shear stress behavior refers to Sec. 2.2.3.

The global friction coefficient is defined as the ratio of the tractive force to the applied normal load,

$$f = \frac{\iint \tau_x dx dy}{w} \quad (2.56)$$

For isothermal EHL traction simulations, it is a two-dimensional problem on plane XOY (Fig.2.28), as shear rate can be assumed to be homogeneous across the film. According to Eq. (2.56), the friction coefficient can be rapidly calculated, since no iteration is needed in this calculation. The distribution of shear rate can be regarded as uniform all over the contact area for isothermal conditions (Assumption 2) and $\dot{\gamma}_x$ can be obtained with $\Delta u/h_{cen}$ using Eq. (2.48). The viscosity η^* in Eq. (2.55) is calculated using the improved Yasutomi equation and the Carreau shear thinning equation listed in Table 2.6, Sec. 2.2.8. When the calculated local shear stress is larger than the corresponding LSS for a pressure at a local node, the shear stress is set to the value of the LSS [Bair, McCabe, Cummings 2002a, 2002b].

2.4 Thermal EHL theory for traction prediction

Both non-Newtonian effect and thermal effect need to be modelled for a complete explanation of the EHL traction. In this section, a thermal EHL model, governing equations and related numerical methods used in this study are introduced.

2.4.1 Theoretical model

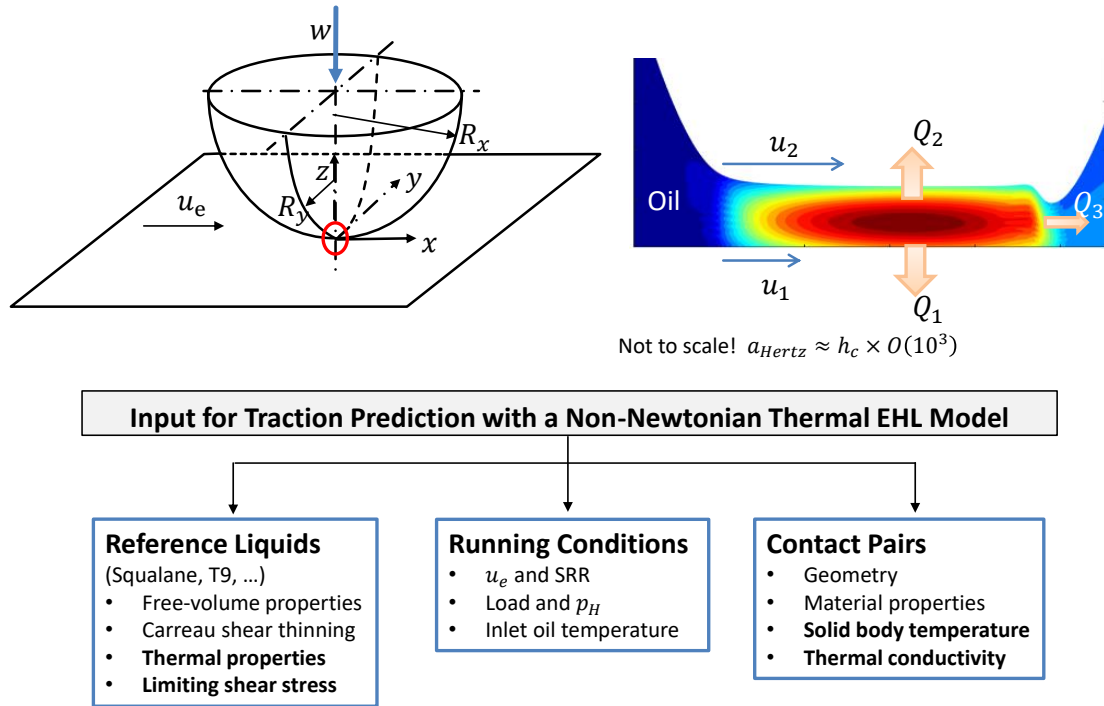


Figure 2-32: Schematic of a rolling/sliding EHL contact and the essential input parameters for modelling the traction accounting for non-Newtonian and thermal EHL effects with model fluids.

Because of the four-step procedure in traction experiments (Sec. 2.1.3.2), the measured traction can be regarded as the mean traction of the two surfaces. Therefore, in simulations, the friction coefficient of a rolling/sliding contact is defined as the average value of the traction coefficients on the upper surface ($z = h$) and on the lower surface ($z = 0$), and it can be written as

$$f = -\frac{1}{2w} \iint \left(\eta^* \left(\frac{\partial u}{\partial z} \right) \Big|_{z=0} + \eta^* \left(\frac{\partial u}{\partial z} \right) \Big|_{z=h} \right) dx dy \quad (2.57)$$

The definition of a rolling/sliding EHL contact problem can be illustrated with Fig. 2.32. Two bodies, a ball (or an ellipsoid) and an elastic half-space, are loaded together and deform elastically to form a circular or an elliptical contact area depending on the geometry and mechanical properties of the contact pairs. They both run in the x -direction with surface velocities of u_1 and u_2 , respectively. The rolling motion entrains the oil into the converging gap. A thin film formed in the approximately parallel conjunction carries the load and it is working under sever conditions, such as the maximum pressure in the order of GPa, at high shear stress and high shear rate, and a possibly high temperature rise. To develop a thermal non-Newtonian EHL model for traction prediction, all these factors need to be modelled and, generally, it consists of three parts; that is, (1) an EHL part for the contact pressure and the film thickness; (2) the Non-Newtonian shearing behavior of the fluids; (3) Temperature feedback and thermal effects. The second part, non-Newtonian fluid models, has been introduced in Sec. 2.2 and a non-Newtonian viscous-plastic model is used in this study, as is expressed in Eq. (2.55) and Fig. 2.31. Note that the shear thinning models in Sec. 2.2 are one-dimensional rheological models and in order to calculate an effective viscosity for a point contact in two dimensions, the shear rate $\dot{\gamma}$ in the rheological model should be replaced by the composite shear rate $\dot{\gamma}_e$ in both x and y directions,

$$\dot{\gamma}_e = \sqrt{\dot{\gamma}_x^2 + \dot{\gamma}_y^2} = \sqrt{(\partial u / \partial z)^2 + (\partial v / \partial z)^2} \quad (2.58)$$

The models and governing equations related to the other two parts for EHL modelling will be introduced below.

2.4.2 Governing equations: EHL part

2.4.2.1 Generalized Reynolds equation

The equation for a steady-state point contact lubricated with a generalized Newtonian lubricant is given by Yang and Wen [1990]

$$\frac{\partial}{\partial x} \left[\left(\frac{\rho}{\eta} \right)_e h^3 \frac{\partial p}{\partial x} \right] + \frac{\partial}{\partial y} \left[\left(\frac{\rho}{\eta} \right)_e h^3 \frac{\partial p}{\partial y} \right] = 12u_e \frac{\partial(\rho^* h)}{\partial x} \quad (2.59)$$

where $u_e = (u_1 + u_2)/2$, $(\rho/\eta)_e = 12(\eta_e \rho'_e / \eta'_e - \rho''_e)$, $\rho^* = [\eta_e \rho'_e (u_2 - u_1) + \rho_e u_1] / u_e$, $\rho_e = (1/h) \int_0^h \rho dz$, $\rho'_e = (1/h^2) \int_0^h \rho \int_0^z (1/\eta^*) dz' dz$, $\rho''_e = (1/h^3) \int_0^h \rho \int_0^z (z'/\eta^*) dz' dz$, $1/\eta_e = (1/h) \int_0^h (1/\eta^*) dz$, and $1/\eta'_e = (1/h^2) \int_0^h (z/\eta^*) dz$. This equation allows density and viscosity to vary not only along the film channel but also across the thin film (in z -direction). This feature is important for the simulations of thermal and/or non-Newtonian effects in EHL, especially for the prediction of the traction. The generalized Reynolds equation proposed by Dowson can also meet this need [Dowson 1962]. The boundary and cavitation conditions must be satisfied, which may be written as

$$\begin{cases} p(x_{in}, y) = p(x_{out}, y) = p(x, \pm y_{out}) = 0 \\ p(x, y) \geq 0 (x_{in} < x < x_{out}, -y_{out} < y < y_{out}) \end{cases} \quad (2.60)$$

The temperature and pressure dependence of viscosity and density, as well as the shear dependence of viscosity, can be found in Sec. 2.2.

2.4.2.2 Film thickness equation

For a point contact, the film thickness equation can be written as

$$h(x, y) = h_{00} + \frac{x^2}{2R_x} + \frac{y^2}{2R_y} + \frac{2}{\pi E'} \iint \frac{p(x', y')}{\sqrt{(x - x')^2 + (y - y')^2}} dx' dy' \quad (2.61)$$

The double integral term represents the approach of the two bodies. The two radius-related terms are the approximated shape of the ball. $R_x = R_y$ for circular contacts. h_{00} is unknown and needs to be determined with the load balance equation.

2.4.2.3 Load balance equation

The applied load w is balanced by the integral of the pressure over the entire domain, *i.e.*

$$\iint p(x, y) dx dy = w \quad (2.62)$$

2.4.3 Governing equations: thermal part

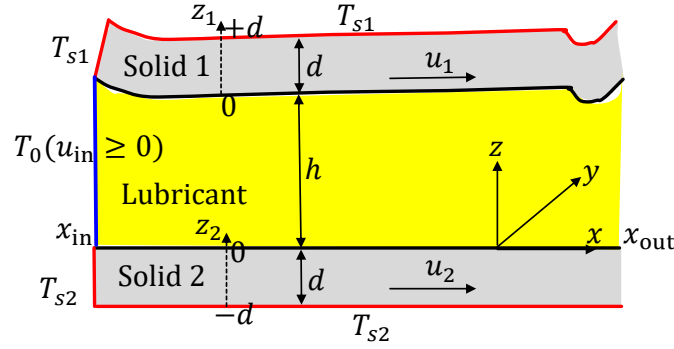


Figure 2-33: Schematic of a point contact thermal EHL problem and the temperature boundary conditions (not to scale; because the film thickness is typically thousand times smaller than the contact width)

2.4.3.1 Energy equation of the oil film

Temperature fields in the lubricating film can be obtained by solving the energy equation in three dimensions for point contacts. Neglecting the thermal conduction terms in the x and y directions compared to the small dimension of the film thickness in z -direction, the oil energy equation can be written as [Cheng 1965]

$$c \left(\rho u \frac{\partial T}{\partial x} + \rho v \frac{\partial T}{\partial y} - q \frac{\partial T}{\partial z} \right) - \frac{\partial (k_{\text{oil}} \partial T / \partial z)}{\partial z} = Q_{\text{comp}} + Q_{\text{shear}} \quad (2.63)$$

where $q = \frac{\partial}{\partial x} \int_0^z \rho u dz' + \frac{\partial}{\partial y} \int_0^z \rho v dz'$. The pressure dependence of the lubricant thermal conductivity refers to Sec. 2.2.7.

Q_{comp} is the heat generation term by compression of the lubricant

$$Q_{\text{comp}} = -\frac{T}{\rho} \frac{\partial \rho}{\partial T} \left(u \frac{\partial p}{\partial x} + v \frac{\partial p}{\partial y} \right) \quad (2.64)$$

Compression heating and decompressive cooling are principally influenced by the gradient of pressure, but also by velocity, temperature and thermal expansion coefficient. Usually, near the inlet and outlet of the EHL contact, where there are high pressure gradients, compressive heating/cooling effects would be important [Sadeghi and Sui 1990; Reddyhoff *et al* 2009a; Kaneta *et al* 2005]. Other than that, compressive heating may be negligible for the traction prediction in rolling/sliding EHL contacts.

Q_{shear} is the heat generation by shearing the film

$$Q_{\text{shear}} = \tau_e \dot{\gamma}_e = \eta^* \dot{\gamma}_e^2 = \eta^* [(\partial u / \partial z)^2 + (\partial v / \partial z)^2] \quad (2.65)$$

According to Yang and Wen [1990], the film velocity components u and v in the x and y directions can be given by

$$\begin{aligned} u &= \left(\int_0^z \frac{z'}{\eta^*} dz' - \frac{\eta_e}{\eta_e'} h \int_0^z \frac{1}{\eta^*} dz' \right) \frac{\partial p}{\partial x} + \frac{\eta_e}{h} (u_2 - u_1) \int_0^z \frac{1}{\eta^*} dz' + u_1 \\ v &= \left(\int_0^z \frac{z'}{\eta^*} dz' - \frac{\eta_e}{\eta_e'} h \int_0^z \frac{1}{\eta^*} dz' \right) \frac{\partial p}{\partial y} \end{aligned} \quad (2.66)$$

The first term in the expression of u is the pressure-driven Poiseuille component of the flow, while the rest are the Couette components. Under pure rolling conditions, owing to the Poiseuille flow, a velocity gradient can exist across the film in z direction, which results in shear heating as a consequence of viscous resistance of the lubricant. Under rolling/sliding conditions, the Couette flow prevails because of the direct velocity gradient across the film through the difference in velocities of the bounding surfaces.

The left boundary temperature of the lubricant film (see Fig. 2.33, at $x = x_{\text{in}}$) represents the temperature of the supplied oil, T_0 , and the boundary condition of oil energy equation is given by

$$T(x_{\text{in}}, y, z) = T_0 \quad (\text{if } u(x_{\text{in}}, y, z) \geq 0) \quad (2.67)$$

Note that at the inlet edge when there is reverse flow ($u(x_{\text{in}}, y, z) < 0$), as well as at other edges, no boundary condition is required for the oil energy equation.

2.4.3.2 Energy equation of the solids

Neglecting the heat generation terms in Eq. (2.63) for the oil, the energy equations of the two solids are

$$\begin{cases} c_1 \rho_1 u_1 \frac{\partial T}{\partial x} = k_{s1} \frac{\partial^2 T}{\partial z_1^2} \\ c_2 \rho_2 u_2 \frac{\partial T}{\partial x} = k_{s2} \frac{\partial^2 T}{\partial z_2^2} \end{cases} \quad (2.68)$$

where k_s is the thermal conductivity of the solid. Note that the heat conduction in the x - and y - directions is ignored in this study for a large Peclet number condition of the solids ($Pe = 2bu/\chi$), *i.e.* it is not close to a stationary heat source problem. For traction test rigs, the specimens are typically made of AISI 52100 bearing steel. The thermal conductivity is 21 W/mK rather than the widely cited value in thermal EHL literature (see Sec. 2.1.3.6). The effect of thermal conductivity on the EHL traction is studied in Chapter 5. Along the z -direction in Fig. 2.33, the temperature domains of solid-1 and solid-2 are defined with a thickness of d , which should be proven large enough to cover the penetration depth; see Appendix C. The temperature boundary conditions of the solids can be expressed as (see Fig. 2.33)

$$\begin{cases} T(x_{\text{in}}, y, z_1) = T_{s1}, & T(x, y, h + d) = T_{s1} \\ T(x_{\text{in}}, y, z_2) = T_{s2}, & T(x, y, -d) = T_{s2} \end{cases} \quad (2.69)$$

The body temperatures of the bounding solids are assumed to be equal, *i.e.* $T_s = T_{s1} = T_{s2}$. Note that in classical EHL simulations, T_s is usually assumed to be equal to the supplied oil temperature T_0 . However, there can be solid body temperature effect as is observed in traction measurements (Sec. 2.1.3.5) resulting in $T_s \neq T_0$. The solid body temperature effect on the EHL film thickness and traction is studied in Chapter 4.

2.4.3.3 Heat flux continuity

On the two oil-solid interfaces, there are two boundary conditions. The first one is for temperature: $T_{s1}|_{z_1=0} = T_{\text{oil}}|_{z=h}$, $T_{s2}|_{z_2=0} = T_{\text{oil}}|_{z=0}$. The other is Eq. (2.70) for the heat flux continuity:

$$\begin{cases} k_{s1} \left(\frac{\partial T}{\partial z_1} \right) \Big|_{z_1=0} = k_{oil} \left(\frac{\partial T}{\partial z} \right) \Big|_{z=h} \\ k_{s2} \left(\frac{\partial T}{\partial z_2} \right) \Big|_{z_2=0} = k_{oil} \left(\frac{\partial T}{\partial z} \right) \Big|_{z=0} \end{cases} \quad (2.70)$$

2.4.4 Numerical solutions

The above equations and boundary conditions were solved in dimensionless forms. The non-dimensional parameters are given in the Nomenclature and they are mainly referred to the Hertzian contact parameters, the entraining speed, and the fluid properties at ambient conditions. Subsequently, they were discretized using a finite difference method. The numerical methods used in this thesis are briefly introduced below.

2.4.4.1 Multigrid methods for the EHL part

Full numerical solution for isothermal EHL problems can be dated back to 1951 [Petrusevich 1951] for a line contact, followed by Dowson and Higginson [1959] for the widely used film thickness equations for line contact. In 1970s, the famous HD equation for point contact was derived by fitting the numerical results from Gauss-Seidel iteration on the Reynolds equation [Hamrock and Dowson 1976, 1977]. The readers are referred to Lubrecht *et al* [2009] for a review. For solving high load conditions, the inverse iteration method, Newton-Raphson direct iteration, and a semi-system method based on half-space simplification have been developed; see the review from Wang [2013].

Multigrid (MG) numerical methods [Venner and Lubrecht 2000] are used in this work for solving the Reynolds equation and the surface deformation equation because of the high performance. The background of multigrid techniques is introduced below. When solving partial differential equations iteratively by finite difference method (FDM) in EHL (*e.g.* for the Reynolds equation), the number of discretized grid points are hard to choose for the computation domain. When the grid is too coarse, it is hard to obtain a converged solution. When the grid is too fine, the calculation time would be long for solving the large algebraic equations discretized from a partial differential equation. Another problem with most relaxation schemes is that the convergence rate decreases or stalls after smoothing the high-frequency components of errors within the first few relaxations. However, low-frequency components are hard to be reduced. Note that the high and low frequency are relative to the mesh-size. From this point of view, a fast solver can be built using grids of different sizes for the relaxation. This is the core of the MG method, a powerful solver, pioneered by Lubrecht [1987] and Venner [1991] in EHL. When solving point contact problems, the computation of the elastic deformation is very expensive for the double integral term. The multi-level multi-integration (MLMI) method [Brandt and Lubrecht 1990] is efficient for this. Since then, there has been a real breakthrough in solving complicated EHL problems, for example transient effects caused by surface roughness or time-dependent operating conditions. For more information about multigrid techniques, readers are referred to Venner and Lubrecht [2000].

While MG is one of the most widely used methods in EHL studies, there are many other numerical methods in the literature, such as the fully coupled differential deflection method [Holmes and Evans *et al* 2003], progressive mesh densification method [Hu, Zhu 2000], fully coupled finite element method (FEM) based on COMSOL software [Habchi 2008], and computational fluid dynamics (CFD) simulations, see for example [Almqvist *et al* 2004; Hartinger *et al* 2008; Bruyere *et al* 2012; Hajishafiee *et al* 2017].

2.4.4.2 Thermal EHL solution

In this study, the temperature in the film and in the solids is evaluated by solving energy equations using the line-by-line relaxation scheme proposed by Yang [Yang 1998; Yang *et al* 2001; Guo, Yang, Qu 2001]. The history of thermal EHL simulations with both Newtonian and non-Newtonian fluids is briefly reviewed below.

The importance of thermal effects in EHL has been known since the pioneering theoretical work of line contacts by Cheng and Sternlicht [1965], and Dowson and Whitaker [1965] in the 1960s. For point contacts, the first full numerical solution was obtained by Zhu and Wen [1984], who solved the three-dimensional energy equation of the film and the heat-conduction equation of the bounding solids. However, the loads considered in their analysis were low which resulted in insignificant thermal effects on pressure and film thickness. Kim and Sadeghi [1992; 1993] carried out simulations for thermal EHL point contact problems at high loads, using the powerful multigrid techniques introduced into EHL by Lubrecht [1987] and Venner [1991]. Their results illustrated that the temperature rise in the film is significant and thermal effects cannot be neglected. They did not solve the solid heat-conduction equation to get the temperature distribution in the contacting solids. Yang and co-workers [Yang 1998; Yang *et al* 2001; Guo, Yang, Qu 2001] developed a thermal EHL model, which includes the three-dimensional temperature fields of the film and the solids. Their results showed that at high SRRs thermal effects are important for all aspects of EHL behavior, such as film thickness, pressure and temperature distributions.

In all models mentioned above the lubricant was assumed to behave Newtonian. However, in the high pressure contact region, where the traction is determined, even the simplest organic liquids behave in a highly non-Newtonian behavior (Sec. 2.2). Therefore, the ability to predict the EHL traction using a thermal Newtonian model is limited. It has also been shown that, for high-molecular-weight base fluids and polymer-blended oil even under pure rolling conditions, inlet shear thinning may occur, which also cannot be captured by a Newtonian fluid model. In 1984, Zhu [1984] presented a numerical solution for the point contact problem considering both non-Newtonian and thermal effects. Since then, several models for non-Newtonian fluid have been used in thermal EHL point contact problems, such as Ma [1998], Kim and Ehret *et al* [2001], Liu *et al* [2005], Habchi *et al* [2008], Kaneta *et al* [2015], Beilicke *et al* [2016]. All results show that thermal effects have a great influence on the EHL traction.

2.4.4.3 2D non-Newtonian methods in this study

The TEHL simulation program was originally written by Guo and Yang [Guo, Yang, Qu 2001; Yang 1998] at Qindao University of Technology based on multigrid methods, which essentially followed that of Venner [1991], and it has been updated by Liu and Zhang *et al* [2019] through implementations of various fluid models for the purpose of traction prediction and fluid model validation with reference fluids (*e.g.* Shell T9, squalane, DEHS). In addition, a novel shear-rate based approach has been used to solve two-dimensional (shear thinning) non-Newtonian problems so that a 2D generalized Newtonian problem can be solved as efficient as that for a 1D problem. The new method is explained below.

Non-Newtonian effects in lubrication problems are usually solved by implementing a specified constitutive equation of lubricants into the generalized Reynolds equation (Eq. (2.59)), and the developed solver for Newtonian problems can be used for non-Newtonian problems by adding a subroutine to calculate the terms of the equivalent/generalized viscosity. The generalized viscosity in the constitutive equation of fluids can be described either with shear rate or with shear stress as the independent variable (see Sec. 2.2.2), *i.e.* $\eta^* = f(\dot{\gamma}_e)$ or $\eta^* = f(\tau_e)$. Using the concept of generalized Newtonian viscosity,

accordingly, two-dimensional non-Newtonian flows in an EHL contact can be solved by two kinds of procedures or algorithms, namely, the shear rate based solution and the shear stress based solution. In the literature, the shear stress based solution has been widely used, see [Liu, Yang *et al* 2005; Liu, Wang, Bair *et al* 2007]. This method is time consuming when calculating the generalized viscosity η^* by firstly determining the shear stress on one solid/liquid boundary with Newton-Raphson method. As a result, in most simulations for EHL point contact problems, only the 1D shear thinning in the entrainment direction is solved. Note that the difficulties in the shear-stress based method disappear when adopting a shear-rate based rheological model. In the shear-rate based solution, the determination of the equivalent viscosity η^* and the shear rate $\dot{\gamma}$ requires only a simple trial-and-error routine as follows,

- (1) Initialize shear rate $\dot{\gamma}(x, y, z)$.
- (2) Calculate the equivalent viscosity $\eta^*(x, y, z)$ with the used shear-rate based shear thinning equation, *e.g.* Carreau equation in Eq. (2.7).
- (3) Calculate the velocity gradient $\partial u/\partial z$ and $\partial v/\partial z$ with Eq. (2.66).
- (4) The composite shear rate $\dot{\gamma}_e$ is calculated with Eq. (2.58) $\partial u/\partial z$ and $\partial v/\partial z$ in Step (3).
- (5) Steps (2)-(4) are repeated until the magnitude of relative difference between the value of $\dot{\gamma}$ obtained on the two consecutive iterations is within an accuracy of 10^{-3} . That is
$$\sum \left| \dot{\gamma}_{i,j,k}^{(\text{new})} - \dot{\gamma}_{i,j,k}^{(\text{old})} \right| / \sum \dot{\gamma}_{i,j,k}^{(\text{new})} < 0.001.$$

With the above procedures, the distributions of η^* , shear rates, and velocity gradients along and across the film can be obtained simultaneously within the solution domain. Note that with this shear-rate based method there is almost no difference in the computation time for solving a 1D or a 2D non-Newtonian problem. Afterwards, η^* can be used in the Reynolds Eq. (2.59) for the pressure distribution calculation in the same way for Newtonian cases.

The limiting shear stress was also implemented using a method similar to Habchi *et al* [2010], that is, during the iterative computation process, the local shear stress $\tau(x, y, z)$ was continuously checked to meet $\tau(x, y, z) \leq \tau_{\text{LSS}}$; and if $\tau(x, y, z) > \tau_{\text{LSS}}$, then let $\tau(x, y, z) = \tau_{\text{LSS}}$ by setting $\eta^* = \tau_{\text{LSS}}/\dot{\gamma}_e$.

This shear-rate based approach has been used in a 1D line contact problem [Khonsari and Hua 1993; Kumar and Khonsari 2009] and recently by Cui [2016] and Liu *et al* [2018] for a point contact problem for an Eyring fluid. This method is applied to solve the 2D Carreau shear thinning problem in this thesis.

2.4.4.4 Overview of the used EHL model and numerical methods

Fig. 2.34 summarizes the structure of the shear-rate based 2D non-Newtonian thermal EHL model and the numerical methods used in this thesis. The numerical solution of the equations is achieved by an iterative process consisting of pressure-film computation cycles (the EHL part in Fig. 2.34) and temperature-shear rate cycles (the thermal part in Fig. 2.34). The pressure field is solved with a multigrid solver with modifications to consider the variations in viscosity and density across the film. The surface deformation is calculated efficiently with the multilevel multi-integration method [Venner and Lubrecht 2000]. The column-by-column sweeping approach developed by Yang [1998] is employed for solving the energy equations with their boundary conditions. The temperatures are solved only on the finest grid. The temperature matrix in one column including influence coefficients of two solids and the lubricant is a sparse matrix, which is not strong coupled with the Reynolds equation and can be solved quickly at the top level of the grid using the Thomas algorithm. For a given temperature field and an assumed shear

rate, the oil generalized viscosity and the density can be calculated on all levels of grids when the multigrid solver for the pressure-film cycle is performed in the EHL part. The resulting pressure and film are then used to determine a new temperature field by solving the energy equations in the thermal part. Also, the shear rate is subsequently updated by the form of constitutive equation in this thermal computation part.

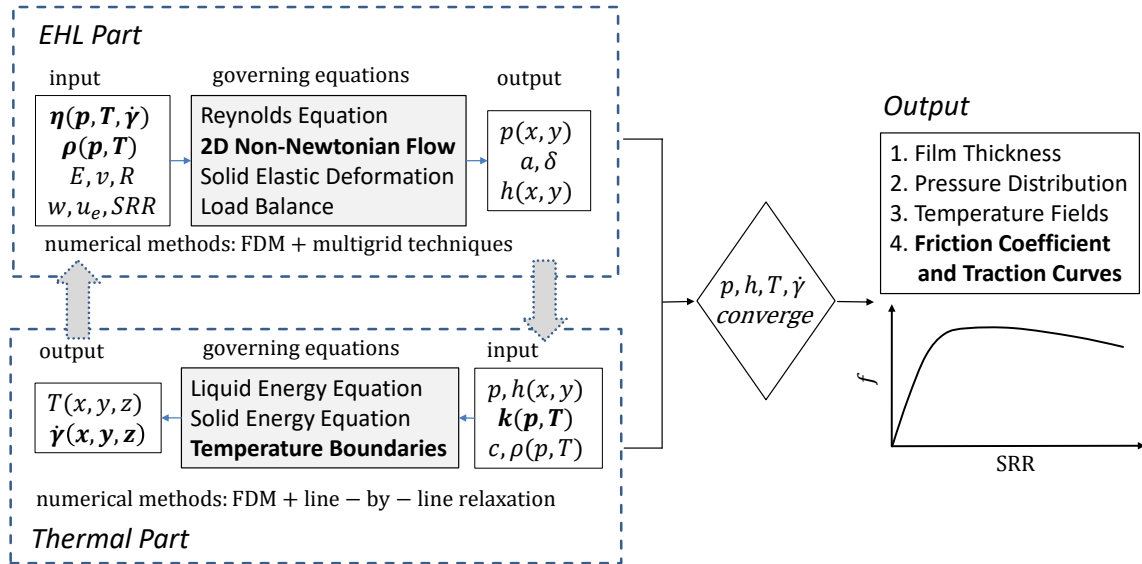


Figure 2-34: Summary of the non-Newtonian thermal EHL model and the numerical methods used in this study. The improvements in this work are marked in bold towards a better traction prediction. For example, 2D non-Newtonian numerical methods, using independently measured viscosity and fluid properties, as well as the change of the temperature boundary condition for solids.

3

Motivation and Outline

EHL traction is influenced by both non-Newtonian behavior of lubricants and thermal effects. Since the 1960s, much effort has been paid to the understanding of the EHL traction by means of traction measurements and numerical simulations; however, only limited success has been achieved. In early studies (*e.g.* till the year 2007), high-pressure rheological parameters and constitutive behavior of fluids were mainly extracted from nonhomogeneous EHL contacts by means of average/mean values. Parameters in the hypothesized fluid models were usually adjustable in thermal non-Newtonian simulations in order to fit the simulation results to experimental results. This was mainly due to the lack of rheological data for lubricants in early days. In the last fifteen years, effort has been made towards the prediction of EHL traction using independently measured thermo-physical rheological properties of model fluids. Up to now, however, there are still considerable discrepancies between numerical simulations and measurements.

This work continues understanding the EHL traction using model fluids (such as squalane), aiming to figure out the influence factors that lead to the differences between experiments and predictions. The influence of disc body temperature, solid/liquid thermal conductivity and contact geometry on the EHL traction curves is highlighted. Fig. 3.1 shows the schematic diagram of this thesis.

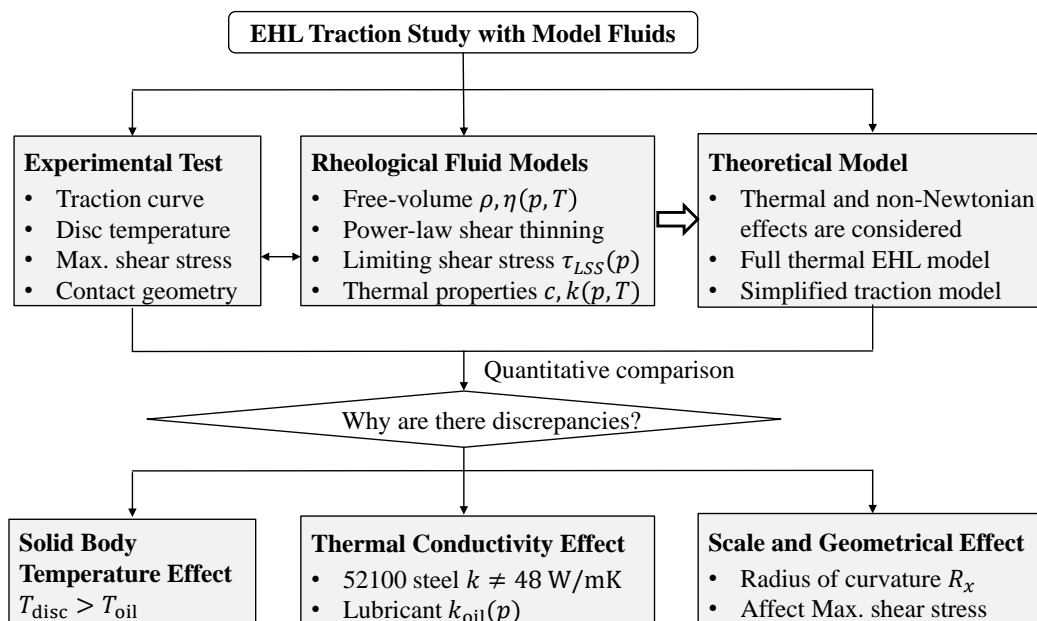


Figure 3-1: Frame diagram of the thesis.

Experimentally, traction curve measurements have been carried out on two traction machines in different contact geometries, *i.e.* twin-disc and ball-on-disc, for the model fluid squalane. Two interesting phenomena have been observed in experiments:

- (1) The first phenomenon is about the repeatability of the traction measurements. One traction rig may give different traction curves in repeated running cycles of measurements (Fig. 2.8, in Sec. 2.1.3.5), even though the setting of the operating conditions (namely, the supplied oil temperature, the entrainment velocity and the load) are identical.

- (2) The second phenomenon is that the used two traction machines give different traction curves for the same set of running parameters, *i.e.* the mean contact pressure, the entrainment velocity and the supplied oil temperature. The friction coefficient is smaller for the twin-disc machine with a larger disc diameter (see Chapter 7).

On one side, these experimental uncertainties complicate the quantitative comparison between experiments and simulations. On the other side, the influence factors and the mechanisms behind the above two experimental phenomena may be useful to improve the existing EHL models towards a better traction prediction.

For the explanation of the above experimental phenomena, a thermal non-Newtonian EHL model has been developed accounting for 2D non-Newtonian flows. Rheological fluid models supported by independent high-pressure measurements for model fluids have been embedded, especially for the viscosity at high pressures. The pressure dependence of limiting shear stress is also considered in the model, see Sec. 2.4.4 for details.

In Chapter 4, the first experimental phenomenon is explained by the influence of the body temperature of the specimens. During traction measurements, the disc heats up and its bulk temperature may exceed the supplied oil temperature. The effect of bulk temperature on the EHL film thickness and the traction has been studied numerically by changing thermal boundary conditions of the solids.

In Chapter 5, the influence of solid and lubricant thermal conductivities on the traction has been studied. The motivation is that Reddyhoff *et al* [2019] pointed out that a wrong thermal conductivity was widely used in thermal EHL simulations for 52100 bearing steel (see Sec. 2.1.3.6). Regarding the thermal conductivity of lubricants, measurements show that at a pressure about 1 GPa it is two time larger than that at ambient pressure (see Sec. 2.2.7); however, a constant value at ambient pressure is usually used in traction simulations. A simplified approach has been developed in Chapter 6 for practical traction predictions in highly-loaded rolling/sliding EHL contacts without solving the Reynolds and surface deformation equations. Thermal and non-Newtonian effects are considered. The predictions were compared with measurements over a wide range of operating conditions using the model fluid squalane.

In Chapter 7, the second experimental phenomenon related to scale effects is analyzed by doing thermal EHL simulations with different contact geometries, *i.e.* the reduced radii of curvature. The mechanism of scale effect on the EHL traction is explored. Suggestions are given towards “isothermal” traction measurements for the study of the LSS of fluids.

4

Thermal Boundary Conditions and Solid Body Temperature Effect

A numerical investigation of non-Newtonian thermal elastohydrodynamic lubrication (EHL) in rolling/sliding point contacts has been carried out to address the solid body temperature effect on film thickness and traction. At a moderate entrainment velocity, the EHL film behavior is dominated by the solid body temperature as the oil heats up to the body temperature before entering the contact zone and thus the film thickness decreases. For high velocity conditions, inlet shear and compressive heating also contribute to the reduction of film thickness. The results indicate that the measured film thickness and traction with disc machines might be lower than the expected values when the disc temperature exceeds the supplied oil temperature.

The work in this chapter has been published as: Liu, H. C., Zhang, B. B., Bader, N., Guo, F., Poll, G., & Yang, P. (2019). Crucial role of solid body temperature on elastohydrodynamic film thickness and traction. Tribology international, 131, 386-397.

DOI: <https://doi.org/10.1016/j.triboint.2018.11.006>

4.1 Introduction

Traditional simulations to predict film thickness and traction in rolling/sliding thermal elastohydrodynamic lubrication (EHL) are mainly based on the assumption that solid body temperature equals the supplied oil temperature. However, for the experimental validation of the EHL theory, *e.g.* during traction measurements using a twin-disc machine, it may take long for the test rig to reach thermal equilibrium and the disc body temperature rarely remains constant with varying slide-to-roll ratios (SRRs). Hence, the fluid behavior and the corresponding measured friction and film thickness might be influenced by the solid body temperature. This effect is investigated in this work.

The solid body temperature can be quite different from the supplied oil temperature during experimental measurements. Isaac *et al* [2018] showed that there are discrepancies of the friction coefficient measured with different traction machines under similar operating conditions. They studied the heat flow of the twin-disc machine using a thermal network method and revealed that the disc bulk temperature has a significant impact on the measured friction coefficient. In their traction tests, discs heat up due to friction and it was recorded that the disc bulk temperature can be 45 °C higher than the supplied oil temperature. Effect of body temperature on traction measurements were also reported recently by Bader *et al* [2017]; see also Sec. 2.1.3.5, which shows the evolution of the disc mass temperature and traction coefficient during repeated traction curve experiments. The shape of the traction curves is affected by the increasing solid body temperature. In practice, the effect of body temperature exists in many other test rigs and may affect the test results, *e.g.* in scuffing tests with a FZG test rig [Castro and Seabra 2018] and in smearing tests with a ring-roller-ring test rig [Fowell *et al* 2014]. So far, solid body temperature effects have not received much attention in EHL contact simulations. Liu

and Yang [2008; Yang and Liu 2009] investigated the body temperature effect on EHL film thickness and friction coefficient of a point contact for both Newtonian and Eyring rheological fluid models. They found that the solid body temperature is more important than the supplied oil temperature at low entraining velocities, whereas at high velocities the solid body temperature effect is not significant.

In this study, the effect of solid body temperature on the film thickness and the traction is investigated in a numerical study with the Carreau-Yasuda shear thinning model for a thermal point contact problem under steady state. The rheological models used to describe the pressure and temperature dependence of viscosity, density, thermal conductivity and heat capacity are adopted based on the well characterized Shell T9 mineral oil [Habchi, Vergne, Bair *et al* 2010] (see Table 2.6 for fluid models and parameters). Under high velocity conditions, the film temperature rise in the inlet region is analyzed and the individual contribution from inlet shear heating, compressive heating and solid body temperature effect is discussed. Another goal of the present work is to reveal the role of solid body temperature effect in the traction curve experiments with disc machines at the EHL contact scale, as this is not addressed in the former work [Yang and Liu 2008, 2009].

4.2 Theoretical EHL models

The non-Newtonian thermal EHL model described in Sec. 2.4 has been used to study the solid body temperature effect by changing the temperature boundary conditions of the two solids being different from the supplied oil temperature.

4.2.1 Thermal boundary conditions

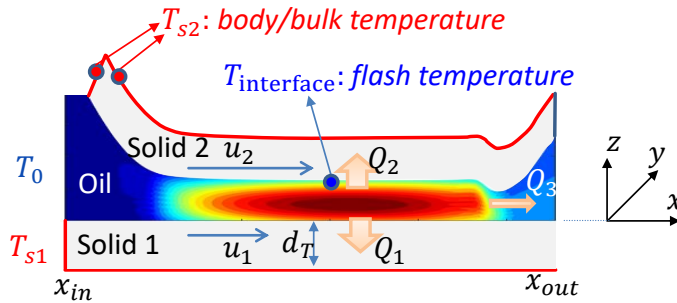


Figure 4-1: Schematic of a circular contact thermal EHL problem and the boundary temperatures (not to scale; note that the body/bulk temperature is different from the oil/liquid interface temperature; and the solid body temperature is the boundary conditions in simulations)

The solid body temperature effect in a rolling/sliding circular contact is illustrated in Fig. 4.1. At the left edge (where $x = x_{in}$), the boundary temperatures of solid-1 and solid-2 are T_{s1} and T_{s2} , respectively, whereas the boundary temperature of the oil film is T_0 , which denotes the temperature of the supplied oil. Along the z -direction in Fig. 4.1, the temperature domains of solid-1 and solid-2 are defined with a thickness of d_T , which has been proven large enough to cover the penetration depth (*e.g.* $d_T \approx 3a$, see Appendix C). It is important to distinguish the body/bulk temperature of the disc from the temperature on the oil-solid interface. The latter is unknown and it is a kind of flash/maximum temperature in the EHL conjunction that needs to be calculated by solving energy equations with suitable boundary conditions, while the former is the solid body/bulk temperature and it works as the temperature boundary condition for solid bodies, which can be expressed as (Fig. 4.1)

$$\begin{cases} T(x_{in}, y, z_{s1}) = T_{s1}, & T(x, y, -d) = T_{s1} \\ T(x_{in}, y, z_{s2}) = T_{s2}, & T(x, y, h + d) = T_{s2} \end{cases} \quad (4.1)$$

in which $T_s = T_{s1} = T_{s2}$ is assumed. To characterize the presence or absence and the extent of the solid body temperature effect, a dimensionless parameter, \bar{T}_s , is defined as

$$\bar{T}_s = T_s/T_0 \quad (4.2)$$

When $\bar{T}_s = 1$, there is no solid body temperature effect as the solid body temperature is the same as the supplied oil temperature. This boundary condition has been widely assumed in traditional EHL simulations ($T_{s1} = T_{s2} = T_{oil}$). When $\bar{T}_s \neq 1$ (i.e. $T_{s1} = T_{s2} \neq T_{oil}$), there is solid body temperature effect and its influence on the inlet oil properties and on the traction is the concerns of this study.

4.2.2 Shear thinning rheological model

The single-Newtonian Carreau-Yasuda equation (Eq. (2.6)) is used to describe the shear-thinning effect. Because shear rate rather than shear stress is the independent variable in this equation and this enables the 2D shear thinning problem to be solved using the built method in Sec. 2.4.4.3. While Eq. (2.6) is a one-dimensional rheological model, for a point contact in two dimensions, Eq. (2.6) becomes

$$\eta^* = \mu \left[1 + \left(\frac{\mu}{\tau_c} \dot{\gamma}_e \right)^a \right]^{(n-1)/a} \quad (4.3)$$

where η^* is the generalized or effective viscosity, μ the low-shear viscosity, and τ_c the critical shear stress. $\dot{\gamma}_e$ is the composite shear rate including components in both x - and y - directions

$$\dot{\gamma}_e = \sqrt{\dot{\gamma}_x^2 + \dot{\gamma}_y^2} = \sqrt{(\partial u/\partial z)^2 + (\partial v/\partial z)^2} \quad (4.4)$$

For Shell T9 used in this study, Eq. (4.3) with $\tau_c = 7.0\text{MPa}$, $a = 5$ and $n = 0.35$ reasonably describes the shear-thinning effect, when it is compared with the measurement results in Fig. 4 of Ref. [Habchi, Vergne, Bair *et al* 2010]. The other fluid parameters of Shell T9 can be found in Table 2.6, Sec. 2.2.8. The temperature and pressure dependence of the low-shear viscosity is expressed by the improved Yasutomi correlation.

4.3 Numerical solution

The numerical methods introduced in Sec. 2.4.4 and validated in Appendix A have been used in this work. It is achieved by an iterative process consisting of pressure-film computation cycles (PH cycles) and temperature-shear rate cycles ($\bar{T}\dot{\gamma}$ cycles). The calculation was carried out in half of the domain only, because of symmetry with respect to the X -axis. The actual calculation domain was $-6.5 \leq X \leq 1.5$, and $0 \leq Y \leq 1.8$, where the number of nodes on the finest grid (level 5) was 513 along the X -direction and 257 along the Y -direction. The number of nodes used for the solution of the 3D energy equations was 21 with equal distances across the film, and 12 with non-equal distances in each solid. The depth of solids' boundary $D_T = d_T/a = 3.15$ was checked and used as sufficiently far from the solid-oil interface; see Appendix C. The influence of mesh density in the x - and y - directions has been checked in Appendix B. The computation began by initializing the temperature distribution as $\bar{T}=1$ and initializing the shear rate an arbitrary guess, $\dot{\Gamma} = 0.01$. For the first iteration, the Hertzian pressure distribution was adopted. H_{00} in the film thickness equation, Eq. (2.61), was initialized by Hamrock-Dowson equation (Eq. (2.51)) and the solid deformation value at Hertzian pressure. The convergence criterion used in the study is as follows:

$$\begin{cases} \left| \frac{\sum P_{i,j}^{(new)} - P_{i,j}^{(old)}}{\sum P_{i,j}^{(new)}} \right| < 0.001 \\ \left| \frac{\sum \bar{T}_{i,j,k}^{(new)} - \bar{T}_{i,j,k}^{(old)}}{\sum \bar{T}_{i,j,k}^{(new)}} \right| < 0.0001 \\ \left| \frac{\sum P_{i,j}^{(new)} dXdY - \frac{2\pi}{3}}{\frac{2\pi}{3}} \right| < 0.001 \end{cases} \quad (4.5)$$

where the upper-scripts “new” and “old” represent states after and before a $PH - \bar{T}\dot{T}$ cycle. All errors were checked on the finest level of grid. Note that absolute convergence criterion should be used in a scientific computation, while a relative convergence criterion is mostly sufficient for engineering practice.

4.4 Results and discussion

Steel-steel circular contacts lubricated with Shell T9 are considered under both pure-rolling and rolling-sliding conditions. The temperature of the supplied oil is assumed to be $T_0 = 333.15\text{K}$ (60°C). Three solid body temperatures are used and they are addressed by the dimensionless values of \bar{T}_s (see Eq. (4.2)), where $\bar{T}_s = 1.00$ means the solid body temperature is equal to the supplied oil temperature as $T_s = T_0 = 333\text{K}$ (60°C), $\bar{T}_s = 1.05$ means $T_s = 1.05T_0 = 350\text{K}$ (77°C), and $\bar{T}_s = 1.10$ means $T_s = 1.10T_0 = 366\text{K}$ (93°C). It is known for a fixed slide-to-roll ratio, the lubricant film thickness is mainly governed by the velocity parameter $U_e = u_e\eta_0/(E'R_x)$, the material parameter $G = \alpha E'$, and the load parameter $W = w/(E'R_x^2)$. Among these parameters, the effects of G and W for the current problem are the same as for conventional problems and, therefore, will not be discussed and fixed to $G = 4757$ and $W = 6.88 \times 10^{-7}$ ($p_H = 0.74\text{GPa}$ with $a = 0.128\text{mm}$). The effect of the velocity parameter U_e , however, is of importance and will be discussed in detail. The input parameters and material properties used in the simulations are summarized in Table 4.1. Note that the thermal conductivity of 46W/mK is not for through-hardening bearing steel.

Table 4-1: Operating conditions and properties of the lubricant T9 and solids

Item/Property	Value
Steel Young's modulus E	210 GPa
Steel Poisson ratio ν	0.3 (-)
Steel special heat/ heat capacity c	470 J/(kgK)
Steel thermal conductivity, k_s	46 W/(mK)
Steel density ρ	7850 kg/m ³
Effective radius $R = R_x = R_y$	12.7 mm
Supplied oil temperature T_0	333 K(60°C)
Solid body temperature T_s	333, 350 and 366 K
Oil viscosity η at $60^\circ\text{C}, p = 0$	4.5 mPas
Oil density ρ at $60^\circ\text{C}, p = 0$	851.94 kg/m ³
Oil viscosity-pressure coefficient α at 60°C	17.66GPa^{-1}
Oil thermal conductivity k at $60^\circ\text{C}, p = 0$	0.1102 W/(mK)
Oil heat capacity c at $60^\circ\text{C}, p = 0$	2147.8 J/(kgK)
Load w	25.54 N
Hertz contact pressure p_H	0.74 GPa
Entrainment speed u_e	1-100 m/s
Slide-to-roll ratio (SRR), SRR	0-150%

The maximum film temperature usually occurs near the mid-film of an EHL rolling/sliding contact, that is, the middle layer of the lubricant film along the central line of the contact in the x -

direction. Therefore, the mid-film temperature distribution will be illustrated and the EHL behavior at mid-film will be mainly discussed. The temperature results will be presented on the Celsius scale $^{\circ}\text{C}$.

During the iterative computation process, the local shear stress was continuously evaluated and it never exceeded the corresponding limiting shear stress τ_{LSS} for all the studied cases at a relatively low contact pressure of 0.74 GPa. In fact, the physical mechanisms of limiting shear stress and the approach to deal with limiting shear in two-dimensional EHL simulation are still subjects of debate [Martinie and Vergne 2016; Myllerup and Hamrock 1993]. See Sec. 2.2.3 for more discussions on the LSS. Hence, this is good for the study of solid body temperature effect with a thermo-shear thinning EHL model and no limiting shear stress is reached for the operating conditions.

4.4.1 Solid body temperature effect in pure rolling EHL

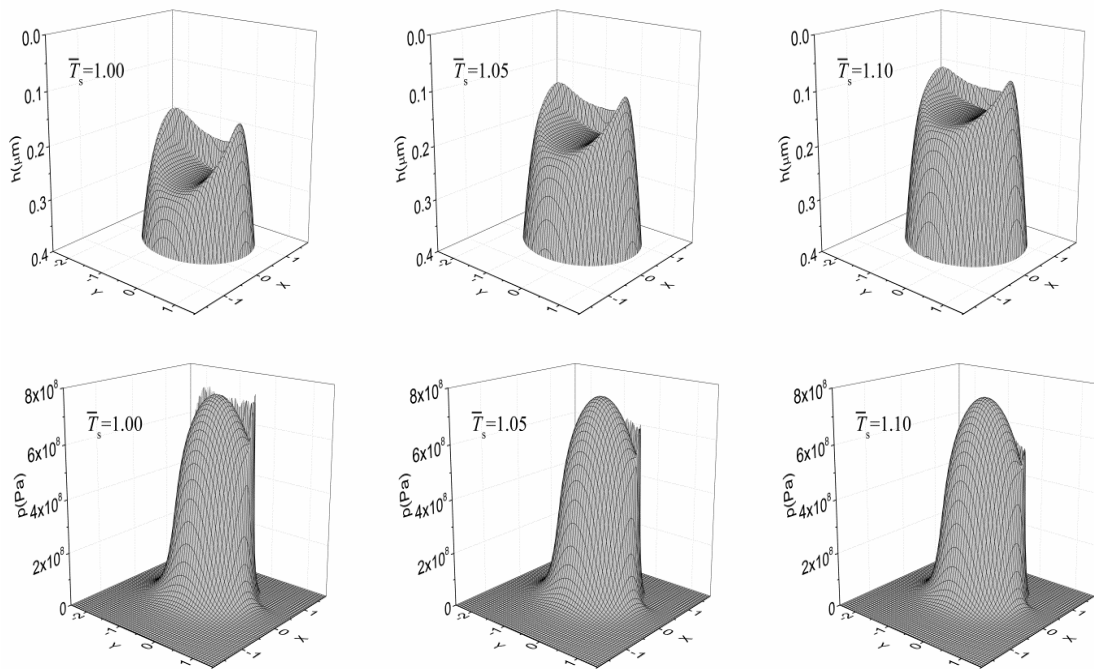


Figure 4-2: Film thickness and pressure distribution for three temperature ratios of $\bar{T}_s = T_s/T_0 = 1.00, 1.05,$ and $1.10,$ respectively, in a pure rolling circular EHL contact. The temperatures of the supplied oil are the same for all cases. ($U_e = 1.54 \times 10^{-11}$, $u_e = 10$ m/s, $SRR = 0$, $T_0 = 60$ $^{\circ}\text{C}$)

The 3D distributions of film thickness h and pressure p for different solid body temperatures are illustrated in Fig. 4.2. It can be seen that the film thickness significantly decreases with increasing solid body temperature, but the pressure only changes little mainly in the height of the second pressure spikes. The film thickness, pressure, and the mid-film temperature along the central line of the contact in the direction of motion (plane $Y = 0$), corresponding to Fig. 4.2, are depicted in Fig. 4.3. Figure 4.3(a) shows the film thickness results for different solid body temperatures. The film thickness is primarily determined by the lubricant viscosity in the inlet region and for the same entrainment velocity it is determined by the viscosity of the oil there. The inlet viscosity depends on the pressure and the temperature in the inlet region as long as inlet shear thinning does not occur. The inlet pressure distributions are almost the same for the three cases and independent of the solid body temperatures (Fig. 4.3(b)). Then there must be a temperature rise in the inlet region, which decreases the inlet viscosity and thus the film thickness. This is confirmed by the mid-film temperature distribution in Fig. 4.3(c). It is

interesting to see that the supplied oil heats up to the solid body temperature when passing through the inlet region from $X=-4.5$ to $X=-2.5$, *i.e.* a distance of two times of the contact radius.

In Fig. 4.3(c), starting from $X=-6.5$ to $X=-4.5$, where is far away from the Hertzian contact zone, the mid-layer temperature remains the same as the supplied oil temperature, which is attributed to the thick film thickness and the distance from the contact zone. As a result, heat from the solids cannot conduct to the mid-layer to give a temperature rise during entrainment. As the lubricant moves further toward the contact zone, the film thickness is decreasing along the converging gap and the mid-film temperature reaches the solid body temperature gradually. From $X=-2.5$ to $X=-1$, the oil temperature stays nearly the same as the solid body temperature. To be precise, there are slight temperature rises for all the three cases due to compressive heating and inlet shear heating as can be seen in Fig. 4.3(c), especially through the case of $\bar{T}_s = 1.00$. In the Hertzian contact area, the oil temperature decreases to the solid body temperature due to heat conduction to the solids and ignorable shear heating in the contact zone in pure rolling conditions. In the outlet region, the mid-film temperature approaches the solid body temperature again.

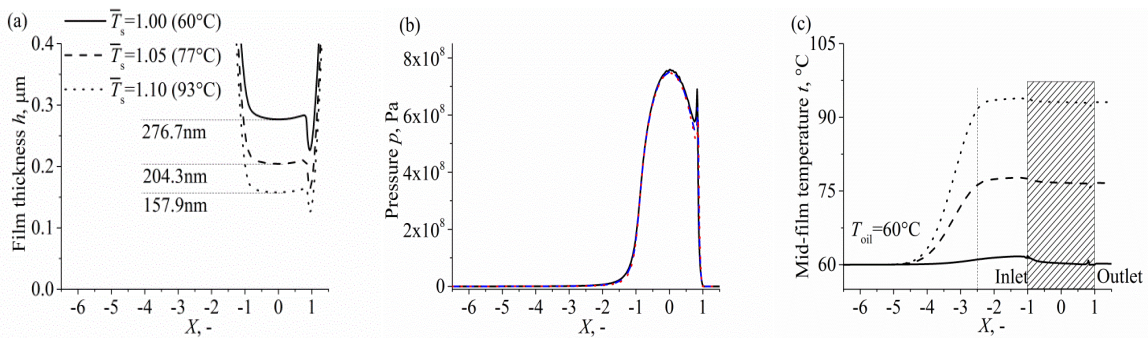


Figure 4-3: Variations of (a) film thickness, (b) pressure, and (c) mid-film temperature with three solid body temperatures along the central line of the contact in the x -direction under pure rolling conditions. The operating conditions are the same as that in Fig. 4.2. ($U_e = 1.54 \times 10^{-11}$, $u_e = 10$ m/s, $SRR = 0$, $T_0 = 60^{\circ}\text{C}$)

It is important to mention that the Peclet number cannot be directly applied here to judge if the oil at mid-layer could heat up to the solid body temperature before entering the contact zone. The velocity distribution varies in the z -direction in the inlet area due to “Poiseuille” flow and potential reverse flow. Fig. 4.4 shows the distribution of the velocity component U in the x -direction (dimensionless form of u in Eq. (2.66)) across the film in the plane of $Y=0$ at different X locations for pure rolling. The operating conditions are the same as the case of $\bar{T}_s = 1.05$ in Fig. 4.2 and Fig. 4.3. At all locations of X , the film velocities U next to the upper and lower surfaces equal 1; that is the solid surface velocities at pure rolling and with the assumption of no-slip boundary conditions. At the Hertzian contact center $X = 0$, there is no pressure gradient and only surface-driven “Couette” flow. Therefore, U equals 1 along the z -direction (Fig. 4.4). However, for the locations in the inlet area ($X \leq -1$), for example at $X = -2$, the velocity U at mid-film ($Z = 0.5$) is much smaller than the surface velocity. As a result, the lubricant, even for the mid-layer, heats up to the solid body temperature before entering the conjunction by thermal conduction to the lubricant layer near the solid surface and by convection through “Poiseuille” and reverse flow.

The film thickness reduction in Fig. 4.3(a) is mainly caused by the inlet temperature rise and the corresponding viscosity drop in the inlet region in the presence of solid body temperature effect. An effective ambient viscosity at the solid body temperature and zero pressure conditions is adopted to

represent the inlet viscosity of the lubricant suffering the solid body temperature effect. According to the viscosity-temperature-pressure relation in the improved Yasutomi correlation (Table 2.6), the effective oil viscosity can be obtained as 4.5, 3, and 2.2 mPas for $\bar{T}_s = 1.00, 1.05, \text{ and } 1.10$, respectively. Substitute them into the central film thickness equation proposed by Hamrock and Dowson (Eq. (2.51)), the ratio of the central film thickness can be calculated as 1: 0.7621: 0.6191, which is roughly the same ratio as the numerical results of the ratio 1: 0.7383: 0.5715 shown in Fig. 4.3(a). This suggests that for low speed cases the film thicknesses and film temperature are dominated by the solid body temperatures rather than by the temperature of the supplied oil. For the effect of velocities and the high entrainment speeds conditions, please see Sec. 4.4.3.

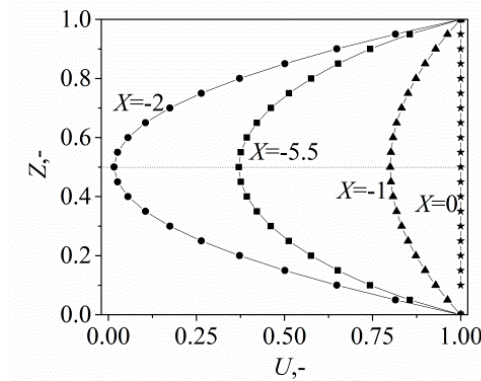


Figure 4-4: Variations of velocity component U across the film thickness in the plane of $Y=0$ at four X positions under pure rolling conditions. ($U_e = 1.54 \times 10^{-11}$, $u_e = 10$ m/s, $SRR = 0$, $T_0 = 60$ °C, $\bar{T}_s = 1.05$)

4.4.2 Effect of solid body temperature effect in rolling/sliding

Rolling/sliding exists widely in EHL lubricated contacts and components, for example in rolling element bearings and gears. The slide-to-roll ratio (SRR), defined as $SRR = (u_1 - u_2)/u_e$, is of great importance to both the temperature rise in the film and to the EHL traction. With the same parameters of U_e , G , and W used in the last section, the influence of the SRR on EHL behavior with solid body temperature effect is investigated.

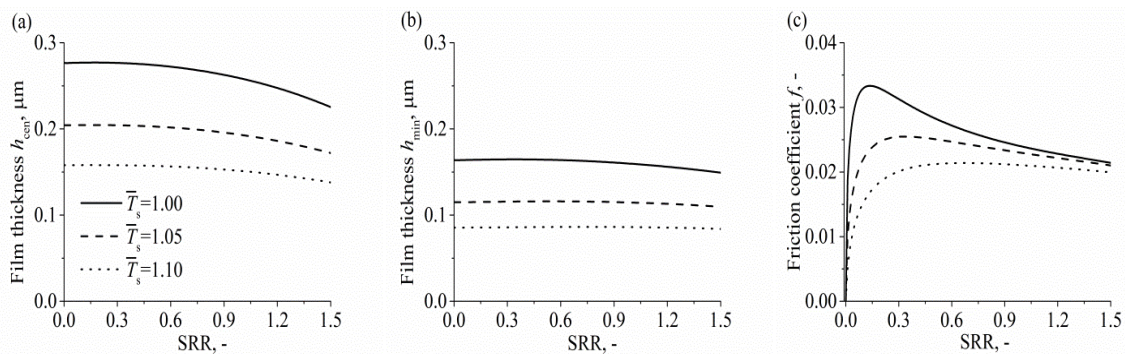


Figure 4-5: Variations of (a) central film thickness, (b) minimum film thickness, and (c) friction coefficient versus slide-to-roll ratios in an EHL contact with three solid body temperatures. ($U_e = 1.54 \times 10^{-11}$, $u_e = 10$ m/s, $T_0 = 60$ °C)

Figure 4.5 illustrates the variations of the central film thickness, minimum film thickness and friction coefficient with the variation of SRR for the three solid body temperatures in a rolling/sliding contact. Both the central film thickness in Fig. 4.5(a) and the minimum film thickness in Fig. 4.5(b) are

significantly reduced by the solid body temperature effect. This is similar to the film thickness reduction phenomenon in Fig. 4.3(a), which is effectively included in Fig. 4.5(a) as a special case of pure rolling, $SRR = 0$. For a specific solid body temperature, the film thickness is not sensitive for small SRRs and decrease slightly for very high SRRs. The influence of solid body temperature on the traction is obvious. As is shown in Fig. 4.5(c), the higher the solid body temperature, the smaller are both the maximum value and the initial slope of the traction curve. At large SRR, *e.g.* $SRR > 120\%$, the effect of solid body temperatures on traction is no longer obvious, but its effect on film thickness is still significant. All the features agree with the experimental traction results in Fig. 2.8, Sec. 2.1.3.5, qualitatively. The crucial role of solid body temperature on EHL traction is confirmed here on an EHL contact scale, while it was modelled by Isaac, Chagnenet *et al* [2018] and Clarke *et al* [2006] on a test rig scale.

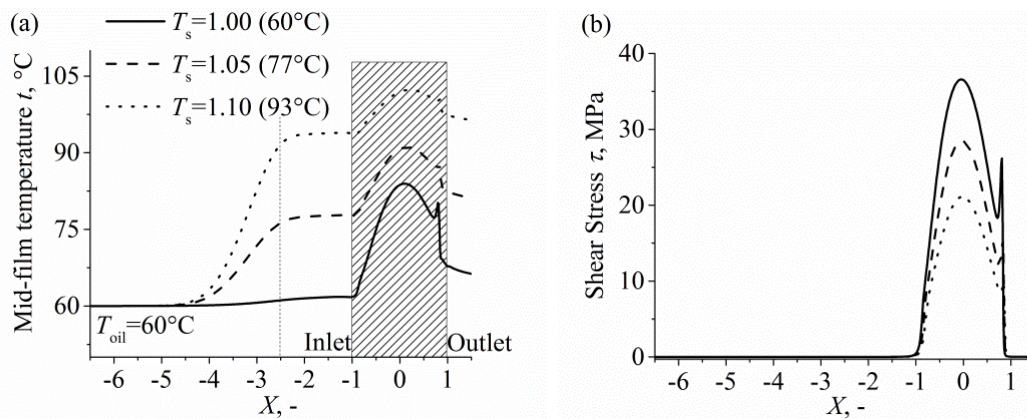


Figure 4-6: Variation of (a) temperature and (b) shear stress in the middle layer of the film along the central line of the contact in x -direction for the slide-to-roll ratio of 20% with three solid body temperatures. ($U_e = 1.54 \times 10^{-11}$, $u_e = 10$ m/s, $SRR = 20\%$, $T_0 = 60^\circ\text{C}$)

Figure 4.6(a) depicts the distribution of the mid-film temperature (plane $Y=0$ and $Z=0.5$) for $SRR = 20\%$ for different solid body temperatures. Within the Hertzian contact zone (from $X=-1$ to $X=1$), the oil temperature shown in Fig. 4.6(a) increases rapidly owing to the heat generated from the shearing of the high viscous oil at high pressures. The main contribution comes from the “Couette” flow in Eq. (2.66). The relative temperature rise in the contact zone is more pronounced for the case of lower solid body temperature, although the absolute maximum temperature is reached for the case of the highest solid body temperature. Compared to the pure rolling case shown in Fig. 4.3(c), it can be seen that the SRR of 20% does not change the temperature distribution in the inlet region (Fig. 4.6(a), from $X=-6$ to $X=-1$). The inlet temperature field and the effective viscosity are still determined by the solid body temperature. This is the reason why the film thicknesses at $SRR = 20\%$ equals the corresponding ones at $SRR = 0$, as is plotted in Fig. 4.5(a). However, traction is mainly determined in the highly pressurized central contact region rather than the low-pressure inlet area. Figure 4.6(b) shows the shear stress distribution for $SRR = 20\%$ in the mid-film. The lubricant undergoes the largest shear stresses at the center of the Hertzian contact for all cases (all are smaller than τ_{LSS} in Table 2.6). Typically, film thickness and shear rate are nearly identical in the flat, central region of an EHL contact. Therefore, the shear stress and the temperature mainly depend on the local viscosity and follows the pressure distribution. The variation of the shear stress (Fig. 4.6(b)) and of the temperature (Fig. 4.6(a)) in the rolling/sliding contact region are thus very similar to the pressure distribution (Fig. 4.3(b)). It is also shown in Fig. 4.6(b) that the shear stress decreases with increasing solid body temperature. This agrees with the friction coefficient curves illustrated in Fig. 4.5(c).

4.4.3 Effect of entrainment velocity

At low and moderate entrainment speeds, there is enough time for the oil molecules to heat up to the solid body temperature in the middle film. However, the lubricant may not reach the solid body temperature at high entrainment speeds. This can be seen in Fig. 4.7, in which at the speed of 80 m/s the mid-film temperature is lower than the solid body temperature at $X=-1$. Note that the two heat generation terms Q_{comp} and Q_{shear} in the oil energy Eq. (2.63) are switched off during the calculation of Fig. 4.7 in order to show the speed effect. However, in reality, reverse flow and shear heating in the inlet zone cannot be ignored at high speeds [Cheng 1965; Sadeghi and Dow 1987]. In this section, the solid body temperature effect is further studied as a function of speed under pure rolling conditions.

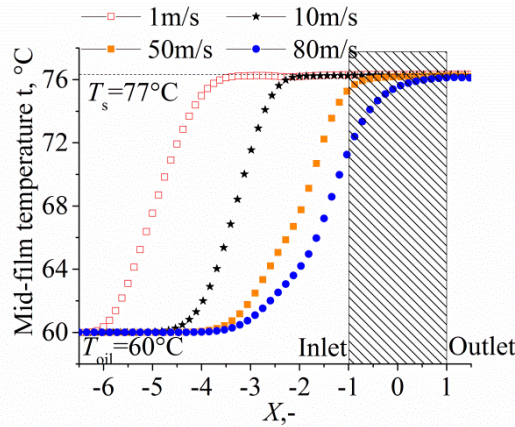


Figure 4-7: Distributions of the mid-film temperature at different entrainment velocities with solid body temperature effect for a pure rolling circular EHL contact. Note that the two heat generation terms in oil energy equation are switched off during calculation and only conduction and convection are working. ($U_e = 1.54u_e \times 10^{-12}$, $SRR = 0$, $T_0 = 60^\circ\text{C}$, $\bar{T}_s = 1.05$)

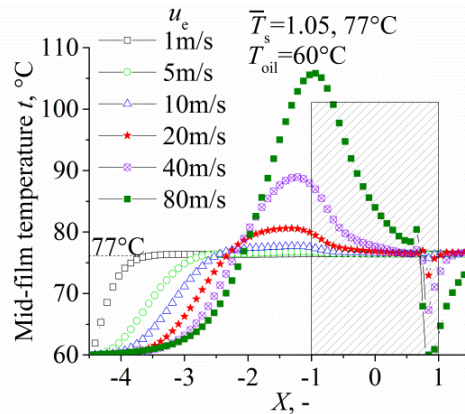


Figure 4-8: Variation of the mid-film temperature at different entrainment velocities with solid body temperature effect for a pure rolling circular EHL contact. Potential full solution, and no term in the energy equation is switched off. ($U_e = 1.54u_e \times 10^{-12}$, $SRR = 0$, $T_0 = 60^\circ\text{C}$, $\bar{T}_s = 1.05$)

Figure 4.8 shows the centerline mid-film temperature at velocities from 1 m/s to 80 m/s with $\bar{T}_s = 1.05$ under pure rolling conditions. When the entrainment speed is lower than 10 m/s, the evolution of the mid-film temperature is similar to that in Fig. 4.3(c). In the inlet region, the oil temperature reaches the body temperature. And the slower the speed, the earlier the body temperature can be reached. Within the contact area, the oil temperature is also almost the same as the solid body temperature. As a

consequence, EHL film behavior is governed by the solid body temperature. By contrast, at higher entrainment speeds, *e.g.* 20 m/s or 40 m/s in Fig. 4.8, a peak mid-film temperature occurs in the inlet zone for pure rolling and the film temperature exceeds the solid body temperature (77 °C) from the location of $X = -2$, due to inlet shear heating and compressive heating. Hence the film thickness is determined not only by the solid body temperature effect as it is for the low speed conditions, but also by inlet shear heating and compressive heating. The significance of each component on inlet temperature rise of the film may be revealed by simply switching this component off in the numerical simulation. However, it is important to note that these effects are nonlinearly related.

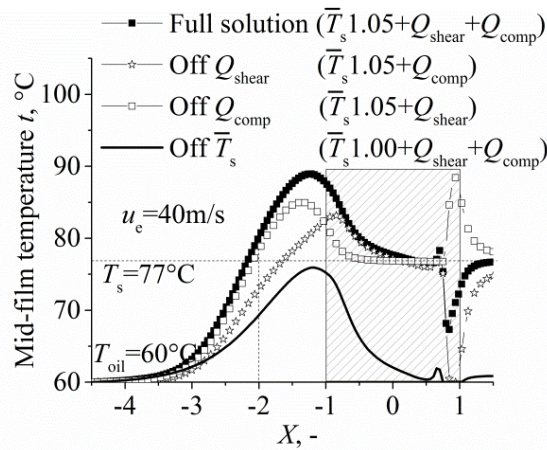


Figure 4-9: Contributions of inlet shear heating, compressive heating and solid body temperature on the mid-film temperature distribution along the central line of the contact in x -direction at a high speed in pure rolling EHL. ($U_e = 1.54u_e \times 10^{-12}$, $u_e = 40$ m/s, $SRR = 0$, $T_0 = 60$ °C, $\bar{T}_s = 1.05$)

Figure 4.9 illustrates the effect of the different components of heat generation for a pure rolling condition at a high speed of 40 m/s. The peak mid-film temperature is 12 °C above the solid body temperature and occurs in the inlet region near the edge of Hertzian contact zone. This is quite different from the sliding condition under which the main temperature rise occurs in the contact zone [Sadeghi and Dow 1987] or see Fig. 4.6(a). Comparing the results between the “Full solution” case and the “Off \bar{T}_s ” case in Fig. 4.9, it is easy to find that solid body temperature still plays a key role on the temperature rise of the film at such a high speed of 40 m/s. From $X=-4$ to $X=-2$, the film temperature rise is controlled by the inlet shear heating and the solid body temperature effect, as the curve of the potential full solution coincides with the one without compressive heating, namely “Off Q_{comp} ”. This is because compressive heating is important mainly at locations of large pressure gradient, typically near $X=-0.9$ and $X=+0.9$. In the main area of the contact zone from $X=-0.7$ to $X=+0.7$, the temperature rise of the film is governed by the solid body temperature effect and the compression heating. The shear heating is quite small in the flat area of the contact zone. For pure rolling, only pressure-driven “Poiseuille” flow works to generate heat by shearing (see Eq. (2.65) and Eq. (2.66)). However, at the contact center there is no pressure gradient and thus there is no “Poiseuille” flow for shear heating. Indeed, in most of the flat Hertzian contact region the gradient of velocity is low for pure rolling conditions, and therefore the shear heat is quite small. However, near the position of the second-spike pressure, locally, there are some shear heating and decompressive cooling effects due to the velocity gradient and the pressure gradient here. As the film thickness is mainly determined in the inlet area from $X=-2$ to $X=-1$, Fig. 4.9 shows the contribution to temperature rise from shear heating is always larger than that from compression heating. But all in all, for higher rolling speeds, these three effects combine to control the inlet film temperature rise and the resulting film thickness.

4.4.4 Film thickness prediction with empirical equations

It would be convenient for engineering practice if the available film thickness equations can still be used with appropriate input to take into account the solid body temperature effects for a wide speed range. The Hamrock-Dowson equation and two thermal correction factors are tested for this purpose. The Hamrock-Dowson equation (HD equation) [1977] for the central thickness in an isothermal circular EHL is

$$\text{HD Equation: } h_{\text{cen,iso}} = 1.90R_x U_e^{0.67} G^{0.53} W^{-0.067} \quad (4.6)$$

where $U_e = u_e \eta_e / (E' R_x)$, $G = \alpha E'$, $W = w / (E' R_x^2)$. η_e is the effective ambient viscosity at the solid body temperature and zero pressure conditions, α pressure-viscosity coefficient obtained following the definition of α_{film} by [Bair 2006] in Eq. (2.54) at the solid body temperature. For $\bar{T}_s = 1.05(77^\circ\text{C})$, it can be calculated that $\alpha|_{T_s=77^\circ\text{C}} = 15.614 \text{ GPa}^{-1}$, $\eta_e = 3 \text{ mPas}$.

Considering the shear heating effect in the inlet zone, Wilson and Sheu [1983] gave a semi-empirical factor to correct the EHL film thickness for high speeds or high viscosity lubricants. Gupta, Cheng *et al* [1992] modified the Wilson and Sheu formula to account for load effects. For the case of pure rolling, these two thermal reduction factors (TRF) can be written as

$$\begin{aligned} \text{Wilson TRF: } \varphi_{\text{thermal}} &= (1 + 0.241L^{0.64})^{-1}, \text{ where } L = \eta_e \beta u_e^2 / k \\ \text{Gupta TRF: } \varphi_{\text{thermal}} &= \frac{1 - 13.2(p_H/E')L^{0.42}}{1 + 0.213L^{0.640}}, \text{ where } L = -\left. \frac{\partial \mu}{\partial T} \right|_{T_s} \frac{u_e^2}{k} \end{aligned} \quad (4.7)$$

where L is the thermal loading parameter, p_H the Hertz contact pressure, β the lubricant temperature-viscosity coefficient, k its conductivity. $-\left. \frac{\partial \mu}{\partial T} \right|_{T_s}$ can be obtained from the improved Yasutomi correlation. β is defined as $\beta(p, T) = -\left. \frac{\partial \ln \mu}{\partial T} \right|_{T_s}$ [Larsson, Kassfeldt *et al* 2001]. For $\bar{T}_s = 1.05(77^\circ\text{C})$, according to the lubricant thermal conductivity equation in Table 2.6, $k|_{p=0} = 0.1102 \text{ W/(mK)}$; and with the improved Yasutomi equation, the temperature-viscosity coefficient is determined at atmospheric pressure $\beta|_{p=0} = 0.0204 \text{ K}^{-1}$.

Once the thermal reduction factor is determined, the reduced central film thickness can be estimated by

$$h_{\text{cen},T} = \varphi_{\text{thermal}} h_{\text{cen,iso}} \quad (4.8)$$

When using the above equations, the input values are all determined by the solid body temperature at $p = 0$. Figure 4.10 compares the film thickness results calculated with Eqs. (4.6) - (4.8) with the results from numerical simulation for pure rolling conditions. Over the whole speed range, the film thickness at $\bar{T}_s = 1.05$ is lower than the corresponding one at $\bar{T}_s = 1.00$ whatever the speed is. Under low speed conditions ($u_e < 10 \text{ m/s}$ in Fig. 4.10), film thickness calculated with different empirical equations, either the isothermal HD equation or the thermal corrected ones, agree with the numerical results. The film behavior at low speeds is governed by the solid body temperature, as is analyzed in Sec. 4.4.1. That is the main reason why using the effective viscosity and pressure-viscosity coefficient at solid temperature as input into the HD equation enables the satisfying prediction of film thickness under solid body temperature conditions. In this speed range, the film thickness versus speed holds a linear relationship on a log-log scale, whereas it does not under high speed conditions ($u_e > 15 \text{ m/s}$). It can be seen that all the empirical equations with thermal reduction factors predict smaller film thickness than the

numerical results at high speeds. Normally, it is hard for this kind of universal semi-empirical factors to predict a specific behavior quantitatively over a wide range of operating parameters. However, it should be pointed out that it is difficult to judge the principle of choosing the input parameters for the equations, *e.g.* at which pressure is calculated. The thermal conductivity k at $p_H = 0.74$ GPa is 0.2089 W/(mK), almost two times of the value of 0.1102 W/(mK) at $p = 0$. When the thermal reduction factor is sensitive to this variable, the effectiveness of prediction can be largely influenced by the principle of choosing the input parameters.

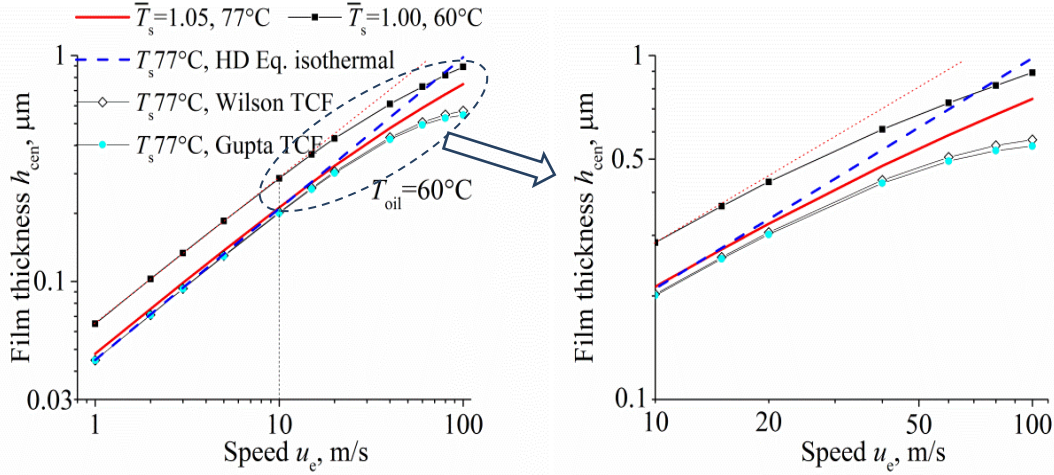


Figure 4-10: Predicted central film thickness from numerical simulation and from another two empirical equations for pure rolling EHL with solid body temperature effect. ($U_e = 1.54u_e \times 10^{-12}$, $SRR = 0$, $T_0 = 60$ °C)

The last interesting and important issue is the speed criterion, below which the film thickness could be governed by the solid body temperature effect and above which inlet heat generation becomes important. Wilson and Sheu [1983] proposed that thermal effects are negligible in the inlet when the thermal loading parameter L in Eq. (4.7) is smaller than 0.1. According to the Wilson thermal loading parameter, the critical speed can be determined as 13.4 m/s for the case studied in Fig. 4.10. The numerical results in Fig. 4.10 and the inlet temperature distribution in Fig. 4.8 show that these thermal effects (*e.g.* shear and compressive heating in the inlet) are not significant up to a speed about 15 m/s. This is roughly in agreement with the prediction from the Wilson parameter. This may suggest that the thermal loading parameter in Eq. (4.7) is suitable for the prediction of the critical speed, although the universal thermal correction factor failed to correct the degree of film thickness reduction for this oil. Therefore, the speed criterion to distinguish between low speeds and the high speeds conditions may be written as

$$\tilde{u}_e = \sqrt{\frac{k}{10\eta_e\beta}} \quad (4.9)$$

When the velocity is smaller than \tilde{u}_e , this means inlet shear heating is not important and the EHL behavior is governed by the solid body temperature. Then, the film thickness can be calculated from isothermal Hamrock-Dowson equation using effective viscosity and pressure-viscosity coefficient determined by the solid body temperature.

4.5 Conclusions

The effect of solid body temperature on the EHL traction, film thickness and temperature rise has been investigated by numerical simulation with a non-Newtonian thermal EHL model for circular

contact. Physically sound rheological models of the lubricant, such as Carreau-Yasuda shear thinning and free volume density models, were adopted and incorporated into the EHL solver to describe the fluid behavior. The dependence of the thermal properties on pressure and temperature was also considered. The traction reduction phenomenon (Sec. 2.1.3.5) regarding the repeatability of the measurements with a disc-machine is explained by the solid body temperature effect, see Fig. 4.5(c). This highlights the potential risk of deriving rheological parameters from measured traction curves, especially with the slope and the maximum friction coefficient, when solid body temperature effects do occur. Under high speed conditions, inlet temperature rise is enhanced by inlet shear heating and compressive heating, leading to substantial reductions in film thickness. The main conclusions are:

(1) Solid body temperature affects the EHL film temperature and film thickness significantly from low to high speeds.

(2) With low and moderate entraining velocities, the temperature of the lubricant rises up to the solid body temperature in the inlet region and the EHL film behavior is dominated by the solid body temperature. The film thickness is controlled by the effective ambient viscosity at solid body temperature and it can be predicted with the isothermal Hamrock-Dowson equation using effective viscosity and pressure-viscosity coefficient at the solid body temperature as input.

(3) With high entraining velocities, the inlet temperature rise and thus the EHL film thickness are determined by comprehensive effects of inlet shear heating, compressive heating, and the solid body temperature effect. The Hamrock-Dowson equation at solid body temperature combining the Wilson or Gupta thermal reduction factors predicts smaller film thickness than the numerical results for the T9 oil and conditions studied.

(4) When the solid body temperature is higher than the supplied oil temperature, both the slope and the maximum friction coefficient in the traction curves are reduced. This indicates the importance of doing traction tests with disc machines at controlled mass temperature, *e.g.* the same as the supplied oil temperature.

5

Role of Solid and Liquid Thermal Conductivity on EHL Traction

*The influence of thermal conductivity of both the contacting solids and the lubricant on the traction in a rolling/sliding EHL contact has been studied numerically. For through-hardened AISI 52100 bearing steel (k was measured as 21 W/mK by Reddyhoff *et al*, see Tribol Lett 67(1):22, 2019), with the improper but widely used thermal conductivity of 46 W/mK in literature, the friction coefficient can be overestimated and the maximum temperature in the lubricating film would be underestimated. The effect of solid thermal conductivity on traction depends on the entrainment speed and the resulting film thickness. For the thermal conductivity of the lubricant, its pressure dependence affects the traction mainly at high speeds and/or at high slide-to-roll ratio (SRR) conditions.*

The work in this chapter has been published as: Liu, H. C., Zhang, B. B., Bader, N., Poll, G., & Venner, C. H. (2020). Influences of solid and lubricant thermal conductivity on traction in an EHL circular contact. Tribology International, 146, 106059.

DOI: <https://doi.org/10.1016/j.triboint.2019.106059>

5.1 Introduction

Film thickness and traction are two important factors concerning elastohydrodynamic lubrication (EHL). The EHL film thickness can be predicted fairly well with either numerical solutions [Venner and Lubrecht 2000] or analytical formulae fit to numerical solutions [Hamrock and Dowson 1977; Katyal and Kumar 2012], while for the EHL traction, there are considerable discrepancies between measurements and simulations [Björling, Habchi, Bair *et al* 2013]. The film thickness is determined by the amount of oil that is entrained into the contact zone in the inlet region, where pressure and shear stress are relatively low. An isothermal assumption mostly holds for the film thickness prediction. Only under severe operating conditions, *e.g.* high speeds and/or high loads, inlet shear heating may reduce the inlet oil viscosity with a consequent reduction in the film thickness [Gohar 2001]. In contrast, the EHL traction is determined by the shear properties of lubricants in the highly pressurized contact zone, where the viscosity and thus the stress are large. The lubricant seldom behaves Newtonian, and shear thinning, limiting shear stress and shear heating may occur [Bair 2019a]. As a result, thermal and non-Newtonian effects are necessary for the EHL traction prediction.

Many fluid models have been proposed for the EHL traction predictions, see references [Johnson and Tevaarwerk 1977; Bair and Winer 1979b; Bair 2019a] as examples. However, it should be noted that which fluid model can best describe the EHL film behavior under high pressure and high shear stress is still an open question. For the validation of the proposed models, traction machines, either twin-disc machines or ball-on-disc test rigs, are widely used to measure the EHL traction. Even with a well characterized lubricant, the deviation of traction between simulations and experiments is still obvious [Björling, Habchi,

Bair *et al* 2013]. There are many possible reasons, *e.g.* the necessity of accurate estimation of the limiting shear stress [Martinie and Vergne 2016; Bader, Wang and Poll 2017; Ndiaye *et al* 2017], the solid body temperature effect pointed out by Björling *et al* [2013] and analyzed recently by the current authors [Liu, Zhang, Bader *et al* 2019]. Besides these, one underlying reason can be the improper thermal conductivity values adopted for both the contacting solids and the lubricant in classical thermal EHL (TEHL) simulations. The specimens of traction machines are typically made of AISI 52100 bearing steel. Recently, Reddyhoff *et al* [Reddyhoff, Schmidt and Spikes 2019] measured the thermal conductivity of through-hardened AISI 52100 steel specimens used in a traction machine with a frequency domain thermoreflectance (FDTR) method. For both the ball and the disc, the thermal conductivity value is 21 W/mK, which is less than half of the value (about 46 W/mK) commonly used in the TEHL traction simulations of an AISI 52100 steel contact, see [Björling, Habchi, Bair *et al* 2013; Habchi, Vergne, Bair *et al* 2010; Shirzadegan, Björling *et al* 2016]. Reddyhoff *et al* show that the discrepancy may result from through-hardening of the steel, which leads to the reduced thermal conductivity. It is important and interesting to understand the influences of steel thermal conductivity on the EHL traction and the maximum film temperature.

Apart from the solid thermal conductivity, the thermal conductivity of lubricants may play an important role on the EHL traction and the film temperature distribution as well. Larsson and Andersson [Larsson and Andersson] measured the thermal conductivity for various oils under elevated pressures using the transient hot-wire method. Their results showed that at 1 GPa the thermal conductivity of all measured lubricants is about two times larger than the value at atmospheric pressure. They gave an empirical equation to describe the pressure dependence of the oil thermal conductivity (Eq. (2.44) in Sec. 2.2.7). A similar phenomenon has also been reported by Bair and Andersson *et al* [2018] for a reference liquid, squalane. However, in classical TEHL simulations, the oil thermal conductivity is usually assumed to be independent of pressure, and the value at atmospheric pressure is employed (about 0.14 W/mK). This means a smaller thermal conductivity is employed in simulations than it should be. Consequently, less heat can be conducted to the solids and hence the temperature rise in the film is higher. This leads to an underestimation of the predicted friction coefficient. This kind of influence has been shown by Habchi *et al* in a quantitative TEHL simulation with Shell T9 mineral oil by adopting the measured thermal conductivity of the oil [Habchi, Vergne, Bair *et al* 2010]. Their traction simulation results agreed with the measurements on a ball-on-disc traction machine. However, in their TEHL simulations, the thermal conductivity of the bearing steel was used as 50 W/mK, which is over two times larger than the new measured value of 21 W/mK.

In this chapter, the influences of solid and lubricant thermal conductivity on the EHL traction and temperature rises are investigated numerically for a steel-steel point contact problem. Squalane, which may be the best characterized reference fluid in EHL study, is employed for the analysis. The role of steel thermal conductivity on traction is shown in Sec. 5.3.1. Sec. 5.3.2 studies the influence of oil thermal conductivity on the EHL traction. The simulated traction curves are compared with measurements with a traction machine and the measurements by Björling *et al* for the same fluid [Björling, Habchi, Bair *et al* 2014]. Finally, the effect of thermal conductivity on the EHL film thickness and the reliability of the thermal reduction factor [Zhu 2013] will be briefly discussed.

5.2 Theoretical model and numerical solution

Numerical simulation of the traction in a rolling/sliding thermal EHL contact requires the modelling of several phenomena simultaneously: thin film flow (*e.g.* Reynolds equation), deformation

of the surfaces (*e.g.* elastic half space model), fluid models (*e.g.* viscosity-pressure-temperature relation, shear thinning and limiting shear model), and thermal parts (*e.g.* oil-solid energy equations). The EHL governing equations and the energy equations can be found in Sec. 2.4. As is suggested by Bair *et al* [Bair 2019b], preliminary measurements of the thermo-physical properties of lubricants are essential for the quantitative simulation of EHL behavior. Squalane, the properties of which (viscosity, thermal conductivity and heat capacity) have been thoroughly measured by Bair and co-workers and thereafter fitted to physically-sound models, is chosen. The rheological model and fluid properties for squalane have been summarized in Table 2.6. In this work, the LSS is assumed to be a linear function of pressure, *i.e.* $\tau_{LSS} = \Lambda p$ and $\Lambda = 0.075$ for squalane [Bair *et al* 2002a, 2002b].

The governing equations were rewritten in dimensionless forms, and subsequently, they were discretized with a finite difference method. The numerical methods introduced in Sec. 2.4.4 and validated in Appendix A have been used. The computation is achieved iteratively between pressure-film fields (PH cycles) and temperature-shear rate fields ($\bar{T}\dot{\Gamma}$ cycles). The Reynolds equation for the pressure distribution and the double integral for surface deformation are solved efficiently by the multigrid method and the multilevel multi-integration method [Venner and Lubrecht 2000], respectively. The temperatures are solved with a column-by-column relaxation scheme introduced by Yang [Yang 1998; Yang *et al* 2001; Guo, Yang, Qu 2001]. The local shear stress $\tau(x, y, z)$ in the iterative computation process was continuously checked to meet $\tau(x, y, z) \leq \tau_{LSS}$; and if $\tau(x, y, z) > \tau_{LSS}$, then let $\tau(x, y, z) = \tau_{LSS}$.

The calculation domain was $-9.0 \leq X \leq 1.6$, and $-3.4 \leq Y \leq 3.4$, where 513 nodes distributed equally on the finest level of grid (level 5) in both the X - and Y - directions. The number of nodes used for solving the 3D energy equations was 10 with equal distances across the film, and 8 with non-equal distances in each solid. The heat penetration depth or the computation boundary $D_T = d_T/a = 6.3$ was checked as sufficiently far from the solid-oil interface; see for example in Appendix C. The D_T value here is two times larger than that used by Guo and Yang [Guo, Yang, Qu 2001] and Habchi [2008]. Further expanding the D_T value of heat penetration or refining the mesh density has negligible effect on the accuracy of the calculated temperature and friction coefficient for the operating conditions in this study. The convergence criterion is:

$$\begin{cases} \sum |P_{i,j}^{(new)} - P_{i,j}^{(old)}| / \sum P_{i,j}^{(new)} < 0.001 \\ \sum |\bar{T}_{i,j,k}^{(new)} - \bar{T}_{i,j,k}^{(old)}| / \sum \bar{T}_{i,j,k}^{(new)} < 0.0001 \\ \sum |\dot{\Gamma}_{i,j,k}^{(new)} - \dot{\Gamma}_{i,j,k}^{(old)}| / \sum \dot{\Gamma}_{i,j,k}^{(new)} < 0.001 \\ \left| \sum P_{i,j}^{(new)} dXdY - \frac{2\pi}{3} \right| / \left(\frac{2\pi}{3} \right) < 0.001 \end{cases}$$

5.3 Results and discussion

Rolling/sliding circular contacts of a ball-on-disc traction rig lubricated with squalane are modeled. Both the ball and the disc are made of bearing steel. The supplied oil temperature is 40 °C and the Hertzian contact pressure is 1.25 GPa. The input parameters for the simulation are given in Table 5.1.

Table 5-1: Material thermo-physical properties and operating conditions

Item/Property	Value
Bearing Steel	
Young's modulus E	210 GPa
Poisson ratio ν	0.3 (-)
Heat capacity $c_{1,2}$	470 J/(kgK)
Thermal conductivity, k_s	21 and 46 W/(mK)
Density ρ	7850 kg/m ³
Squalane	
Viscosity η at 40 °C, $p = 0$	0.015 Pas
Density ρ at 40 °C, $p = 0$	795.8 kg/m ³
Viscosity-pressure coefficient α at 40 °C	18 GPa ⁻¹
Thermal conductivity k_{oil} at 40 °C, $p = 0$	0.1282 W/(mK)
Heat capacity c at 40 °C, $p = 0$	1960.3 J/(kgK)
Operating Conditions	
Effective radius $R = R_x = R_y$	10.314 mm
Supplied oil and solid body temperature T_0	313 K(40 °C)
Load w	80 N
Hertz contact pressure p_H	1.25 GPa
Entrainment speed u_e	0.1-10 m/s
Slide-to-roll ratio (SRR), Σ	0-100%

5.3.1 Effect of solid thermal conductivity

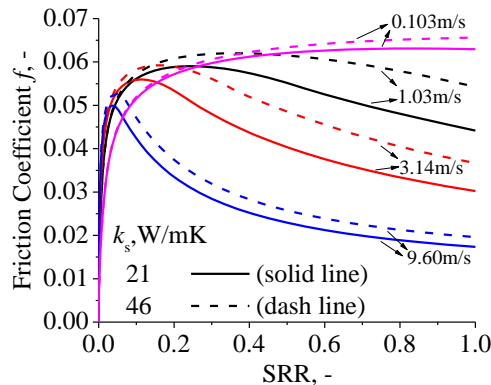


Figure 5-1: Traction curves with two solid thermal conductivities of $k_s = 21$ W/mK (solid lines) and 46 W/mK (dash lines), respectively, at four entrainment speeds in a circular EHL contact. (squalane, $T_0 = 40$ °C, $p_H = 1.25$ GPa; 21 W/mK was measured by Reddyhoff *et al* [2019] for hardened AISI 52100 steel, while 46 W/mK is the common cited but improper value in thermal EHL literature.)

Two thermal conductivities, k_s , of the AISI 52100 bearing steel are used. 21 W/mK is the thermal conductivity of hardened AISI 52100 bearing steel measured by Reddyhoff *et al*, and 46 W/mK represents the thermal conductivity that was usually adopted in TEHL simulations. Figure 5.1 compares the calculated traction curves for the two solid thermal conductivities over a wide SRR range at four velocities. For each group of traction curves of the same thermal conductivity, the friction coefficient decreases with increasing speed at moderate and large SRRs. This is simply due to enhanced heat generation at a higher entrainment speed. For the same speed, the traction curve can be highly influenced by the solid thermal conductivity. With the smaller thermal conductivity of 21 W/mK, less heat could be conducted out the film, which leads to a higher film temperature rise and thus lower viscosity and smaller friction coefficient. The maximum oil temperature rises for the two thermal

conductivities with the variation of SRR are shown in Fig. 5.2. The smaller solid thermal conductivity gives a larger temperature rise within the EHL film and then results in the reduced friction in Fig. 5.1. This friction reduction phenomenon caused by two solid thermal conductivities looks similar to the work done by Björling *et al* by coating the steel surface with a low thermal conductivity material, *e.g.* an insulating DLC coating [Björling, Habchi, Bair *et al* 2014].

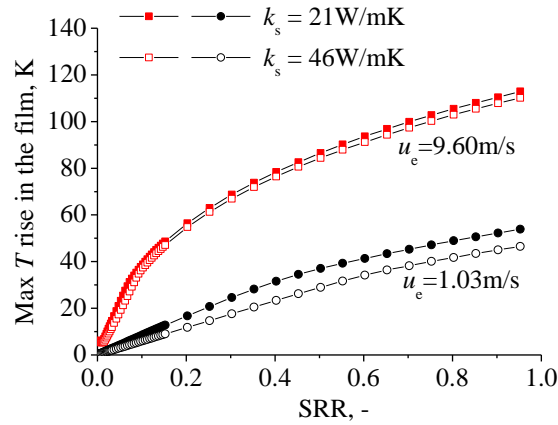


Figure 5-2: Maximum oil temperature rise for two thermal conductivities at a low entrainment speed of 1.03 m/s and a high speed of 9.60 m/s. The running conditions are the same as that in Fig. 5.1. (squalane, $T_0 = 40\text{ }^\circ\text{C}$, $p_H = 1.25\text{ GPa}$)

An unexpected phenomenon is that the solid thermal conductivity influences both the traction (Fig. 5.1) and the temperature rise (Fig. 5.2) more obviously at a relatively low entrainment speed of 1.03 m/s, but not at a high speed of 9.60 m/s where more heat is generated. This is especially the case for the traction at high SRRs. The distributions of the mid-film and the two surface temperatures along the central line of the contact (plane $Y = 0$) are depicted in Fig. 5.3 for cases of 1.03 m/s and 9.60 m/s corresponding to Fig. 5.1 at SRR = 50%. It shows the same trend, that is, at the low speed of 1.03 m/s the temperature difference in mid-film temperature at two thermal conductivities is larger than that at 9.60 m/s. This may be explained by the differences in film thickness. As is known, EHL film is sensitive to entrainment speed ($h_{cen} \propto U_e^{0.67}$), and the thermal conductivity of oil is quite low (*e.g.* 0.14 W/mK at ambient pressure), which is around two hundred times smaller than that of the bearing steel. This means that the generated heat near the center plane of the film is hard to reach the solids and then to conduct out from a relatively thick film caused by a high speed. The calculated central film thicknesses are 124.3 nm and 505.1 nm for the two speeds, respectively. It can be seen from Fig. 5.3 that with the same k_s value of 21 W/mK, the difference between mid-film temperature and any of the two surface temperatures is smaller for the low film thickness case (low speed case, Fig. 5.3a) than that for the thick film thickness case (high speed case, Fig. 5.3b). As can be imagined, if the film thickness is thick enough or the speed is high enough, the heat is mainly kept in the EHL film (thermal and shear localization in the mid-film) and the solid thermal conductivity has almost no influence on the traction and the maximum temperature rise. From Fig. 5.1 and the above analysis, it can be known that the effect of the solid thermal conductivity on the EHL traction is of speed and/or film thickness dependence.

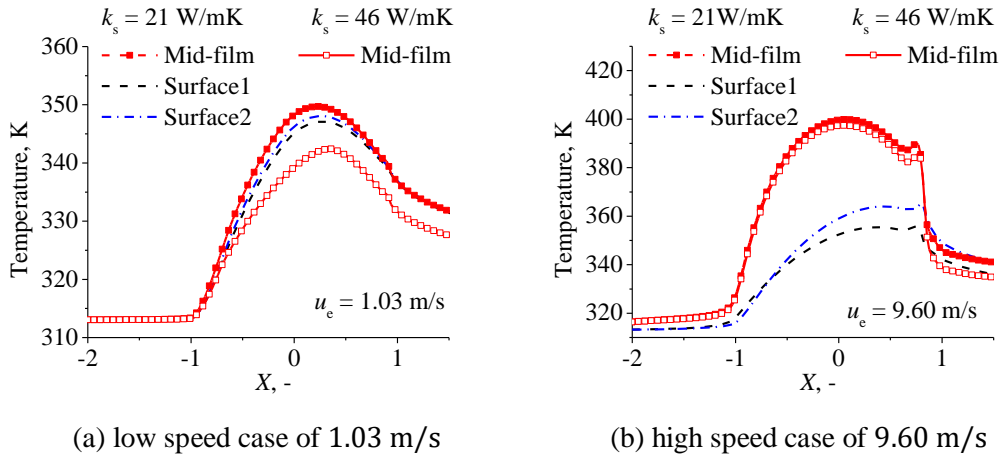


Figure 5-3: Temperature distribution for two thermal conductivities at a low entrainment speed and a high speed. The running conditions are the same as that in Fig. 5.1 with SRR = 50%. Plane $Y = 0$. (squalane, $T_0 = 40$ °C, $p_H = 1.25$ GPa)

5.3.2 Effect of lubricant thermal conductivity

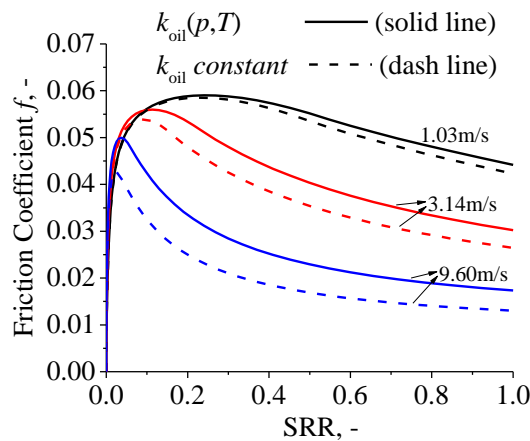


Figure 5-4: Influence of pressure dependence of lubricant thermal conductivity on traction at three entrainment speeds in a circular EHL contact. (squalane, $T_0 = 40$ °C, $p_H = 1.25$ GPa, $k_s = 21$ W/mK)

To evaluate the effect of pressure dependence of thermal conductivity, traction curve calculations are carried out by setting the liquid thermal conductivity to a constant value of 0.1282 W/mK ($p = 0$, 40 °C) or by using the equation in Table 2.6 to consider its pressure dependence. The two cases are labeled as $k_{oil}(p,T)$ and $k_{oil} constant$, respectively. The calculated traction curves for these two cases are compared in Fig. 5.4. After considering the $k_{oil}(p,T)$ relation, the friction coefficient becomes larger than that of $k_{oil} constant$, because more heat can conduct through the film to the solids. In other words, the EHL traction can be underestimated by simply ignoring the pressure and oil thermal conductivity relation, especially at high SRRs and/or at high speed running conditions. A similar phenomenon has been reported by Habchi *et al* [2010] with TEHL simulation using Shell T9 mineral oil. Note that the thermal conductivity of squalane increases dramatically with increasing pressure, whereas it changes slightly in terms of temperature. Hence, the thermal conductivity may be modelled as pressure dependent only [Larsson and Andersson 2000].

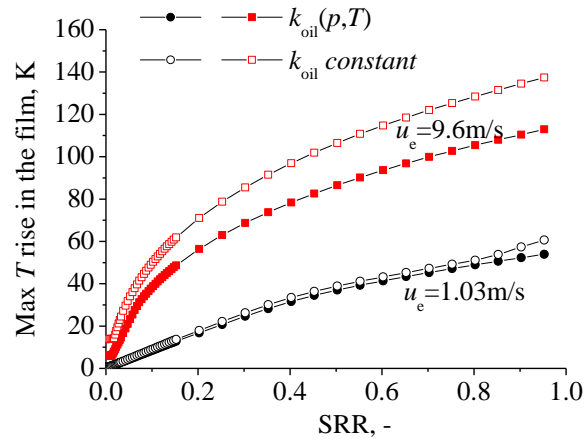


Figure 5-5: Influence of pressure dependence of lubricant thermal conductivity on maximum oil temperature rise at a low entrainment speed and a high speed. The running conditions are the same as that in Fig. 5.4. (squalane, $T_0 = 40\text{ }^\circ\text{C}$, $p_H = 1.25\text{ GPa}$, $k_s = 21\text{ W/mK}$)

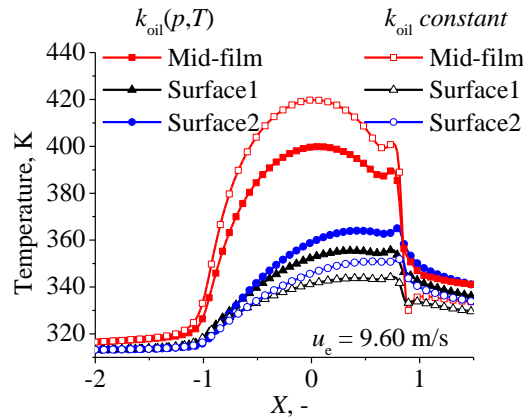


Figure 5-6: Temperature distributions of mid-film and two solid interfaces with the influence of lubricant thermal conductivity at a high speed. The running conditions are the same as that in Fig.6 with $\text{SRR} = 50\%$. Plane $Y = 0$. (squalane, $T_0 = 40\text{ }^\circ\text{C}$, $p_H = 1.25\text{ GPa}$, $k_s = 21\text{ W/mK}$, $u_e = 9.60\text{ m/s}$)

As can be seen in Fig. 5.4, this kind of pressure-enhanced liquid thermal conductivity effect on the traction is obvious for the high entrainment speed condition rather than for the low speed condition, which is different from the influence of solid thermal conductivity in Fig. 5.1 of Sec. 5.3.1. All heat is originally generated in the film, *e.g.* mainly by shear heating. At a low speed, the amount of generated heat is small and its distribution across the resulting thin film is almost regardless of the changes in lubricant thermal conductivity. This can be seen in Fig. 5.5 that there is almost no temperature difference for the low speed case. Indeed, the temperature distribution is mainly controlled by the solid thermal conductivity for a thin film, as is shown in Fig. 5.1 (*e.g.* $u_e = 1.03\text{ m/s}$). As a contrast, at a high entrainment speed and therefore a thick EHL film, the amount of heat generation is rather large. The increase in lubricant thermal conductivity would enhance the heat diffusion from the mid-plane of the film towards the solids through heat conduction. As a result, when the pressure and temperature dependence of thermal conductivity are considered for the high speed case, the maximum temperature rise near the mid-film should be lower (see Fig. 5.5, the high speed case), while the temperature of the two solid surfaces should be higher than the results obtained with $k\text{ constant}$, due to the heat redistribution across the film (see Fig. 5.6).

5.3.3 Traction comparison with experiments

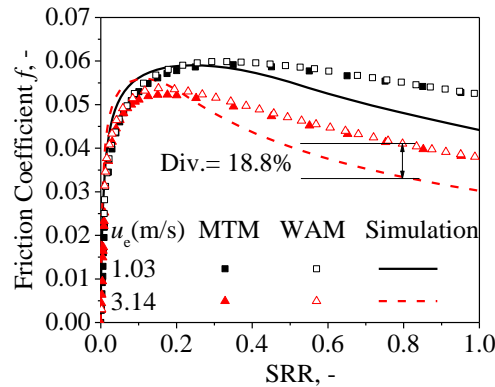


Figure 5-7: Quantitative traction curve comparison with squalane at two speeds. The traction curves were measured by two traction machines. ($T_0 = 40\text{ }^\circ\text{C}$, $p_H = 1.25\text{ GPa}$, $k_s = 21\text{ W/mK}$, $k_{oil}(p, T)$)

Björling *et al* [Björling, Habchi, Bair *et al* 2013, 2014] once measured the traction curves for squalane on a WAM ball-on-disc traction machine. The ball and disc are made of AISI 52100 steel, but there is no measurement of the thermal conductivity of these specimens. The samples measured by Reddyhoff *et al* are specified for the MTM ball-on-disc traction machine. For this reason, traction measurements have also carried out with an MTM machine at Volkswagen AG in Wolfsburg. The running conditions are the same as the conditions adopted in the simulations (Sec. 5.3.1, Table 5.1). As is mentioned in Sec. 2.1.3.3, roller compliance can contribute to the SRR under high pressure. The measured traction curves have been corrected with Eq. (2.4) to give a pure fluid behavior.

The experimental results from the MTM and WAM traction rigs are compared with the simulated traction curves in Fig. 5.7. The measurements from the two test rigs agree well for the operating conditions. The simulated traction curves capture all features of the experimental ones; however, the largest deviation can be 18.8%. Surface roughness could not be the main reason for the deviation. The combined root mean square (RMS) surface roughness R_q is about 14 nm for the MTM ball-on-disc contact. For the lower speed of 1.03 m/s, the minimum film thickness is 69 nm, which is over three times larger than the surface roughness. Moreover, the amplitude of roughness would be reduced due to the high EHL pressure in the contact zone. In such a full film condition, the effect of surface roughness on the traction should be ignorable. The reason for the discrepancy between measurements and simulations may lie in the accuracies and uncertainties of the used fluid models, such as high shear viscosity and the pressure and (possible) temperature dependence of the limiting shear stress. The detailed analysis requires comparison over a wide range of operating conditions; see Chapter 6.

5.3.4 Effect of thermal conductivity on film thickness

As is known, inlet shear heating reduces the film thickness at a high speed even for pure rolling because of the reverse flow and heat convection. Both the solid and the lubricant thermal conductivities should affect the inlet temperature rise through inlet heat dissipation and, therefore, affect the inlet oil viscosity and the EHL film thickness. There are several semi-empirical thermal reduction factors (TRF) available to account for the inlet thermal effect for line contacts [Zhu 2017]. The oil thermal conductivity has been embodied in these factors, while there is no variable related to the thermal conductivity of the contacting solids. Therefore, it is necessary to evaluate the influence of solid thermal conductivity on the EHL film thickness.

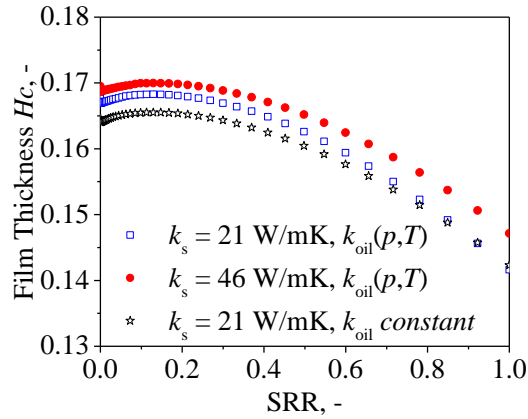


Figure 5-8: Non-dimensional central film thickness at different SRRs with different solid thermal conductivities and lubricant thermal conductivities. (squalane, $T_0 = 40\text{ }^\circ\text{C}$, $p_H = 1.25\text{ GPa}$, $u_e = 9.60\text{ m/s}$)

For a circular steel-steel contact working at a high speed of 9.60 m/s, the dimensionless central film thicknesses, $H_c = h_{\text{cen}}R_x/a^2$, are plotted as a function of SRR in Fig. 5.8 for three cases. In the first case, the solid thermal conductivity is 21 W/mK and the temperature and pressure dependence of lubricant thermal conductivity has also been considered in the simulation. The central film thickness calculated from the first case is regarded as the most accurate results and works as a reference for the other two cases. The other two cases are simulated either by changing the k_s to the value of 46 W/mK or by setting the k_{oil} as a constant. As can be seen in the figure, the case of $k_s = 21\text{ W/mK}$ and $k_{\text{oil}}\text{ constant}$ gives the lowest film thickness, as both the solid and the liquid thermal conductivities contribute to increase the inlet film temperature. The largest deviation among different cases is less than 3% over the calculation ranges. This may be negligible for engineering practice. Therefore, for steel-steel circular contacts, the solid thermal conductivity and the $k_{\text{oil}}(p, T)$ relation are not important for the prediction of the EHL film thickness concerning inlet shear heating.

The isothermal EHL central film thickness can be calculated simply by turning off the thermal calculation function in the program. For pure rolling (SRR = 0), it is 0.182 in a dimensionless form. Accordingly, the result of thermal EHL simulation is 0.167, which is 8.24% smaller than the isothermal one. The reduced film thickness is mainly caused by inlet shear heating. In Fig. 5.8, the central film thickness firstly increases slightly to a maximum value and then decreases with increasing SRRs. The increase of central film thickness at small/moderate SRRs may be attributed to the thermal expansion of the lubricant [Kaneta, Yang, Krupka *et al* 2015].

5.4 Outlook and Suggestions

Regarding the thermal conductivity of AISI 52100 bearing steel, one can find different values in different literature and catalogs, usually ranging from 19 W/mK to 55 W/mK. The thermal conductivity is influenced by heat treatment and the phase composition of the steel [Wilzer *et al* 2013]. There is usually retained austenite with controlled content in AISI 52100 bearing steel. The thermal conductivity of austenite phase is smaller than that of the martensite phase, and they are reported as 16.8 W/mK and 39.3 W/mK, respectively, at ambient conditions [Mustak *et al* 2016]. Recently Habchi and Bair [2020] provided a brief literature review on the thermal conductivity of steel. Thermal conductivity depends on the hardness of the steel and it is around 21 W/mK for through-hardened AISI 52100 steel. Through thermal EHL simulation using Shell-T9 oil, they found that the friction coefficient is significantly overestimated in the thermo-viscous friction regime when the improper value of

46 W/mK is adopted. In this work, we did simulations over a wide range of speed and found that the effect of solid thermal conductivity depends on the entrainment speed and the EHL film thickness. It is not obvious for either extra low speed or extra high speed conditions at high SRRs, whereas it is important for the traction at moderate entrainment speeds. At high speeds, the influence of solid thermal conductivity on traction is decreasing in the thermo-viscous regime, while its effect on the maximum friction coefficient of traction curves is still noticeable (Fig. 5.1).

During the service life of machine elements or even during manufacturing, there may be oxidization or tribo-layer formation on the interface, and thermal properties of the layer may differ from the bulk material. This would also influence the temperature rise in the EHL film and also the traction. Therefore, the FDTR technique for measuring near-surface thermal conductivity introduced by Reddyhoff *et al* [2019] is important and necessary for temperature and traction predictions. Before doing traction tests, the thermal conductivities of the specimens of the traction rig are suggested to be measured.

In literature, Kaneta and Yang did TEHL analysis with different solid materials, mainly glass-to-steel for the optical EHL rig, to show the thermal wedge mechanism on dimple formation [Kaneta and Yang 2003; 2010]. In this study, only a steel-steel contact was studied, in which the influence of the solid thermal conductivity on the thermal correction factor and on the pure rolling film thickness seems to be not important. However, if the same conclusion can be drawn for a ceramic-steel contact in a high speed ceramic rolling bearing is still a question to be answered.

5.5 Conclusions

The influences of solid and lubricant thermal conductivities on the EHL traction, temperature distribution and film thickness have been investigated with a non-Newtonian TEHL model for a steel-steel contact. On the influence of the solid thermal conductivity, the simulation focuses on the through-hardened AISI 52100 bearing steel, whose thermal conductivity was recently measured as 21 W/mK in contrast to the value of 46 W/mK widely used in TEHL simulations for traction machines. On the influence of the lubricant thermal conductivity, its dependence on pressure and temperature was considered for the EHL traction prediction. Squalane was used because its thermo-physical properties have been measured with great efforts and fitted to physically-sound rheological models, *e.g.* Carreau shear thinning model and free-volume based viscosity models. Simulated traction curves are compared with measurements from two traction rigs using the same fluid, squalane. The largest deviation is about 18.8%. The main conclusions are:

(1) For through-hardened AISI 52100 steel, with the improper thermal conductivity of 46 W/mK rather than the new measured value of 21 W/mK, the temperature rise in the EHL film is underestimated, while the friction coefficient is overestimated.

(2) The effect of solid thermal conductivity on the EHL traction depends on the entrainment speed and the resulting film thickness. At high speeds, the influence of solid thermal conductivity on traction is decreasing in the thermo-viscous regime, while its effect on the maximum friction coefficient is still noticeable in traction curves.

(3) The pressure dependence of lubricant thermal conductivity needs to be considered at high velocities and at high SRR conditions for traction predictions. Otherwise, the traction can be underestimated and the maximum temperature can be overestimated.

6

Fast Traction Prediction Method for Highly Loaded EHL Contacts

A simplified traction prediction approach has been developed for highly loaded EHL contacts accounting for non-Newtonian and thermal effects. For validation, a reference fluid squalane was used for traction measurements at high Hertzian contact pressures (1.25 to 2.66 GPa) at three velocities of 5, 10 and 15 m/s. Good agreement was seen for traction curves on a semi-log scale at a low speed of 5 m/s, whereas for higher speeds at 10 m/s and 15 m/s, the measured traction curves are lower than the predicted ones. This reduced friction in the experimental results is caused by the increase in mass temperature of the discs. Two possible mechanisms for this reduced friction due to solid body temperature effects are discussed.

*The work in this chapter has been published as: Liu, H. C., Zhang, B. B., Bader, N., Venner, C. H., & Poll, G. (2020). Simplified traction prediction for highly loaded rolling/sliding EHL contacts. *Tribology International*, 106335.*

DOI: <https://doi.org/10.1016/j.triboint.2020.106335>

6.1 Introduction

There are still considerable discrepancies in EHL traction between the results of theoretical simulations and measurements even with model fluids [Björling, Habchi, Bair *et al* 2013 and 2014]. This is especially true for highly loaded rolling/sliding EHL contacts.

Unlike the EHL film thickness which is determined in the inlet region of relatively low pressure (in MPa), the traction is mainly determined by the non-Newtonian shear of the fluid in the central of the contact (in GPa). For quantitative traction prediction, it is necessary to know the constitutive equation and the thermo-physical properties of the lubricant at high pressures and at high shear rates. This constitutive equation describes the variation of shear stress with shear rate for a bulk fluid under pressure. Typically, with increasing shear, the fluid may show Newtonian, shear thinning, limiting shear stress (LSS) [Smith 1960; Bair 2019a], and shear heating behavior. Along the entrainment direction of a rolling/sliding EHL contact, the local stress in the film is inhomogeneous due to the semi-elliptic pressure distribution and the variation in the distribution of viscosity and shear stress in the contact. The LSS may be reached near the contact center, while in the surrounding low-pressure area the fluid still shows shear thinning or even Newtonian behavior. In the 1970s, the relation between averaged shear stress and shear rate deduced from experimental traction curves of an EHL contact in a specific test approach was often taken as constitutive equation of the fluid (flow curve) [Johnson and Tevaarwerk 1977; Bair 2019b]. This was mainly due to the lack of independent-of-contact high pressure rheological data for oils.

Since 2007, much progress has been made in EHL studies with independent measurements of the rheological properties of reference fluids using high pressure viscometers. The measured data (*e.g.* free volume, viscosity, and thermal conductivity) are fitted into physically-sound fluid models. These models are then used in EHL simulations. The simulation results are compared with the experimental results, such as film thickness and traction. Liu *et al* [Liu, Wang, Bair and Vergne 2007] pointed out that inlet shear thinning may occur at pure rolling, and the Newtonian inlet assumption would not hold for the studied PAO-650 oil of large molecular size. The measured film thickness and traction agree well with the isothermal simulation results based on free-volume density-viscosity model and the Carreau-type shear thinning equation. This work showed the importance of the out-of-contact independent measurements of the constitutive behavior for the prediction of EHL behavior. Thermal effects were ignored, justified by the relatively low contact pressure, and the LSS cannot be reached. Habchi *et al* [Habchi, Vergne, Bair *et al* 2010] did thermal EHL simulations for highly loaded EHL contacts with a well-characterized mineral oil, Shell T9. The LSS was implemented to obtain a reasonable traction prediction [Habchi, Bair, Vergne 2013]. In the literature, efforts have also been made on quantitative traction prediction using other model fluids, such as squalane. Björling *et al* [Björling, Habchi, Bair *et al* 2013 and 2014] did a comprehensive comparison of traction over a wide range of entrainment velocities, SRRs, and contact pressures. The observed difference between measurements and simulation results varies with running conditions and was as high as 25% at 1.94 GPa. One reason could be the use of the incorrect exponent of the Carreau equation during the simulations [Björling, Habchi, Bair *et al* 2019]. Also, the thermal conductivity used for the specimens made of bearing steel was taken as 46.6 W/mK (a common value in thermal EHL literature), whereas, it should be around 21 W/mK for hardened bearing steel [Reddyhoff, Schmidt, Spikes 2019].

There are several other factors that complicate the accurate prediction of traction. Firstly, the physical nature of the LSS is still unknown [Martinie and Vergne 2016]. For a highly loaded EHL contact, the plateau regime in a traction curve is believed to be dominated by the LSS [Bair 2019a; Johnson and Tevaarwerk 1977; Habchi, Bair and Vergne 2013; Evans and Johnson 1986a and 1986b], which is often assumed to increase almost linearly with pressure [Bair 2019a; Evans and Johnson 1986a]. For traction prediction, an appropriate equation describing the relation between the LSS and the pressure is essential. In Refs. [Björling, Habchi, Bair *et al* 2013; Habchi, Vergne, Bair *et al* 2010], it is assumed that the LSS passes through the origin of coordinates and it is temperature independent, *i.e.* $\tau_{LSS} = \Lambda p$. However, recent work shows that this is only true at a certain temperature and mostly the LSS does not pass through the coordinate origin [Ndiaye, Martinie, Philippon *et al* 2017; Bader, Wang and Poll 2017]. Secondly, during measurements of traction curves, the specimen heats up and the mass temperature may exceed the supplied oil temperature [Isaac, Chagnenet *et al* 2018; Liu, Zhang, Bader *et al* 2019]. This higher solid body temperature reduces the inlet oil viscosity and thereby the film thickness [Liu *et al* 2019], and the EHL traction. This mass temperature effect is rarely considered in EHL traction simulations, except for Refs. [Liu, Zhang *et al* 2019; Yang and Liu 2009; Clarke, Sharif, Evans *et al* 2006]. Thirdly, many numerical methods have been developed for highly loaded EHL contact problems [Lubrecht 1987; Venner 1991; Ai 1993; Hu and Zhu 2000; Holmes, Evans *et al* 2003; Liu, Jiang, Yang *et al* 2005; Habchi 2008]. However, full simulations are time consuming when solving transient problems or applications of a machine element with multiple EHL contacts. Furthermore, numerical convergence problems still exist. Therefore, simplified and rapid EHL traction calculation methods for engineering purpose have been proposed [Olver and Spikes 1998; Bair, McCabe and Cummings 2002a and 2002b; Morgado, Otero *et al* 2009; Shirzadegan, Björling, Almqvist *et al* 2016; Itagaki, Ohama and Rajan 2019]. Few of them use independently measured rheological properties and/or compared results with measured traction curves quantitatively over a wide range of running conditions. Moreover,

the temperature gradient and the viscosity variation across the film are seldom modelled in simplified traction calculations. The EHL film is often treated as a single layer of uniform temperature (and uniform viscosity across the film) as for an isothermal problem in the above-mentioned simplified methods. This limits the accuracy of the prediction for the maximum temperature rise and the friction coefficient.

In this chapter, a fast traction calculation approach is presented for highly loaded rolling/sliding EHL contacts using measured viscosity and thermal properties as input. For the reference fluid squalane, it is tested and validated. By solving the reduced energy equations for solids and film, the temperature fields across the lubricant film and in the solids can be obtained. The pressure dependence of the mean limiting shear stress (the maximum shear stress τ_{MSS} in Eq. (6.8) and Eq. (6.9)) was derived from a set of traction curves measured at high contact pressures on a twin-disc machine. Traction curve measurements have been carried out at loads resulting in Hertzian pressures from 1.25 to 2.66 GPa over velocities from 5 to 15 m/s, and a SRR up to 12.5%. The traction prediction at small SRRs and high contact pressure regime is of significant importance to the application for rolling bearings. However, this has not been compared in detail in quantitative EHL literature, *e.g.* in Refs. [Björling, Habchi, Bair *et al* 2013 and 2014; Habchi, Vergne, Bair *et al* 2010]. In this work, special attention is given to the traction at small SRRs with semi-log plots for the traction curves. The solid body temperature effect on EHL traction and two possible mechanisms leading to experimentally observed lower traction than predictions are discussed.

6.2 Simplified EHL traction model

In this section, the assumptions and the governing equations for the simplified traction model are described. The rheological properties of the lubricant (squalane) are also given.

6.2.1 Assumptions and governing equations

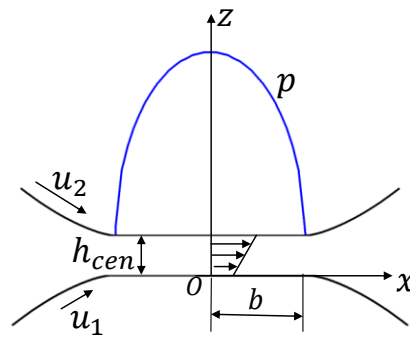


Figure 6-1: Schematic representation of the EHL film formed in a rolling/sliding elliptical contact at high load conditions (xoz view; not to scale; Hertzian pressure distribution).

The following assumptions are made for the rolling/sliding elliptical EHL contact of smooth surfaces, which is schematically shown in Fig. 6.1.

(1) A Hertzian pressure distribution. This assumption does not hold for an EHL contact at a low pressure, where the pressurized region is much larger than the Hertzian contact zone due to a large inlet region and possibly a pressure spike. At high loads, however, the pressure is mainly confined to the Hertzian contact region and is close to the Hertzian pressure distribution [Johnson 1987]:

$$p(x, y) = p_H \sqrt{1 - \left(\frac{x}{b}\right)^2 - \left(\frac{y}{a}\right)^2} \quad (6.1)$$

The contact axes, a and b , are calculated from the empirical formulas in [Markho 1987], which can be found in Sec. 2.3.2 or in the nomenclature.

(2) Couette dominant flow. The shear stress contribution of the Poiseuille or pressure-driven flow can be neglected for traction prediction. Firstly, in the center of the contact zone where the major portion of the shear stress originates, the Poiseuille flow is weak, as the viscosity is very large and the film thickness is very thin. Secondly, taking plane xoz in Fig. 6.1 as an example, the signs of the pressure gradient in the inlet and outlet region are opposite, so that the contributions of the outlet and the inlet to the traction almost cancel each other. Therefore, it is justified to assume that the shear resistance is dominated by the surface-driven flow. For isothermal EHL at small SRRs, the shear rate in the film can be expressed as,

$$\dot{\gamma} = \partial u / \partial z \approx \Delta u / h_{cen} = (u_2 - u_1) / h_{cen} \quad (6.2)$$

because in that case the viscosity does not vary across the film. When thermal effects or non-Newtonian effects are taken into account, the viscosity and the temperature may vary across the film (z -direction in Fig. 6.1). For this reason, the shear rate should be calculated from

$$\dot{\gamma} = \partial u / \partial z \quad (6.3)$$

When ignoring the Poiseuille flow, the local fluid velocity u may be expressed as [Yang and Wen 1990]

$$u = \frac{\eta_e}{h} (u_2 - u_1) \int_0^z \frac{1}{\eta^*} dz' + u_1 \quad (6.4)$$

where $\frac{1}{\eta_e} = \frac{1}{h} \int_0^h \frac{1}{\eta^*} dz$ with $h \approx h_{cen}$ here, η^* the high-shear viscosity. The shear rate in Eq. (6.3) then becomes

$$\dot{\gamma} = \frac{\partial u}{\partial z} = -\frac{\eta_e}{\eta^*} \frac{u_1 - u_2}{h_{cen}} \quad (6.5)$$

(3) Use of a corrected Hamrock-Dowson (HD) equation [1977] for central film thickness. It is assumed that the contact is fully flooded and the film thickness is uniform in the EHL contact zone. The classical HD equation is corrected for thermal and shear thinning reduction by factors from Gupta *et al* [Gupta, Cheng, Zhu *et al* 1992] and Bair [2005], respectively.

$$\begin{cases} h_{cen} = h_{HDcen,iso} * \varphi_{thermal} * \varphi_{thinning} \\ h_{HDcen,iso} = 2.69 R_x U_e^{0.67} G^{0.53} W^{-0.067} (1 - 0.61 e^{-0.73 \epsilon}) \\ \varphi_{thermal} = \frac{1 - 13.2 (p_H / E') L^{0.42}}{1 + 0.213 (1 + 2.23 \Sigma^{0.83}) L^{0.640}} \\ \varphi_{thinning} = 1.0 / \{1 + 0.79 [(1 + \Sigma) \Gamma]^{1/(1+0.2\Sigma)}\}^{3.6(1-n)^{1.7}} \end{cases} \quad (6.6)$$

where ϵ is the contact ellipticity parameter $\epsilon = 1.03 (R_y / R_x)^{0.64}$, $U_e = u_e \eta_0 / (E' R_x)$ is the speed parameter, $G = \alpha E'$ the material parameter, $W = w / (E' R_x^2)$ the load parameter, $L = -\frac{\partial \mu}{\partial T} \frac{u_e^2}{k_{oil}}$ the thermal loading parameter, $\Gamma = \frac{u_e \eta_0}{h_{HDcen,iso} \tau_c}$ the inlet Weissenberg number, $\Sigma = SRR = \Delta u / u_e$ the slide-to-roll ratio, n is the power-law component in the shear thinning equation. The pressure-viscosity coefficient α is calculated using the definition of α_{film} in Eq. (2.4) from Bair *et al* [Bair, Liu and Wang 2006].

(4) Assume heat generated from shearing and dissipated by conduction in z -direction. The heat generation mechanisms in an EHL film are: (a) inlet shear heating (even at pure rolling), due to Poiseuille flow and possible reverse flow [Cheng 1965; Sadeghi and Dow 1987]; (b) compressive heating, which mainly affects the inlet region [Reddyhoff, Spikes and Olver 2009a; Kaneta, Shigeta and Yang 2005; Habchi and Vergne 2015]; (c) viscous shear of the EHL film in the rolling/sliding conjunction. This third effect dominates the other two at a small SRR [Kaneta *et al* 2005; Habchi and Vergne 2015]. The amount of heat generated through (c) depends on the viscosity and the shear stress in the confined film, and thus on the pressure and the velocity of the running conditions. Heat conduction across the film plays a dominant role in heat removal, whereas heat convection by the film can be ignored [Yang, Qu, Kaneta *et al* 2001], due to the fact that the EHL film is very thin (usually less than 1 μm). For the contacting solids, material convection and heat conduction contribute to the heat dissipation. The complete form of energy equation given in Sec. 2.4.4.2 can be simplified to:

$$\begin{aligned} \text{For oil film: } & -\frac{\partial(k_{\text{oil}}\partial T/\partial z)}{\partial z} = \eta^* \left(\frac{\partial u}{\partial z}\right)^2 \\ \text{For solids: } & c_{s(i)}\rho_{s(i)}u_{s(i)}\frac{\partial T}{\partial x} = k_{s(i)}\frac{\partial^2 T}{\partial z^2}, i = 1, 2 \end{aligned} \quad (6.7)$$

At the solid/fluid boundaries, the heat flux should be continuous. Note that for the hardened 52100 steel used in this study, the thermal conductivity, $k_{s(i)}$, is 21 W/mK rather than 46 W/mK [Reddyhoff *et al* 2019]. The effects of this value on the EHL traction were analyzed recently in [Liu, Zhang, Bader *et al* 2020a] and [Habchi and Bair 2020]. The increase of oil thermal conductivity with pressure is considered in this study.

(5) No solid body temperature effect. In most thermal EHL models, the mass temperatures (refers to the body temperature of the disc in a certain depth with near zero temperature gradient rather than the maximum surface temperature) of the two discs are assumed to be equal to the supplied oil temperature, even though this is rarely true [Issac *et al* 2018; Liu *et al* 2019]. The disc heats up during the measurements of traction curves with a traction machine, to which extent, depends on the running condition, *e.g.* the sliding speed and the load. The effect of this solid body temperature on the maximum friction coefficient is discussed in Sec. 6.4.2.1.

(6) Assuming the LSS depends only on pressure. The LSS is very important for traction prediction at low SRRs. However, it is also the most weakly understood parameter [Bair 2019a]. For traction prediction, whether LSS should be modelled as temperature dependent is still unclear, see [Bair 2019a; Habchi *et al* 2010; Bader *et al* 2017] vs. [Ndiaye *et al* 2017]. The experimental traction curves in this work were measured at a constant oil jet temperature of 40 $^{\circ}\text{C}$. For simplicity, the mean maximum shear stress (MSS) derived from measured traction curves at a low speed is used to represent the LSS and it is assumed to depend on pressure only (*e.g.* in [Björling *et al* 2013 and 2014; Habchi *et al* 2010, 2013, 2015 and 2020]). The method to determine the pressure dependence of the MSS is given in Sec. 6.2.3, and the possible influence of temperature on the LSS and the MSS is discussed in Sec. 6.5.

6.2.2 Properties of squalane

Squalane ($\text{C}_{30}\text{H}_{62}$) is a model fluid of which the thermo-physical properties (except for LSS) were thoroughly characterized, and has been used in the traction measurements and simulations. The viscosity and thermal conductivity as a function of pressure and temperature have been measured and fitted into models by Bair and co-workers [Björling *et al* 2013; Bair, Andersson, Qureshi *et al* 2018; Bair 2006; Bair, McCabe and Cummings 2002a and 2002b]. The piezo-viscous behavior of lubricants is very important for the traction prediction. For all typical lubricants, the pressure response of viscosity is greater-than-

exponential beyond a critical pressure. This sigmoidal shape on a semi-log scale results from changes in free volume and compressibility under pressure for fluids, which can be modelled more accurately using free-volume based models (such as Tait-Doolittle and improved Yasutomi) than the classical Roelands equation. The low shear viscosity was expressed by the improved Yasutomi model for squalane (measurement up to 1.5 GPa). The thermal conductivity of oil doubles the value at a typical EHL pressure of 1 GPa. This should be considered in EHL simulations for highly loaded conditions. The models and equations have been summarized in Table 2.6.

The shear thinning behavior is modelled by a power-law Carreau-type equation in this work. Note that there is still controversy on which shear thinning model is to be used for EHL film at high shear stresses, *i.e.* the Carreau power-law or the Eyring sinh-law. In thermal EHL simulations, the Eyring shear thinning model has been widely used. There is only a single parameter (the critical/Eyring shear stress) in this model and by adjusting this parameter, the simulated traction curves can be easily fitted to measurements. The Eyring model was used to describe the constitutive behavior of lubricants by Johnson and Tevaarwerk [1977] after studying the average shear stress versus average shear rate obtained from traction curves. However, Bair [2019b] pointed out that a traction curve is not a flow curve, and the shear stress versus shear rate relationship of the liquid does not have the same form as the average shear stress versus average shear rate from a traction curve. He showed that the power-law Carreau-type equation could describe the shear thinning behavior for both the EHL film thickness and the traction, see [Liu *et al* 2007] for PAO650. Recently, Jadhao and Robbins [2019] did molecular dynamics simulations and showed that the transition from Carreau to Eyring is generic for squalane. Bair [2019b] argued that the Eyring model was proposed under influence of shear heating rather than a pure shear thinning behavior. He [Bair 2020] also questions the transition from Carreau to Eyring for constitutive behavior from Jadhao and Robbins, as this would break the shifting rule of time-temperature-pressure superposition. Moreover, Bair and coworkers [Bair, McCabe *et al* 2002a and 2002b] also did MD simulations for squalane and they supported Carreau-type shear thinning. Indeed, more work is needed to understand the inconsistent conclusions from MD simulations for the same fluid.

6.2.3 Maximum shear stress determination at different pressures

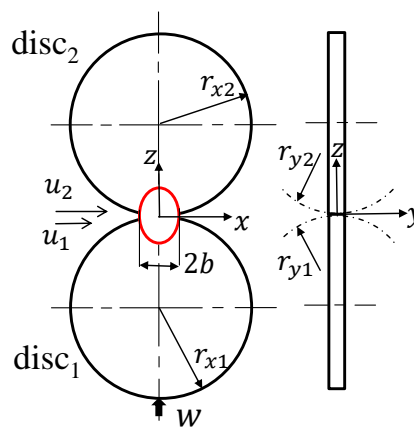


Figure 6-2: The geometry of the discs of the twin-disc machine (not to scale; $r_{x1} = r_{x2} = 60$ mm, $r_{y2} = 50$ mm, $r_{y1} = \infty$; ellipticity ratio $k_e = 1.43$).

As mentioned above, the maximum friction coefficient of a traction curve is highly influenced by the LSS property of lubricants for high loaded contacts. An appropriate LSS equation as a function of pressure is essential for the EHL traction prediction. The LSS of a bulk fluid could be measured with

independent high-pressure techniques, such as the thin-film high-pressure Couette viscometer designed by Bair and Winer [1990], the axially translating concentric cylinder device [Bair and Winer 1982] and the high pressure chamber designed by Höglund and Jacobson [1986]. In practice, there are many difficulties in shearing a pressurized homogeneous fluid at high shear stress and at high shear rate while maintaining a nearly constant temperature. As an averaged approach, the traction machine has been widely used as a rheometer for the characterization of the LSS of lubricants. What can be measured is the MSS, which is a mean shear stress over the EHL contact corresponding to the maximum friction coefficient in a traction curve (see Eq. (6.8)). The MSS is not an inherent property of the lubricant. However, for highly loaded contacts with the assumptions that the LSS is reached almost everywhere in the contact zone and thermal effects are negligible till the occurrence of the maximum friction coefficient, the value of the measured MSS in a traction curve is close to the LSS at that corresponding mean contact pressure. In this work, the pressure dependence of the mean LSS for squalane is approximated from measured traction curves (MSS) using the approach in [Poll and Wang 2012]. The method is explained below.

Fig. 6.2 schematically shows the geometry of the discs of the traction machine used in this study. The two discs are loaded together by a hydraulic cylinder and driven separately by two motors to allow variation of the SRRs, during which process the forces for shearing the EHL film are recorded. In this study, traction curves are shown as friction coefficient against SRR.

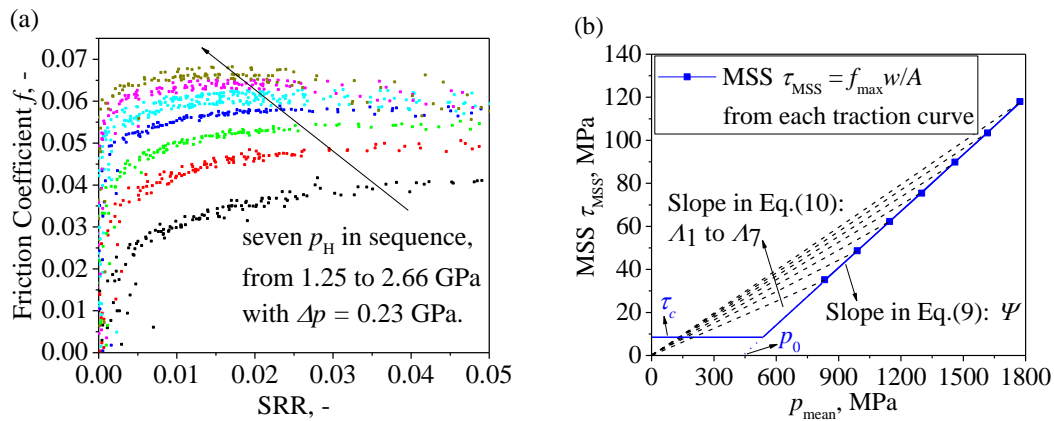


Figure 6-3: Determination of the pressure dependence of the MSS for squalane based on measured traction curves at high contact pressures. (a) the measured traction curves with a twin-disc machine at 5 m/s and 40 °C; (b) the bilinear function of the maximum averaged shear stress versus the mean contact pressure.

Figure 6.3(a) shows a set of measured traction curves for squalane at different loads. The supplied oil temperature is 40 °C and the entrainment velocity is 5 m/s. Seven loads were used giving Hertzian contact pressures in sequence, from 1.25 GPa to 2.66 GPa with an increment Δp about 0.23 GPa. To be precise, the seven Hertzian pressures are 1.25, 1.48, 1.72, 1.95, 2.20, 2.42 and 2.66 GPa. The composite surface roughness R_q of the discs is 224 nm. The entrainment velocity, 5 m/s, was chosen so that full film lubrication was achieved for all operating conditions (the lambda ratio of central film thickness to combined surface roughness R_q is in the range of 2.0 to 2.4). Using Eq. (6.8),

$$\tau_{\text{MSS}} = \frac{f_{\text{max}} w}{\pi a b} \text{ and } p_{\text{mean}} = \frac{w}{\pi a b} \quad (6.8)$$

the maximum friction coefficient f_{max} in each traction curve is reconstructed into a plot of the MSS τ_{MSS} against mean contact pressure p_{mean} . The results are shown in Fig. 6.3(b).

In Fig. 6.3(b), the MSS increases linearly with the mean contact pressure whereas the fitting curve does not go across the origin of the coordinates. This has also been reported by [Ndiaye *et al* 2017; Poll and Wang 2012]. According to Poll and Wang [2012], the variation of the MSS with pressure in Fig. 6.3(b) can be expressed by a bilinear form

$$\tau_{\text{MSS}} = \begin{cases} \psi (p - p_0), & \text{for } p \geq p_0 + \tau_c/\psi \\ \tau_c, & \text{for } p < p_0 + \tau_c/\psi \end{cases} \quad (6.9)$$

where τ_c is the critical shear stress, which indicates the onset of shear thinning of the fluid. In Eq. (6.9) τ_c (9.3 MPa used here for squalane) is set as the lower limit to avoid the occurrence of negative MSS values in the low pressure region. Fitting the curve in Fig. 6.3(b), one obtains $\psi = 0.08785$, $p_0 = 437$ MPa for squalane at 40 °C.

It should be noted that there are many other types of LSS/MSS equations in literature [Johnson and Tevaarwerk 1977; Ndiaye *et al* 2017; Houpert *et al* 1981; Bair and Winer 1992; Wikström and Höglund 1994]; see Table 2.4 in Sec. 2.2.3.3. The most widely used one in quantitative EHL study is in the form

$$\tau_{\text{LSS}} = \Lambda p \quad (6.10)$$

The pressure-LSS coefficient Λ can be determined by measuring one traction curve at a high Hertzian pressure and it equals the measured maximum friction coefficient in the plateau regime of the measured traction curve. The pressure-LSS coefficient Λ appears to be material dependent [Bair 2019a] and for most lubricants Λ is in the range of 0.04 and 0.12. Bair *et al* [Bair, McCabe 2002a and 2002b] measured $\Lambda = 0.075$ for squalane at $p_H = 1.93$ GPa using a skewed roller traction rig.

One apparent difference between Eq. (6.9) and Eq. (6.10) is whether the fitting curve of the MSS/LSS passes through the origin of the coordinates. Actually, Eq. (6.10) predicts a larger LSS value than Eq. (6.9) in the low pressure region. This can be seen from Fig. 6.3(b) as one gets a coefficient Λ according to Eq. (6.10) for each pressure. With increasing pressure the coefficient Λ (Λ_1 to Λ_7 , the slope of the dashed curves in Fig. 6.3(b)) increases slightly, whereas the rate of the increase is becoming smaller and smaller. It can be expected that at an extremely high pressure the two equations would predict the same value of the LSS/MSS under well-controlled isothermal conditions. However, it is hard to determine which one best represents the true LSS behavior of the fluid at relatively low pressures. This is mostly due to the fact that the pressure-MSS/LSS coefficient, either the Λ in Eq. (6.10) or the ψ in Eq. (6.9), is determined within an EHL contact of inhomogeneous fluid state and may be influenced by thermal effects, which is not the case of homogeneous bulk fluid at high pressure and at high shear stress out-of-contact. In this study, the bilinear Eq. (6.9) for MSS is adopted.

6.3 Simplified traction calculation method

6.3.1 Traction and temperature calculation method

The overall friction coefficient is defined as the ratio of the tractive force to the applied normal load,

$$f = \frac{\iint \tau_x dx dy}{w}, \text{ where } \tau_x = \min[\dot{\gamma}\eta^*(p, T, \dot{\gamma}), \tau_{\text{LSS}}] \quad (6.11)$$

For isothermal EHL traction simulation, it is a two-dimensional problem in a plane XOY , as the shear rate is homogeneous across the film. Fig. 6.4(a) shows the computational domain and the nodes for the calculation of the local pressure and the shear stress. The distribution of the shear rate is uniform all

over the contact area for isothermal conditions and $\dot{\gamma}$ can be obtained with Eq. (6.2). The viscosity η^* in Eq. (6.11) is calculated using the improved Yasutomi equation and the Carreau shear thinning equation listed in Table 2.6. When the calculated local shear stress is larger than the corresponding LSS (MSS in Eq. (6.9) used here) at that pressure or that local point, the shear stress is set to the value of the MSS [Bair, McCabe *et al* 2002a]. In this way, the friction coefficient can be rapidly calculated according to Eq. (6.11). The calculation area is $-1.0 \leq X \leq 1.0$, $-k_e \leq Y \leq k_e$ with 257 nodes in each direction. It should be noted that all governing equations are solved in dimensionless forms. The non-dimension parameters can be found in the nomenclature.

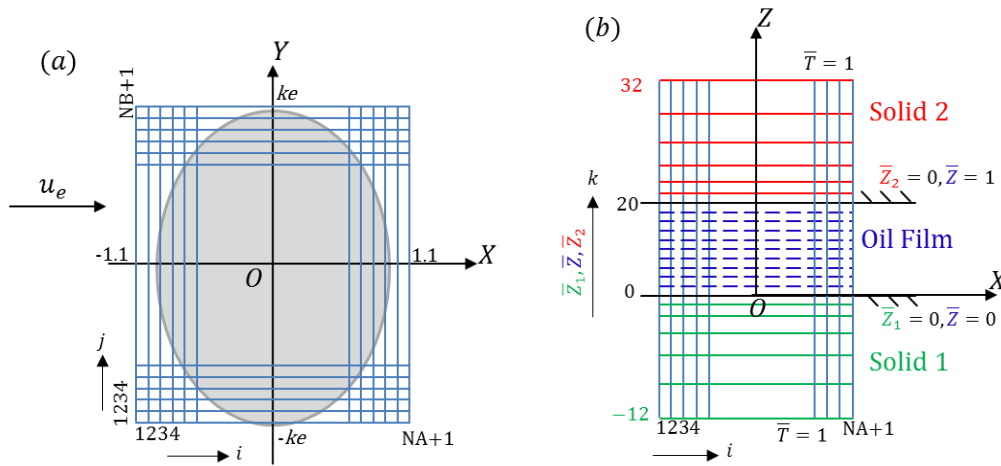


Figure 6-4: Computational domain and the finite difference meshing for elliptical contacts in non-dimensional coordinates (not to scale) (a) pressure and local shear stress domain on plane XOY ; (b) grids in the temperature computation domain on plane XOZ .

When thermal effects are modelled, the computational complexity increases due to the coupling between the shear stress and the temperature rise. The viscosity and the shear rate may vary across the film due to the temperature gradient. Therefore, Eq. (6.3) is used for local shear rate calculation instead of Eq. (6.2). The traction calculation becomes a three-dimensional problem, by adding the z -component compared with an isothermal problem. Fig. 6.4(b) schematically shows the grids in z -direction for the temperature calculation on plane XOZ . There are 20 equally distributed nodes in the EHL film and 12 non-equally distributed nodes within each of the discs. The heat penetration depth D_T is 6.3, which is large enough to reach near zero temperature gradient. The temperature fields are calculated line-by-line in z -direction by solving the simplified energy equations, Eq. (6.7), using the difference scheme and the relaxation method proposed by Yang [1998; 2013].

The flow chart for the traction and temperature calculation is shown in Fig. 6.5. It starts with an isothermal computation of pressure and film thickness described above. Then, the local shear rate and flow velocity are initialized. By fixing the values of those variables, the temperature calculation is carried out and the resulting temperatures are used to update the viscosity, velocity and shear rate. This is an iterative process until the temperature and the shear rate fields are converged with a relative error smaller than 0.001. Finally, friction coefficient and temperature fields are saved. It takes around one minute for the calculation of one SRR with MATLAB-R2016a at 2.6 GHz CPU.

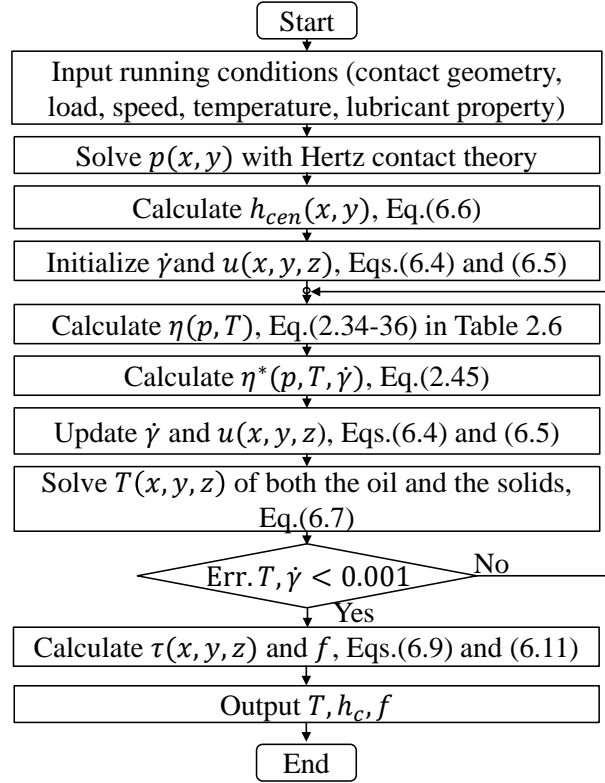


Figure 6-5: Flow chart of procedures for the simplified calculation of temperature fields and the friction coefficient at one SRR in a rolling/sliding EHL contact.

6.3.2 Model validation

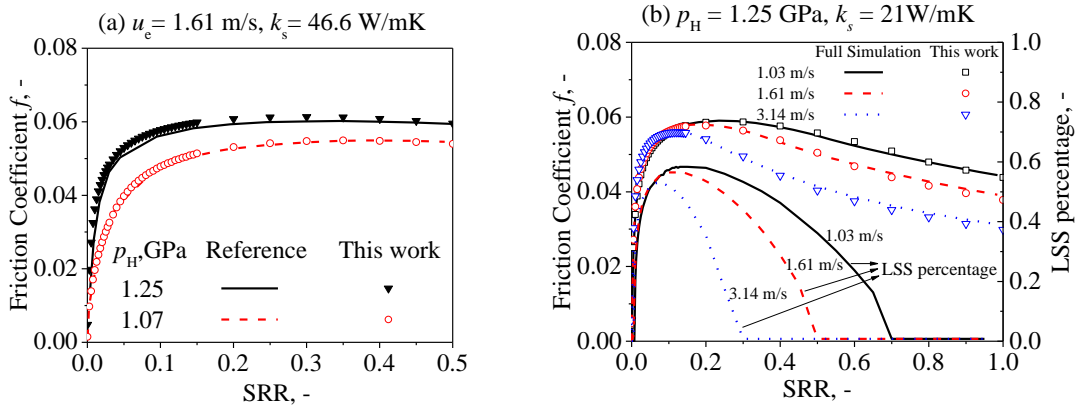


Figure 6-6: Comparison of traction curves between current simulation and the full numerical simulation for squalane fluid ($T_0 = 40$ °C). (a) compared with the full calculation from Habchi *et al* [Björling, Habchi *et al* 2013, 2014 and 2019]; (b) compared with the full simulation [Liu, Zhang *et al* 2019]. ($\tau_{LSS} = 0.075p$ was used here for comparison purposes)

In Fig. 6.6 traction curves are given for squalane. The current simplified calculation results and the results from two full numerical simulations are given. The so-called full numerical simulation refers to the EHL simulation by solving the Reynolds equation and the other governing equations, *e.g.* energy equations and elastic deformation equation. Fig. 6(a) compares the results with Björling, Habchi *et al* [Björling, Habchi *et al* 2013, 2014], in which the power-law exponent n of squalane was misused as the one of Shell T9 oil [Björling, Habchi *et al* 2010] and the thermal conductivity was 46.6 W/mK instead of

21 W/mK. For the validation of the numerical method, these two improper values are used for Fig. 6.6(a). Other than that, the results are all calculated with the proper Carreau exponent of squalane and with the thermal conductivity of 21 W/mK for hardened bearing steel. Fig. 6.6(b) compares the results from the current simplified traction approach with the full numerical simulation built in the former work by the current author [Liu, Zhang *et al* 2019]. The calculated traction curves show good agreement. Fig. 6.6(b) shows the percentage of the LSS-reached area along the x -axis on plane xoz for the three speeds. It can be seen for $p_H = 1.25$ GPa the LSS has not been reached in large portions of the contact. This may explain why the maximum friction coefficient in Fig. 6.6(b) is smaller than the LSS-pressure coefficient of 0.075 used in this comparison. At a large SRR, oil viscosity and shear stress decrease due to thermal effects and then even fewer portions can reach the LSS.

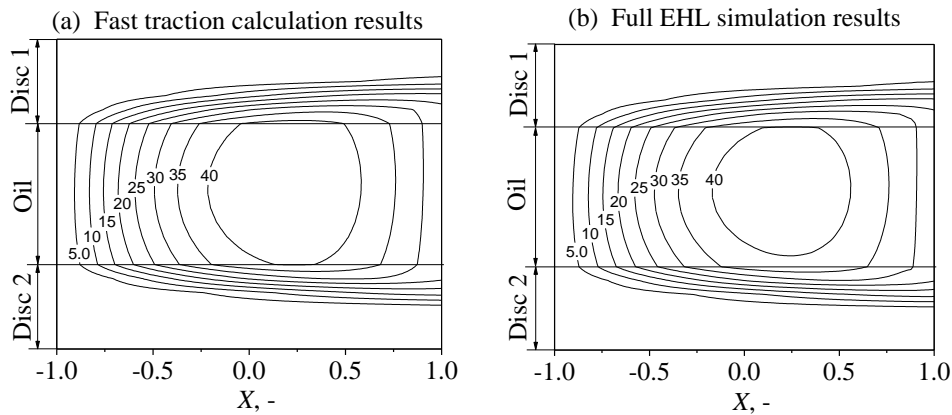


Figure 6-7: Plots of the temperature rise in the solids and in the lubricant from (a) current simplified simulation and (b) the full EHL simulation (Plane XOZ , squalane liquid, $p_H = 1.25$ GPa, $u_e = 1.61$ m/s, $T_0 = 40$ °C, SRR = 50%, $k_s = 21$ W/mK, $\tau_{LSS} = 0.075p$ was assumed).

Fig. 6.7(a) and (b) show the counter plots for the temperature rise on plane XOZ , respectively, using the current simplified calculation method and the full numerical method of Liu, Zhang *et al* [2019]; also see Sec. 2.4. The temperatures from the two methods are close in both the solids and in the film.

Through the traction comparison in Fig. 6.6 and the temperature field comparison in Fig. 6.7, it may be concluded that the accuracy of the simplified traction calculation method is quite good for highly loaded EHL contacts.

6.4 Results and discussion

Steel-steel elliptic contacts formed by the twin-disc machine (geometry see Sec. 6.2.3) and lubricated with squalane (properties in Table 2.6) are modeled for traction simulation. The corresponding experimental traction curves were also measured using this traction rig with squalane at 40 °C. Three entrainment velocities were chosen to enable full separation of the surfaces at all operating conditions and they are 5, 10, and 15 m/s. For each velocity, traction curves were measured at seven Hertzian contact pressures in sequence, from 1.25 GPa to 2.66 GPa with an increment about 0.23 GPa, as described in Sec. 6.2.3 for the determination of the MSS. Table 6.1 summarizes the parameters used for both the simulation and the measurements, including the running parameters of the twin-disc machine and the properties of the lubricant at ambient pressure and at 40°C.

As has been discussed in Sec. 2.1.3.3, disc compliance contributes to the SRR at high pressures during traction measurements. This effect is obvious for small SRRs, say $SRR < 0.01$. In order to study

the traction behavior of the fluid, the true SRR may be calculated by subtracting the portion of roller creep from the total recorded SRR of the rig through the following equation [Bair and Kotzalas 2006],

$$\text{SRR} = \text{SRR}_{\text{fluid}} = \text{SRR}_{\text{total}} - f \frac{p_H}{G_s} \quad (6.12)$$

where f is the friction coefficient, G_s the shear modulus (78 GPa for steel). All measured traction curves are corrected with Eq. (6.12) for the study of pure fluid behavior.

Table 6-1: Lubricant properties and operating conditions of the twin-disc machine

Item/Property	Value
Squalane (C ₃₀ H ₆₂) liquid	
Viscosity η at 40°C, $p = 0$	0.0156 Pas
Density ρ at 40°C, $p = 0$	795.8 kg/m ³
Viscosity-pressure coefficient α at 40 °C	18.0 GPa ⁻¹
Thermal conductivity k_{oil} at 40 °C, $p = 0$	0.1282 W/(mK)
Heat capacity c at 40 °C, $p = 0$	1960.3 J/(kgK)
Twin-disc machine and operating conditions	
Radius $r_{x1} = r_{x2}$	60 mm
Crowned radius r_{y1}, r_{y2}	$\infty, 50$ mm
Ellipticity ratio k_e	1.43
Supplied oil temperature T_0	313 K (40 °C)
Load w	1.14 to 11.0 kN
Hertz contact pressure p_H	1.25 to 2.66 GPa
Entrainment speed u_e	5, 10, 15 m/s
Slide-to-roll ratio (SRR), Σ	0 to 0.125 (12.5%)
Disc material and its properties	
Material	AISI 52100 steel
Young's modulus E	210 GPa
Poisson ratio ν	0.3 (-)
Heat capacity $c_{1,2}$	470 J/(kgK)
Thermal conductivity, $k_s = k_{s1} = k_{s2}$	21 W/(mK)
Density ρ	7850 kg/m ³

6.4.1 Traction curves at 5 m/s

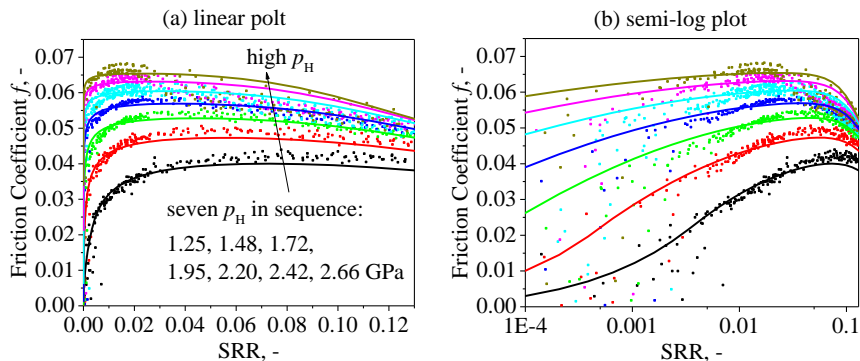


Figure 6-8: Traction curve comparison of simplified traction calculations (solid lines) and twin-disc measurements (dots) at a low speed of 5 m/s for the seven contact pressures. (Squalane, $T_0 = 40$ °C, $k_s = 21$ W/mK)

Fig. 6.8(a) compares the calculated and the measured traction curves at a relatively low entrainment velocity of 5 m/s for the seven contact pressures. The experimental traction curves here are the same as

the ones in Fig. 6.3(a). The predicted traction curves agree well with the experimental results over all the studied pressures and the SRRs. The maximum friction coefficient increases with increasing Hertzian contact pressure. However, the increase rate is decreasing at higher pressures, which corresponds to the trend of variation regarding the coefficient Λ with pressures in Fig. 6.3(b). It can be imagined that at an infinitely large pressure there would be no further increase in the maximum friction coefficient in Fig. 6.8(a) with increasing pressure and the maximum friction coefficient would equal the value of Λ .

In the literature, whether oil viscoelasticity plays a role on EHL traction at small SRRs is a matter of debate [Johnson and Tevaarwerk 1977; Poll and Wang 2012; Habchi and Bair 2019]. In order to have an explicit comparison of the traction at small SRRs, Fig. 6.8(b) replots the data from Fig. 6.8(a) onto a semi-log scale. The pure viscous calculation predicts the traction well with the viscous-plastic fluid models in Sec. 6.2.3 and Table 2.6, while no elastic property of squalane is considered in the simulation. It may be concluded that the effect of viscoelasticity is not important for the traction prediction of squalane. Recently, Habchi and Bair [2019] did EHL traction simulation with measured elastic shear modulus (in order of GPa) based on Maxwell model and found that shear viscoelasticity is negligible for traction prediction. Through Fig. 6.8(b), it can be seen that it is hard to measure the traction accurately when the SRR is smaller than 0.005 using the current twin-disc machine. Indeed, at such a small SRR, the elastic compliance of the solid disc would dominate the traction rather than the oil elasticity [Poll and Wang 2012; Habchi and Bair 2019].

6.4.2 Traction curves at higher speeds

6.4.2.1 Traction curve comparison and the solid body temperature effect

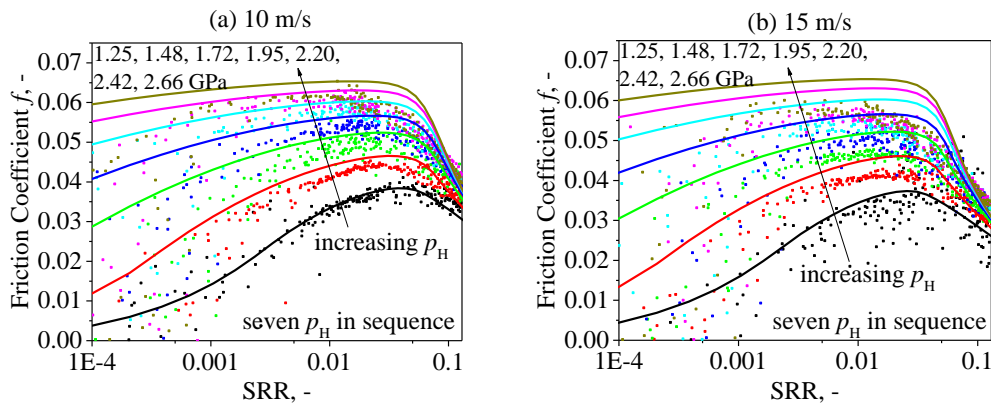


Figure 6-9: Traction curve comparison between simplified traction calculation (solid lines) and twin-disc measurements (dots) for higher speeds at (a) 10 m/s and (b) 15 m/s. (Squalane, $T_0 = 40^\circ\text{C}$, $k_s = 21\text{ W/mK}$)

Fig. 6.9 shows two sets of traction curves at higher entrainment velocities of 10 and 15 m/s. Except for the change of the velocity, the other working parameters are kept the same as the low speed case for Fig. 6.8, Sec. 6.4.1. Agreement can be achieved only for the case at the lowest contact pressure, *i.e.* 1.25 GPa, in Fig. 6.9 (a) and (b). Other than that, the predicted curves are always higher than the measured ones. It can be seen that the difference between the prediction and the measurement is becoming larger with increasing contact pressure and/or with a higher speed. The largest difference occurs at 2.66 GPa and 15 m/s in Fig. 6.9(b) and it is about 15%. There are many possible reasons for the errors. Firstly, oil viscoelasticity may start to be obvious at elevated velocity as the film passes through the contact in a shorter time than before. Secondly, the measured traction curves can be affected by the body temperature of the disc, as during measurements the disc heats up. In Fig. 6.9(a) and (b), it is

remarkable that the traction curve at 2.66 GPa nearly coincides with the one at 2.42 GPa. This phenomenon cannot be seen in Fig. 6.8 for the low speed case of 5 m/s and it cannot be explained by oil viscoelasticity. The effect of solid body temperature could be the main reason and its influence on the maximum friction coefficient is discussed below.

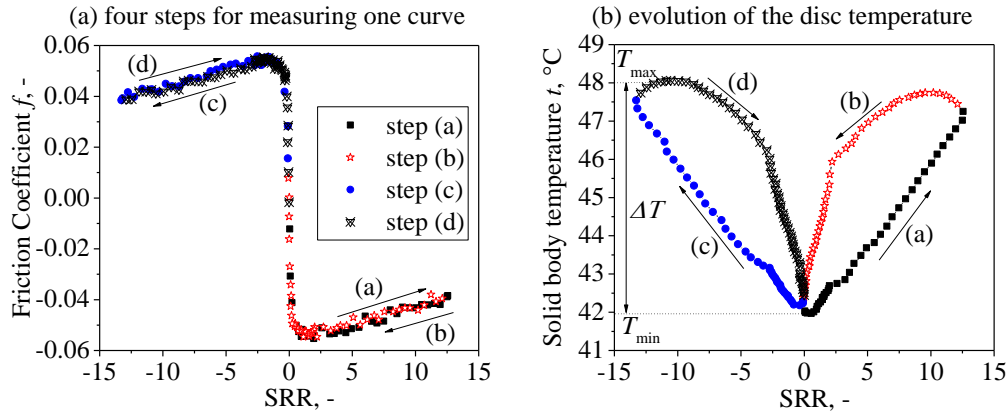


Figure 6-10: The four steps for the measurement of one traction curve (a) and the evolution of the solid body temperature of the disc during this process (b). (Squalane, the supplied oil temperature is well-controlled at $T_0 = 40$ °C, $u_e = 10$ m/s, $p_H = 1.95$ GPa, $t = 7$ mins).

The mass temperature of the disc was recorded by an embedded thermal couple around 1.5 mm beneath the working surface. One curve was measured in 7 minutes with four steps: (a) SRR from 0 to 12.5%; (b) SRR from 12.5% back to 0; (c) SRR from 0 to -12.5%; and (d) SRR from -12.5% to 0. One typical traction curve during these four steps was shown in Fig. 6.10(a). This kind of procedure is widely adopted in traction test, in order to eliminate the influence of the supporting bearings. One traction curve is the average of the absolute values from those four steps. During this process it is unavoidable the disc heats up due to heat generated by shearing the film, see Fig. 6.10(b) for example.

Table 6-2: Solid body temperatures of the disc recorded by a thermal couple for different conditions (the supplied oil is controlled at 40 °C)

p_H , GPa	10 m/s			15 m/s		
	T_{min}	T_{max}	ΔT	T_{min}	T_{max}	ΔT
1.25	40.1	41.5	1.4	38.5	40.5	2.0
1.48	39.7	42.5	2.8	41.5	45.1	3.6
1.72	41.0	45.5	4.5	43.0	49.0	6.0
1.95	42.0	48.0	6.0	46.0	54.5	8.5
2.20	40.9	52.1	11.2	47.8	60.1	12.3
2.42	43.0	58.0	15.0	49.3	67.4	18.1
2.66	45.5	65.0	19.5	52.8	75.3	22.5

Table 6.2 shows the minimum and the maximum mass temperature of the disc for all working conditions at 10 and 15 m/s, as well as the temperature rise during the measurement of each curve. They are notated as T_{min} , T_{max} , and ΔT , respectively, and schematically marked in Fig. 6.10(b). T_{min} represents the body temperature of the disc at the starting point of a new measurement of the curve. T_{max} is the recorded largest temperature of the disc during the measurement of the curve. The temperature rise, ΔT , equals the absolute difference between T_{min} and T_{max} . For the two cases (10 m/s and 15 m/s) at the lowest pressure of 1.25 GPa, the temperature rises ΔT are lower than 2 °C during the measurements and the effect of such a small temperature rise on traction measurements may be

negligible. Correspondingly, the predicted traction curves for 1.25 GPa agree well with the measurements in Fig. 6.9(a) and (b). Except for this low pressure case, it is easy to see from Table 6.2 that the solid body temperature, either T_{\min} or T_{\max} , is higher than the supplied oil temperature, which is well controlled at 40 ± 1 °C. The higher the running speed and pressure, the larger T_{\max} and the temperature rise ΔT . For the most demanding operating condition at 15 m/s and 2.66 GPa, the temperature rise is 22.5 °C. As a result, the measured traction curves are lower than the predicted ones (Fig. 6.9(b)), as mass temperature effect was not considered in the current simulation (Assumption (5)). It can be seen from Fig. 6.11 that the measured maximum friction coefficient decreases with increasing speeds for the same loading condition, while for the simulated results the maximum friction coefficient stays rather constant. Since the film thickness increases with speed in the simulation ($h_{\text{cen}} \propto u_e^{0.67}$, Eq. (6.6)), it can be known that for an extremely high contact pressure the friction coefficient has almost no relation with the film thickness at the plateau regime of the traction curve (Fig. 6.11(b)), which is dominated by LSS and may be affected by the disc mass temperature like the decreasing values with speeds in Fig. 6.11(a). For a relatively lower contact pressure in Fig. 6.11(b), such as 1.25 GPa, the maximum friction coefficient decreases with speeds.

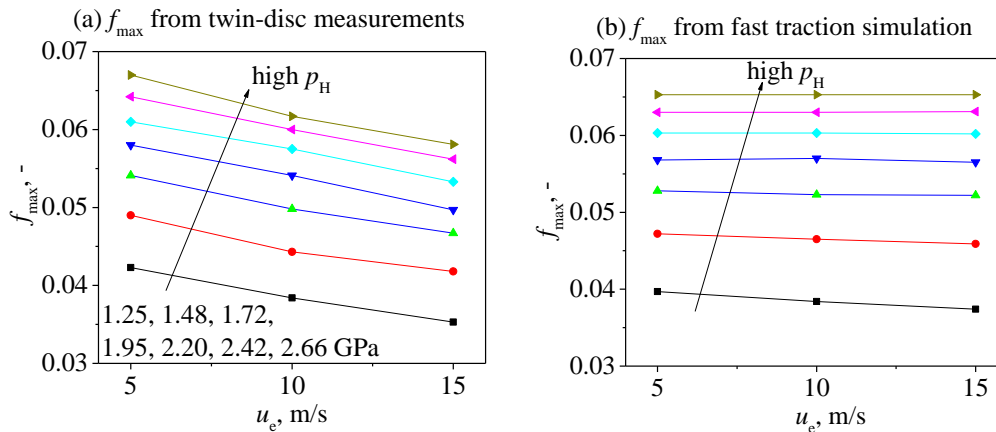


Figure 6-11: The measured (a) and the simulated (b) maximum friction coefficient at three entrainment velocities of 5, 10 and 15 m/s for highly loaded EHL contacts. (Squalane, $T_0 = 40$ °C)

6.4.2.2 Shear stress correction to consider solid body temperature effect

As discussed above, the disc mass temperature affects the MSS and the maximum friction coefficient. For the temperature boundary condition in the current simulation, the solid body temperature is assumed to be equal to the supplied oil temperature, which leads to the differences in comparison with the experimental results at 15 m/s. In the following, the simulated MSS are corrected with the recorded solid body temperatures for each curve and compared again with the measured values at 15 m/s. For this purpose, the decrease rate of the MSS in terms of temperature at high pressures needs to be known.

Traction curve measurements were carried out with squalane at another two lower temperatures of 20 °C and 30 °C. The Hertzian contact pressures were also from 1.25 GPa to 2.66 GPa. The maximum friction coefficients in the curves were changed into the corresponding MSS using Eq. (6.8). After comparing the values of the maximum stress at different temperatures, it is found that the MSS decreases approximately at a rate of 0.5 MPa/K with increasing temperatures regardless of the mean contact pressure. Generally, the rate of 0.5 MPa/K agrees with the measurements from Ndiaye *et al* [2017] and Bader *et al* [2017] for Shell T9 and FVA3 oils, respectively. This value is adopted here for the correction of the MSS from the simplified traction calculations with the mean solid body temperature ($T_{\text{mean}} = (T_{\min} + T_{\max})/2$, Table 6.2). As can be seen in Fig. 6.12, the corrected results are very close to

the measured maximum stresses at different mean contact pressures. The accuracy of the simplified traction prediction can be improved in this way to consider the disc mass temperature.

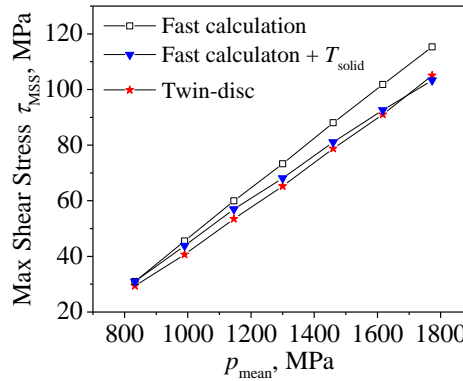


Figure 6-12: Comparison of the maximum shear stress at different pressures among simplified traction calculation (open square), twin disc measurements (star), and the corrected simulation results with the mean solid body temperature of the disc (triangle). (Squalane, $T_0 = 40^\circ\text{C}$, $u_e = 15\text{ m/s}$)

6.5 Possible mechanisms of friction reduction due to solid body temperature effect

When the disc heats up to a higher temperature than the supplied oil temperature, the measured traction would be reduced and becomes smaller than that from prediction. There are two possible mechanisms for the friction reduction regarding this kind of solid body temperature effect. One is that the LSS itself may depend on temperature, even though the MSS/LSS is only modeled as a linear function of pressure in this study (Assumption (6) and Eq. (6.9) in Sec. 6.2.3). The increase in solid body temperature may reduce the LSS itself and hence the maximum friction coefficient decreases as this plateau traction regime is dominated by the LSS. Another possibility is that the LSS is still mainly a function of pressure rather than temperature, as assumed in this study. The reduction of friction coefficient due to the increased solid body temperature can be a purely viscous behavior, that is, the oil viscosity at the highly pressurized zone decreases due to the higher mass temperature and therefore a smaller fraction of the contact zone can reach the LSS. During the process, the local LSS itself does not change as long as the local pressure stays the same. However, at the present point of time, it seems to be impossible to distinguish those two mechanisms. In reality, it can also be possible that the two mechanisms work together for the solid body temperature effect.

For an EHL contact at a low pressure (*e.g.* $p_H < 0.8\text{ GPa}$), the shear stress is relatively small and the LSS usually cannot be reached. The decrease of viscosity caused by mass temperature in the contact zone is the reason of friction reduction, which was analyzed by Liu and Zhang *et al* [2019]. For the high contact pressures used in this study, when SRR is large, the influence of solid body temperature on traction becomes unobvious (*e.g.* in Fig. 6.9 when the SRR is larger than 5%). The shear heating effect dominates the traction behavior at large SRRs and the LSS is hard to be reached due to the decrease in viscosity. Meanwhile, the temperature on the two oil/disc interfaces can be higher than the mass temperature. As a result, the solid body temperature effect is not so obvious at large SRRs.

6.6 Limitation of the method and outlook

The limitations of the simplified traction prediction method mainly come from the assumptions in Sec. 6.2.1. Assumptions (1), (2), and (4) are reasonable for the rapid calculation, while the others can be weakened or removed in the future work. For example, in Assumption (5), the boundary conditions should

be set to the measured mass temperature instead of the supplied oil temperature. Similarly, the EHL film thickness, in Assumption (3), could be predicted more accurately by using the viscosity and the pressure-viscosity coefficient at the solid body temperature [Liu *et al* 2019]. Regarding the LSS in Assumption (6), whether LSS is of temperature dependence and, if so, whether this is important for traction prediction are still questions to be answered. In literature, it is generally agreed that LSS is related to the molecular structure of the fluid and is more sensitive to pressure than temperature. However, the physical nature of the LSS is still unclear (described in Sec. 2.2.3), and the measurement of LSS out of EHL contacts at a large shear stress with well-controlled temperature is not an easy task [Bair and Winer 1992]. This could be the reason why traction machines are widely adopted to characterize the LSS through the measured maximum friction coefficient. There is a problem on choosing an appropriate entrainment speed. The speed should be high enough to enable a full separation of the contacting surfaces without introducing the effect of surface roughness. Note that surface roughness may affect the traction at full film conditions [Guegan *et al* 2016] through its effect on pressure/temperature fluctuation and local viscosity variation. Meanwhile, the speed should not be too high to introduce more heat generation and the resulting solid body temperature effect. Otherwise, the measured maximum friction coefficient and thus the LSS would be lower than the real value, *e.g.* for the 15 m/s cases in Sec. 6.4.2.

In this work, the LSS/MSS equation was derived from a twin-disc machine and then it was used for traction predictions for this specified geometrical configuration. It is important to derive a machine independent LSS equation for a specific lubricant. The future work is to measure traction curves with different contact geometries and roller sizes and then to validate and to improve the built simplified traction model.

Except for the experimental techniques on the LSS, molecular dynamics may shine light on the behavior of thin compressed film under severe shearing, see [Ewen *et al* 2019; Porras-Vazquez *et al* 2018] for example.

6.7 Conclusions

A simplified prediction method has been developed for EHL traction prediction in highly loaded rolling/sliding contacts with consideration of lubricant rheology. The simplified traction calculation method proposed in this work does traction calculation in a simple way without solving the Reynolds equation and the solid deformation equations. The assumptions for the model were described in detail in Sec. 6.2.1. Non-Newtonian effects and thermal effects are considered in the simulation. The 3D temperature fields in the oil and in the contacting solids can be obtained by solving the simplified energy equations. Squalane, a model fluid with measured thermo-physical properties, was adopted in this study. The pressure dependence of MSS was determined from a set of measured traction curves at high contact pressures using a twin-disc machine and expressed by a bilinear MSS equation, Eq. (6.9). Traction measurements were carried out with the twin-disc machine using squalane at three speeds. The simulated traction curves are compared with the measured curves on a semi-log scale, in order to know the traction behavior at small SRRs. The main conclusions are:

(1) At a relatively low entrainment velocity of 5 m/s, using the bilinear MSS equation extracted from the twin disc machine, the predicted traction curves from viscous traction calculation agree with the experimental results over the studied Hertzian pressure ranges from 1.25 GPa to 2.66 GPa. The effect of lubricant viscoelasticity is not obvious on the EHL traction for squalane even at small SRRs.

(2) At a higher speed of 10 or 15 m/s, the measured maximum friction coefficient in traction curves is smaller than the predicted value. The reduced friction is mainly attributed to the mass temperature rise of the disc and the resulting solid body temperature effect. The prediction error can be 15% for the highest pressure of 2.66 GPa at the highest speed of 15 m/s used in this study.

(3) There are two possible mechanisms for the reduced friction caused by the solid body temperature effect. One could be that LSS is a function of temperature and the LSS itself is reduced by the mass temperature of the disc. The other possibility is that the viscosity decreases in the contact zone and less fraction of the area is able to reach the LSS, which stays constant for that pressure. Note that more recently Ndiaye *et al* [2020] shows that the onset of the plateau behavior in traction curves occurs for Hertzian pressure close to the glass transition pressure, corresponding to a very small fraction of lubricants in a “nominal glassy state” within the contact. However, it is unknown whether the LSS is related to the glassy state, because the measured macroscopic friction (LSS) is increasing with pressure even though the pressures are larger than the glass transition pressure [Bair 2019a].

7

Contact Geometry and Scale Effect on the EHL Traction

Plint (IMechE 182(1):300-306,1967) reported a reduced coefficient of friction with increasing roller sizes in EHL traction measurements. In this study, a similar scale effect has been observed when comparing measured traction curves at the same operating conditions between a ball-on-disc rig and a twin-disc machine of different geometrical sizes. This scale effect has been studied numerically for point contacts of different radii of curvature R_x based on thermal EHL simulations. Results show that the reduced friction for large R_x is caused by an increase in film thickness and the enhanced thermal effects. The mechanisms are: (1) heat is hard to conduct across a thicker EHL film due to bad thermal conductivity; (2) shear is mainly localized in the middle film.

The work in this chapter has been published as: Liu, H. C., Zhang, B. B., Bader, N., Venner, C. H., & Poll, G. (2020). Scale and contact geometry effects on friction in thermal EHL: twin-disc versus ball-on-disc. Tribology International, 106694.

DOI: <https://doi.org/10.1016/j.triboint.2020.106694>

7.1 Introduction

The traction in elastohydrodynamically lubricated rolling/sliding contacts has been widely evaluated using traction machines covering a range of pressures, temperatures, speeds and slide-to-roll ratios (SRRs) for lubricants, see for examples [Willermet 1999; Björling *et al* 2013; Zhang *et al* 2017; Ebner *et al* 2018]. Traction machines are typically in a twin-disc or a ball-on-disc configuration with a fixed size/diameter of disc/ball. To date, few traction tests [Plint 1967; Ciulli 2013] have been carried out using discs or balls of different diameters for the same lubricant. In practice, however, EHL lubricated components or machine elements (such as CVT transmissions, gears and rolling element bearings) are different in sizes/diameters, *e.g.* the relative radius of curvature R_x in the entrainment direction. Then, a question arises whether there is a scale effect. If the answer is yes, what is the physical mechanism behind it?

In the literature, there is some experimental evidence showing the existences of scale effects related to the EHL traction. Plint [1967] reported that the maximum coefficient of friction (CoF) is reduced for a larger roller size through measurements of traction curves with three twin-disc machines covering disc diameters from 1 inch to 9 inch at constant velocity, pressure and supplied oil temperature. This implies that a rolling contact with a larger R_x has a lower CoF than that with a smaller radius. Plint correlated this scale effect with the limiting shear stress (LSS) of lubricants, and he thought the LSS is a function of the roller size, as well as the temperature on the plane of shear failure [Plint 1967]. Other experimental evidence of scale effects is found in [Ciulli 2013] and [Martins *et al* 2015]. Ciulli [2013] investigated the effect of contact scale on the EHL traction and film thickness by doing measurements

with a ball-on-disc machine using three balls in different diameters. However, the measurements were carried out at a constant load rather than at a constant Hertzian pressure. This introduced the contact pressure as another independent variable except the ball diameter. Recently, Martins *et al* [2015] showed that through geometrical design the friction loss in gears can decrease 25%, part of which may be contributed by the scale effect reported by Plint.

Scale effects may be important for both practical application and fundamental research. Firstly, in practice, traction curves measured on a specific traction rig over a range of operating parameters (traction mapping) are being used to predict the frictional performance of machine elements of different sizes, *e.g.* for CVT transmissions [Saito and Lewis 2018] and for rolling bearings [Li *et al* 2019]. The accuracy of this approach may be questionable if there is a scale effect. Secondly, the LSS of lubricants is important for the EHL friction prediction of rolling/sliding EHL contacts [Ndiaye *et al* 2017; Bair 2019a; Evans and Johnson 1986b], especially for the maximum CoF in highly-loaded contacts and for the CoF at small SRRs. However, the LSS of a lubricant is hard to measure with independent high-pressure rheometers or chambers [Jacobson 1991; Bair 2019a]. As an alternative method, traction machines have been widely adopted for characterizing the mean LSS in terms of mean contact pressure and temperature by assuming the corresponding maximum shear stress (MSS) extracted from a traction curve being equal to the mean LSS, see [Ndiaye *et al* 2017; Evans and Johnson 1986b; Poll and Wang 2012; Liu, Zhang *et al* 2020b]. However, according to Plint's scale effect, a smaller mean MSS/LSS would be measured if the traction machine used has a larger disc/ball. This kind of uncertainty in the LSS characterization for liquids would bring errors for traction predictions.

Perhaps the first theoretical analysis for the above-mentioned scale effect was given by Johnson and Greenwood [1980]. They predicted a decrease in the maximum CoF with increasing roller size using a derived closed-form expression through thermal analysis for an Eyring fluid. Recently, Liu and Cui *et al* [2012] carried out thermal EHL numerical simulations for line contacts using the Eyring fluid model and studied the scale effect for different equivalent radii R_x using the same set of Dowson-Higginson parameters, namely $U_e = u_e \eta_e / (E' R_x)$, $G = \alpha E'$, $W = w / (E' R_x^2)$. The non-dimensional film thickness h_{cen} / R_x is almost independent of R_x , while the CoF decreases significantly with increasing R_x . Similar results have been shown by Piccigallo [1996] and Zhang and Wang *et al* [2020] in simulations for a line contact. Liu *et al* [2012] further discussed the particular contributions of thermal effects and shear thinning effects on the reduced CoF by doing isothermal non-Newtonian and thermal Newtonian simulations. They found the scale effect to be a purely thermal effect. In their study, the LSS (viscoplastic behavior of a confined fluid at high shear stress [Bair 2019a; Evans and Johnson 1986b]) was not considered. This may only be acceptable for low pressure conditions, where the LSS cannot be reached in most of the contact. The speed u_e varies with R_x in their simulations in order to keep the dimensionless speed parameter U_e constant. This is however not the case when comparing traction curves among different traction rigs, in which conditions the speed u_e is a constant rather than U_e .

In this study, Plint's experimental findings have been confirmed by comparing traction curves measured from a twin-disc machine ($R_x = 30$ mm) and a ball-on-disc machine ($R_x = 10.314$ mm) for a reference fluid at the same supplied oil temperature, mean pressure and speed. The influence of scale effect (ball radius R_x) on the EHL traction is analyzed with a thermal non-Newtonian model for circular contacts at constant speed u_e , pressure and temperature. In both experiments and simulations, a model fluid squalane was used. Squalane is one of the best characterized fluids (*e.g.* thermo-physical properties and rheological fluid models) and has been widely used in EHL studies [Björling *et al* 2013; Liu *et al* 2020a and 2020b; Bair *et al* 2002a and 2002b]. The LSS property of squalane was considered in simulations for

a better understanding of scale effects on the maximum CoF in a traction curve. This work explains why two traction machines of different geometrical sizes give different traction curves even under comparable conditions. Since the maximum CoF in a traction curve is of practical importance for the understanding of the LSS of fluids, suggestions are given towards isothermal MSS (or mean LSS) measurements accounting for the studied scale effect.

7.2 Experimental and numerical methods

7.2.1 Experimental evidence of the scale effect

Table 7-1: Geometrical configuration and operating conditions of the two traction machines (the contact pressure, supplied oil temperature and speed are kept the same for the two machines; steel/steel contacts; x along the direction of motion and y in the transverse direction; r_{y2} is crown radius)

Items and parameters	TD machine	WAM machine
Configuration	cylindrical disc – crowned disc	Ball-disc
Geometry and Roughness		
radius r_{x1} , mm	60	10.314
radius r_{y1} , mm	∞	10.314
radius r_{x2} , mm	60	∞
radius r_{y2} , mm	50 crown radius	∞
reduced radius R_x , mm	30	10.314
combined roughness R_q , nm	224	43
Operating Conditions		
lubricant	squalane	squalane
oil temperature T_0 , °C	40	40
speed u_e , m/s	5, 10	5, 10
load w , N	4300	300
SRR, %	0 to 12%	0 to 50%
Hertzian Contact		
Hertzian pressure p_H , GPa	1.945	1.945
contact half axis b/a , mm	0.859/1.229	0.272/0.272
Ellipticity ratio $k_e = a/b$	1.43	1.0

Table 7-2: Properties of AISI 52100 steel and squalane liquid

Property	Value
AISI 52100 Steel	
Young's modulus E	210 GPa
Poisson ratio	0.3 (–)
Heat capacity $c_{1,2}$	470 J/(kgK)
Thermal conductivity, $k_s = k_1 = k_2$	21 W/(mK)
Density ρ	7850 kg/m ³
Lubricant Squalane	
Viscosity η at 40 °C, $p = 0$	0.0156 Pas
Density ρ at 40 °C, $p = 0$	795.8 kg/m ³
Viscosity-pressure coefficient α at 40 °C	18.0 GPa ⁻¹
Thermal conductivity k_{oil} at 40 °C, $p = 0$	0.1282 W/(mK)
Heat capacity c at 40 °C, $p = 0$	1960.3 J/(kgK)

A traction curve comparison has been carried out between two test rigs with different R_x for the reference fluid squalane. The first one is a ball-on-disc machine (WAM, Wedeven Associates Inc) at

Lulea University of Technology with R_x of 10.314 mm, and traction curves have been measured by Björling *et al* [2013]. The second traction rig is a twin-disc machine with R_x of 30 mm at Hannover University (TD, IMKT Institute). The geometrical configurations of these two machines are schematically shown in Fig. 2.4, and the operating parameters are listed and compared in Table 7.1. The detailed descriptions of the two test rigs and measurement procedures have been introduced in Sec. 2.1.3.1, also refer to Björling *et al* [2013] for the WAM and Bader [2018] for the TD. The specimens are all made of 100Cr6 (AISI 52100) bearing steel. The properties of the steel and squalane are listed in Table 7.2. All traction curves were measured at full film conditions and the lowest lambda ratio λ_{film} is 2.4. Note that λ_{film} is the ratio of the predicted oil central film thickness h_{cen} with smooth surfaces using Hamrock-Dowson equation [Hamrock and Dowson 1981] to the composite surface roughness R_q (Table 7.1) of the contacting pairs. The influence of surface roughness on the traction results is expected to be negligible. The reasons are discussed later.

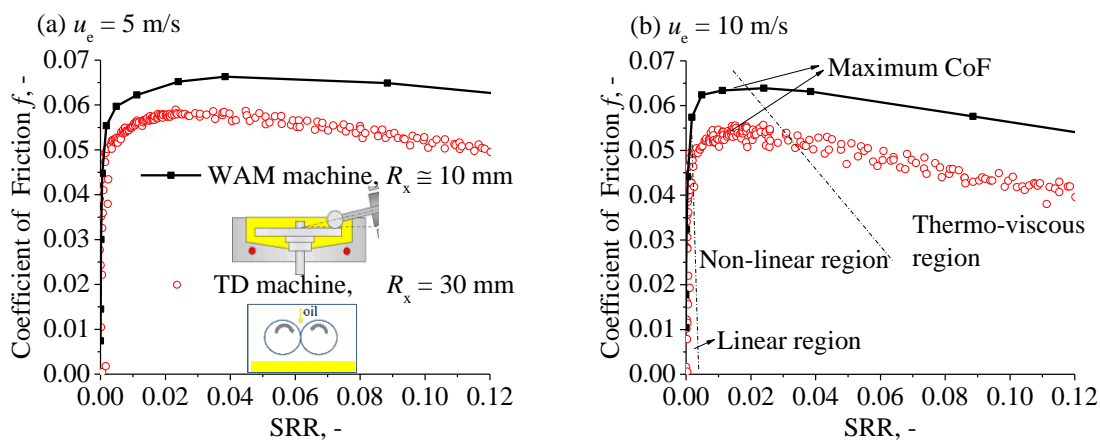


Figure 7-1 Traction curves measured with two test rigs in different geometrical configurations at constant mean contact pressure, speed and supplied oil temperature, (a) $u_e = 5$ m/s; (b) $u_e = 10$ m/s. (open circle: TD twin disc results, $k_e = 1.43$, $R_x = 30$ mm; solid square: WAM ball-on-disc results, $k_e = 1.0$, $R_x = 10.314$ mm; with a reference liquid squalane, $p_H = 1.945$ GPa, $T_0 = 40$ °C; at full film lubrication)

The scale effect can be seen in Fig. 7.1 by comparing traction curves measured using the two traction machines at comparable conditions, *i.e.* at the same Hertzian pressure ($p_H = 1.945$ GPa), entrainment velocity ($u_e = 5, 10$ m/s) and supplied oil temperature ($T_0 = 40$ °C). The maximum CoF measured with the TD ($R_x = 30$ mm) is smaller than that with the WAM machine ($R_x = 10.314$ mm), which agrees with Plint's finding that the maximum CoF is reduced for a larger R_x . Indeed, except for the linear traction regime at small SRRs, the CoF measured with the TD is always smaller than that with the WAM. It is interesting and important to know why two traction machines give different traction results at comparable conditions for the same fluid.

From the characteristics of measured traction curves in Fig. 7.1, it may be known that the experiments were carried out at full-film EHL conditions and the effect of surface roughness can be negligible. Firstly, the friction coefficient in a traction curve decreases with increasing entrainment speed u_e and SRR for full-film EHL contact when the influence of surface roughness is not obvious, because the enhanced thermal effects reduce the lubricant viscosity. These two characteristics can be seen in Fig. 7.1 when comparing traction curves at the two speeds or looking at the thermal-viscous regime in a measured traction curve (for example marked in Fig. 7.1(b), including the maximum CoF). If the effect of surface roughness is pronounced or even it is in mixed lubrication, the friction coefficient would increase for a higher u_e and/or for a higher SRR, because more solid asperities are into contact with the

enhanced thermal effects. Secondly, the surface roughness of the twin-disc specimen is larger than that of the ball-disc machine. If it was not full-film and asperity contact of surface roughness is important (*i.e.* mixed lubrication and/or micro-EHL), the twin-disc machine with a smaller λ_{film} should give a larger friction coefficient. This is not the case in the measured traction curves in Fig. 7.1. Thirdly, in the experiments, the calculated lowest λ_{film} is 2.4. In reality, the λ_{film} must be even larger due to the deformation of roughness peaks in the high pressure Hertzian contact zone. Therefore, surface roughness is not considered in the study of scale effects.

As is known, the CoF in the non-linear and the thermo-viscous traction regimes of a traction curve is determined by both non-Newtonian behavior of the confined fluid under shear and the resulting thermal/heating effects [Evans and Johnson 1986b; Bair 2019a; Spikes and Zhang 2014]. From Table 7.1, it can be seen that the difference between the two traction rigs lies in contact geometrical parameters, *i.e.* the reduced radius R_x , the Hertzian contact size $A_c = \pi ab$ and the ellipticity ratio k_e . Because the difference in k_e is not significant between the two test rigs (1.0 and 1.43 as shown in Table 7.1), this study focuses on the effect of the first two factors, *i.e.* R_x and the Hertzian contact area A_c , on the EHL traction by doing thermal non-Newtonian EHL simulations for circular contacts. The model is briefly introduced in the following section.

7.2.2 Theoretical EHL model

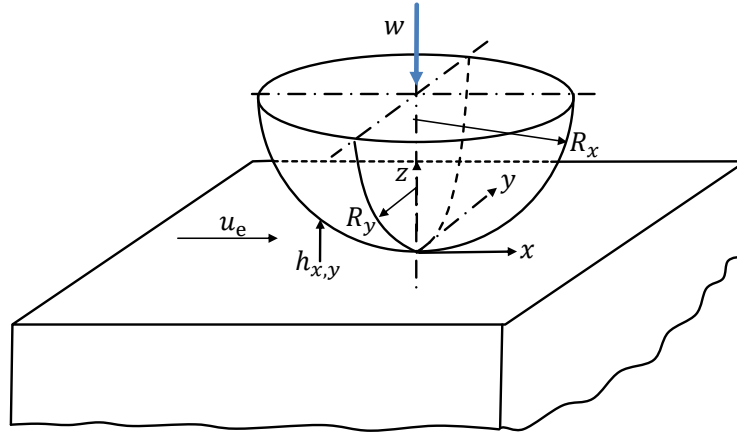


Figure 7-2: Schematic representation of a rolling/sliding elliptical EHL contact formed by an ellipsoid with reduced radii R_x and R_y and an elastic half-space. ($R_x = R_y$ for circular contacts in this study)

A thermal non-Newtonian EHL solution, which has been introduced in Sec. 2.4.4 and used in the previous work of the author, *e.g.* influence of solid and oil thermal conductivity on the EHL traction in [Liu *et al* 2020a] and the solid body temperature effect in [Liu *et al* 2019], was adopted in this study. Fig. 7.2 schematically shows an equivalent point contact model. In order to simulate the operating conditions of traction machines regarding scale effects, numerical simulations have been performed for circular contacts of three radii ($R_x = R_y = 10 \text{ mm}, 30 \text{ mm}, 100 \text{ mm}$), while the mean contact pressure p_{mean} , entrainment speed u_e and supplied oil temperature T_0 are all kept as constants, *i.e.*, $u_e = 1.0 \text{ m/s}$, $p_H = 1.5 p_{\text{mean}} = 1.25 \text{ GPa}$, $T_0 = 40 \text{ }^\circ\text{C}$. The operating parameters used in the simulations for the three values of R_x are listed in Table 7.3. Note that in this study u_e rather than $U_e = u_e \eta_e / (E' R_x)$ is a constant accounting for the operating settings in traction experiments, and U_e is inversely proportional to R_x . This is different from the simulations by Liu and Cui *et al* [2012].

Table 7-3: Operating conditions for the numerical study of scale effects in circular contacts at different R_x ($u_e = 1.0$ m/s, $p_H = 1.25$ GPa, $T_0 = 40$ °C, $k_e = 1.0$; $G = 4153.85$, $W = 3.28 \times 10^{-6}$)

Case	$R_x = R_y$, mm	Load w , N	Hertz half axis a , mm	Contact area A_c , mm ²	$h_{cen} - HD$, nm
1	10	76	0.170	0.091	118
2	30	683	0.511	0.819	170
3	100	7590	1.702	9.104	253

The EHL model and numerical methods are briefly introduced here. Two-dimensional non-Newtonian effects are taken into account by solving a generalized Reynolds equation with multigrid techniques for the film thickness and the pressure distribution. Thermal effects and temperature fields were evaluated by solving energy equations for both lubricant and solids with a column-by-column scanning approach. The mesh size, computational domains are the same as that in [Liu *et al* 2020a]. Thermo-physical properties and fluid models of squalane refer to Bair and coworkers, and they are tabulated in Table 2.6. The low-shear viscosity was described by a free-volume based equation (*i.e.* the improved Yasutomi correlation, see Sec. 2.2.6). Shear thinning was modelled by a power-law Carreau equation and the LSS was assumed to be a linear function of pressure, *i.e.*

$$\tau_{LSS} = \Lambda p \quad (7.1)$$

where τ_{LSS} is the LSS and Λ is the pressure-LSS coefficient. For squalane, $\Lambda = 0.075$ was extracted from traction measurements [Bair *et al* 2002a].

7.3 Results and discussion

7.3.1 Isothermal results

It is hard to measure an ‘‘isothermal’’ traction curve in experiments; as a contrast, isothermal conditions can be achieved easily in numerical simulations by ‘‘turning off’’ thermal calculation sub-functions. In this section, isothermal traction computations have been carried out based on Newtonian and Carreau shear-thinning models, respectively. For both cases, the local shear stress in the computational domain is limited by the LSS in Eq. (7.1), *i.e.*

$$\begin{aligned} \tau_{x,y} &= \min\{\dot{\gamma}\eta^*(p), \tau_{LSS}(p)\} \\ &\approx \min\{(\Delta u/h_{cen})\eta^*(p), \tau_{LSS}(p)\} \end{aligned} \quad (7.2)$$

where $\tau_{x,y}$ is the local shear stress in the x - and y - directions respectively, η^* the generalized Newtonian viscosity or the high-shear viscosity. For isothermal calculations, the shear rate $\dot{\gamma}$ may be expressed as the ratio of the speed difference Δu of the two surfaces to the central film thickness h_{cen} , *i.e.* $\Delta u/h_{cen}$. When there is a large temperature gradient across the thin film, shear may be localized mainly in the middle film and $\dot{\gamma}$ cannot be calculated by $\Delta u/h_{cen}$, see Fig. 7.9 and Sec. 7.3.2.

Since the EHL film thickness is mainly determined by inlet oil properties (*i.e.* viscosity and piezo-viscous behavior at inlet pressures) and operating parameters (*e.g.* speed, load, oil volume/starvation), h_{cen} could be assumed to be a constant as a function of SRR for a certain R_x in isothermal simulations. Fig. 7.3(a) compares the simulated traction curves for the three R_x listed in Table 7.3. In the beginning, the CoF in each traction curve increases linearly with SRR (Fig. 7.3(a)) because of the increase in sliding velocity $\Delta u = u_e \cdot \text{SRR}$ and thus the increase in shear rate $\dot{\gamma} = \Delta u/h_{cen}$, as well as for the local shear stress $\tau = \dot{\gamma}\eta^*(p)$. Afterwards, the rate of increase is reduced as the LSS is reached in some portions of the contact. From the semi-log plot in Fig. 7.3(b), it can be seen that the larger the R_x , the smaller the CoF in this non-linear region. Finally, the three traction curves level out to almost the

same maximum CoF independent of R_x . Note that the maximum CoF in a traction curve is mainly determined by the LSS property of the lubricant and in Fig. 7.3 it is about 0.07, which is smaller than the LSS-pressure coefficient of $\Lambda = 0.075$ in the fluid model, see Eq. (7.1). The reason could be that the Hertzian pressure 1.25 GPa here is not high enough so that the LSS has not been reached in some portions of the contact [Liu *et al* 2020b]. Note that for non-conformal contacts, the Hertzian pressure is typically in a range from 0.5 GPa to 4.0 GPa. 1.25 GPa is already a high pressure; however, it is still relatively low for the extraction of the LSS property of fluid in an EHL model contact through traction measurements. For the LSS modeling of fluid in terms of pressure, a Hertzian pressure ranging from 1.25 GPa to 2.66 GPa was used by the current authors in [Liu *et al* 2020b] and a range from 0.75 GPa to 3.0 GPa was used by Ndiaye *et al* [Ndiaye *et al* 2017].

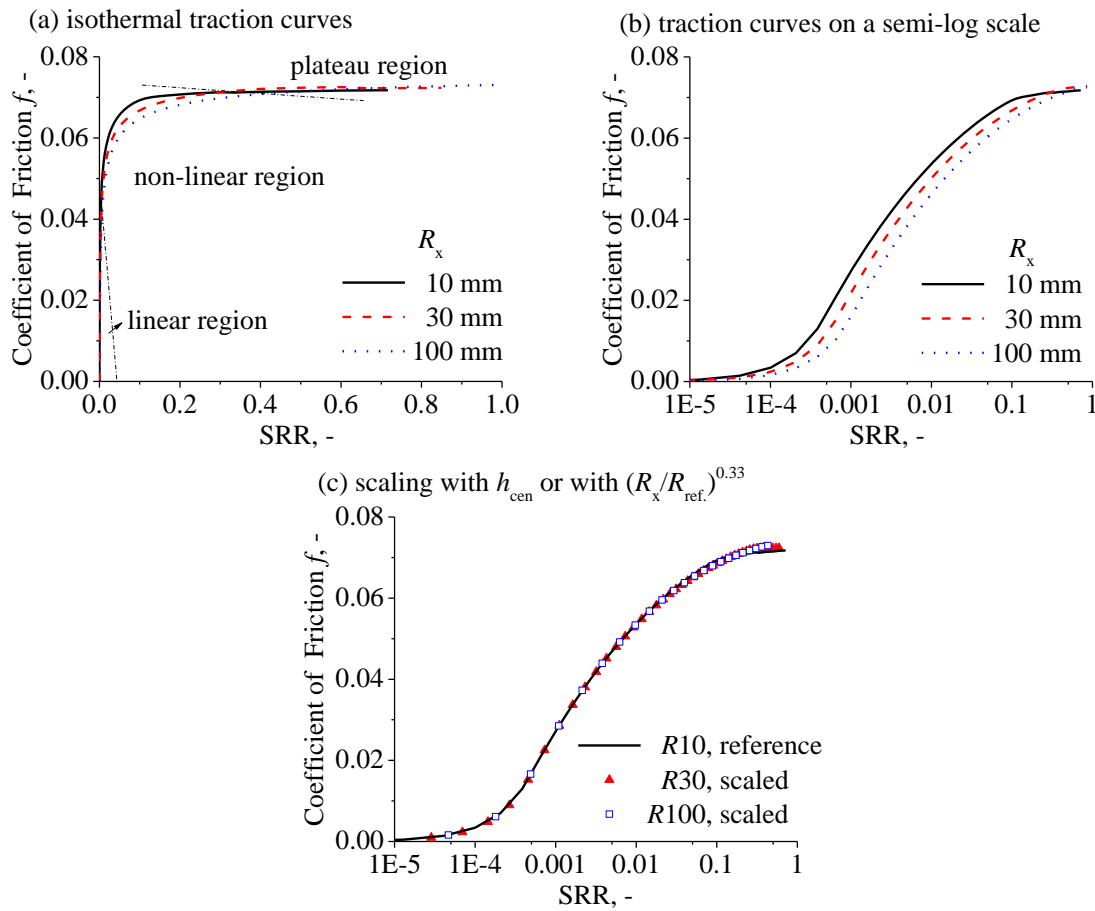


Figure 7-3: Isothermal traction curves for three ball radii R_x calculated from Newtonian fluid model with a limiting shear stress at the same speed, mean contact pressure and supplied oil temperature, (a) isothermal traction curves; (b) traction results on a semi-log plot; (c) scaling with film thickness h_{cen} or with $(R_x/R_{ref})^{0.33}$. (circular contact; no thermal effects; squalane; parameters see Table 7.3)

Through Fig. 7.3, the differences in CoF can only be seen in the non-linear traction region for isothermal calculations and this cannot explain the scale effects in the experimental results in Fig. 7.1, *e.g.* the reduced maximum CoF. Refer to Eq. (7.2), the reduced CoF in the non-linear region of Fig. 7.3(b) for different R_x should be related to the differences in the central film thickness h_{cen} and thus in the shear rate. Because the other parameters are the same for the studied three cases, such as the speed u_e is identical and there should be no obvious difference in viscosity $\eta^*(p)$ owing to the near Hertzian pressure distribution. This suggests that the three traction curves for different R_x in Fig. 7.3(b) could be

scaled into one curve with h_{cen} . This is confirmed in Fig. 7.3(c). The scaling parameter can also be expressed as $(R_x/R_{\text{ref}})^{0.33}$, because h_{cen} is approximately proportional to $R_x^{0.33}$ for point contacts according to empirical EHL film thickness equations, *e.g.* Hamrock-Dowson equation [1977], in which $h_{\text{cen}}/R_x \propto U_e^{0.67}$ and the influence of load on hard EHL film thickness is not obvious.

Fig. 7.4(a) shows the isothermal traction curves calculated with the Carreau shear thinning model and the linear LSS fluid model in Eq. (7.1). The results with shear thinning here are close to the Newtonian results in Fig. 7.3 and the traction curves at different R_x can also be scaled into one curve using h_{cen} as the scaling parameter, which means that this isothermal non-Newtonian simulation also failed to predict the observed scale effects in experiments. As EHL traction is influenced by both non-Newtonian and thermal effects, this implies that the origin of the observed scale effects is thermal, and thermal traction results are shown in the next section.

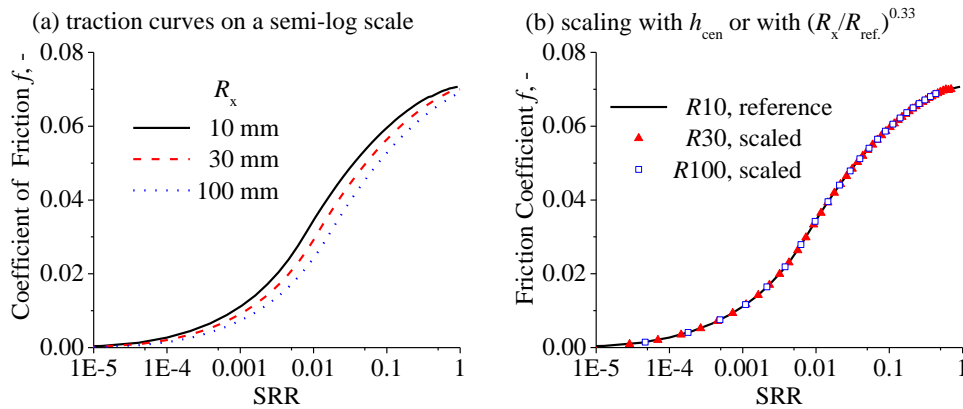


Figure 7-4: Isothermal traction curves for three ball radii R_x calculated from non-Newtonian shear thinning model with a limiting shear stress at constant speed, mean contact pressure and supplied oil temperature, (a) isothermal traction curves on a semi-log plot; (b) scaling with film thickness h_{cen} or with $(R_x/R_{\text{ref}})^{0.33}$. (circular contact; no thermal effects; Carreau shear thinning model; squalane, parameters see Table 7.3)

7.3.2 Thermal results

Fig. 7.5(a) shows the simulation results for the three values of R_x when thermal effects are considered in circular contacts. The operating conditions and settings are exactly the same as the last section; also see Table 7.3. Over almost all SRRs, the CoF follows: $f_{R_x=100} < f_{R_x=30} < f_{R_x=10}$, which qualitatively agrees with the experimental results from the two traction machines in Fig. 7.1. The maximum CoF decreases with increasing R_x and this trend agrees well with Plint's experimental findings on the scale effects. By comparing traction curves between the thermal results in Fig. 7.5(a) and the isothermal results in Fig. 7.3(a), it can be seen that thermal effect is crucial for understanding the scale effects. The maximum temperature in the film as a function of SRR for the three ball diameters is shown in Fig. 7.5(b), and for a certain SRR it is: $(\bar{T}_{\text{max}})_{R_x=100} > (\bar{T}_{\text{max}})_{R_x=30} > (\bar{T}_{\text{max}})_{R_x=10}$. The higher film temperature at a larger R_x reduces the oil viscosity and thus reduces the CoF. The reduced maximum CoF with larger roller size in Plint's traction measurements could be explained by thermal effects. As is shown in Fig. 7.5(c), the traction curves at different R_x in Fig. 7.5(a) from thermal simulations cannot be scaled into a master curve using h_{cen} or using $(R_x/R_{\text{ref}})^{0.33}$ as the scaling parameter except for the isothermal traction regime when $\text{SRR} < 0.005$.

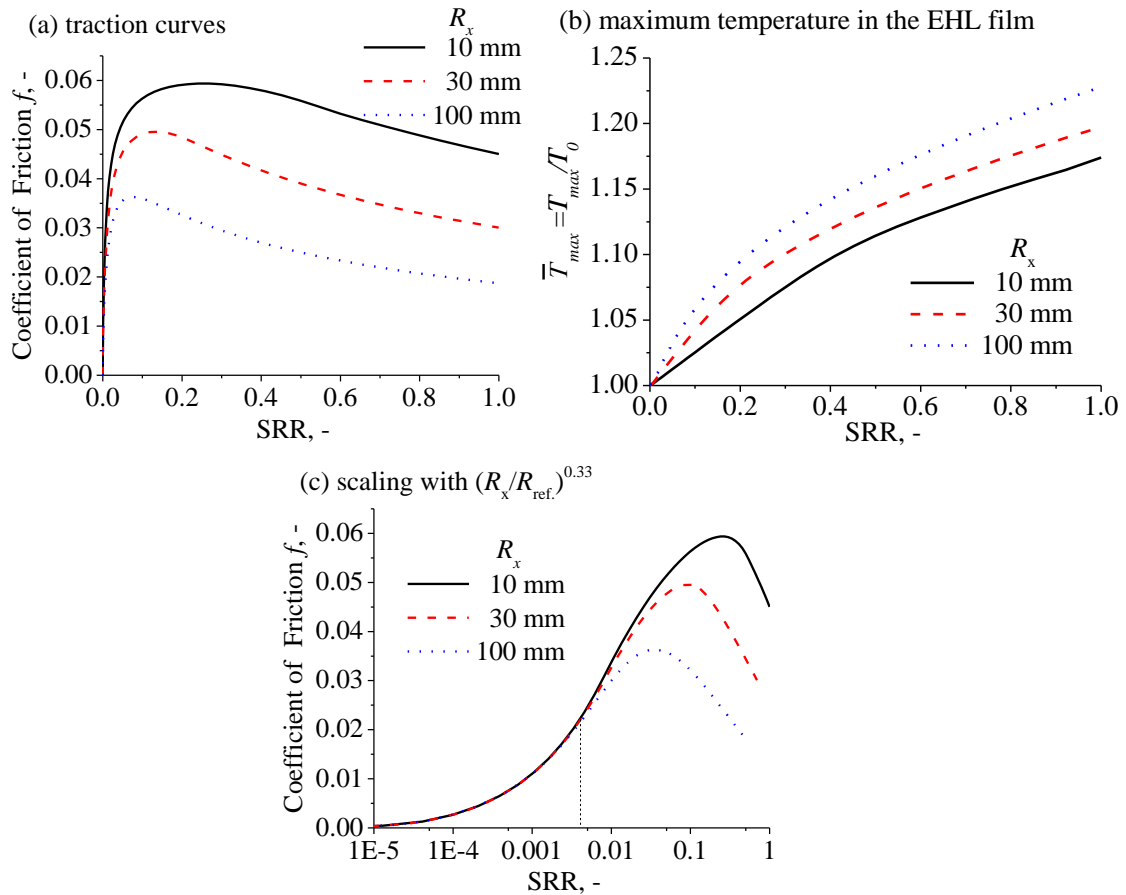


Figure 7-5: Comparison of calculated traction curves at three ball radii R_x for a shear thinning fluid with a limiting shear stress and thermal effects at the same speed, mean contact pressure, and supplied oil temperature, (a) traction curves considering thermal effects; (b) the maximum temperature in the EHL film with SRR; (c) scaling with $(R_x/R_{ref})^{0.33}$. (circular contact; squalane, see Table 7.3)

An unanswered question is why the temperature rise is larger for a large R_x (e.g. in Fig. 7.5(b)) and why the maximum CoF is reduced, e.g. see Fig. 7.5(a) theoretically and Fig. 7.1 experimentally. The difference in R_x leads to differences in the nominal contact area A_c , load w and central film thickness h_{cen} in order to keep a constant mean Hertzian pressure. On one side, it can be seen from Table 7.3 that with an increase in R_x , all the above parameters (i.e. A_c , w and h_{cen}) are getting larger. Correspondingly, frictional power ($= fw\Delta u$, in W) and heat generation by shearing the film may be larger because the load w is an order of magnitude larger for a larger R_x (see Table 7.3). On the other side, a larger ball or R_x shows a larger contact area A_c , which helps to conduct the generated heat into the solids. From this point, it is still unclear why a higher maximum temperature is observed for a larger R_x . Indeed, the EHL film is not an isolated system and the flash (maximum) temperature in the film is a balancing result of heat generation and heat removal for the whole EHL system, including the two contacting solids and the thin oil film. The temperature rise in the EHL film is influenced by operating conditions and the properties of the whole system, such as rolling and sliding speeds, film thickness h_{cen} [Bair 2020], half-contact width a , thermal diffusivity of the lubricant and the solids (see Chapter 5). In this system, heat is mainly generated by viscous shear of the film because compressive heating may be negligible for sliding/rolling EHL contacts. Heat conduction across the thin EHL film dominates the heat transfer, because the diffusion time by conduction in the z -direction (Eq. (7.3)) is about two orders-of-magnitude smaller than the advection time in the x -direction (Eq. (7.4)). The characteristic time of the heat

conduction to the oil/solid interface can be expressed by (assuming equal heat partition from the mid-film)

$$t_{\text{oil},z\text{-conduction}} = \frac{(h_{\text{cen}}/2)^2}{k/(\rho c)} = \frac{h_{\text{cen}}^2}{4\chi_{\text{oil}}} \quad (7.3)$$

where the lubricant thermal diffusivity $\chi_{\text{oil}} = k/(\rho c)$ is $8.22 \times 10^{-8} \text{ m}^2/\text{s}$ for squalane at ambient pressure, and ρ , c and k are the lubricant density, heat capacity and thermal conductivity. As h_{cen} is typically $\approx 10^{-7} \text{ m}$ in an EHL contact (also see Table 7.3), the diffusion time $t_{\text{oil},z\text{-conduction}} \approx 10^{-5} \sim 10^{-6} \text{ s}$. The advection time in the x -direction is

$$t_{\text{oil},x\text{-convection}} = \frac{2a}{u_e} \quad (7.4)$$

It is generally 10^{-3} s , as $u_e = 1 \text{ m/s}$. The ratio of Eq. (7.3) and Eq. (7.4), the Graetz number [Raisin and Fillot *et al* 2015], is $10^{-2} \sim 10^{-3}$. As it is much smaller than unity, heat conduction across the film to the solid-oil interfaces is the main mechanism for heat diffusion. However, oil is a bad thermal conductor, because the oil thermal conductivity (about 0.13 W/mK at ambient pressure) is at least one hundred time smaller than that of steel (*e.g.* 21 W/mK for 52100 steel). Eq. (7.3) implies that a thicker film slows down thermal diffusion across the film. Since a larger R_x gives a thicker film thickness h_{cen} , the generated heat is hard to conduct to the oil/solid interfaces. Hence, a higher maximum temperature is shown in the film for a larger R_x in Fig. 7.5(b). Afterwards, the heat is dissipated in the two solids through material convection and heat conduction into depth. The heat conduction in the x -direction is usually negligible, except for high SRR and low speed conditions (*i.e.* at a low Peclet number and close to stationary heat source problems). The Peclet number Pe represents the ratio of convected heat by motion to the diffused heat through conduction in the x -direction, and it may be written as

$$Pe = \frac{2au_s\rho_s c_s}{k_s} = \frac{2au_s}{\chi_{\text{solid}}}, \quad s = 1,2 \text{ (surface 1 or 2)} \quad (7.5)$$

where the thermal diffusivity of solids $\chi_{\text{solid}} = k_s/(\rho_s c_s)$ is $5.69 \times 10^{-6} \text{ m}^2/\text{s}$ for AISI 52100 steel. For $a \approx 10^{-4} \sim 10^{-3} \text{ m}$ in Table 7.3 and $u_s = 1 \text{ m/s}$ in this study or other typical velocity values, $Pe \approx 10^2 \sim 10^3$, which is larger than unity. At such a high Peclet number the boundary conditions for the EHL film can refer to Carslaw and Jaeger's temperature equation for moving surfaces [Carslaw and Jaeger 1959], which work equally to the solid energy equations here. The upper surface boundary temperature for a line contact is

$$T(x, 0) = T_0 + \frac{1}{\sqrt{\pi u_s \rho_s c_s k_s}} \int_{-\infty}^x q_f \frac{1}{\sqrt{x-x'}} dx', \quad (7.6)$$

$$q_f = k_{\text{oil}} \left[\frac{\partial T}{\partial z} \right]_{z=0}$$

in which x' is the dummy variable for x . By normalizing the above equation into a new coordinate with respect to half of the Hertzian width a and assuming the local heat flux density q_f (in W/m^2) being roughly the same for different R_x in the dimensionless coordinate, Cheng [1965] pointed out that the surface temperature rise is proportional to \sqrt{a} . A larger R_x gives a higher surface temperature. This can be seen in Fig. 7.6 by comparing the temperature fields for different R_x at SRR = 10% and at constant speed and mean contact pressure. The oil/solid boundary temperature, the mid-film temperature and the

temperature gradient across the film are higher for a larger R_x . A similar result has been shown in the numerical simulation of Liu *et al* [2012].

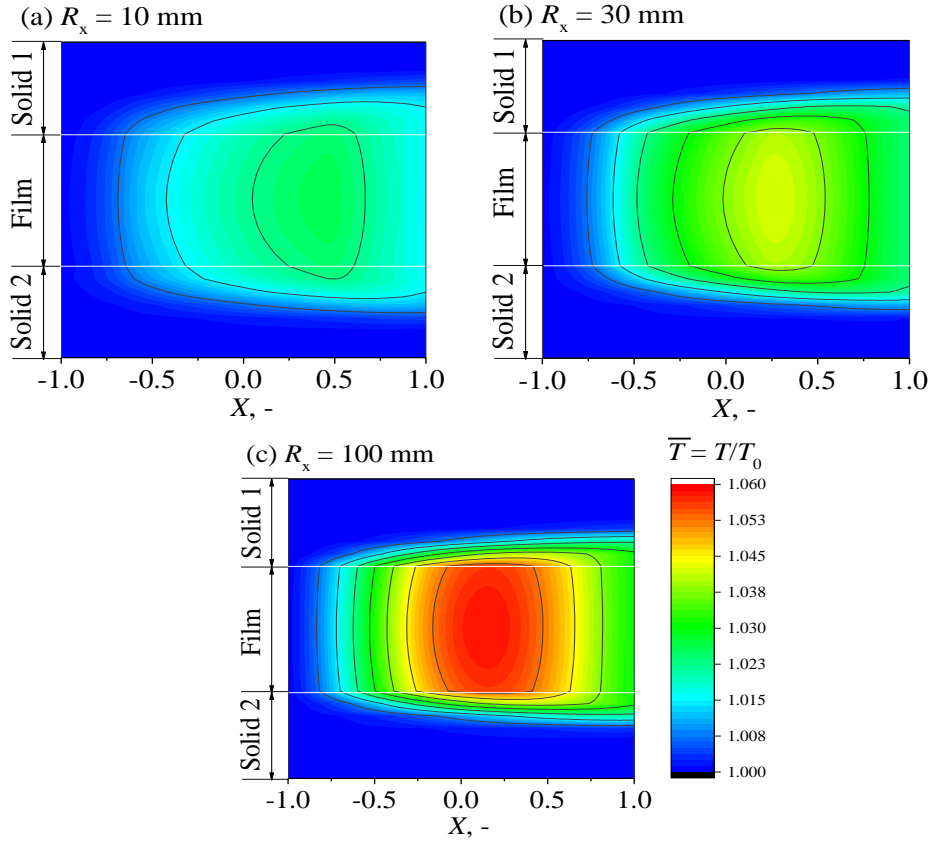


Figure 7-6: Temperature fields in the EHL film and the contacting solids for three ball radii R_x at constant speed, SRR, mean contact pressure and supplied oil temperature. (a) $R_x = 10$ mm; (b) $R_x = 30$ mm; (c) $R_x = 100$ mm ($\bar{T} = T/T_0$, the operating conditions are the same as that in Fig. 7.3, *i.e.* squalane, SRR = 10%, $u_e = 1.0$ m/s, $p_H = 1.25$ GPa, $T_0 = 40$ °C, $k_e = 1$). All figures share the same color scale in Fig. 7.6(c).

Fig. 7.7 calculates the variations of CoF f , temperature rise in the film ΔT and film thickness h_{cen} as a function of R_x at a fixed SRR of 10%. The CoF decreases with an increase in R_x , while h_{cen} and ΔT increase. One may be confused about the temperature rise in the film for a larger R_x , because of the reduced friction coefficient and the reduced shear rate if it were calculated by

$$\dot{\gamma} = \Delta u / h_{cen} \quad (7.7)$$

However, it is important to point out that the above equation cannot be used to calculate the shear rate for an inhomogeneous EHL film where shear localization could occur due to temperature gradient across the film and/or non-Newtonian (*e.g.* LSS) effects. Under such conditions, the shear rate should be determined by Eq. (7.8) rather than Eq. (7.7).

$$\dot{\gamma} = \frac{\partial u}{\partial z} \quad (7.8)$$

Based on Eq. (7.8), Fig. 7.8 shows the calculated velocity profile of the EHL film in the z -direction for two R_x being equal to 10 mm and 100 mm, respectively. The other parameters are kept the same as that for Fig. 7.7. It can be seen that the smaller R_x case gives a linear velocity profile in a corresponding

relatively thin film, while the larger R_x case shows a localized shear in the middle of the relatively thick EHL film. This kind of inhomogeneous shear results in a higher temperature rise and a smaller CoF for the large R_x in Fig. 7.7. Note that the results based on thermal Newtonian simulation show similar trend as the thermal non-Newtonian ones in Fig. 7.7 and Fig. 7.8 and therefore the thermal Newtonian results are not shown in this short communication. It means the studied scale effects can also be covered with a thermal Newtonian model, but the CoF is unrealistic ranging from 0.27 to 0.064 for the same operating parameters used in Fig. 7.7.

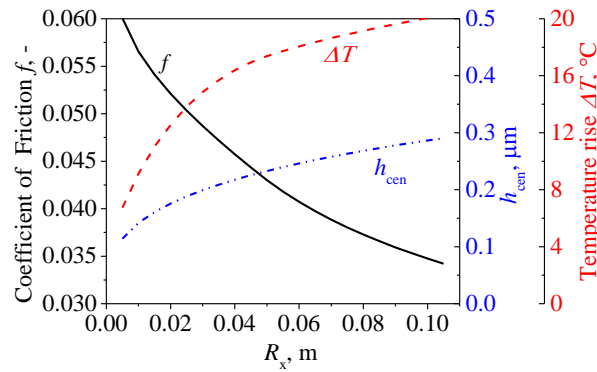


Figure 7-7: Friction coefficient, central film thickness and temperature rise as a function of relative radius of curvature R_x for circular contacts at constant speed, mean contact pressure and supplied oil temperature. (squalane, SRR = 10%, $u_e = 1.0$ m/s, $p_H = 1.25$ GPa, $T_0 = 40$ °C, $k_e = 1$)

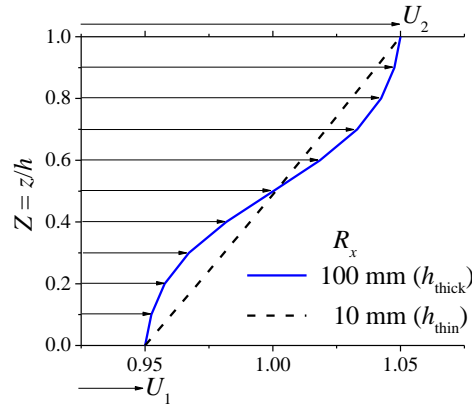


Figure 7-8: Calculated velocity profile of the EHL film in the z -direction for two radius of curvature R_x of circular contacts at constant speed, mean contact pressure and supplied oil temperature. (squalane, SRR = 10%, $u_e = 1.0$ m/s, $p_H = 1.25$ GPa, $T_0 = 40$ °C, $k_e = 1$)

From the above analysis, it could be concluded that the reduced maximum CoF in scale effects is a result of thermal effects induced by a thicker EHL film thickness with longer thermal diffusion time for a large roller diameter and the thermal effect is enhanced by shear localization in the middle of the EHL film. These are schematically shown in Fig. 7.9. Through the studied scale effect, it has been revealed that the maximum CoF and the corresponding mean LSS/MSS may be underestimated when they were measured with a traction machine in large R_x . This could give an explanation to the differences on the reported mean LSS or the maximum CoF measured by different traction machines (see for example: Fig. 5.2.8 in [Bader 2018] for Santotrac 50). In practice, in order to extract the LSS property of fluid according to the measured maximum CoF in traction curves, *e.g.* in [Ndiaye and Martinie

et al 2017; Poll and Wang 2012; Liu and Zhang *et al* 2020b; Lohner and Michaelis *et al* 2016; Zhang and Spikes 2020], it would be better to use a traction rig in a small R_x and to do the measurements under a thin film, for example at a low speed and a small surface roughness. It should be noted that the studied scale effect is for EHL lubrication regime in which heat conduction across the film is the main mechanism for heat removal; whereas for hydrodynamic lubrication (HL) heat convection in the direction of velocity is important. Therefore, the studied scale effect and thermal analysis cannot be directly applied to the HL regime.

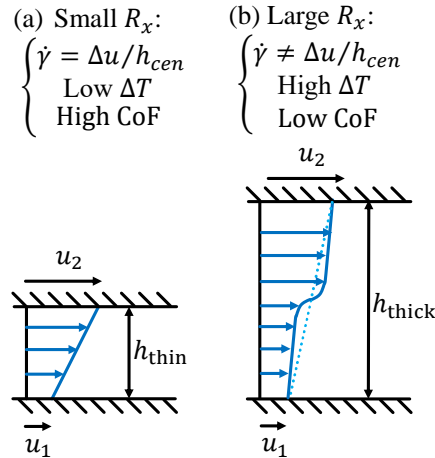


Figure 7-9: Schematic representation of the film and velocity profile for the studied scale effect of (a) a small R_x and (b) a large R_x . Thermal effects are enhanced and the CoF is reduced for a larger R_x due to thicker film thickness for heat conduction and the localized shear in the middle film.

7.3.3 Comparison between experiments and simulations

Fig. 7.10 compares the traction curves between the experimental results in Fig. 7.1 and the simulation results for the two test rigs in different scale and contact geometry. The simulation results show a reduced CoF for the TD of a larger R_x regarding both the maximum CoF and the CoF in the thermo-viscous regime. The simulation results agree qualitatively with the experimental results by representing the scale effects. However, quantitatively, the simulation results are higher than the experimental results. The bilinear LSS model in [Poll and Wang 2012; Bader 2018; Liu and Zhang *et al* 2020b] and in [Ndiaye and Martinie *et al* 2017] may result in a better traction prediction for future work, because generally the bilinear LSS equation predicts lower LSS values than the used linear LSS in Eq. (7.1). In [Ndiaye and Martinie *et al* 2017], the LSS is modeled not only as a function of pressure, but also as a function of temperature. It should be pointed out that the two parameters in the bilinear LSS equation for squalane extracted from the twin-disc machine in Chapter 6 may be influenced by thermal effects according to the scale effects in this study. It is interesting to see that a good comparison can be achieved for 5 m/s for the specified contact geometry (Fig. 6.8). In order to obtain a test-rig-independent LSS function for a lubricant, thermal effects should be minimized in traction curve measurements.

In Sec. 5.3.3, traction was compared between two ball-on-disc machines, namely WAM and MTM. The two machines gave identical friction coefficients over the studied parameters. Scale effect could be ignorable, because the diameters of the ball for the two rigs are very close and they are 10.314 mm and 9.525 mm, respectively.

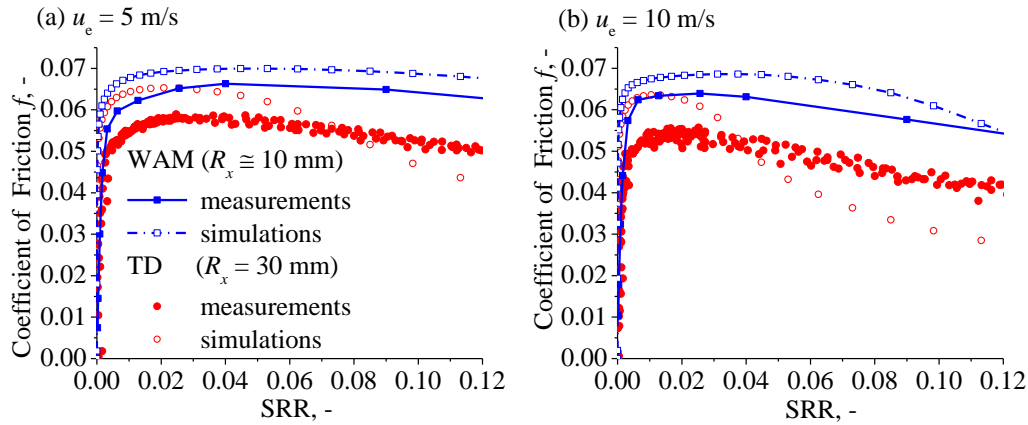


Figure 7-10: Traction curve comparison between experiments and simulations for two different geometrical configurations at constant mean contact pressure, speed, and supplied oil temperature, (a) $u_e = 5$ m/s; (b) $u_e = 10$ m/s. (TD twin disc: $k_e = 1.43, R_x = 30$ mm; WAM ball-on-disc: $k_e = 1.0, R_x = 10.314$ mm; with a reference liquid squalane, $p_H = 1.945$ GPa, $T_0 = 40$ °C)

7.4 Outlook

In the EHL literature, the relation between traction and film thickness is rarely discussed. Because the EHL film thickness is inlet dominant (relatively low pressure zone), while the traction is determined by the non-Newtonian shear property of the confined thin EHL film in the contact center (high pressure zone). However, from the scale effect in this study, it is interesting to know that the EHL film thickness may influence the traction not only through the change in shear rate for an isothermal case, but also through a thick film which enhances thermal effects and increases the middle-film temperature by reducing the rate of heat conduction in the z -direction. And possibly the shear is mainly localized in the middle of a thick EHL film. All these factors in scale effects would reduce the EHL traction. The relation between the film thickness and the EHL traction needs to be clarified, especially for the maximum CoF and for the thermo-viscous traction regime. This would help to design operating parameters towards the measurement of isothermal traction curves using traction machines for the modeling of the LSS property of fluids, which should be test rig independent. For example, the LSS of a fluid should be independent of shear rate and speed, whereas the maximum CoF derived from traction measurements in a traction rig sometimes is reported to be speed dependent [Loewenthal and Douglas 1983; Sharif, Evans, Snidle *et al* 2004] for a highly loaded contact in which the LSS may be reached in most portions of the contact, especially in the contact center of large pressure and high shear stress. These experimental observations on the reduced MSS/LSS at high speeds could be caused by a larger film thickness and enhanced thermal effects and the thermal-induced shear localization in the middle film.

Note that the instant temperature field of an EHL contact and even the temperature distribution across the thin film can be measured by infrared (IR) technique, *e.g.* [Yagi *et al* 2004] and [Lu and Reddyhoff *et al* 2018]. Velocity profiles of lubrication film may be obtained by photobleached imaging, *e.g.* see [Ponjavic *et al* 2013] and [Han and Guo *et al* 2019]. These techniques would help to valid the scale and thermal effects in this study. While ball-on-disc machines have a circular contact zone, twin-disc machines typically show elliptical contacts. In practice, the maximum load can be applied to a traction machine and the radii of the two discs in the direction of motion are usually fixed with design. Using a disc of smaller crown radius in the transverse direction enables the measurements of traction curves at a higher Hertzian pressure. In this way, ellipticity ratio k_e of the contact is becoming an independent variable regarding scale effects for comparable operating conditions (*i.e.* at constant speed, Hertzian

pressure and supplied oil temperature). Even though the effective radius R_x stays the same, the EHL film thickness varies for different k_e because of changes in side-leakage under different loads. It is therefore interesting to know the effect of ellipticity ratio on the EHL traction in the future work.

It should be pointed out that there is another kind of reported isothermal scale effect for a ball of small radius by showing reduced film thickness [Krupka, Bair, Kumar *et al* 2009], which is caused by inlet shear thinning as a result of the increased pressure gradient for a small R_x . Inlet shear thinning may occur for additive or base oils of high-molecular-weight, for blended oils, as well as for a small R_x condition [Krupka *et al* 2009]. The scale effect in this study is mainly a kind of thermal effect for a large R_x , which reduces the EHL traction. More work needs to be carried out to know the R_x boundary of these two kinds of scale effects.

Note that the thermal scale effect in this study is investigated under full film lubrication regime, as well as in the experimental comparison of CoF between twin-disc and ball-on-disc. More recently Bergseth *et al* [2020] compared the CoF between these two kinds of test rigs under mixed and boundary lubrication regimes and reported that the friction can differ by a factor of two and the wear mechanism differs for the two test rigs. They thought the reason is related to contact geometry and thermal behavior. It is interesting to see scale and contact geometrical effects exist in another lubrication regime. Much work needs to be carried out for a better understanding of the scale effects in mixed lubrication regime.

7.5 Conclusions

In this work, it has been shown experimentally that traction machines in different radii of curvature R_x show different results of traction at comparable conditions, *i.e.* at constant speed, Hertzian pressure and supplied oil temperature. The influence of the scale effect on the EHL traction can be predicted qualitatively by a thermal non-Newtonian EHL model. The main conclusions are:

1. Tractions curves made at the same operating parameters must consider scale effects that exist in EHL friction: the maximum friction coefficient is reduced for a larger roller size.
2. The studied scale effect here is a kind of thermal effect rather than shear-thinning effect. The film thickness becomes larger with the increase of R_x , and the generated heat is hard to conduct to the solids due to the resulting thick film thickness and bad thermal conductivity of oil. Moreover, shear may be localized mainly in the middle of the EHL film and this further enhances heat generation, which leads to a reduced coefficient of friction for full-film EHL conditions.
3. The friction coefficient measured from a specific traction machine for a lubricant may fail to represent the frictional behavior of machine elements in different sizes and contact geometries, *e.g.* in different R_x . From this point of view, numerical simulations need to be carried out for a better traction prediction in machine elements than using database of lubricants measured with a traction machine of a certain contact geometry and R_x .
4. $\dot{\gamma} = \Delta u/h_{cen}$ is widely used in simplified traction simulation. However, this equation cannot be used for the local shear rate calculation when there is shear localization which may be caused by thermal effects and temperature gradient in a relatively thick EHL film (*e.g.* large R_x and high u_e) and/or non-Newtonian (*e.g.* LSS) effects.

For a quantitative understanding of the limiting shear stress behavior of fluids, *e.g.* its pressure and temperature dependence, isothermal conditions in an EHL film formed in a traction rig may be achieved by using small R_x and doing traction measurements at a thin EHL film, *e.g.* at a low speed and may even at starved conditions.

8

Conclusions and Recommendations for Future Work

8.1 Conclusions

Based on traction measurements and thermal non-Newtonian EHL simulations with a model fluid squalane, several factors have been revealed to contribute to the discrepancies in the EHL traction prediction (see the problem description in Chapter 3). They are solid body temperature effect, lubricant and solid thermal conductivities, scale effects, and type of the LSS model. The main conclusions are:

(1) The EHL film thickness is dominated by the solid body temperature rather than the supplied oil temperature, and it can be predicted with the isothermal Hamrock-Dowson equation using effective viscosity and pressure-viscosity coefficients at the solid body temperature as input. The bulk temperature also reduces the maximum friction coefficient of traction curves. The solid body temperature affects traction measurements significantly for high speed and highly-loaded conditions. It should be modelled by an appropriate boundary condition for a better traction prediction.

(2) The effect of solid thermal conductivity on the EHL traction depends on the entrainment speed and the resulting film thickness. At high speeds, the influence of solid thermal conductivity on the traction is decreasing in the thermo-viscous regime, while its effect on the maximum friction coefficient of traction curves is still noticeable. Because heat is mainly confined in the middle of the thick film and it is hard to conduct to the solids. The pressure dependence of lubricant thermal conductivity needs to be considered at high velocities and at large SRR conditions for a better traction prediction. Otherwise, the traction can be underestimated and the maximum temperature can be overestimated.

(3) Traction curves made at the same operating parameters (*i.e.* speed, velocity and supplied oil temperature) must consider scale effects that exist in EHL friction: the maximum friction coefficient is reduced for a larger roller size. The scale effect studied here is a kind of thermal effect, which is caused by an increase in film thickness for a larger R_x and the enhanced thermal effects due to poor conductivity of lubricants, *i.e.* heat is hard to conduct into the solids for a thicker film and thus a higher temperature rise in the film and a lower friction. Moreover, shear may be mainly localized in the middle of the EHL film and this further enhances heat generation, which leads to a reduced coefficient of friction for full-film EHL conditions.

(4) The EHL film thickness can affect the EHL traction through the change in shear rate, even though the former is determined in the inlet EHL zone while the latter is high-pressure contact center dominated. A well-known mechanism is through the change in isothermal shear rate, which can be calculated by $\Delta u/h_{cen}$ for isothermal conditions, *e.g.* small SRRs. This study shows another mechanism that the EHL film may affect the traction. It is through thermal-induced shear localization for a thicker EHL film (high speed, large R_x) due to bad thermal conductivity of the lubricant and in such thermal case $\dot{\gamma} \neq \Delta u/h_{cen}$.

(5) EHL traction can be predicted more precisely by using the bilinear LSS model, which can be extracted from traction experiments. The 2D isothermal simplified traction model has been extended to

a 3D thermal EHL traction model accounting for thermal and non-Newtonian effects. The developed simplified method predicts traction curves with acceptable accuracy (max. error < 15%) for highly loaded rolling/sliding EHL contacts over a wide range of operating conditions. The local shear rate should be calculated by $\partial u/\partial z$ rather than $\Delta u/h_{cen}$, because of the temperature and viscosity gradient and the possible localized shear across the thin EHL film.

8.2 Recommendations for future work

There are still some open questions related to high pressure rheological fluid models in EHL traction prediction, such as the nature of limiting shear stress, the best shear thinning model, the criterion of glassy state. Moreover, is there any relation between glassy transition and the LSS behavior? If the answer is yes, will the viscoelasticity property of the lubricant be more significant for EHL lubrication or can the liquid be treated as an elastic solid with a yield stress [Bair 2019c]? What is the role of glassy state on the EHL traction? On the physical nature of the LSS, molecular dynamics simulations [Washizu *et al* 2017; Porras-Vazquez *et al* 2018; Ewen *et al* 2018] and advanced experimental techniques [Ndiaye *et al* 2020; Bair 2019a] may shine light. Molecular dynamics simulations may also help to develop new lubricants with better shear properties at a high pressure to reduce the friction in rolling/sliding EHL contacts. On a macroscale of a rolling/sliding contact, the following work is recommended:

(1) For the modelling of the LSS of a fluid with traction machine (towards isothermal characterization), the EHL film thickness should be kept as thin as possible. The solid body temperature should also be controlled being approximately equal to the supplied oil temperature.

(2) Any kind of in-situ and local experimental techniques for an EHL model contact would help to give a better understanding of the confined thin lubricating film, e.g. local temperature, velocity, viscosity measurements in 3D.

Temperature measurements have been carried out by the author with thermography techniques; however, the repeatability of the calibration and the measurements was not satisfying. More work needs to be done on film-surface temperature measurements, see for example by [Lu and Reddyhoff *et al* 2018], for the validation of the thermal simulations and for a better understanding of the extent that the LSS depends on temperature.

(3) It is meaningful to develop a simplified traction model considering mixed friction. Note that this study is confined to the friction behavior of lubricants, and therefore full-film was used in all experiments and simulations. However, machine elements mostly work under mixed lubrication regime, in which the asperity contact also contributes to the friction. For full-film EHL contact, the temperature rise in the film reduces the friction coefficient; while for mixed lubrication, the temperature rise in the contact is expected to increase the friction coefficient. For engineering practice, simplified traction calculation and empirical equations that can cover different traction regimes with acceptable error (say less than 20%) are in demand. Such effort can be found by Jacod *et al* [2001].

Appendix A Validation of the Non-Newtonian Thermal EHL Model

The used model in this study is validated by comparing simulation results with literature. Figure A-1 compares the film thickness and shear stress distribution from the current thermal EHL model with the simulation results by Liu *et al* [Liu, Wang, Bair and Vergne 2007] and measurements by Bair *et al* [Bair, Vergne, Querry 2005] with PAO650. The calculated central film thicknesses in Fig. A-1(a) agree with the measured values by Bair and Vergne [2005]. They are smaller than the predictions with the Newtonian fluid model. Fig. A-1(b) shows that the calculated shear stress distributions agree with the simulation by Liu *et al* [2007]. In the inlet region, the calculated shear stress with the Carreau shear thinning is smaller than that with the Newtonian fluid model. Inlet shear thinning does occur for PAO650 at pure rolling conditions. Figure A-2 shows the comparison of traction curves for squalane. Generally, the current result agrees with the finite element simulations done by Habchi and the measurements done by Björling *et al* in [Björling, Habchi, Bair *et al* 2019].

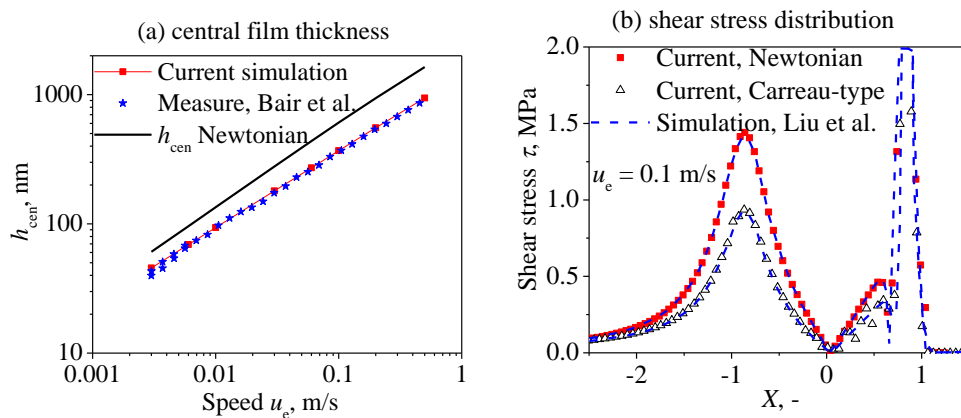


Figure A-1: Comparison between current simulation and results in literature [Liu, Wang, Bair *et al* 2007; Bair, Vergne, Querry 2005] (PAO650, $T_0 = 75\text{ }^\circ\text{C}$, $p_H = 0.528\text{ GPa}$, pure rolling)

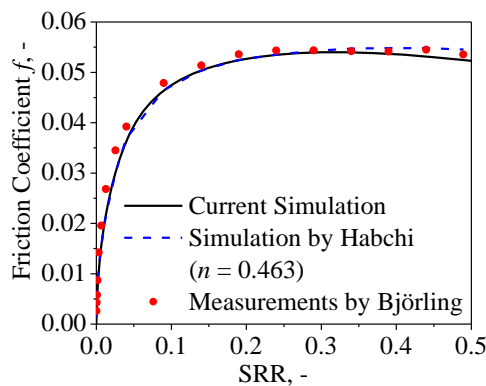


Figure A-2: Traction curve comparison between current simulation and results in literature [Björling, Habchi, Bair *et al* 2019] (squalane, $T_0 = 40\text{ }^\circ\text{C}$, $p_H = 1.07\text{ GPa}$, $k_s = 46\text{ W/mK}$, $k_{oil}(p, T)$, setting see Sec. 5.2)

Appendix B

Mesh Density on the Accuracy of Simulation Results

The influence of the mesh density applied in the multilevel solver has been checked for the case of $\bar{T}_s = 1.00$ in Fig. 4.5. The results of the frictional coefficient, the central film thickness, the minimum film thickness, and the highest film temperature at plane $Y=0$ and $Z=0.5$ with different mesh densities are listed in Table B-1. It can be seen that the errors induced by the mesh density are not significant, especially in the case of increasing the mesh density in the y -direction. Conclusion can be made that the errors made by the mesh density used in this work are negligible for the investigated problem. The mesh with at least 513×257 points is used in the study.

Table B-1: Effect of the mesh densities on the accuracy of a representative case using multigrid method
(T9 Oil, $T_o=T_s=60^\circ\text{C}$, $\text{SRR}=20\%$, $p_H=0.74\text{GPa}$, 10m/s , $R=12.7\text{mm}$, $U_e = 1.54 \times 10^{-11}$,
 $W = 6.88 \times 10^{-7}$, $G=4757$, $D_T = 3.15$)

Mesh($x \times y$)	frictional coefficient, f , (-)	h_{cen} , μm	h_{min} , μm	T_{max} , $^\circ\text{C}$
257×129	0.0331	0.285	0.165	84.35
513×129	0.0329	0.277	0.163	83.95
513×257	0.0328	0.277	0.164	83.85
1025×257	0.0327	0.275	0.163	83.75

Appendix C Computational Zone (Depth) on the Accuracy of Simulation Results

Heat conduction in the z -direction and material convection by the solids are the two main mechanisms of heat removal for a rolling/sliding EHL contact. Along the z -direction, the temperature domains of solid-1 and solid-2 are defined with a thickness of d in Fig. 2.33 or d_T in Fig. 4.1 (named as D_T in its dimensionless form in Chapter 4-7), which should be proven large enough to cover the heat penetration depth. The influence of the depth D_T applied in the thermal simulation (Sec. 2.4) has been checked for the case of $\bar{T}_s = 1.00$ in Fig. 4.5. The results of the frictional coefficient, the central film thickness, the minimum film thickness, and the highest film temperature at plane $Y=0$ and $Z=0.5$ with different computation depth are listed in Table C-1. It can be seen that when the heat penetration depth D_T in the z -direction is half of the Hertzian semi-axis, the output of friction coefficient, film thickness and maximum temperature in the film has become stable. The computational depth at least $3.15a$ is used in the study. Conclusion can be made that the errors made by the heat penetration depth used in this work are negligible for the investigated problem.

Table C-1: Effect of the computational depth in z -direction of the solids on the accuracy of a representative case using multigrid and line-by-line relaxation method (T9 Oil, $T_o=T_s=60^\circ\text{C}$, $\text{SRR}=50\%$, $p_H=0.74\text{GPa}$, 10m/s , $R_x=12.7\text{mm}$, $U_e = 1.54 \times 10^{-11}$, $W = 6.88 \times 10^{-7}$, $G=4757$, mesh 513×257 , in z -direction 12 nodes in the solids and 20 nodes in lubricants)

Depth $D_T (= d_T/a)$	frictional coefficient, f , (-)	h_{cen} , μm	h_{min} , μm	T_{max} , $^\circ\text{C}$
0.001	0.03477	0.2770	0.1638	373.8
0.01	0.03400	0.2763	0.1631	374.3
0.5	0.02848	0.2737	0.1623	379.7
3.15	0.02846	0.2736	0.1623	379.7

Appendix D Infrared Temperature Measurements

In addition to the bulk temperature measurements with thermocouple in Sec. 2.1.3.5, the instant temperature field of an EHL contact could be measured by infrared (IR) techniques, see for example [Ausherman *et al* 1967, Yagi 2005, Reddyhoff 2009b, Lu and Reddyhoff *et al* 2018]. The thermal EHL model used in this study is mainly validated by comparing with numerical simulations in literature. For a further validation of the thermal model and simulations, IR temperature measurements have been carried out using the same twin-disc test rig by replacing one steel shaft with a hollow sapphire shaft (see Fig. D-1), as was adopted by Johannes [2015] and Bader [2018]. The contact is formed between the sapphire disc and a steel disc. The material property and contact parameters of the two discs are listed in Table D-1. The detector of the IR camera is indium antimonide (InSb 640 SM, from DCG systems) with 640×512 pixel at full frame rate of 100 Hz. The detectable spectral range is $1.1 - 5.3 \mu\text{m}$ giving a resolution of $15 \mu\text{m}$ with the objective from MWIR Wecheslobjektiv Makro. For details, it is referred to Johannes [2015] and Bader [2018].

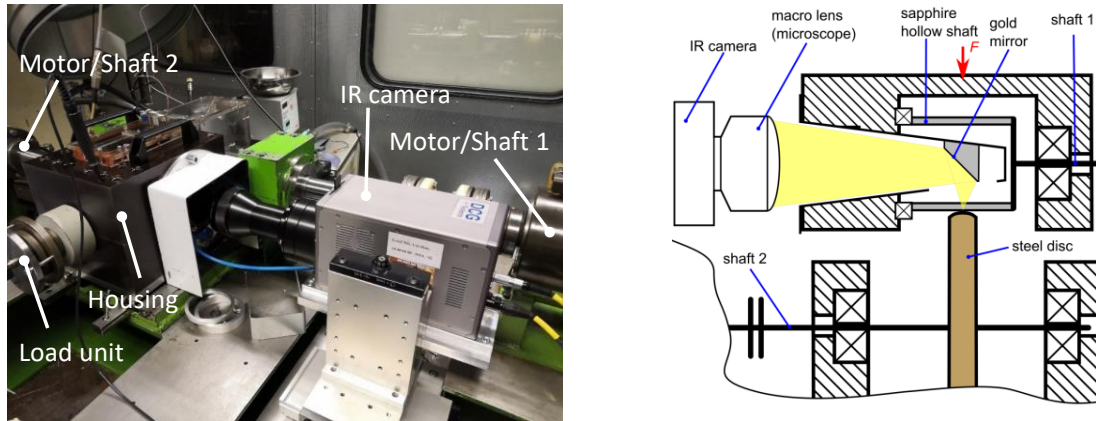


Figure D-1: Setup of modified twin-disc machine for IR temperature measurements. Left: twin-disc and IR camera; Right: light path and the contact formed between a hollow sapphire shaft and a steel disc [Bader 2018]

Table D-1: Material property and geometrical parameters of the two discs used in IR temperature experiments

	Steel Disc	Sapphire Disc
Material	52100 steel	Al ₂ O ₃
Radius r_x , rolling direction, mm	110	41
Radius r_y , crown radius, mm	100	∞
Thermal conductivity, W/mK	21, 33, 46 (25 °C)	40 (25 °C)
Young's modulus, GPa	210	360 – 450
Transmittance	-	$0.2 - 5.5 \mu\text{m}$

The electrical signal from the IR camera was calibrated for different temperatures with the Hertzian contact zone of the twin-disc machine at zero speed by supplying oil at controlled temperatures from 20 °C to 110 °C . The two discs were slightly loaded. During calibration, for example for the supplied oil temperature at 70 °C , it took hours for the camera signal to reach a plateau because it takes long for the whole disc-shaft system to reach an equilibrium. This may indicate the emission received by the IR camera comes mainly from the solid surfaces. In other words, the measured temperature in the current setup may be roughly the surface temperature of the solid rather than the temperature of the lubricant. Note that the highest temperature rise in an EHL contact usually occurs in the middle of the lubricating film.

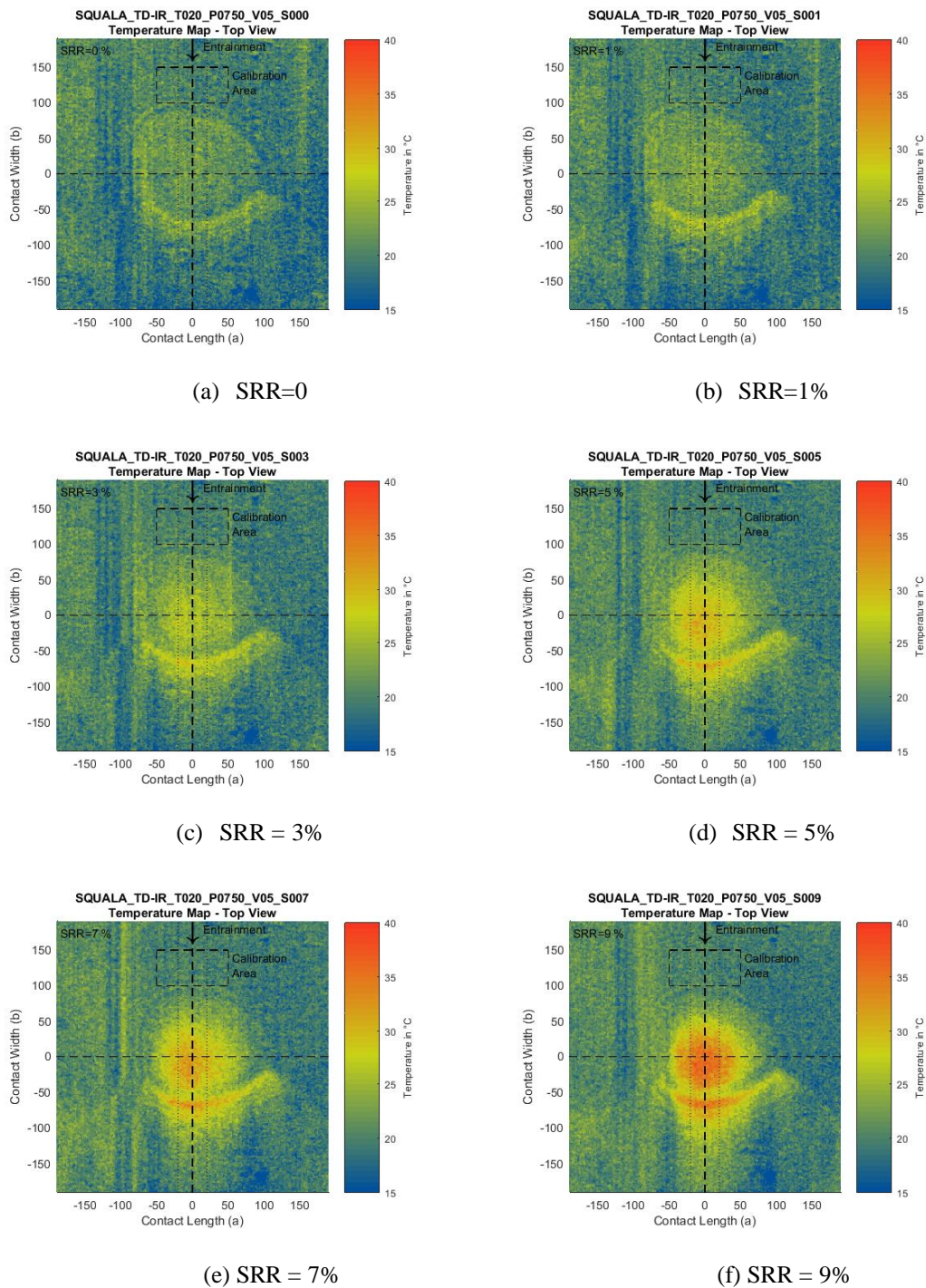


Figure D-2: Temperature map at different SRRs measured by IR camera for squalane ($T_0 = 20\text{ }^\circ\text{C}$, $p_H = 1.125\text{ GPa}$, $u_e = 5\text{ m/s}$)

Fig. D-2 shows the measured temperature map for squalane at different SRRs, from 0 to 9%. It can be seen that the temperature rise is increasing with SRR due to enhanced shear heating effects, especially at the contact center where the pressure is very high. The temperature distribution for different SRRs on the centerline in the entrainment direction is plotted in Fig. D-3. These experimental temperature distributions show some typical features as those predicted by numerical simulations, for example in Fig. 5.3. For a fixed SRR, the maximum temperature occurs close to the contact center and the temperature rise is becoming larger with increasing slip/SRR.

At the outlet region, there is a pronounced temperature peak. At moment, it is hard to judge whether the location of the peak is inside the Hertzian contact zone or in the cavitation zone. If it is inside the contact, the temperature increase may be caused by the local high pressure there. If it is in the cavitation area, the peak could be a false temperature information and it may be a result of a change in oil-air emissivity or reflectivity. It should be pointed out that the temperature values shown in Fig. D-2 and Fig. D-3 are not absolute values and they are shifted using the temperature in the inlet as a reference to avoid the negative measured temperatures after the normal calibration procedure introduced above. This kind of shift is based on assumptions that the inlet temperature equals the supplied oil temperature and the temperature-voltage response of the IR camera is linear, even though these two assumption are rarely true. In the inlet of an EHL contact, the temperature can be higher than the supplied oil temperature due to inlet shear heating effects caused by reverse flow. Another problem is the response of the camera detector is non-linear at different temperature. The resolution is becoming better for a higher temperature, *e.g.* at 70 °C.

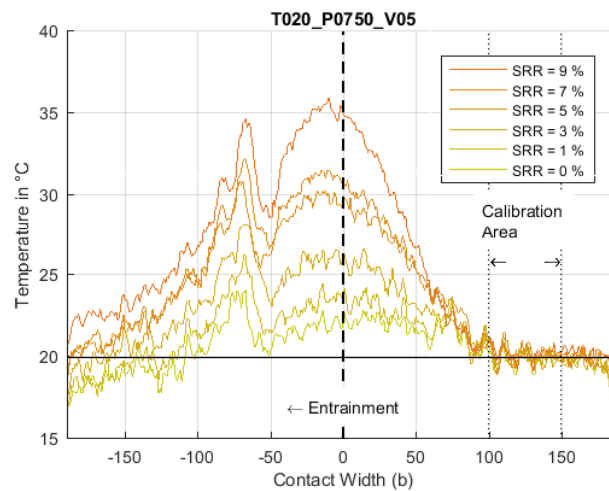


Figure D-3: Temperature distribution on the centerline for different SRRs (squalane, $T_0 = 20\text{ °C}$, $p_H = 1.125\text{ GPa}$, $u_e = 5\text{ m/s}$)

For the future temperature measurement, it is suggested to do the calibration of the IR camera at pure rolling, $SRR=0$. (This is not possible for the current shaft design because of the heat generation of the sealed supporting bearings; the shaft and housing can be 70 °C after a running of 15 mins) This may enable the temperature of the whole disc is relatively uniform. In the current twin-disc setup, the size of the disc is very large ($r_x = 110\text{ mm}$), and it seems there is always a temperature gradient in the disc during the calibration at zero speed by supplying temperature-controlled oil to the local area between the steel disc and the sapphire shaft. For the ball-on-disc machine, the temperature calibration could be controlled better, as the ball is usually half immersed in the lubricant and the temperature of the whole system (ball-disc-shaft) is relatively uniform.

Attentions should also be paid to the emissivity spectra of the lubricant and the solid specimens, which should match the detectable range of the IR camera system, especially when an optical filter is used in the system.

In the literature, temperature of the mid-film and the two solid surfaces can be measured separately with coating and filter techniques, see [Ausherman *et al* 1967, Yagi 2005, Reddyhoff 2009b, Lu and Reddyhoff *et al* 2018].

Bibliography

- Ashurst, W. T., & Hoover, W. G. (1975). Dense-fluid shear viscosity via nonequilibrium molecular dynamics. *Physical Review A*, 11(2), 658.
- Ai, X. L. (1993). *Numerical analyses of elastohydrodynamically lubricated line and point contacts with rough surfaces by using semi-system and multigrid methods* [Ph.D thesis]. Northwestern University. Evanston, USA.
- Almqvist, T., Almqvist, A., & Larsson, R. (2004). A comparison between computational fluid dynamic and Reynolds approaches for simulating transient EHL line contacts. *Tribology international*, 37(1), 61-69.
- Barlow, A. J., & Lamb, J. (1959). The visco-elastic behaviour of lubricating oils under cyclic shearing stress. *Proceedings of the Royal Society of London. Series A. Mathematical and Physical Sciences*, 253(1272), 52-69.
- Barlow, A. J., Lamb, J., Matheson, A. J., Padmini, P. R. K. L., & Richter, J. (1967). Viscoelastic relaxation of supercooled liquids. I. *Proceedings of the Royal Society of London. Series A. Mathematical and Physical Sciences*, 298(1455), 467-480.
- Barlow, A. J., Harrison, G., Irving, J. B., Kim, M. G., Lamb, J., & Pursley, W. C. (1972). The effect of pressure on the viscoelastic properties of liquids. *Proceedings of the Royal Society of London. A. Mathematical and Physical Sciences*, 327(1570), 403-412.
- Ausherman, V. K., Nagaraj, H. S., Sanborn, D. M., & Winer, W. O. (1976). Infrared temperature mapping in elastohydrodynamic lubrication. *J. of Lubrication Tech*, 98(2):236-242.
- Bair, S., & Winer, W. O. (1979a). Shear strength measurements of lubricants at high pressure. *Journal of lubrication technology*, 101(3), 251-257.
- Bair, S., & Winer, W. O. (1979b). A rheological model for elastohydrodynamic contacts based on primary laboratory data. *Journal of lubrication technology*, 101(3), 258-264.
- Bair, S., & Winer, W. O. (1982). Some observations in high pressure rheology of lubricants. *Journal of Lubrication Technology*, 104(3), 357-364.
- Bair, S., & Winer, W. O. (1990). The high shear stress rheology of liquid lubricants at pressures of 2 to 200 MPa. *Journal of Tribology*, 112(2), 246-252.
- Bair, S., & Winer, W. O. (1992). The high pressure high shear stress rheology of liquid lubricants. *Journal of Tribology*, 114(1), 1-9.
- Bair, S., Qureshi, F., & Winer, W. O. (1993). Observations of shear localization in liquid lubricants under pressure. *Journal of Tribology*, 115(3), 507-513.
- Bair, S., & Winer, W. O. (1993). A new high-pressure, high-shear stress viscometer and results for lubricants. *Tribology Transactions*, 36(4), 721-725.
- Bair, S. (1995). Recent developments in high-pressure rheology of lubricants. In *Tribology series* (Eds Dowson, D., Taylor, C., Childs, T., Dalmaz, G.), Elsevier, Vol. 30, 169-187.
- Bair, S., & Winer, W. O. (1997). A simple formula for EHD film thickness of non-Newtonian liquids. In *Tribology Series*, Elsevier, Vol. 32, 235-241.
- Bair, S., Jarzynski, J., & Winer, W. O. (2001). The temperature, pressure and time dependence of lubricant viscosity. *Tribology International*, 34(7), 461-468.
- Bair, S. (2002a). The shear rheology of thin compressed liquid films. *Proceedings of the Institution of Mechanical Engineers, Part J: Journal of Engineering Tribology*, 216(1), 1-17.
- Bair, S. (2002b). The nature of the logarithmic traction gradient. *Tribology International*, 35(9), 591-597.
- Bair, S., McCabe, C., & Cummings, P. T. (2002a). Comparison of nonequilibrium molecular dynamics with experimental measurements in the nonlinear shear-thinning regime. *Physical Review Letters*, 88(5), 058302.
- Bair, S., McCabe, C., & Cummings, P. T. (2002b). Calculation of viscous EHL traction for squalane using molecular simulation and rheometry. *Tribology Letters*, 13(4), 251-254.
- Bair, S., & McCabe, C. (2004). A study of mechanical shear bands in liquids at high pressure. *Tribology international*, 37(10), 783-789.
- Bair, S. (2005). Shear thinning correction for rolling/sliding elastohydrodynamic film thickness. *Proceedings of the Institution of Mechanical Engineers, Part J: Journal of Engineering Tribology*, 219(1), 69-74.
- Bair, S. (2006). Reference liquids for quantitative elastohydrodynamics: selection and rheological characterization. *Tribology Letters*, 22(2), 197-206.
- Bair, S., & Gordon, P. (2006). Rheological challenges and opportunities for EHL. In *IUTAM Symposium on Elastohydrodynamics and Micro-elastohydrodynamics* (pp. 23-43). Springer, Dordrecht.
- Bair, S., & Kotzalas, M. (2006). The contribution of roller compliance to elastohydrodynamic traction. *Tribology Transactions*, 49(2), 218-224.
- Bair, S., Liu, Y., & Wang, Q. J. (2006). The pressure-viscosity coefficient for Newtonian EHL film thickness with general piezoviscous response. *Journal of Tribology*, 128(3):624-31.

- Bair, S., Fernandez, J., Khonsari, M. M., Krupka, I., Qureshi, F., Vergne, P., & Wang, Q. J. (2009). An argument for a change in elastohydrodynamic lubrication philosophy. *Proceedings of the Institution of Mechanical Engineers*, 223(J4), 1.
- Bair, S., Yamaguchi, T., Brouwer, L., Schwarze, H., Vergne, P., & Poll, G. (2014). Oscillatory and steady shear viscosity: The Cox–Merz rule, superposition, and application to EHL friction. *Tribology International*, 79, 126-131.
- Bair, S., Vergne, P., Kumar, P., Poll, G., Krupka, I., Hartl, M., ... & Larsson, R. (2015). Comment on “History, origins and prediction of elastohydrodynamic friction” by Spikes and Zhang. *Tribology Letters*, 58(1), 16.
- Bair, S., Martinie, L., & Vergne, P. (2016). Classical EHL versus quantitative EHL: a perspective part II—super-Arrhenius piezoviscosity, an essential component of elastohydrodynamic friction missing from classical EHL. *Tribology Letters*, 63(3), 37.
- Bair, S. S., Andersson, O., Qureshi, F. S., & Schirru, M. M. (2018). New EHL modeling data for the reference liquids squalane and squalane plus polyisoprene. *Tribology Transactions*, 61(2), 247-255.
- Bair, S. (2019a). High pressure rheology for quantitative elastohydrodynamics. second ed. Amsterdam, The Netherlands: Elsevier.
- Bair, S. (2019b). The rheological assumptions of classical EHL: what went wrong?. *Tribology International*, 131, 45-50.
- Bair, S. (2019c). The viscosity at the glass transition of a liquid lubricant. *Friction*, 7(1), 86-91.
- Bair, S. (2020). Viscous heating in compressed liquid films. *Tribology Letters*, 68(1), 7.
- Bezot, P., Hesse-Bezot, C., Berthe, D., Dalmaz, G., & Vergne, P. (1986). Viscoelastic parameters of 5P4E as a function of pressure and temperature by light scattering technique. *Journal of tribology*, 108(4), 579-583.
- Brandt, A., & Lubrecht, A. A. (1990). Multilevel matrix multiplication and fast solution of integral equations. *Journal of Computational Physics*, 90(2), 348-370.
- Bayer, Raymond George (1994). *Terminology and Classifications*". Mechanical Wear Fundamentals and Testing. CRC Press. p.3. ISBN:0-8247-4620-1.
- Bruyere, V., Fillot, N., Morales-Espejel, G. E., & Vergne, P. (2012). Computational fluid dynamics and full elasticity model for sliding line thermal elastohydrodynamic contacts. *Tribology International*, 46(1), 3-13.
- Björling, M., Habchi, W., Bair, S., Larsson, R., & Marklund, P. (2013). Towards the true prediction of EHL friction. *Tribology International*, 66, 19-26.
- Björling, M., Habchi, W., Bair, S., Larsson, R., & Marklund, P. (2014). Friction reduction in elastohydrodynamic contacts by thin-layer thermal insulation. *Tribology letters*, 53(2), 477-486.
- Björling, M., Miettinen, J., Marklund, P., Lehtovaara, A., & Larsson, R. (2015). The correlation between gear contact friction and ball on disc friction measurements. *Tribology International*, 83, 114-119.
- Björling, M., Habchi, W., Bair, S., Larsson, R., & Marklund, P. (2019). Corrigendum to “Towards the true prediction of EHL friction” [Tribol. Int. 66 (2013) 19–26]. *Tribology International*, 133: 297.
- Beilicke, R., Bobach, L., & Bartel, D. (2016). Transient thermal elastohydrodynamic simulation of a DLC coated helical gear pair considering limiting shear stress behavior of the lubricant. *Tribology International*, 97, 136-150.
- Bader, N., Wang, D., & Poll, G. (2017). Traction and local temperatures measured in an elastohydrodynamic lubrication contact. *Proceedings of the Institution of Mechanical Engineers, Part J: Journal of Engineering Tribology*, 231(9), 1128-1139.
- Bader, N. (2018). *Traction in EHL-contacts: the influence of local fluid rheology and temperatures* (Doctoral dissertation, Hannover: Leibniz Universität Hannover).
- Bergseth, E., Zhu, Y., & Söderberg, A. (2020). Study of Surface Roughness on Friction in Rolling/Sliding Contacts: Ball-on-Disc Versus Twin-Disc. *Tribology Letters*, 68(2).
- Cutler, W. G., McMickle, R. H., Webb, W., & Schiessler, R. W. (1958). Study of the compressions of several high molecular weight hydrocarbons. *The Journal of Chemical Physics*, 29(4), 727-740.
- Carslaw HS, Jaeger JC. Conduction of heat in solids. *Oxford: Clarendon Press; 1959*.
- Crook, A. W. (1961). The lubrication of rollers II. Film thickness with relation to viscosity and speed. *Philosophical Transactions of the Royal Society of London. Series A, Mathematical and Physical Sciences*, 254(1040), 223-236.
- Crook, A. W. (1963). The lubrication of rollers IV. Measurements of friction and effective viscosity. *Philosophical Transactions of the Royal Society of London. Series A, Mathematical and Physical Sciences*, 255(1056), 281-312.
- Cheng, H. S. (1965). A refined solution to the thermal-elastohydrodynamic lubrication of rolling and sliding cylinders. *ASLE TRANSACTIONS*, 8(4), 397-410.
- Cheng, H. S., & Sternlicht, B. (1965). A numerical solution for the pressure, temperature, and film thickness between two infinitely long, lubricated rolling and sliding cylinders, under heavy loads. *Journal of Basic Engineering*, 87(3), 695-704.
- Cheng, H. S. (1972). Isothermal elastohydrodynamic theory for the full range of pressure-viscosity coefficient. *ASME Journal Lubrication Technology*, 94, 35-43.
- Carreau, P. J. (1972). Rheological equations from molecular network theories. *Transactions of the Society of Rheology*, 16(1), 99-127.

- Chittenden, R. J., Dowson, D., Dunn, J. F., & Taylor, C. M. (1985). A theoretical analysis of the isothermal elastohydrodynamic lubrication of concentrated contacts. I. Direction of lubricant entrainment coincident with the major axis of the Hertzian contact ellipse. *Proceedings of the Royal Society of London. A. Mathematical and Physical Sciences*, 397(1813), 245-269.
- Clarke, A., Sharif, K. J., Evans, H. P., & Snidle, R. W. (2006). Heat partition in rolling/sliding elastohydrodynamic contacts. *ASME Journal of Tribology*, 128(1), 67-78.
- Ciulli, E. (2013). Thermal effects of different kind influencing lubricated non-conformal contacts. *Tribology International*, 59, 181-189.
- Cui, J.L. (2016). *On the theory of thermo rheological lubrication and its application in EHL*. PhD thesis, Qingdao University of Technology.
- Castro, J., & Seabra, J. (2018). Influence of mass temperature on gear scuffing. *Tribology International*, 119, 27-37.
- Dow, R. B. (1956). Some rheological properties under high pressure. In *Rheology* (pp. 243-319). Academic Press.
- Dowson, D., & Higginson, G. R. (1959). A numerical solution to the elasto-hydrodynamic problem. *Journal of mechanical engineering science*, 1(1), 6-15.
- Dowson, D. (1962). A generalized Reynolds equation for fluid-film lubrication. *International Journal of Mechanical Sciences*, 4(2), 159-170.
- Dyson, A. (1965). Flow properties of mineral oils in elastohydrodynamic lubrication. *Philosophical Transactions of the Royal Society of London. Series A, Mathematical and Physical Sciences*, 258(1093), 529-564.
- Dowsor, D., & Whitaker, A. V. (1965). A numerical procedure for the solution of the elastohydrodynamic problem of rolling and sliding contacts lubricated by a Newtonian fluid. *Proceedings of the Institution of Mechanical Engineers*, 180(Part 3), 57-71.
- Dowson, D., & Higginson, G. T. (1966). *Elastohydrodynamic Lubrication, The Fundamentals of Roller and Gear Lubrication*, Pergamon Press, Oxford, Great Britain.
- Dowson, D. (1998), *History of Tribology*, second edition, Professional Engineering Publishing Limited, London.
- Daivis, P. J., Evans, D. J., & Morriss, G. P. (1992). Computer simulation study of the comparative rheology of branched and linear alkanes. *The Journal of chemical physics*, 97(1), 616-627.
- Eyring, H. (1936). Viscosity, plasticity, and diffusion as examples of absolute reaction rates. *The Journal of chemical physics*, 4(4), 283-291.
- Ewell, R. H., & Eyring, H. (1937). Theory of the Viscosity of Liquids as a Function of Temperature and Pressure. *The Journal of Chemical Physics*, 5(9), 726-736.
- Evans, D. J., & Morriss, G. P. (1984). Nonlinear-response theory for steady planar Couette flow. *Physical Review A*, 30(3), 1528.
- Evans, C. R., & Johnson, K. L. (1986a). The rheological properties of elastohydrodynamic lubricants. *Proceedings of the Institution of Mechanical Engineers, Part C: Journal of Mechanical Engineering Science*, 200(5), 303-312.
- Evans, C. R., & Johnson, K. L. (1986b). Regimes of traction in elastohydrodynamic lubrication. *Proceedings of the Institution of Mechanical Engineers, Part C: Journal of Mechanical Engineering Science*, 200(5), 313-324.
- Ebner, M., Yilmaz, M., Löhner, T., Michaelis, K., Höhn, B. R., & Stahl, K. (2018). On the effect of starved lubrication on elastohydrodynamic (EHL) line contacts. *Tribology International*, 118, 515-523.
- Ewen, J. P., Heyes, D. M., & Dini, D. (2018). Advances in nonequilibrium molecular dynamics simulations of lubricants and additives. *Friction*, 6(4), 349-386.
- Ewen, J. P., Gao, H., Müser, M. H., & Dini, D. (2019). Shear heating, flow, and friction of confined molecular fluids at high pressure. *Physical Chemistry Chemical Physics*, 21(10), 5813-5823.
- Fowell, M., Ioannides, S., & Kadiric, A. (2014). An experimental investigation into the onset of smearing damage in nonconformal contacts with application to roller bearings. *Tribology Transactions*, 57(3), 472-488.
- Grubin, A. N. (1949). Investigation of the contact of machine components. *Central Scientific Research Inst. Tech. & Mech. Eng.*
- Greenwood, J. A. (1985). Formulas for moderately elliptical Hertzian contacts. *Journal of Tribology*, 107(4), 501-504.
- Gupta, P. K., Cheng, H. S., Zhu, D., Forster, N. H., & Schrand, J. B. (1992). Viscoelastic effects in MIL-L-7808-type lubricant, Part I: analytical formulation. *Tribology transactions*, 35(2), 269-274.
- Gohar, R. (2001). *Elastohydrodynamics*. World Scientific.
- Guo, F., Yang, P., & Qu, S. (2001). On the theory of thermal elastohydrodynamic lubrication at high slide-roll ratios—circular glass-steel contact solution at opposite sliding. *Journal of Tribology*, 123(4), 816-821.
- Gao, J., Luedtke, W. D., Gourdon, D., Ruths, M., Israelachvili, J. N., & Landman, U. (2004). Frictional forces and Amontons' law: from the molecular to the macroscopic scale. *The Journal of Physical Chemistry B*, 108(11), 3410-3425.
- Guegan, J., Kadiric, A., Gabelli, A., & Spikes, H. (2016). The relationship between friction and film thickness in EHD point contacts in the presence of longitudinal roughness. *Tribology Letters*, 64(3), 33.
- Gohar R., & Rahnejat, H. (2019). *Fundamentals of tribology (third edition)*. World Scientific.
- Hertz, H. (1881). About the contact of elastic solid bodies (Über die Berührung fester elastischer Körper). *J Reine Angew Math*, 5, 12-23.

- Hahn, S. J., Eyring, H., Higuchi, I., & Ree, T. (1958). Flow properties of lubricating oils under pressure. *NLGI Spokesman*, 21(3), 123-128.
- Hahn, S. J., Ree, T., & Eyring, H. (1959). Flow mechanism of thixotropic substances. *Industrial & Engineering Chemistry*, 51(7), 856-857.
- Horowitz, H. H. (1958). Predicting Effects of Temperature and Shear Rate on Viscosity of Viscosity Index-Improved Lubricants. *Industrial & Engineering Chemistry*, 50(7), 1089-1094.
- Hutton, J. F., & Phillips, M. C. (1969). Analysis of the Linear Viscoelastic Relaxation of a Liquid Hydrocarbon. *The Journal of Chemical Physics*, 51(3), 1065-1072.
- Hutton, J. F. (1972). Theory of rheology In *Interdisciplinary Approach to Liquid Lubricant Technology* (Ed. Ku, P. M.), pp. 195, 207 (National Aeronautics and Space Administration, Washington, DC).
- Hutton, J. F., & Phillips, M. C. (1972). Shear modulus of liquids at elastohydrodynamic lubrication pressures. *Nature Physical Science*, 238(87), 141.
- Hutton, J. F., Phillips, M. C., Ellis, J., Powell, G., & Wyn-Jones, E. (1978). Viscoelastic studies of lubricants and other liquids in shear and bulk deformation. In *Proceedings of 5th Leeds-Lyon Symposium on Tribology, Leeds*.
- Hutton, J. F. (1984). Reassessment of rheological properties of LVI 260 oil measured in a disk machine. *Journal of tribology*, 106(4), 536-537.
- Hamrock, B. J., & Dowson, D. (1976). Isothermal elastohydrodynamic lubrication of point contacts: Part 1—Theoretical formulation. *Journal of Lubrication Technology*, 98(2), 223-228.
- Hamrock, B. J., & Dowson, D. (1977). Isothermal elastohydrodynamic lubrication of point contacts: part III—fully flooded results. *Journal of Lubrication Technology*, 99(2), 264-275.
- Hamrock, B. J., & Dowson, D. (1981). *Ball bearing lubrication: the elastohydrodynamics of elliptical contacts*. (Wiley, New York, 1981)
- Hamrock, B. J., & Brewe, D. (1983). Simplified solution for stresses and deformations. *Journal of Lubrication Technology*, 105(a), 171-177.
- Hirst, W., & Moore, A. J. (1979). Elastohydrodynamic lubrication at high pressures II. Non-Newtonian behaviour. *Proceedings of the Royal Society of London. A. Mathematical and Physical Sciences*, 365(1723), 537-565.
- Hirst, W., & Moore, A. J. (1980). The effect of temperature on traction in elastohydrodynamic lubrication. *Philosophical Transactions of the Royal Society of London. Series A, Mathematical and Physical Sciences*, 298(1438), 183-208.
- Houpert, L., Flamand, L., & Berthe, D. (1981). Rheological and thermal effects in lubricated EHD contacts. *J. of Lubrication Tech.* 103(4): 526-532.
- Houpert, L. (1985). New results of traction force calculations in elastohydrodynamic contacts. *Journal of tribology*, 107(2), 241-245.
- Höglund E, & Jacobson, B. O. (1986). Experimental investigation of the shear strength of lubricants subjected to high pressure and temperature. *J. Tribol*, 108, 571-577.
- Hieber, C. A., & Chiang, H. H. (1992). Shear-rate-dependence modeling of polymer melt viscosity. *Polymer Engineering & Science*, 32(14), 931-938.
- Hu, Y. Z., & Zhu, D. (2000). A full numerical solution to the mixed lubrication in point contacts. *Journal of Tribology*, 122(1), 1-9.
- Holmes, M. J. A., Evans, H. P., Hughes, T. G., & Snidle, R. W. (2003). Transient elastohydrodynamic point contact analysis using a new coupled differential deflection method part 1: theory and validation. *Proceedings of the Institution of Mechanical Engineers, Part J: Journal of Engineering Tribology*, 217(4), 289-304.
- Habchi, W. (2008). *A Full-system finite element approach to elastohydrodynamic lubrication problems* [Ph.D thesis]. INSA. Lyon, France.
- Habchi, W., Eyheramendy, D., Bair, S., Vergne, P., & Morales-Espejel, G. (2008). Thermal elastohydrodynamic lubrication of point contacts using a Newtonian/generalized Newtonian lubricant. *Tribology letters*, 30(1), 41.
- Habchi, W., Vergne, P., Bair, S., Andersson, O., Eyheramendy, D., & Morales-Espejel, G. E. (2010). Influence of pressure and temperature dependence of thermal properties of a lubricant on the behaviour of circular TEHD contacts. *Tribology International*, 43(10), 1842-1850.
- Habchi, W., Bair, S., & Vergne, P. (2013). On friction regimes in quantitative elastohydrodynamics. *Tribology International*, 58, 107-117.
- Habchi, W., & Vergne, P. (2015). On the compressive heating/cooling mechanism in thermal elastohydrodynamic lubricated contacts. *Tribology International*, 88, 143-152.
- Habchi, W., & Bair, S. (2019). Is viscoelasticity of any relevance to quantitative EHL friction predictions?. *Tribology International*, 135, 96-103.
- Habchi, W., & Bair, S. (2020). The role of the thermal conductivity of steel in quantitative elastohydrodynamic friction. *Tribology International*, 142, 105970.
- Hartinger, M., Dumont, M. L., Ioannides, S., Gosman, D., & Spikes, H. (2008). CFD modeling of a thermal and shear-thinning elastohydrodynamic line contact. *Journal of Tribology*, 130(4), 041503.

- Holmberg, K., Andersson, P., & Erdemir, A. (2012). Global energy consumption due to friction in passenger cars. *Tribology international*, 47, 221-234.
- Holmberg, K., & Erdemir, A. (2015). Global impact of friction on energy consumption, economy and environment. *Fme Trans*, 43(3), 181-185.
- Hajishafiee, A., Kadiric, A., Ioannides, S., & Dini, D. (2017). A coupled finite-volume CFD solver for two-dimensional elasto-hydrodynamic lubrication problems with particular application to rolling element bearings. *Tribology International*, 109, 258-273.
- Han, S. L., Guo, F., Shao, J., Bai, Q. H., & Han, L. L. (2019). On the Velocity Profile of Couette Flow of Lubricant Within a Micro/Submicro Gap. *Tribology Letters*, 67(4), 114.
- Imai, Y., & Brown, N. (1976). Environmental crazing and intrinsic tensile deformation in polymethylmethacrylate. *Journal of Materials Science*, 11(3), 417-424.
- Isaac, G., Changenet, C., Ville, F., Cavoret, J., & Becquerelle, S. (2018). Thermal analysis of twin-disc machine for traction tests and scuffing experiments. *Proceedings of the Institution of Mechanical Engineers, Part J: Journal of Engineering Tribology*, 232(12), 1548-1560.
- Itagaki, H., Ohama, K., & Rajan, A. N. R. (2019). Method for estimating traction curves under practical operating conditions. *Tribology International*, 105639. DOI:<https://doi.org/10.1016/j.triboint.2019.02.047>.
- Jost, H. P. (1966). Lubrication (tribology) education and research. *A Report on the Present Position and Industry Needs, Department of Education and Science, HM Stationary Office, London*.
- Jost, H. P. (1990). Tribology—origin and future. *Wear*, 136(1), 1-17.
- Johnson, K. L., & Cameron, R. (1967). Fourth paper: shear behaviour of elasto-hydrodynamic oil films at high rolling contact pressures. *Proceedings of the Institution of Mechanical Engineers*, 182(1), 307-330.
- Johnson, K. L., & Tevaarwerk, J. L. (1977). Shear behaviour of elasto-hydrodynamic oil films. *Proceedings of the Royal Society of London. A. Mathematical and Physical Sciences*, 356(1685), 215-236.
- Johnson, K. L., & Greenwood, J. A. (1980). Thermal analysis of an Eyring fluid in elasto-hydrodynamic traction. *Wear*, 61(2), 353-374.
- Johnson, K. L. (1987). *Contact mechanics*. Cambridge university press.
- Johnson, K. L. (1993). Non-Newtonian effects in elasto-hydrodynamic lubrication. In *Tribology Series* (Vol. 25, pp. 15-26). Elsevier.
- Jacobson, B. O. (1985). A high pressure-short time shear strength analyzer for lubricants. *Journal of Tribology*, 107(2), 220-223.
- Jacobson, B. O. (1991). *Rheology and elasto-hydrodynamic lubrication* (Vol. 19). Elsevier.
- Jacobson, B. O. (2006). High-pressure chamber measurements. *Proceedings of the Institution of Mechanical Engineers, Part J: Journal of Engineering Tribology*, 220(3), 199-206.
- Jacob, B., Venner, C. H., & Lugt, P. M. (2001). A generalized traction curve for EHL contacts. *Journal of Tribology*, 123(2), 248-253.
- Jackson, A., & Webster, M. N. (2003). The role of tribology research in the development of advanced lubricants. In *Tribology Series* (Vol. 41, pp. 439-448). Elsevier.
- Jadhao, V., & Robbins, M. O. (2017). Probing large viscosities in glass-formers with nonequilibrium simulations. *Proceedings of the National Academy of Sciences*, 114(30), 7952-7957.
- Jadhao, V., & Robbins, M. O. (2019). Rheological properties of liquids under conditions of elasto-hydrodynamic lubrication. *Tribology Letters*, 67(3), 66.
- Kamal, I., & McLaughlin, E. (1964). Pressure and volume dependence of the thermal conductivity of liquids. *Transactions of the Faraday Society*, 60, 809-816.
- Kohlrausch, F. (1888). On the thermal conductivity of hard and soft steel. *The London, Edinburgh, and Dublin Philosophical Magazine and Journal of Science*, 25(156), 448-450.
- Kim, K. H., & Sadeghi, F. (1992). Three-dimensional temperature distribution in EHD lubrication: part I—circular contact. *Journal of tribology*, 114(1), 32-41.
- Kim, K. H., & Sadeghi, F. (1993). Three-dimensional temperature distribution in EHD lubrication: part II—point contact and numerical formulation. *Journal of tribology*, 115(1), 36-45.
- Khonsari, M. M., & Hua, D. Y. (1993). Generalized non-Newtonian elasto-hydrodynamic lubrication. *Tribology international*, 26(6), 405-411.
- Kaneta, M., & Yang, P. (2003). Effects of thermal conductivity of contacting surfaces on point EHL contacts. *Journal of Tribology*, 125(4), 731-738.
- Kaneta, M., Shigeta, T., & Yang, P. (2005). Effects of compressive heating on traction force and film thickness in point EHL contacts. *Journal of Tribology*, 127(2), 435-442.
- Kaneta, M., & Yang, P. (2010). Effects of the thermal conductivity of contact materials on elasto-hydrodynamic lubrication characteristics. *Proceedings of the Institution of Mechanical Engineers, Part C: Journal of Mechanical Engineering Science*, 224(12), 2577-2587.

- Kaneta, M., Yang, P., Krupka, I., & Hartl, M. (2015). Fundamentals of thermal elastohydrodynamic lubrication in Si₃N₄ and steel circular contacts. *Proceedings of the Institution of Mechanical Engineers, Part J: Journal of Engineering Tribology*, 229(8), 929-939.
- Kim, H. J., Ehret, P., Dowson, D., & Taylor, C. M. (2001). Thermal elastohydrodynamic analysis of circular contacts part 2: Non-Newtonian model. *Proceedings of the Institution of Mechanical Engineers, Part J: Journal of Engineering Tribology*, 215(4), 353-362.
- Krupka, I., Bair, S., Kumar, P., Khonsari, M. M., & Hartl, M. (2009). An experimental validation of the recently discovered scale effect in generalized Newtonian EHL. *Tribology Letters*, 33(2), 127-135.
- Kumar, P., & Khonsari, M. M. (2009). Traction in EHL line contacts using free-volume pressure-viscosity relationship with thermal and shear-thinning effects. *Journal of Tribology*, 131(1), 011503.
- Katyal, P., & Kumar, P. (2012). Central film thickness formula for shear thinning lubricants in EHL point contacts under pure rolling. *Tribology international*, 48, 113-121.
- Loewenthal, S. H., & Rohn, D. A. (1983). Regression analysis of traction characteristics of two traction fluids (Vol. 2154). *National Aeronautics and Space Administration*, Scientific and Technical Information Branch.
- Lubrecht, A. A. (1987). *Numerical Solution of the EHL Line and Point Contact Problem Using Multigrid Techniques*. [Ph.D thesis], University of Twente, Enschede, The Netherlands.
- Lubrecht, A. A., Venner, C. H., & Colin, F. (2009). Film thickness calculation in elasto-hydrodynamic lubricated line and elliptical contacts: the Dowson, Higginson, Hamrock contribution. *Proceedings of the Institution of Mechanical Engineers, Part J: Journal of Engineering Tribology*, 223(3), 511-515.
- Larsson, R., & Andersson, O. (2000). Lubricant thermal conductivity and heat capacity under high pressure. *Proceedings of the Institution of Mechanical Engineers, Part J: Journal of Engineering Tribology*, 214(4), 337-342.
- Larsson, R., Kassfeldt, E., Byheden, Å., & Norrby, T. (2001). Base fluid parameters for elastohydrodynamic lubrication and friction calculations and their influence on lubrication capability. *Journal of Synthetic Lubrication*, 18(3), 183-198.
- Liu, X., Jiang, M., Yang, P., & Kaneta, M. (2005). Non-Newtonian thermal analyses of point EHL contacts using the Eyring model. *J. Trib.*, 127(1), 70-81.
- Liu, X., & Yang, P. (2008). Influence of solid body temperature on the thermal EHL behavior in circular contacts. *Journal of Tribology*, 130(1).
- Liu, X., Cui, J., & Yang, P. (2012). Size effect on the behavior of thermal elastohydrodynamic lubrication of roller pairs. *Journal of Tribology*, 134(1), 011502.
- Liu, X., Ma, M., Yang, P., & Guo, F. (2018). A new method for Eyring shear-thinning models in elliptical contacts thermal elastohydrodynamic lubrication. *Journal of Tribology*, 140(5), 051503.
- Liu, Y., Wang, Q. J., Bair, S., & Vergne, P. (2007). A quantitative solution for the full shear-thinning EHL point contact problem including traction. *Tribology Letters*, 28(2), 171-181.
- Liu, H. C., Guo, F., Guo, L., & Wong, P. L. (2015). A dichromatic interference intensity modulation approach to measurement of lubricating film thickness. *Tribology Letters*, 58(1), 15.
- Liu, H. C., Zhang, B. B., Bader, N., Guo, F., Poll, G., & Yang, P. (2019). Crucial role of solid body temperature on elastohydrodynamic film thickness and traction. *Tribology international*, 131, 386-397.
- Liu, H. C., Zhang, B. B., Bader, N., Poll, G., & Venner, C. H. (2020a). Influences of solid and lubricant thermal conductivity on traction in an EHL circular contact. *Tribology International*, 146, 106059.
- Liu, H. C., Zhang, B. B., Bader, N., Venner, C.H., & Poll, G. (2020b). Simplified traction prediction for highly loaded rolling / sliding EHL contacts. *Tribology International*, 106335.
- Lohner, T., Michaelis, K., & Stahl, K. (2016). Limiting shear stress formulation for TEHL simulation. *Proceedings of the 7th ECCOMAS Congress, Greece 2016*, pp. 5-10. DOI: 10.7712/100016.1910.9225.
- Liu, P., Lu, J., Yu, H., Ren, N., Lockwood, F. E., & Wang, Q. J. (2017). Lubricant shear thinning behavior correlated with variation of radius of gyration via molecular dynamics simulations. *The Journal of chemical physics*, 147(8), 084904.
- Lu, J., Reddyhoff, T., & Dini, D. (2018). 3D measurements of lubricant and surface temperatures within an elastohydrodynamic contact. *Tribology Letters*, 66(1), 7.
- Li, Z., Lu, Y., Zhang, C., Dong, J., Zhao, X., & Wang, L. (2019). Traction behaviours of aviation lubricating oil and the effects on the dynamic and thermal characteristics of high-speed ball bearings. *Industrial Lubrication and Tribology*, 72(1):15-23.
- Martin, H. M. (1916). Lubrication of gear teeth. *Engineering*, 102, 119.
- Murnaghan, F. D. (1944). The compressibility of media under extreme pressures. *Proceedings of the national academy of sciences of the United States of America*, 30(9), 244.
- Mooney, M. (1957). A theory of the viscosity of a Maxwellian elastic liquid. *Transactions of the Society of Rheology*, 1(1), 63-94.
- MacDonald, J. R. (1966). Some simple isothermal equations of state. *Reviews of Modern Physics*, 38(4), 669.
- Mohrenstein-Ertel, A. (1984). Die Berechnung der hydrodynamischen Schmierung gekrümmter Oberflächen unter hoher Belastung und Relativbewegung (Calculation of the hydrodynamic lubrication for curved surfaces under high load and relative motion). *Fortschritt-Berichte VDI-Z, Reihe, 1*, 189.

- Markho, P. H. (1987). Highly accurate formulas for rapid calculation of the key geometrical parameters of elliptic Hertzian contacts. *Journal of tribology*, 109(4), 640-647.
- Moes, H. (1992). Optimum similarity analysis with applications to elastohydrodynamic lubrication. *Wear*, 159(1), 57-66.
- Myllerup, C. M., & Hamrock, B. J. (1993). Local effects in thin film lubrication. In *Tribology Series* (Vol. 25, pp. 39-57). Elsevier.
- Ma, M. T. (1998). Effects of the non-Newtonian behavior of lubricants on the temperature, traction, and film thickness in an elliptical EHD contact under heavy loads. *Journal of tribology*, 120(4):685-694
- Morgado, P. L., Otero, J. E., Lejarraga, J. S. P., Sanz, J. M., Lantada, A. D., Munoz-Guijosa, J. M., ... & García, J. M. (2009). Models for predicting friction coefficient and parameters with influence in elastohydrodynamic lubrication. *Proceedings of the Institution of Mechanical Engineers, Part J: Journal of Engineering Tribology*, 223(7), 949-958.
- Mayer, C. (2010). *Reibung in hoch belasteten EHD-Wälzkontakten* (Doctoral dissertation, Hannover: Leibniz Universität Hannover).
- Marx, J. (2015). Weiterentwicklung und Inbetriebnahme eines Thermografiesystems zur Bestimmung der Temperatur in einem EHD-Kontakt (Bachelor dissertation, Hannover: Leibniz Universität Hannover).
- Martins, R. C., Fernandes, C. M., & Seabra, J. H. (2015). Evaluation of bearing, gears and gearboxes performance with different wind turbine gear oils. *Friction*, 3(4), 275-286.
- Martinie, L., & Vergne, P. (2016). Lubrication at extreme conditions: a discussion about the limiting shear stress concept. *Tribology Letters*, 63(2), 21.
- Mustak, O., Evcil, E., & Simsir, C. (2016). Simulation of through-hardening of SAE 52100 steel bearings—Part I: Determination of material properties: Simulation der Durchhärtung vom Wälzlagerstahl SAE 52100—Teil I: Bestimmung der Materialeigenschaften. *Materialwissenschaft und Werkstofftechnik*, 47(8), 735-745.
- Nelias, D., Legrand, E., Vergne, P., & Mondier, J. B. (2002). Traction behavior of some lubricants used for rolling bearings in spacecraft applications: experiments and thermal model based on primary laboratory data. *J. Trib.*, 124(1), 72-81.
- Ndiaye, S. N., Martinie, L., Philippon, D., Devaux, N., & Vergne, P. (2017). A quantitative friction-based approach of the limiting shear stress pressure and temperature dependence. *Tribology Letters*, 65(4), 149.
- Ndiaye, S., Martinie, L., Philippon, D., Gonon-Caux M, Margueritat J and Vergne P. (2020). On the Influence of Phase Change in Highly Loaded Frictional Contacts. *Tribol Lett*, 68, 54.
- Ohno, N., Shiyatake, A., Kumamoto, T., Nishina, S., Kuwano, N., & Hirano, F. (1997). Occurrence of shear bands at high pressure. In *Proceedings of the JAST Tribology Conference* (pp. 515-7). (in Japanese)
- Olver, A. V., & Spikes, H. A. (1998). Prediction of traction in elastohydrodynamic lubrication. *Proceedings of the Institution of Mechanical Engineers, Part J: Journal of Engineering Tribology*, 212(5), 321-332.
- Petrusevich, A. I. (1951). Fundamental conclusions from the contact-hydrodynamic theory of lubrication. *Izv. Akad. Nauk. SSSR (OTN)*, 2, 209-33.
- Plint, M. A. (1967). Third paper: traction in elastohydrodynamic contacts. *Proceedings of the Institution of Mechanical Engineers*, 182(1), 300-306.
- Paul, G. R., & Cameron, A. (1979). The ultimate shear stress of fluids at high pressures measured by a modified impact microviscometer. *Proceedings of the Royal Society of London. A. Mathematical and Physical Sciences*, 365(1720), 31-41.
- Piccigallo, B. (1996). A fast method for the numerical solution of thermal-elastohydrodynamic lubrication problems. *Wear*, 193(1), 56-65.
- Poll, G. W. G., & Wang, D. (2012). Fluid rheology, traction/creep relationships and friction in machine elements with rolling contacts. *Proceedings of the Institution of Mechanical Engineers, Part J: Journal of Engineering Tribology*, 226(6), 481-500.
- Ponjavic, A., Chennaoui, M., & Wong, JS (2013). Through-thickness velocity profile measurements in an elastohydrodynamic contact. *Tribology Letters*, 50 (2), 261-277.
- Porras-Vazquez, A., Martinie, L., Vergne, P., & Fillot, N. (2018). Independence between friction and velocity distribution in fluids subjected to severe shearing and confinement. *Physical Chemistry Chemical Physics*, 20(43), 27280-27293.
- Reynolds, O. (1886). IV. On the theory of lubrication and its application to Mr. Beauchamp tower's experiments, including an experimental determination of the viscosity of olive oil. *Philosophical transactions of the Royal Society of London*, 177, 157-234.
- Roelands, C. J. A. (1966). *Correlational aspects of the viscosity-temperature-pressure relationship of lubricating oils*. Doctoral thesis, Technische Hogeschool te Delt.
- Richmond, J., Nilsson, O., & Sandberg, O. (1984). Thermal properties of some lubricants under high pressure. *Journal of Applied Physics*, 56(7), 2065-2067.
- Ramesh, K. T., & Clifton, R. J. (1987). A pressure-shear plate impact experiment for studying the rheology of lubricants at high pressures and high shearing rates. *Journal of Tribology*, 109(2), 215-222.
- Roland, C. M., Bair, S., & Casalini, R. (2006). Thermodynamic scaling of the viscosity of van der Waals, H-bonded, and ionic liquids. *The Journal of Chemical Physics*, 125(12), 124508.

- Reddyhoff, T., Spikes, H. A., & Olver, A. V. (2009a). Compression heating and cooling in elastohydrodynamic contacts. *Tribology letters*, 36(1), 69-80.
- Reddyhoff, T., Spikes, H. A., & Olver, A. V. (2009b). Improved infrared temperature mapping of elastohydrodynamic contacts. *Proceedings of the Institution of Mechanical Engineers, Part J: Journal of Engineering Tribology*, 223(8), 1165-1177.
- Reddyhoff, T., Schmidt, A., & Spikes, H. (2019). Thermal conductivity and flash temperature. *Tribology Letters*, 67(1), 22.
- Raisin, J., Fillot, N., Dureisseix, D., Vergne, P., & Lacour, V. (2015). Characteristic times in transient thermal elastohydrodynamic line contacts. *Tribology International*, 82, 472-483.
- Smith, F. W. (1960). Lubricant behavior in concentrated contact—some rheological problems. *ASLE Transactions*, 3(1), 18-25.
- Sadeghi, F., & Dow, T. A. (1987). Thermal effects in rolling/sliding contacts: Part 2-Analysis of thermal effects in fluid film. *Journal of Tribology*, 109(3):512-517.
- Sadeghi, F., & Sui, P. C. (1990). Thermal elastohydrodynamic lubrication of rolling/sliding contacts. *J. Tribol*, 112(2): 189-195.
- Stachowiak, G. W. and Batchelor A. W. *Engineering Tribology*, Elsevier Science Publishers B.V., Amsterdam, 1993.
- Sharif, K. J., Evans, H. P., Snidle, R. W., & Newall, J. P. (2004). Modeling of film thickness and traction in a variable ratio traction drive rig. *J. Trib.*, 126(1), 92-104.
- Spikes, H., & Jie, Z. (2014). History, origins and prediction of elastohydrodynamic friction. *Tribology Letters*, 56(1), 1-25.
- Schirru, M. M., & Dwyer-Joyce, R. S. (2016). A model for the reflection of shear ultrasonic waves at a thin liquid film and its application to viscometry in a journal bearing. *Proceedings of the Institution of Mechanical Engineers, Part J: Journal of Engineering Tribology*, 230(6), 667-679.
- Shirzadegan, M., Björling, M., Almqvist, A., & Larsson, R. (2016). Low degree of freedom approach for predicting friction in elastohydrodynamically lubricated contacts. *Tribology International*, 94, 560-570.
- Saito, T., & Lewis, A. (2018). Development of Traction Fluid Property Tables for a Toroidal CVT Multi-Body Simulation. *SAE Technical Paper* (No. 2018-01-1061).
- Spikes, H. (2018). Stress-augmented thermal activation: Tribology feels the force. *Friction*, 6(1), 1-31.
- Tabor, D. (1981). The role of surface and intermolecular forces in thin film lubrication. In *Tribology Series* (Vol. 7, pp. 651-682). Elsevier.
- Tower, B. (1883). First report on friction measurement. *Proc. Inst. Mech. Eng.*, 1883, Nov, pp. 632-659
- Tanner, R. I. (1985). *Engineering Rheology*. Clarendon Press, Oxford.
- Venner, C. H. (1991). *Multilevel solution of the EHL line and point contact problems*. (PhD. Thesis) University of Twente. Enschede, The Netherlands.
- Venner, C. H., Couhier, F., Lubrecht, A. A., & Greenwood, J. A. (1997). Amplitude reduction of waviness in transient EHL line contacts. In *Tribology Series* (Vol. 32, pp. 103-112). Elsevier.
- Venner, C. H., & Lubrecht, A. A. (Eds.). (2000). *Multi-level methods in lubrication*. Elsevier.
- Vergne, P., & Bair, S. (2014). Classical EHL versus quantitative EHL: a perspective part I—real viscosity-pressure dependence and the viscosity-pressure coefficient for predicting film thickness. *Tribology Letters*, 54(1), 1-12.
- Weitz, A., & Wunderlich, B. (1974). Thermal analysis and dilatometry of glasses formed under elevated pressure. *Journal of Polymer Science: Polymer Physics Edition*, 12(12), 2473-2491.
- Wilson, W. R. D., & Sheu, S. (1983). Effect of inlet shear heating due to sliding on elastohydrodynamic film thickness. *Journal of Lubrication Technology*, 105(2):187-188.
- Wikström, V., & Höglund, E. (1994). Investigation of parameters affecting the limiting shear stress-pressure coefficient: a new model incorporating temperature. *ASME J Tribol*, 116:612-620.
- Wong, P. L., Lingard, S., & Cameron, A. (1995). High pressure viscosity and shear response of oil using the rotating optical micro-viscometer. In *Tribology Series* (Vol. 30, pp. 199-205). Elsevier.
- Willermet, P. A., McWatt, D. G., & Wedeven, L. D. (1999). Traction behavior under extreme conditions. *SAE Technical Paper* (No. 1999-01-3612).
- Werner, M., Baars, A., Eder, C., & Delgado, A. (2008). Thermal conductivity and density of plant oils under high pressure. *Journal of Chemical & Engineering Data*, 53(7), 1444-1452.
- Wang, W. Z. (2013). EHL, Full numerical solution methods. In: Wang Q.J., Chung YW. (eds) *Encyclopedia of Tribology*. Springer, Boston, MA.
- Wilzer, J., Lüdtké, F., Weber, S., & Theisen, W. (2013). The influence of heat treatment and resulting microstructures on the thermophysical properties of martensitic steels. *Journal of Materials Science*, 48(24), 8483-8492.
- Washizu, H., Ohmori, T., & Suzuki, A. (2017). Molecular origin of limiting shear stress of elastohydrodynamic lubrication oil film studied by molecular dynamics. *Chemical Physics Letters*, 678, 1-4.
- WTC. (2017). Opening video. *Word Tribology Conference*. Tsinghua University.
- Wang, J., & Zhu D. (2019). *Interfacial mechanics: theories and methods for contact and lubrication*. CRC Press.

- Yasuda, K. Y., Armstrong, R. C., & Cohen, R. E. (1981). Shear flow properties of concentrated solutions of linear and star branched polystyrenes. *Rheologica Acta*, 20(2), 163-178.
- Yasutomi, S., Bair, S., & Winer, W. O. (1984). An application of a free volume model to lubricant rheology I—dependence of viscosity on temperature and pressure. *Journal of tribology*, 106(2), 291-302.
- Yang, P., & Wen, S. Z. (1990). A generalized Reynolds equation for non-Newtonian thermal elastohydrodynamic lubrication. *ASME J Tribol*, 112(4):631-6.
- Yang, P. (1998). *Numerical analysis of fluid lubrication*. National Defense Industry Press: Beijing, China (in Chinese).
- Yang, P., Qu, S., Kaneta, M., & Nishikawa, H. (2001). Formation of steady dimples in point TEHL contacts. *J. Trib.*, 123(1), 42-49.
- Yang, P., & Liu, X. (2009). Effects of solid body temperature on the non-Newtonian thermal elastohydrodynamic lubrication behaviour in point contacts. *Proceedings of the Institution of Mechanical Engineers, Part J: Journal of Engineering Tribology*, 223(7), 959-969.
- Yang, P. (2013). Thermal EHL Theory. In: Wang QJ, Chung YW. (eds) *Encyclopedia of Tribology*. Boston:Springer.
- Yagi, K., Kyogoku, K., & Nakahara, T. (2004). Relationship between temperature distribution in EHL film and dimple formation. In *International Joint Tribology Conference*, Vol. 41812, pp. 459-468.
- Zhu, D. (1984). *A Thermal analysis of the elastohydrodynamic lubrication in elliptical contacts* (Doctoral dissertation, Ph. D. thesis, Tsinghua University, Beijing, China (in Chinese).
- Zhu, D., & Wen, S. Z. (1984). A full numerical solution for the thermoelastohydrodynamic problem in elliptical contacts, *J. Tribol.*, 106(2):246-254.
- Zhu, D. (2013). Thermal reduction of EHL film thickness. In: Wang QJ, Chung YW. (eds) *Encyclopedia of Tribology*. Boston:Springer.
- Zhang, J., Tan, A., & Spikes, H. (2017). Effect of base oil structure on elastohydrodynamic friction. *Tribology Letters*, 65(1), 13.
- Zhang, J., & Spikes, H. (2020). Measurement of EHD friction at very high contact pressures. *Tribology Letters*, 68(1), 1-12.
- Zhang, M., Wang, J., Yang, P., Shang, Z., Liu, Y., & Dai, L. (2020). A thermal EHL investigation for size effect of finite line contact on bush-pin hinge pairs in industrial chains. *Industrial Lubrication and Tribology*. DOI:10.1108/ILT-10-2019-0448.

Lebenslauf

Persönliche Daten

Name	HaiChao LIU
Geburtsdatum	26. September 1990
Geburtsort	YanTai, ShanDong, China
Staatsangehörigkeit	chinesisch
Status	Ledig

Berufliche Tätigkeit

seit 10/2016	Doktorand am Institut für Maschinenkonstruktion und Tribologie (IMKT), Fakultät für Maschinenbau, Leibniz Universität Hannover
06/2014 - 09/2015	Wissenschaftlicher Mitarbeiter, Fakultät für Maschinenbau und Biomedizintechnik, City University of Hong Kong

Ausbildung und Schule

07/2013 - 01/2016	Masterstudium Maschinenbau an der Technische Universität Qingdao
10/2009 - 06/2013	Bachelorstudium Maschinenbau an der Technische Universität Qingdao
09/2006 - 06/2009	No.4 Schule HaiYang, YanTai
09/2002 - 06/2006	No.2 Schule XingCun, YanTai